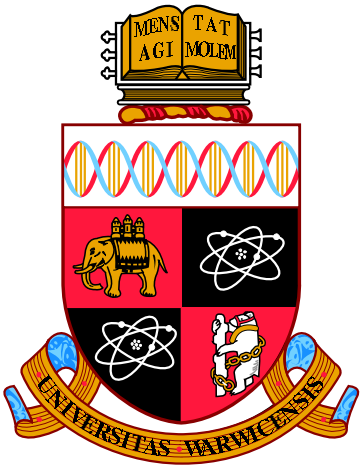

Defect screening of pipelines using circumferential guided waves

by

Matthew Alexander Clough

Thesis

Submitted to the University of Warwick

for the degree of

Doctor of Engineering in Non-Destructive Evaluation

Department of Physics

September 2016

Contents

List of Tables **v**

List of Figures **vi**

Acknowledgments **xii**

Declarations **xiii**

Abstract **xv**

Abbreviations **xvi**

Nomenclature **xvii**

Chapter 1 Introduction **1**

1.1 Industrial Motivation 1
1.2 Non Destructive Evaluation 5
1.3 Visual and basic surface techniques 5
1.4 Thermography 6
1.5 Electromagnetic methods 7
1.5.1 Eddy currents 7
1.5.2 Magnetic flux leakage 8
1.5.3 Magnetic Tomography method and Metal Magnetic Memory method 9
1.6 Radiography 10
1.7 Ultrasonics 11
1.7.1 Bulk wave ultrasonics 12
1.7.2 Guided wave ultrasonics 13
1.7.3 Generation of guided waves 15
1.8 Thesis Outline 16

Chapter 2 Ultrasonic Inspection Theory **18**
2.1 Ultrasonic Waves and their propagation 18
2.2 Ultrasound in elastic media 19
2.3 Theory of elasticity 19
2.4 Waves in elastic media 21
2.5 Longitudinal and Shear waves 23
2.6 Interactions with interfaces 24
2.7 Basic thickness measurement 25
2.8 Phase velocity vs group velocity 27
2.9 Guided Waves and Surface Acoustic Waves 28
2.10 Guided waves 29
2.10.1 Lamb Waves 30
2.10.2 SH Waves 31
2.11 Dispersion curves in different geometries 36
2.12 Dispersion curves in an annulus 38
2.13 Ultrasonic Transduction 41
2.13.1 Piezoelectric transducers 42
2.13.2 Principles of EMATs 44
2.13.3 Skin effect 45
2.13.4 Lorentz force 47
2.13.5 Magnetisation force 49
2.13.6 Magnetostriction 50
2.13.7 Receiving ultrasound with EMATs 51
2.13.8 The Periodic Permanent Magnet EMAT 53
2.13.9 Bandwidth of Probes 56
2.13.10 Alternative Methods for the generation of ultrasound 62

Chapter 3 Experimental system **64**
3.1 Basic sample measurements 65
3.2 Optimising generation frequency 65
3.3 Confirming Shear wave speed in sample 76
3.4 Planning an inspection 77
3.4.1 Procedure for setting up an inspection 77
3.4.2 Probe positioning 78
3.5 Characterisation of Pulser Receiver system 80
3.5.1 Pulser receiver considerations 80
3.5.2 Experimental rig considerations 81

Chapter 4 Finite Element Analysis **84**
4.1 Finite Element theory 85
4.2 Spatial profiles as an input 89

Chapter 5 Experimental results **93**
5.1 Samples of interest 93
5.2 Defects 96
5.3 Pipe Screening 98
5.3.1 Defect effect on the circumferential SH0 mode 98
5.3.2 Defect effect on the circumferential SH1 mode 100
5.4 Initial measurements 102
5.4.1 Sample Parameters 102
5.4.2 Recorded data and experimental setup 104
5.4.3 Filtering 104
5.4.4 Circumferential scan raw data 105
5.4.5 Encoded scan data 113
5.4.6 Axial sizing of defects 117
5.4.7 Presentation of encoded scans 120
5.4.8 Reflections and mode conversion 122
5.5 Finite element modelling of the artificial defect 126
5.5.1 Graphical representation of mode behaviour. 134
5.5.2 Different defect depths. 136
5.5.3 Different circumferential extent defects. 140
5.6 Conclusions 144

Chapter 6 In-service corrosion patches, calibration defects and welds **147**
6.1 In-service defects 148
6.1.1 Manual Scan 150
6.1.2 Encoded Scan 152
6.2 Blind trials 156
6.3 Multiple variable sized defects 159
6.4 Modelling different geometries, other calibration defects. 166
6.5 Flat bottomed holes experimentally 170
6.6 Welded areas 172
6.7 Conclusions 175

Chapter 7 Conclusions **177**
7.1 Main Conclusions 177
7.2 Further work 181

References **184**

List of Tables

2.1 Summary of design parameters for 10 mm and 8.8 mm wavelength PPM EMATs used in the Thesis 56

5.1 Summary of the pipe samples for which data is shown in this Thesis. 95

6.1 Summary of the defect axial extent information from the 864 mm circumference 6.4 mm pipe wall thickness sample. 164

List of Figures

1.1 Schematic diagram of common pipe supports. 2
1.2 Schematic diagram of common defects in a pipeline. 3
1.3 Schematic diagram of an in-line inspection pig. 4
1.4 Schematic diagram of the shear horizontal wave EMAT system that is considered in this thesis. 4
1.5 Schematic diagram of the standard apparatus for thermographic testing. 7
1.6 Schematic diagram of an eddy current inspection. 8
1.7 Schematic diagram of the standard equipment for Magnetic Flux Leakage testing of pipelines. 9
1.8 Schematic diagram of the standard apparatus for radiographic double wall imaging of pipeline. 10
1.9 Schematic of the standard apparatus for CHIME inspections showing the waves generated and interrogated area. 13
1.10 Schematic of apparatus for Long range guided wave ultrasonic testing of pipeline. 16

2.1 Particle motion and direction of propagation of different ultrasonic waves. 24
2.2 Schematic diagram of the thickness measurement and defect depth measurements using a pulse echo technique. 26
2.3 Schematic diagram showing a waveform and its envelope. 28
2.4 Schematic diagram illustrating the generation of Lamb waves. 31
2.5 Schematic diagram showing the generation of shear horizontal guided waves 32
2.6 Displacement profiles through the thickness of the plate for SH wave forces. 34
2.7 SH guided wave phase velocity dispersion curve for a steel plate . . . 35
2.8 SH guided wave group velocity dispersion curve for a steel plate . . . 36

2.9 SH wave phase velocity in a plate and circumferentially around a pipe of the same wall thickness. 40
2.10 SH wave group velocity in a plate and circumferentially around a pipe of the same wall thickness. 40
2.11 Schematic of a basic design of a piezoelectric transducer including an active element, backing and matching layers. 44
2.12 Schematic diagram of the Lorentz force mechanism of force generation by EMATs. 48
2.13 Construction of the PPM EMAT, schematic plan and photograph of the probe structure. 54
2.14 Schematic diagram of the side view of a PPM array. 54
2.15 Schematic diagram of the generation of the Lorentz force in a sample using the PPM array. 55
2.16 SH wave phase velocity dispersion curves for a plate with nominal wavelength line. 57
2.17 SH wave phase velocity dispersion curves for a steel plate with the spatial bandwidth indicated. 58
2.18 Illustration of the in plane SH forces generated by the PPM EMAT and the corresponding spatial frequency. The use of a similar profile transmitter and receiver will narrow this bandwidth as will the addition of more magnets in the array. 59
2.19 Frequency and wavelength bandwidths of an 8.8 mm nominal wavelength probe excited with a 5 cycle tone burst at a frequency of 386 kHz onto a 7 mm thick 170 mm outer diameter pipe sample. 60
2.20 Operation areas of an 8.8 mm nominal wavelength EMAT probe for a plate and pipe. 61
2.21 Amplitudes of the peak excitation frequency for the SH0 and SH1 modes. 62
2.22 Amplitudes of the peak excitation frequency for the CSH0 and CSH1 modes. 62

3.1 Techniques used for carrying out Shear wave speed measurement and frequency sweep measurements. 67
3.2 Frequency sweep in the axial direction to determine optimum operation frequency of a set of probes on a sample. 68
3.3 Figure highlighting the different modes in the axial frequency sweep. 68

3.4 A-scan and frequency data for optimum frequency of operation of the SH guided wave modes in a plate. 69
3.5 Orientation of the probes for a frequency sweep in the circumferential direction. 70
3.6 Frequency sweep data for the circumferentially travelling guided waves. 71
3.7 Figure highlighting the different modes in the circumferential frequency sweep. 72
3.8 A-scan and frequency data for optimum frequency of operation of the SH guided wave modes in a pipe. 74
3.9 Figure highlighting the spatial profiles of probes in different orientations. 75
3.10 Confirmation of shear wave speed in a sample. 76
3.11 Schematic diagram of the positioning of probes on the pipe surface and of the EMAT rig used to carry the probes. 78
3.12 Schematic diagram of the different paths the ultrasound can take around the pipe circumference. 79
3.13 Photograph of the experimental rig used for scanning in this Thesis. 82
3.14 Photograph of the experimental rig used for scanning in the subsea application. 83

4.1 Illustration of the concept of meshing in finite element methods. . . 86
4.2 Illustration of convergence in a finite element model. 87
4.3 Illustration of the difficulty of representing a curved surface with square elements. 88
4.4 Illustration of how the spatial profile is used with the excitation signal and mapped to the mesh. 91

5.1 Diagram showing how the EMAT is held onto the pipe and the extra lift off that a coating creates. 96
5.2 Photograph showing an in-service corrosion patch. 97
5.3 Phase and group velocity dispersion curves for a 7 mm pipe wall thickness, 86 mm outer radius sample with operation points for a clear area and thinner walled area indicated for the CSH0 mode. . . 99
5.4 Phase and group velocity dispersion curves for a 7 mm pipe wall thickness, 86 mm outer radius sample with operation points for a clear area and thinner walled area indicated for the CSH1 mode. . . 101
5.5 Schematic diagram showing the dimensions of the pipe sample with the artificial defect. 103

5.6 Time and frequency records for the receiver not attached to the sample to show signal leakage from within the experimental system. . . . 105
5.7 Image of the filter application screen for the Innerspec system. . . . 106
5.8 A-scan data from the experimental system illustrating different levels of filtering. . . . 108
5.9 A-scan data for a defect free sample with a 7 mm pipe wall thickness and 534 mm outer circumference. . . . 109
5.10 Illustration of the areas of the A-scan signal that will be affected by a defect at different circumferential positions. . . . 110
5.11 STFT representation of the received data in a defect free area of 7 mm pipe wall thickness, 534 mm circumference pipe. . . . 111
5.12 Encoded scan of the 7 mm pipe wall thickness, 534 mm circumference sample with artificial wall thinning defect. . . . 114
5.13 Encoded scan of the 7 mm pipe wall thickness, 534 mm circumference sample with single artificial wall thinning defect, for a smaller axial distance. . . . 115
5.14 Encoded scan of the 7 mm pipe wall thickness, 534 mm circumference sample with single artificial wall thinning defect, at a higher frequency. 116
5.15 Time gated encoded scan of the 7 mm pipe wall thickness, 534 mm circumference sample with single artificial wall thinning defect to isolate the long path CSH1 mode. . . . 117
5.16 Amplitude profile of the RMS of the long path CSH1 mode. . . . 118
5.17 Normalised amplitude profile of the RMS of the long path CSH1 mode, with the outer extent of the defect effect shown. . . . 120
5.18 Adjusted amplitude encoded scan, showing low amplitude modes. . . 121
5.19 Adjusted amplitude encoded scan, showing different modes that arise from interaction of the guided waves with the defect. . . . 123
5.20 A-scan data from experimental scans showing interaction with a defect and schematic representation of the paths of these signals. . . . 124
5.21 Encoded adjusted amplitude scans of the sample, with the defect at different circumferential positions relative to the transducers. . . . 125
5.22 Comparison of A-scan data in obtained experimentally and in a finite element simulation for a defect free sample. . . . 128
5.23 Visualisation of the in-plane velocity generated by the transducer area in the finite element simulation. . . . 129

5.24 Visualisation of the in-plane velocity in the sample after an amount of time has passed in the finite element simulation, illustrating the presence of different modes. 130
5.25 Schematic of the defect and remaining wall thickness of the sample in the defect area. 132
5.26 A-scan data from simulated interaction with a defect and schematic representation of the paths of these signals. 132
5.27 Comparison of experimental and simulated data for the interaction of the guided waves with a defect. 133
5.28 Graphical representations of the propagation of the CSH0 mode and its interaction with a defect. 134
5.29 Graphical representations of the interaction of the CSH1 mode with a defect. 135
5.30 Graphical representation of the reflected CSH1 mode from a defect and the modes travelling in the opposite direction around the pipe. . 136
5.31 Simulated STFT data for defects of the same circumferential extent but different depths. 138
5.32 Simulated STFT data for defects with the same depth but varying circumferential extent, above the cut-off thickness of the CSH1 mode. 142
5.33 Simulated STFT data for defects with the same depth but varying circumferential extent, below the cut-off thickness of the CSH1 mode. 143

6.1 Photograph of defect with single corrosion patch style defect. 149
6.2 Screening scan of a single corrosion patch defect using transducers with minimised separation, on a 7 mm pipe wall thickness, 534 mm circumference sample. 150
6.3 Raw A-scan data for a defect free area of a 7 mm pipe wall thickness, 534 mm circumference sample, with minimised transducer separation. 151
6.4 A-scan signals from the defect area of a 7 mm pipe wall thickness, 534 mm circumference sample for different levels of wall loss. 152
6.5 Schematic diagram of the in-service corrosion patch scanned here (not to scale) 153
6.6 Adjusted encoded amplitude scan data for a real corrosion patch in a 7 mm pipe wall thickness, 534 mm circumference sample. 154
6.7 A-scan data for different axial positions in the pipe, to show the difference in behaviour as different parts of the defect are encountered. 155

6.8 Adjusted encoded amplitude scan data for various blind trial samples of pipe wall thickness 9 mm and 864 mm circumference. 158
6.9 Photographs of different defects to show a range of corrosion stages. 160
6.10 Schematic diagram of the axial and circumferential positioning of defects in the multiple defect sample. 161
6.11 Encoded amplitude scan data of a long axial extent sample with multiple defects at various circumferential and axial positions, with a 6.4 mm pipe wall thickness and 861 mm circumference. 162
6.12 Schematic diagrams of the flat bottomed and constant depth defects in a pipe. 167
6.13 A-scan data and STFT representation of a simulated flat bottomed hole defect in a 534 mm circumference, 7 mm pipe wall thickness sample. 169
6.14 A-scan data and STFT representation of a simulated flat bottomed hole defect in a 534 mm circumference, 7 mm pipe wall thickness sample. 170
6.15 Schematic diagram of the samples with artificial flat bottomed defects. 171
6.16 Experimental encoded scan data for closely spaced 20 and 30 mm circumference flat bottomed defects of varying depths on the internal and external surfaces of a 7.5 mm pipe wall thickness, 535 mm circumference sample. 171
6.17 Dimensions of the sample and positions of the welds for the sample with a wrapper plate. 173
6.18 Encoded scan data for an 8.18 mm pipe wall thickness, 695 mm circumference sample with welded wrapper plate and artificial defects. 174

Acknowledgments

Firstly I must thank my academic supervisor, Professor Steve Dixon for giving me the opportunity to work on this project and for his support and guidance throughout. I must also thank my industrial supervisor Matthew Fleming and others at Sonomatic who have helped me or provided data. I would like to thank the whole of the ultrasonics group for their help with my work particularly Phil Petcher for helping me obtain various sets of data. Thanks go to all the members of physics I have shared an office or coffee breaks with for our chats especially Sam Hill and Will Blackmore for sport related talks. I'd also like to thank Yav Arnaudov for helping me with Matlab and putting up with my appalling code, as well as for many fruitful discussions about Bulgaria. Tobias Eriksson must also get a mention for his knowledge of obscure tv and film references.

I would like to thank the canoe and canoe polo clubs at the university for filling numerous evenings and weekends with great fun. I must of course give thanks to my family for their support and encouragement, without them this work wouldn't have been possible. A special thanks in that regard must go to Andy and Madi for numerous instances of moving my things, giving up a room to store them and giving me a place to stay when I didn't have one. Most importantly, I must thank my fiancée Claire Wooldridge for her love, support and patience throughout all our time together and particularly in the last four years when her help and encouragement has been invaluable.

Lastly, I would like to acknowledge the funding provided by the Research Centre for Non-Destructive Evaluation (RCNDE) and by Sonomatic Ltd. which have made this work possible.

Declarations

I declare that the work presented in this thesis is my own except where stated otherwise and was carried out entirely at the University of Warwick or in conjunction with the sponsoring company Sonomatic Ltd during the period between October 2012 and September 2016, under the supervision of Prof. Steve Dixon. The research reported here has not been submitted, either wholly or in part, in this or any other academic institution, for admission to a higher degree. Parts of this work and other work not reported in this thesis have appeared in other forms, listed here.
Peer-reviewed journal articles:

- M.Clough, M.Fleming and S.Dixon, "Circumferential Guided Wave EMAT System for Pipeline Screening using Shear Horizontal ultrasound", *NDT & E International*, vol. 86, pp. 20 - 27, March 2017

Conference proceedings:

- M.Clough, M.Fleming, M.Stone and S.Dixon, "Evaluating an SH wave EMAT system for the screening of petrochemical pipeline and extending capability into quantitative defect measurements" in 54th Annual British Conference of Non-Destructive Testing (NDT 2015), Telford, UK, Sep 2015

- M.Clough, M.Fleming, S.Dixon and M.Stone,"Evaluating an SH wave EMAT system for pipeline screening and extending into quantitative defect measurements", in AIP Conference Proceedings, vol 1706, Minneapolis (Minnesota), USA: AIP, 2015

- M.Clough and S.Dixon, "Guided Wave EMATs for the detection of corro-

sion in pipelines" in 53rd Annual Conference of the British Institute of Non-Destructive Testing (NDT 2014), Manchester, UK, Sep 2014

Presentations at national and international conferences:

- M.Clough, M.Fleming, M.Stone and S.Dixon, "Evaluating an SH wave EMAT system for the screening of petrochemical pipeline and extending capability into quantitative defect measurements" presented at 54th Annual British Conference of Non-Destructive Testing (NDT 2015), Telford, UK, Sep 2015. Talk

- M.Clough, M.Fleming, S.Dixon and M.Stone,"Evaluating an SH wave EMAT system for pipeline screening and extending into quantitative defect measurements", presented at the Annual Review of Progress in Quantitative Nondestructive Evaluation (QNDE 2015) Minneapolis (Minnesota), USA July 2015. Talk

- M.Clough, M.Fleming, S.Dixon and M.Stone,"SH Wave EMAT System for Pipeline Screening and Extension into Quantitative Defect Measurements", presented at the Annual Review of Progress in Quantitative Nondestructive Evaluation (QNDE 2015) Minneapolis (Minnesota), USA July 2015. Poster

- M.Clough and S.Dixon, "Guided Wave EMATs for the detection of corrosion in pipelines" presented at 53rd Annual Conference of the British Institute of Non-Destructive Testing (NDT 2014), Manchester, UK, Sep 2014. Talk

Abstract

A system for the shear horizontal guided wave screening of pipelines is developed and optimised. The system is considered in terms of the circumferential shear horizontal guided wave behaviour as opposed to the majority of other studies that approximate the structure of an unwrapped pipe as a plate. This allows for consideration of the effect of a defect on both the lowest order symmetric and antisymmetric modes. The assessment of the guided wave interaction with a corrosion patch defect is carried out for a basic defect from which the axial sizing can be determined from encoded scans of the sample and amplitude changes. The circumferential positioning capabilities can be found using the effect seen on different modes and the presence of reflections. The behaviour of the two lowest order shear horizontal modes when incident on a defect above and below the cut off thickness of the lowest order antisymmetric mode can be seen in the experimental measurements and visualised through finite element modelling.

Once the behaviour of the modes when they interact with different depths of a defect is understood, the technique is expanded to a real corrosion patch of known dimensions. It is extended to more complex samples with multiple, varied positioned corrosion patches and blind trial situations where the geometry and depth of defects is unknown. Although the size and depth of these defects is unknown, the knowledge of the interaction of the waves with the other defects can be used to estimate the defect size and depth. The calculation of the remaining wall thickness in the current iteration of the system is limited to a broad range, unless there is prior knowledge of the defect geometry. This is because the defect geometry is shown to have a large effect on the arrival time of the through transmitted waves. Consideration is given to the effect of welds on a signal and the differences between calibration defects and real corrosion patch style defects.

The system has been tested further in extended blind trials and proved effective as a screening tool for the detection of corrosion patch style defects, with detection capabilities dependent on the axial size and depth of the defect.

Abbreviations

Chap.	Chapter
CHIME	Creeping/Head wave Inspection MEthod
CSH	Circumferential Shear Horizontal
Def. Dims.	Defect dimensions
DFT	Discrete Fourier Transform
Dims.	Dimensions
EMAT	ElectroMagnetic Acoustic Transducer
FEA	Finite Element Analysis
FFT	Fast Fourier Transform
ILI	In Line Inspection
MFL	Magnetic Flux Leakage Acoustic Transducer
NDE	Non-Destructive Evaluation
NDT	Non-Destructive Testing
OD	Outer Diameter
PPM	Periodic Permanent Magnet
Rx	Receiver
SAW	Surface Acoustic Wave
SH	Shear Horizontal
STFT	Short Time Fourier Transform
ToFD	Time of Flight Diffraction
Tx	Transmitter
WT	Wall Thickness

Nomenclature

A	Area	F_s	Surface force
A_0	Amplitude	fd	Frequency thickness
A,B	Arbitrary constants	f_0	Fundamental working
B	Magnetic field		frequency
a	Inner radius	H	Magnetic field strength
b	Outer radius	h	Plate thickness/2,
C	Acoustic wave velocity		pipe thickness
	(thickness measurement)	I	Current
C_{ijkl}	Elastic stiffness tensor	i	$\sqrt{(-1)}$
c_{11}, c_{44}	Material constants	J	Current density
c_g	Group velocity	J_e	Eddy current density
c_p	Phase velocity	$J_{\hat{k}}(x)$	Bessel function of the
D	Electrical displacement		1st kind
d	Distance (sample thickness), depth	k	Wavenumber
d_e	Thickness of a piezoelectric element	M	Magnetisation
d_p	Piezoelectric charge constant	m	Mass of electron
E	Electric field	N	Ion density
e	Electron charge	q	Charge
F	Force	S	Strain (piezoelectrics)
F_v	Body force per unit volume	s^E	Mechanical compliance

Continued on the next page

S_{IJ}^{H}	Component of the compliance matrix (piezomagnetic)
S_I	Component of the strain (piezomagnetic)
T	Stress (piezoelectric)
t	Time
u	Displacement
v	Velocity
v_e	Mean electron velocity
x,y,z	Cartesian coordinates
$Y_{\hat{k}}(x)$	Bessel function of the 2nd kind
r,θ,z	Cylindrical coordinates
Z_i	Ion charge
z	Acoustic impedance

δ	Electromagnetic skin depth
δ_{ij}	Kronecker delta
ϵ_{ij}	Strain tensor
ϵ_r	Relative permittivity
ϵ^T	Permittivity of Piezoelectric
ϵ_0	Permittivity of free space
λ	Wavelength
λ, μ	Lam*é* constants
μ_r	Relative permeability
μ_0	Permeability of free space
ξ	Displacement vector
ρ	Density
ρf	Free charge density
σ	Conductivity
σ_{ij}	Stress tensor
τ	Mean time between electron scattering events
ϕ	Scalar Potential
ψ	Vector potential
ω	Angular frequency
$\times$	Vector product
$\cdot$	Scalar product

Chapter 1

Introduction

1.1 Industrial Motivation

The oil and gas industry is a major part of the world's economy and its associated infrastructure is correspondingly vast. In order to support this industry there are a large number of drilling rigs and processing plants with a network of pipelines to connect the facilities for procurement and storage. The environments in which these pipelines are found are often hostile and damage can occur to the line simply because of the surrounding environmental conditions [1, 2]. The exposure of this pipe network to the environment means that inspection cannot simply be based on whether the product damages the pipeline from the inside but must also consider the damage to the pipeline from external factors [3] .

Routine inspection is therefore necessary in order to prevent the loss of income, environmental damage and human costs that pipeline failure can cause. The problem here being that many miles of these pipelines exist and often access to them is severely limited, with full circumferential access impossible in some cases. Important examples of sections of pipeline that are particularly susceptible to corrosion are pipe support areas and subsea pipelines that are often resting on the sea bed.

The many miles of pipeline that are used are usually held off of the ground via the use of pipe supports. There is a varied range of pipe supports tailored to the pipeline's needs, the most basic of which would simply be a beam on which the pipeline rests. However, the most common type is a saddle type support where the pipe is supported from below in a cradle of metal. In both the simple and more complex support situations as shown in Figure 1.1, problems arise in that the support areas provide a position where water can be trapped and pool, remaining close to the surface of the pipeline for long periods of time [1, 3]. The presence of

this water can lead to a softening of the pipeline coating and subsequent chemical reactions that further attack the pipeline material. When the coating of the sample is breached, the water can gain contact with the steel of the pipeline surface and cause corrosion. The water can then move underneath the coating layer to spread the problem wider and cause a thinning of the pipe wall over a relatively wide area. As this occurs there is little visual evidence of the corrosion unless the pipe is raised from its support.

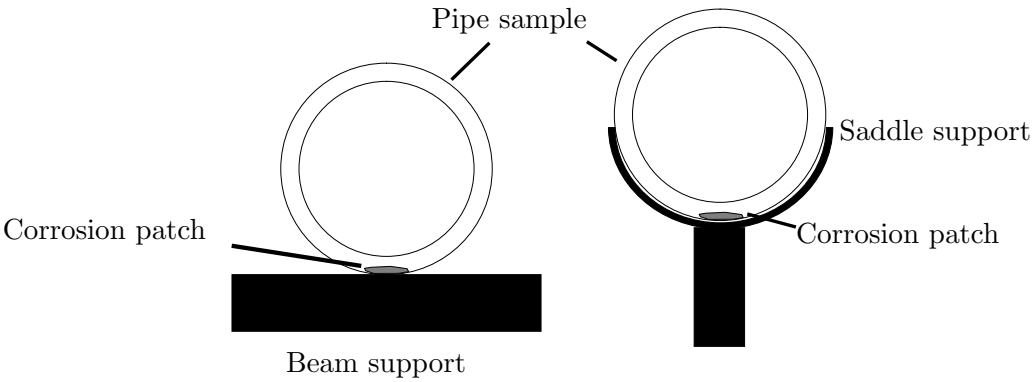

Figure 1.1: Schematic diagram of the most common types of supports, showing a beam support and saddle support and the likely areas of corrosion at the contact points with the support.

Where the corrosion is at an advanced stage, the evidence can become apparent with rust on the pipe surface around the support and water stains clearly visible. By this stage the corrosion is so advanced that it is likely the only course of action would be to replace the pipeline section. Therefore it would be preferable to be able to screen a pipeline for corrosion, with particular emphasis on the pipe support areas where defects may not be apparent. This screening should be able to detect small corrosion patches of at least 20 mm diameter and 25 percent wall thinning and give an idea of their depth and extent so that areas of corrosion can be located early on in their development and measures taken to deal with the issue before it risks the integrity of the pipeline. The corrosion patch style defect is the defect of interest from crevice corrosion at a pipe support but it should also be noted that other defect types are possible in pipe samples and often required to be tested for including pitting corrosion as a progenitor of a corrosion patch and axial cracking in pipelines due to the stress that these pipelines are under in general operation, the examples of these different defects are shown in Figure 1.2, with the location of the defects not representative of where they would be expected to form.

Current methods of detecting corrosion in pipelines in industry vary [4, 5],

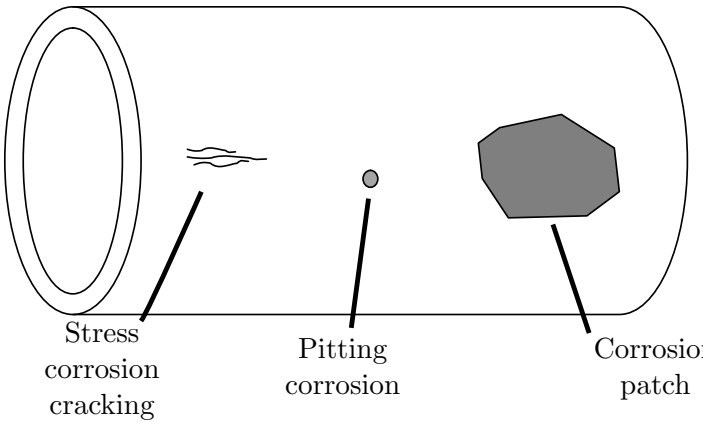

Figure 1.2: Schematic diagram of the most common types of defects in a pipeline section, shown for comparison, positioning not representative of likely positioning on a pipeline.

with no single technique being suitable for all situations. Often an in-line inspection (ILI) tool is used which travels through the pipe and uses magnetic flux leakage (MFL) tools and ultrasound [6, 7] to ascertain where defective areas of the pipe may be. The inspection of samples using an in line tool will be described in more detail in Section 1.5.2. The obvious downside here is that the tool is applied on the interior of the pipe and as such may require process shut-down for inspections and requires that the line be able to accommodate a scanning 'pig' which is not always possible, with some pipe diameters simply unable to accommodate the size of scanning platform required. These have however, been successfully applied for many pipeline configurations and can use either MFL tools and ultrasonic transducers to locate defects. These scanning rigs generally consist of a modular structure with rubber caps to centre the rig, an instrument section in which the magnet and magnetic sensor is housed, a section of the power source of the rig and odometers to ensure that the positioning of defects can be recorded, a schematic diagram to show the basic implementation of this is shown in Figure 1.3.

Another popular method of detecting defects in pipeline over long distances is to use axially propagating guided waves, utilising the change in reflection of modes to identify the presence of a defect. However, problems arise using these methods, as they require a large number of transducers to cover the entire circumference of the pipeline and also need full circumferential access at at least one point on the line in order to apply these probes, these again will be considered in more detail later in the section.

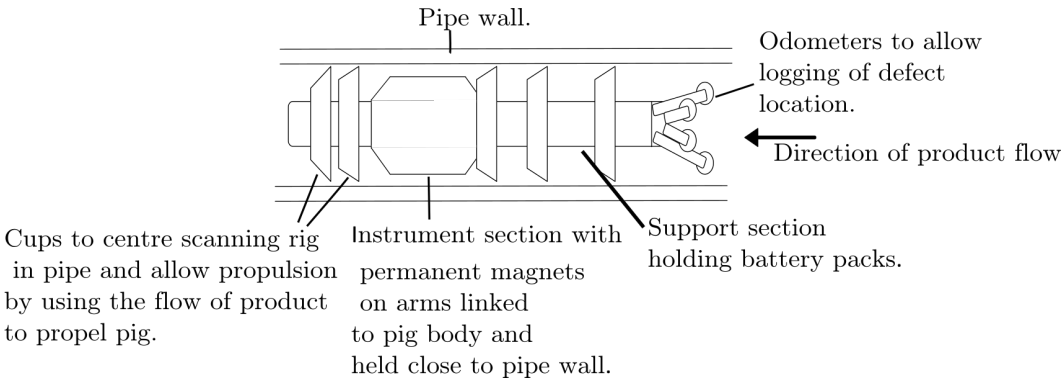

Figure 1.3: Schematic diagram of an in-line inspection pig for detection of defects in a pipeline primarily axial cracking style defects caused by stress.

The focus here is on developing an understanding of circumferentially travelling SH guided waves [8] generated by an EMAT (Electromagnetic Acoustic Transducer) probe [9]that can be applied from the exterior of the pipeline, remotely from the suspected site of a defect. The system should work through thin coatings up to a thickness of 1 mm and cover the whole circumference of the pipe at any one point using two transducers in a pitch catch arrangement as shown in Figure 1.4. This arrangement has the advantages of low power demands, a non contact nature and the ability to be applied when only a small section of the pipe circumference is available, with no shut down of process required in order to effect a scan.

The theoretical basis behind the design and operation of such a system is established, with the behaviour of the waves when interacting with a defect clarified via simulation. The system is characterised in terms of its ability to be used on samples of varying diameter, pipe wall thickness and coating thickness in order to locate and size defects that arise due to corrosion of the pipe wall.

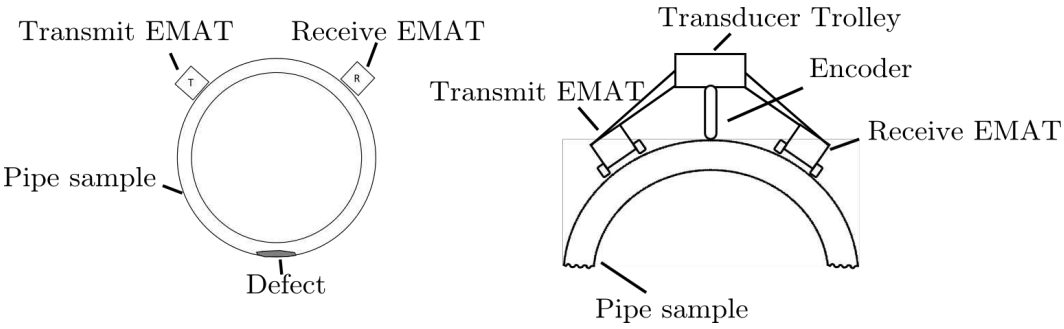

Figure 1.4: Schematic diagram of the shear horizontal wave EMAT system that is considered in this thesis.

1.2 Non Destructive Evaluation

The field of Non Destructive Evaluation (NDE), often used synonymously with Non Destructive Testing (NDT), spans a wide range of different methods that can be used to inspect components without damaging them [10, 11, 12, 13, 14]. In an industrial context, this means that components can be tested whilst they are in service or in the manufacturing stages. The purpose of such inspections is to ensure the component is of the required strength at every point, to ensure that they can be used for as long as possible without the risk of in-service failure. Non destructive testing (NDT) can be applied for a range of uses, from thickness gauging of components [15, 16, 17], to determination of material micro structure [18], to defect detection [7, 19, 20]. Given the broad nature of the field, it is appropriate to consider the various techniques that are available to give context to their respective strengths and weaknesses and how they can be used not just in isolation but also as complimentary techniques.

The array of NDT methods that are available for inspecting components is varied, with different techniques more appropriate for different applications and for detecting different types of defects. Some for example are sensitive to small cracks in the surface of a sample such as magnetic particle inspection and dye penetrant inspection, whereas others may be more suited to detecting defects within the bulk of a sample or in finding defects away from the position at which the technique is applied such as phased array and guided wave techniques. When presented with an NDT problem, it is prudent to consider all techniques and then narrow the focus of an inspector to the techniques that are the most appropriate to detect and size the defects of interest. Inevitably when dealing with industry a factor that becomes important is the cost of such techniques in terms of the equipment expense and time outlay required for a successful measurement.

1.3 Visual and basic surface techniques

The simplest technique that can be applied to a problem is visual inspection of a sample [14]. Examination of a component by eye for abnormalities on a surface can be a good indicator that the sample contains defects. It can also be useful in manufacturing to assess obvious differences between one part and the next within a production process, where these differences can make a component more likely to fail. The effectiveness of such an inspection is very dependent on the operator's skill and judgement, but with the large capacity for human error inherent in these measurements and the limits on visibility available in many NDT scenarios, the

likelihood of getting repeatable, consistent measurements is low.

The quality of such an inspection can be improved with the use of visual aids such as magnifying lenses, and tools such as borescopes to examine positions with limited access to the surface, but there is clearly a limit on what can be achieved. Despite these disadvantages it is still a useful tool for guiding the application of more complex methods, particularly in situations where the coating of samples can be seen to be damaged, which can indicate further damage to the structure of the component as a consequence of the coating damage.

A visual check of pipe support areas would be routinely made in industry, with rust marks on a pipeline at a pipe support indicating that corrosion is taking place even if the position where corrosion is occurring cannot be seen.

Several other techniques that concern the visualisation of defects on the surface of a sample are available in dye penetrant inspection[21] and magnetic particle inspection [22]. These methods focus on finding surface breaking cracks that may not be visible using visual methods. They are both useful techniques in their own right and are applied in industry, but they require direct access to the defect area and deal with much smaller defects such as micro cracks (less than 1 mm) than is desired to be considered in this work so their application is not suited to this scenario.

More appropriate methods to scan pipe samples for corrosion are presented by other more complex techniques that can consider larger areas and many of the following are used in industry to locate defects in pipeline [4].

1.4 Thermography

Thermal methods have been shown to be an effective way of detecting defects in samples where large areas of material have to be tested [19]. They have proved particularly effective in areas where composite materials are used, to find delaminations [23] or impact damage and as such have found effective uses in the aerospace industry [24]. These methods use the diffusion of energy in the form of heat through a sample. The heat is applied either actively through heating lamps or passively by the movement of heated product through the sample, but in both cases the subsequent cooling of the sample is monitored using an infra red imaging system, where the heating and cooling behaviour can locate defects and provide depth information.

In active thermography, after an initial heating pulse provided by flash or flood lamps, the flow of heat within the sample is monitored using an infra red camera as illustrated in Figure 1.5. The presence of a defect is indicated by the

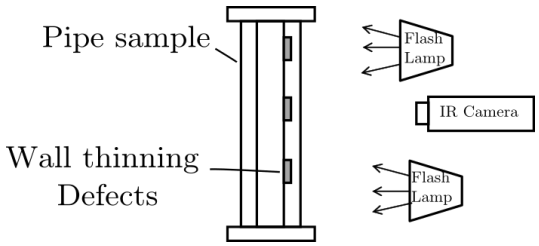

Figure 1.5: Schematic diagram of the standard apparatus for thermographic testing.

disruption of the heat flow into the sample and appears as a hot spot. The time the spot takes to appear can then be used to estimate the depth of the defect [25]. Although this method has been used to detect internal corrosion in pipelines [26], it has proved relatively inefficient and generally requires a black coating to be applied to samples to aid with the absorption of heat into the sample [27]. It then requires deep, wide internal defects in order to operate satisfactorily and it often proves difficult to provide uniform heating across the pipe surface, limiting its application for such situations.

1.5 Electromagnetic methods

1.5.1 Eddy currents

A more complex near surface NDT method that has been used to determine sample thickness and the presence of defects is eddy current testing. Eddy current testing manifests in several forms ranging from the basic eddy current probe[28], through pulsed eddy current testing [29] and eddy current arrays [30].

In basic eddy current testing, a wire carrying an alternating current is held near the sample to be tested [28]. The electric field generated by this coil in turn generates a magnetic field, inducing eddy currents down to the skin depth of the sample, which then produce their own magnetic field to counteract the original magnetic field. A schematic of eddy current operation is shown in Figure 1.6, the new magnetic field is observed due to impedance changes in the generator coil or in a separate detector. The presence of a defect in the path of the eddy currents will disrupt the behaviour of the measured impedance, with changes in phase and amplitude [31] being used to determine the surface size of the defect and its position in the sample.

This style of testing has been effectively used to find very small defects on a sample's surface through coatings but its efficacy in the bulk of a sample is limited by the penetration of the electromagnetic field into the sample. This is determined

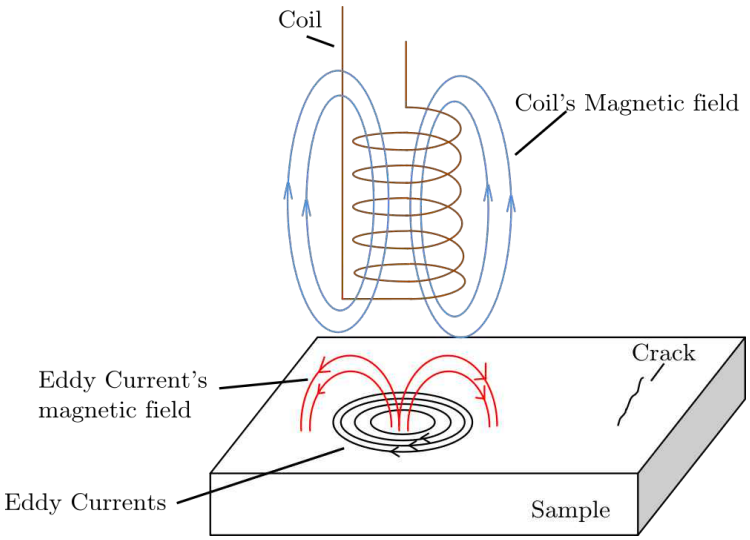

Figure 1.6: Schematic diagram of an eddy current inspection.

by the electromagnetic skin depth [32] which is dependent on the sample material and the frequency of the inspection but is typically of the order of a few hundred microns. A basic eddy current test will be carried out at a single chosen frequency, which given the skin depth is inversely proportional to frequency[32], results in a fixed depth of inspection for basic scans, restricting the technique to detection of defects to a certain depth in the sample.

Pulsed eddy current inspections provide a solution to this restriction by using a range of frequencies and hence a range of depths of inspection can be reached by this method without compromising the high surface sensitivity [29, 33]. Eddy currents have been applied in industry to detect defects under protective coatings in areas such as offshore steel risers [34]. An issue here is the need to scan around the full circumference of the pipe at each point to detect defects at each point, which although rapid, suffers where access to the pipeline is impeded.

Further versatility is provided by the use of eddy current arrays [30] which can be used to provide large area coverage that is not possible with a single coil. Although the use of an eddy current array allows for greater scan sizes, the need to apply the array at the surface point at which the defect is expected is prohibitive for the inspections.

1.5.2 Magnetic flux leakage

An often used tool in pipe inspection is the Magnetic flux leakage method for finding small cracks (1 mm and below). This type of method is concerned with finding

surface or near surface defects such as cracks in a sample. It has been effectively applied to find stress corrosion cracking in the interior of pipelines and is regularly used on pipe inspection pigs within pipes to detect the loss of pipe wall material. It involves magnetising a ferromagnetic sample and measuring the resultant magnetic field in the sample. If the sample is uniform then the magnetic field lines will also be uniform. When the sample contains defects such as cracks or inclusions that contain material that is non magnetic such as the air gap encountered with a crack then the magnetic field is perturbed from what is expected and the resulting change can be measured using a suitable probe [35].

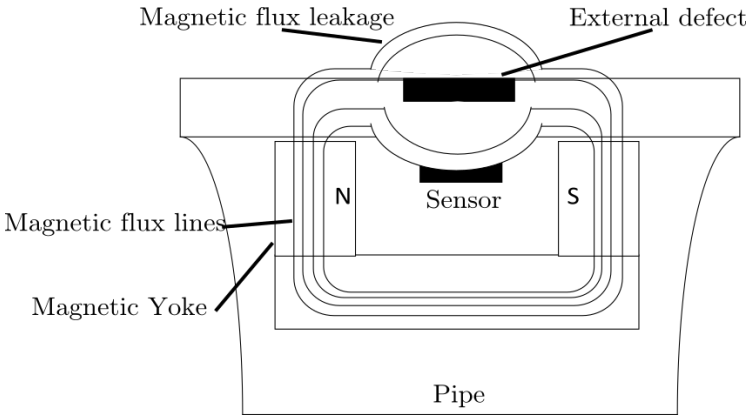

Figure 1.7: Schematic diagram of the standard equipment for Magnetic Flux Leakage testing of pipelines.

These techniques are very useful for fast monitoring of a pipeline, with the arrangement of the inspection shown in Figure 1.7 as they are non contact and can be automated to allow for the in-line inspections to take place at a high speed, but as a result the pipelines need to be able to accommodate an inspection pig and the process may need to be shut down to allow for the inspection to take place. The received signals can be used to obtain good sizing information for the defect in terms of size, shape and orientation with respect to the field [7, 6] but cracks that run in parallel to the magnetic flux lines are difficult to detect due to the small amount of perturbation of the magnetic field that they cause.

1.5.3 Magnetic Tomography method and Metal Magnetic Memory method

Other methods of detecting defects using Electromagnetic methods include the Magnetic Tomography Method (MTM) and Metal Magnetic Memory method (MMM). The Metal Magnetic Memory method involves finding areas of stress in a sample

that have led to microscopic defects and altered the magnetic domain structures of a material, it has been used to find defects in welds [36, 37, 38]. Magnetic tomography involves using a magnetometer to map a sample, detecting the changes to a magnetic field caused by defects. Image reconstruction is then achieved by using the amplitudes of induced voltages in the sample or phase perturbations. This method draws heavily from its development in the medical sector but is developing into a technique to be used to assess materials in manufacture [39] and pipe and plate in a screening method [40].

1.6 Radiography

Another method that has been successfully applied to the problem of pipeline inspection is that of radiography [41]. This is a popular technique for inspections as it gives an unambiguous image of a defect in the bulk of a sample. In radiographic methods, a source of radiation is used to transmit energy through a sample, with its intensity after transmission then recorded by the exposure of film or digital detectors. The experimental set up of such a scan is provided in Figure 1.8. As different materials attenuate radiation to differing extents, the resulting image shows how much of a material the radiation has passed through, allowing the size and extent of defects to be calculated [41, 12].

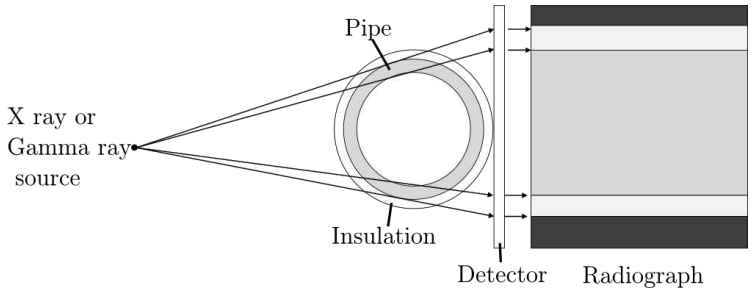

Figure 1.8: Schematic diagram of the standard apparatus for radiographic double wall imaging of pipeline.

In the practical application of radiographic tests in NDT, either X rays or Gamma rays are used. Although the physical principles of radiation X rays and gamma rays are very similar [28], the generation method of the radiation is significantly different and affects the ways these techniques may be used in practice in order to make sure the NDT operator risks the lowest dose of radiation possible [41].

X rays are often preferred from a health and safety perspective as they have a greater level of control over the generation of the radiation due to the X rays being

generated by accelerating electrons and colliding them with a target material, which means the generation mechanism can be switched on and off easily. Gamma rays by contrast are generated from the decay of unstable isotopes and hence much less control is afforded to the operator and directionality of the radiation is more difficult to achieve resulting in large (many metres) exclusion zones around an inspection site [42, 43].

The large costs (storage, health and safety) and extra precautions necessary for radiographic inspections can make them unattractive and due to the transmission nature of the scans, access to both sides of the component is necessary, which is not possible in some of the limited access situations mentioned for pipeline inspection. Additionally, the scans can take some time to reach the exposure level required for sufficient contrast and the flaw orientation to the beam has a large effect on whether the scan can successfully locate the defect of interest. Despite the restrictions placed by the above conditions, radiography has been effectively applied to pipe studies particularly in areas where corrosion is expected [44].

1.7 Ultrasonics

Ultrasonic NDE describes a very broad field of techniques that operate both in the bulk and on the surface of materials. Ultrasonic inspection of materials uses the propagation of sound with frequencies above 20kHz into a material and uses the interaction of these signals with the sample to gain information about a material. By measuring aspects of the received ultrasonic signals after they have travelled through the material, certain properties can be inferred [13].

By measuring the attenuation of signals, amplitude of reflections [45] and time of flight [46] of the ultrasonic signals, material properties of a sample can be determined, with information also possible on the presence, size, location, orientation and depth of defects as well as the thickness of a sample.

The main advantage of using ultrasonic methods as compared to many of the techniques described previously is the ability to interrogate the sample from a single side so that full access to the sample is unnecessary. This is enhanced by the ability to use guided waves which use the structure of the sample to guide the ultrasonic energy to where the defect is situated [8]. This allows for scans of the sample to be carried out from a more suitable position than directly above the defective area where access may be restricted. Ultrasonic methods, wave generation and transducers will be studied in detail in a subsequent section but a short summary here is intended to guide the reader on the differences between bulk and guided wave

ultrasonics.

1.7.1 Bulk wave ultrasonics

Bulk wave methods of ultrasonics are concerned with the generation and detection of ultrasound in the bulk of a sample. Two main types of waves exist in longitudinal and shear waves that differ from each other in the direction of movement of the particles in the material in relation to the direction of movement of the energy of the wave. Using these waves, the most common techniques consider the time of flight of a signal. Given the fixed speed of sound in a material, the time of flight can be measured and from this the distance of propagation of a signal calculated, giving a measurement for the thickness of a sample at a point [15].

This is used widely in industry for spot thickness measurements of samples, with a change in thickness relating to a change in arrival time. It can also be used to locate defects in a sample, with the depth of a defect within the sample calculated using the arrival time of the defect signals and the defect extent in the other directions calculated using the 6dB drop method [47].

Different design of transducers such as angled probes allow ultrasound to be directed at areas of interest such as a weld root or cap to find defects in these areas. Introducing ultrasound into a sample at an angle is also taken advantage of in methods such as TOFD [48] where diffraction from crack tips within the bulk of a sample is used to characterise the size and position of defects. Inspections for defects in the bulk can be tailored to concentrate on areas at which defects are expected to occur and can provide accurate measures of the size and position of defects.

Other complex methods of detecting defects include using phased array ultrasonics [49], which use an array of detectors and receivers to emit ultrasound into a sample and detect the signal at different elements on the array. Using the time of flight for signals reflected from features in the sample such as the back wall and any included defects, an accurate representation of features in a sample can be found. In these methods, the information from all the elements on the array can be captured and the focus on a defect can be achieved in post processing methods providing a very effective method for detecting defects and calculating their position and dimensions.

More particular to the application of interest is the CHIME method [50]. This method is currently used in industry to detect corrosion in pipes and plate in difficult to access areas and is shown schematically in Figure 1.9. It involves a piezoelectric transducer pair on angled shoes, at a critical angle to generate creeping waves on both surfaces of a sample, which continually generate a shear wave propagating

into the bulk, known as a head wave. Also generated, due to the finite size of the transducer, are longitudinal and shear bulk ultrasonic waves. The head waves are generated at the critical angle of the shear wave in the sample and reflect varying numbers of times as a head wave before converting to a creeping wave for the remaining distance. This results in a continuum of received signals, with the initial bulk waves interfering with the initial head/creeping wave combinations before an array of peaks from the head wave signals is detected as strong peaks in the latter half of the signal.

Any defects in the path of the wave affect the received signal magnitude and arrival time, with reflections from defects also being able to be assessed to find cracks. This method is effective for detecting defects, but can lose the ability of full coverage of the thickness for different inner to outer pipe radius ratios. It also delivers no direct relation to defect depth but is a useful tool for pipe screening.

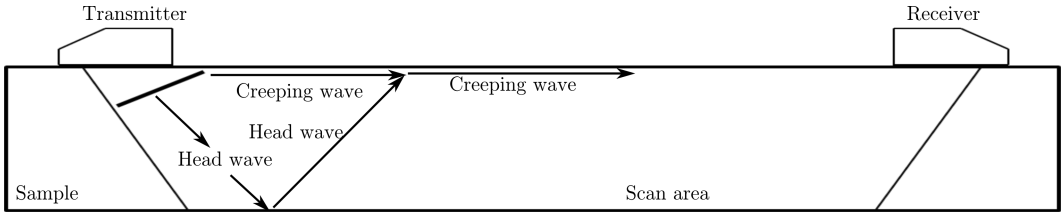

Figure 1.9: Schematic of the standard apparatus for CHIME inspections showing the waves generated and interrogated area.

Bulk wave techniques as described above use the characteristics and geometry of samples to get ultrasound to the position of interest for an inspection and use the well characterised behaviour of ultrasound within a material to draw conclusions from these received signals. Another way of directing ultrasound to an area of interest is to use guided waves.

1.7.2 Guided wave ultrasonics

Guided waves can be used for defect detection at a distance from the area of interest, these wave modes exist in thin structures such as plates and pipes, where the waves are guided along the structure by the restriction of the sample walls [8]. This allows them to travel long distances within samples away from the transmitter and so allows a single measurement to interrogate much larger sections of a sample [51].

The main disadvantage of guided waves is that understanding and interpretation of results is complicated by the presence of multiple wave modes in a signal. This is due to a family of different solutions to the equations for guided waves which generate distinctly different wave modes. As a result of this, generation of these

waves is either restricted by the specific design of transducers [52] or by more complex signal processing and in depth knowledge of the behaviour of modes [53]. The resolution of measurements using guided waves is determined both by the frequency used and the dispersive nature of the wave as well as the beam divergence from the transducer, with the divergence and dispersion increasing with distance.

Defect detection using guided waves is possible in a range of different situations. For each different geometry sample the dispersion relations governing the modes that can be generated differ. Guided waves have been studied in their original plate form, through rail track [54] and pipeline [55, 56], with the equations for the guided waves in these structures varying not just from structure to structure, but also in the direction in which the waves are propagating. For example in pipes, the dispersion relations are dependent on which direction the waves are transmitted in the structure i.e whether they are sent axially or circumferentially around the pipe [57].

Experimental set-ups involve either pitch catch measurements with a transmitter and receiver or pulse echo measurements with a single probe that acts as both transmitter and receiver, usually used as an element in a belt of transducers where many transmitters and receivers are used to provide full coverage of the pipeline [58, 59]. Conclusions about the state of the sample and any defects that occur in it can then be drawn from the time of flight, relative amplitude of signals and the amplitude of echoes from features within the sample.

As with bulk wave measurements, different varieties of guided waves exist in Lamb waves and Shear Horizontal waves [8]. These differ in the manner of their excitation and the direction of movement of the vibrations that establish the waves, with different polarisations to one another. They are suitable for different purposes as well as being generated more easily by different types of transducers.

The choice of guided wave mode used for inspections is dependent on the inspection scenario, because of the way Lamb waves are generated and propagate by a combination of longitudinal and shear vertical waves, they feature both in-plane and out-of-plane displacements as the wave propagates. The displacement profiles within a sample also then differ depending on the frequency at which a wave is generated, meaning that at different frequencies the in plane and out of plane displacement can vary and can drop to zero at the surface [8]. This displacement out-of-plane of the sample at the surface can lead to the phenomena of 'leaky' waves where energy in the Lamb wave is lost into the sample and its surrounding media, decreasing the energy that is available for an inspection.

By contrast SH waves are generated by a shearing motion within the plane

of the sample. This method of generation results in less likelihood of energy being lost out of the plane of the plate or pipe especially in cases where there is a surrounding medium such as water that cannot support the shearing motion [8]. The displacement profiles of SH waves also show that the displacement is at a maximum at the outer surfaces of the sample, ensuring that the signals can be detected at the surface in all cases. The consistent nature of the displacements at the surface of the sample and the retention of wave energy in marine environments is a major motivation behind the focus on SH waves in this work as the operation of probes and detection methods was desired to be applied both above ground at pipe support areas and for subsea applications where the sample is surrounded by water.

1.7.3 Generation of guided waves

Generation of guided waves in a sample can be achieved in several ways, some of which are more suited for laboratory application than in service. The most common ways of generating guided waves are to use laser generation [60], piezoelectrics [61], or EMATs [9]. Laser generated guided waves have been used to detect small defects [60] but laser inspections tend to struggle in industrial situations due to the need for a well prepared, polished surface and the restricted use of high powered laser sources in terms of health and safety requirements. Piezoelectric transducers find widespread use in the NDE sector due to their rugged nature, high signal to noise ratio and ease of use, but require contact with a sample and can have their signals severely disrupted by obstacles such as paint layers, which can cause ringing in the signal. Piezoelectric transducers have been used to generate Lamb waves and are in use in long range ultrasonic guided wave methods that are prevalent at present in industry as a ring of transducers clamped to the sample using pulse echo [62] or tomographic methods [63]. Pulse echo methods take into account the amplitude of reflections from defects to locate them and judge their severity. Through transmission methods can also be used with two rings on the sample on opposite sides of the area that is desired to be tested to give greater localisation of defects. Figure 1.10 shows the application of the belts on a sample, for pulse echo methods a single ring of transducers would be used, with two rings used for through-transmission imaging of the defect area.

EMATs are an effective way of generating both Lamb and Shear horizontal guided waves due to the control over the generation that is provided by using a combination of electric and magnetic fields [9]. In EMATs the desired profile of surface displacements is generated either by having a single magnet and generating periodicity with a meander line coil or with an array of magnets and a racetrack coil to provide a periodic force on a sample to generate guided waves of a certain

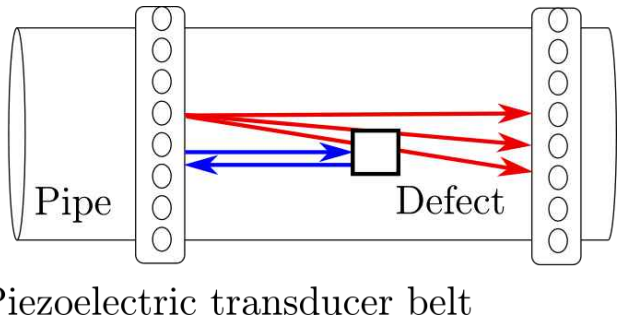

Figure 1.10: Schematic of apparatus for Long range guided wave ultrasonic testing of pipeline. Pulse echo application with one transducer ring shown in blue, with through transmission operation with two transducer rings shown in red.

wavelength.

The benefits of using EMATs for generating guided waves is that they can generate the wave without being in contact with the sample due to the generation of ultrasound within the sample surface, this removes any inconsistencies relating to the coupling of the ultrasonic probes to a sample. These probes also generate satisfactorily through thin coatings, meaning that the sample protection does not have to be compromised in order to test it. There is also the option to operate these probes at high temperatures, allowing a wider range of applications for testing with EMATs. With respect to piezoelectric transducers they have a lower signal to noise ratio, (the ratio of the strength of the desired signal to that of the unwanted interference) which can make measurements less straight forward and require more processing of data.

1.8 Thesis Outline

This thesis first considers the theory of ultrasound and ultrasonic inspections in general in Chapter 2 before considering the more specific cases of guided waves and in particular shear horizontal guided waves. Dispersion curves for guided waves in a plate and a pipe are considered, to illustrate their differences and the principles of operation of electromagnetic acoustic transducers are considered to give context to the results presented subsequently in the thesis. The excitation of periodic permanent magnet array style electromagnetic acoustic transducers is considered to guide inspections.

Chapter 3 is used to illustrate the measurements that can be obtained and the steps that can be taken to optimise inspections including confirming the shear wave speed in a sample, the differences between axial and circumferential guided

wave generation in terms of theoretical speeds and frequencies and the orientation of the probe. A characterisation of the pulser receiver equipment used in the research is carried out to assess its suitability to the inspection scenario, with this equipment used to represent tools used in industry at present so that it can be directly applicable to industrial situations.

Chapter 4 introduces the theory of finite element modelling and its application in this research considering the density of elements necessary to provide a good representation of the experimental situation. The main theme of this thesis is seen through Chapters 5 and 6.

Chapter 5 sees the experimental system applied to industry standard samples with artificial defects to ascertain the defect depth measuring capabilities, axial sizing methods and circumferential positioning and sizing of defects. Subsequent finite element modelling of the experimental situation is shown to match well with the experimental results and used to gain a greater understanding of the physics involved when the guided waves interact with a defect, this is extended to different defect depths and circumferential extents.

Chapter 6 takes the knowledge of the guided wave behaviour gained in Chapter 5 and extends it to real corrosion patches in samples taken from industry to assess how the system performs on these samples and whether the same level of information can be obtained from irregular size and shape defects that represent real corrosion damage to a sample. The advantages of the system as a screening tool and the disadvantages in terms of the difficulty in obtaining sizing information from real corrosion patches that may be small or overlap with one another is considered. After considering corrosion in a range of different pipe wall thickness and outer circumference samples, the chapter continues to show finite element modelling of commonly used calibration defects in industry and illustrates how they are not a good approximation to the real corrosion patch style defects. This is confirmed with examination of flat bottomed hole style defects, which illustrates the detection of smaller scale defects than in the previous cases, while illustrating the difficulties of quantifying defects that are close to one another in the axial direction. The chapter concludes by assessing the effect on measurements using this method close to a welded area on the pipe surface, which is a feature that this tool will likely interact in its screening application.

The conclusions and suggested further work to build on the work presented here are given in Chapter 7.

Chapter 2

Ultrasonic Inspection Theory

Ultrasonic methods of non-destructive testing are widespread in industry and have been used for many years to characterise materials and potential defects therein. This chapter briefly introduces the theoretical background behind ultrasonic waves in general and the particular ultrasonic waves used in this study including their generation and propagation in, and interaction with a medium. In the following section these processes will be discussed including how wave propagation is related to the material properties of the medium and how these properties can be exploited in non destructive testing of materials. Basic principles of ultrasonic inspection with reference to some of the signal processing methods used in later sections will be considered to give context to the theory discussed, particularly in the case of ultrasonic guided waves with which this thesis is primarily concerned.

2.1 Ultrasonic Waves and their propagation

Ultrasonic waves are defined as having a frequency that is higher than the range of human hearing. They have a starting frequency of above 20 kHz, continuing through the megahertz range and at around 1 GHz going into the hypersonic regime [64]. They have been proven to be a useful tool in a wide range of disciplines from geophysics, through medical applications to non destructive testing, which is due to their ability to penetrate solid, liquid and gaseous materials [64]. NDT is usually concerned with the inspection of solid media, where a range of different wave modes can be supported, that are distinct from each other in terms of the direction of particle and wave movement and difference in velocities [8, 65, 13].

As mentioned in Chapter 1, bulk waves are a popular tool for interrogating materials: there are two categories known as longitudinal and shear waves. Lon-

gitudinal waves have their particle motion parallel to the direction of propagation of the wave and shear waves have their particle motion perpendicular to the wave propagation. As a result they also have differing velocities and interact with defects in different ways, so they are used for different inspections [28]. For these waves, there is no particular consideration of the boundary conditions of a material except in terms of the percentage of transmission or reflection of waves from an interface between two different media [65]. They therefore travel within the 'bulk' of a material and can be used to determine properties of that material. The theory behind the generation of these wave modes will be shown in Section 2.4.

Guided waves by contrast, come from the same constituent equations, but the solutions to the wave equations are dependent on the boundary conditions of the material which defines the guided wave type [8]. These waves tend to have more complicated interactions with the material and the theory behind these waves will be considered in Section 2.9.

Regardless of the wave type, the particle motion of the ultrasound is generated by an initial disturbance that forces the particles of the material to move away from their equilibrium position, and a subsequent force that acts to return the system to equilibrium, deforming the material and propagating the disturbance [13, 64, 66].

2.2 Ultrasound in elastic media

The simplest case to consider to illustrate the propagation of ultrasound is that of an isotropic, homogeneous solid, where no boundary conditions are considered [67]. Another constraint is that the ultrasound used is desired to be non destructive such that it does not permanently alter the material in which it travels. This means that the ultrasound considered here will always be relatively low amplitude in order to remain in the elastic regime [13].

2.3 Theory of elasticity

Ultrasonic vibrations begin with an initial impulse that disturbs the particles of a medium, moving them away from their position at equilibrium as mentioned. The medium reacts to this perturbation with an internal restoring force that acts to return the particles to their starting equilibrium position. This deforms the material and it is this deformation that causes the force to be transmitted through the material [8, 65]. For the wave to continue propagating through the medium, the

deformation must be large enough to overcome the forces that act to maintain the equilibrium of the system. The relationship between the deforming and restoring forces within the sample is determined by the stress (σ) and strain (ϵ) in the material. The stress and strain are symmetric rank two tensors due to being applied in three dimensions and can be expressed in Cartesian coordinates as,

$$\sigma_{ij} = \begin{pmatrix} \sigma_{xx} & \sigma_{xy} & \sigma_{xz} \\ \sigma_{yx} & \sigma_{yy} & \sigma_{yz} \\ \sigma_{zx} & \sigma_{zy} & \sigma_{zz} \end{pmatrix} \tag{2.1}$$

$$\epsilon_{ij} = \begin{pmatrix} \epsilon_{xx} & \epsilon_{xy} & \epsilon_{xz} \\ \epsilon_{yx} & \epsilon_{yy} & \epsilon_{yz} \\ \epsilon_{zx} & \epsilon_{zy} & \epsilon_{zz} \end{pmatrix} \tag{2.2}$$

Where the strain tensor describes how a material deforms when a given force is applied and the stress tensor describes how a force is applied over an area, A on a particular plane. The stress components are given for the force F_x as

$$\sigma_{xx} = \frac{F_x}{A_x}, \sigma_{xy} = \frac{F_x}{A_y}, \sigma_{xz} = \frac{F_x}{A_z} \tag{2.3}$$

In general the linear relation between the components of the stress and strain tensors is given by [65, 66],

$$\sigma_{ij} = C_{ijkl}\epsilon_{kl} \tag{2.4}$$

Where the Einstein convention is used here such that when a suffix appears twice in the same term, summation over the repeated indices is implied [68]. The different indices in the above represent the spatial directions.

The term C_{ijkl} here is the fourth order elastic stiffness tensor, which acts as the proportionality constant that would be expected in Hooke's Law. Although this tensor can have 81 components, the nature of the medium can be used to reduce the number of independent constants. Since the stress and strain each have six independent components, the stiffness tensor has a maximum of 36. Using further symmetry arguments, this number of components can be narrowed down to 21 independent components, allowing the system to be greatly simplified [64, 65]. Using the assumption of elastic isotropy allows the constant C_{ijkl} to be expressed as a function of two independent variables Where λ and μ are the two Lam*é* constants of the material which are dependent on the material micro structure such as grain size and conditions such as temperature and applied load:

$$C_{ijkl} = \lambda\delta_{ij}\delta_{kl} + \mu(\delta_{ik}\delta_{jl} + \delta_{il}\delta_{jk}) \tag{2.5}$$

This can then be simplified to

$$\sigma_{ij} = \lambda\epsilon_{kk}\delta_{ij} + 2\mu\epsilon_{ij} \tag{2.6}$$

For the homogeneic isotropic case, the stiffness tensor is then presented as

$$c_{ij} = \begin{bmatrix} \lambda+2\mu & \lambda & \lambda & 0 & 0 & 0 \\ \lambda & \lambda+2\mu & \lambda & 0 & 0 & 0 \\ \lambda & \lambda & \lambda+2\mu & 0 & 0 & 0 \\ 0 & 0 & 0 & \mu & 0 & 0 \\ 0 & 0 & 0 & 0 & \mu & 0 \\ 0 & 0 & 0 & 0 & 0 & \mu \end{bmatrix} \tag{2.7}$$

The relationship between stress and strain has here been described for the static case, in that time dependence has not been considered. However, considering both Hookes law and the equation of motion of the material will allow the time dependence to be taken into account and the wave speeds to be defined.

2.4 Waves in elastic media

Using the equations of motion defined by Newton and Hooke's law, as defined in equation 2.5, the dynamic behaviour of waves in elastic solids can be characterised. For bulk waves, physical arguments suggest that in three dimensions, one would expect to find one longitudinal branch of solutions to the wave equation and two shear branches, all with orthogonal polarisation. The following derivation shows how this arises from the equations of motion and how the subsequent wave speeds of the bulk wave modes can be calculated.

Written in terms of the tensor notation, Newton's law becomes [64]

$$\frac{\partial\sigma_{ij}}{\partial x_j} = \rho\frac{\partial^2 u_i}{\partial t^2} \tag{2.8}$$

Where ρ is the density of the material and u_i is the i^{th} component of the displacement of the particle. This can be combined with the equation for the relation between stress and strain seen earlier in equation 2.5, and choosing the case where the decoupling between longitudinal and shear modes is most apparent, the relation reduces to [64] :

$$\sigma_{ij} = (c_{11} - 2c_{44})\epsilon_{kk}\delta_{ij} + 2c_{44}\epsilon_{ij} = (c_{11} - 2c_{44})\epsilon_{kk}\delta_{ij} + c_{44}\left(\frac{\partial u_i}{\partial x_j} + \frac{\partial u_j}{\partial x_i}\right) \quad (2.9)$$

Here the λ and μ from 2.5 have been replaced with a combination of the material constants c_{11} and c_{44} that make up these quantities in the stiffness matrix and δ_{ij} is the Kronecker delta [68]. The equation in 2.9 can then be substituted into the equation of motion defined in 2.8, given that $\epsilon_{kk} = \frac{\partial u_k}{\partial x_k}$ to obtain a new form of the equation of motion that is the wave equation, valid for waves in an isotropic three dimensional medium.

$$\rho\frac{\partial^2 u_i}{\partial t^2} = (c_{11} - 2c_{44})\frac{\partial^2 u_j}{\partial x_j \partial x_i} + c_{44}\left(\frac{\partial^2 u_i}{\partial x_j^2} + \frac{\partial^2 u_j}{\partial x_j \partial x_i}\right) \quad (2.10)$$

This can be written using vector notation by applying both the gradient operator

$$\nabla = \left(\frac{\partial}{\partial x_i}, \frac{\partial}{\partial x_j}, \frac{\partial}{\partial x_k}\right) \quad (2.11)$$

and the Laplacian operator

$$\nabla^2 = \left(\frac{\partial^2}{\partial x_i^2}, \frac{\partial^2}{\partial x_j^2}, \frac{\partial^2}{\partial x_k^2}\right) \quad (2.12)$$

to simplify it to [8, 13, 64, 65]:

$$\rho\frac{\partial^2 \mathbf{u}}{\partial t^2} = (c_{11} - c_{44})\nabla(\nabla \cdot \mathbf{u}) + c_{44}\nabla^2\mathbf{u} \quad (2.13)$$

The relation is now in vector form with the single $\mathbf{u}$ representing the components $u_i, u_j \quad and \quad u_k$. Since the displacement is a vector and any vector can be written as the gradient of a scalar and the curl of a vector, the scalar potential ϕ and vector potential ψ can be introduced and the displacement can be written as [64, 8]

$$\mathbf{u} = \nabla\phi + \nabla \times \boldsymbol{\psi} \quad (2.14)$$

Using this expression for the displacement field, the wave equation can be separated into a term that is purely a scalar and a term that is purely a vector:

$$\nabla\left(\rho\frac{\partial^2\phi}{\partial t^2} - c_{11}\nabla^2\phi\right) + \nabla \times \left(\rho\frac{\partial^2\psi}{\partial t^2} - c_{44}\nabla^2\psi\right) = 0 \quad (2.15)$$

For a non trivial solution to this equation, it is required that the scalar and vector potential components are separately equal to zero [64], such that:

$$\rho\frac{\partial^2\phi}{\partial t^2} = c_{11}\nabla^2\phi \tag{2.16}$$

$$\rho\frac{\partial^2\psi}{\partial t^2} = c_{44}\nabla^2\psi \tag{2.17}$$

Given that it was defined earlier that $c_{11} = \lambda + 2\mu$ and $c_{44} = \mu$, these equations can be related to longitudinal and shear waves respectively.

2.5 Longitudinal and Shear waves

The previous equations illustrate that two types of wave can be supported in an isotropic bulk media, longitudinal and shear waves. The longitudinal wave as described in [8, 64] is defined by a scalar quantity with no change of angle or rotation and hence must alter the volume of the material as it propagates, with alternating regions of compression and rarefaction in the same direction as the wave propagation. It is defined as,

$$C_L = \sqrt{\frac{c_{11}}{\rho}} = \sqrt{\frac{(\lambda + 2\mu)}{\rho}} \tag{2.18}$$

Where C_L is the longitudinal velocity of the wave. The shear wave is defined by the vector potential, with no change of volume and must have two orthogonal states of polarisation, with the particle displacement of these waves perpendicular to the propagation direction. The propagation velocity can also be calculated from the wave equation to be,

$$C_T = \sqrt{\frac{c_{44}}{\rho}} = \sqrt{\frac{\mu}{\rho}} \tag{2.19}$$

Where C_T is the shear (transverse) velocity in a material. It should be noted that in a three dimensional material there are two possible directions for the polarisation of the shear wave in order for the movement of the particles to be orthogonal to the propagation direction of the wave. These are generally referred to as Shear Vertical (SV) and Shear Horizontal (SH), but due to the considerations above being for an isotropic medium, the SV and SH waves will travel with the same phase velocity. The main difference between the two polarisations is how they interact with an interface, with differences in the reflection and transmission of the waves occurring because of the different polarisations. More complex solutions

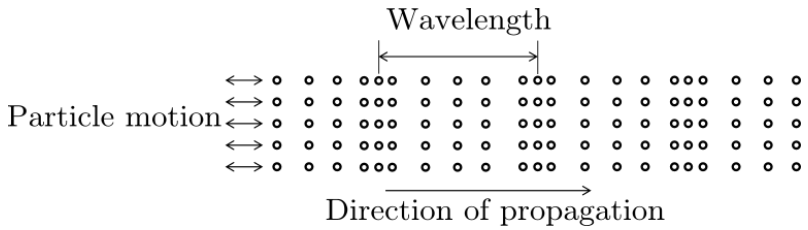

(a) Longitudinal waves

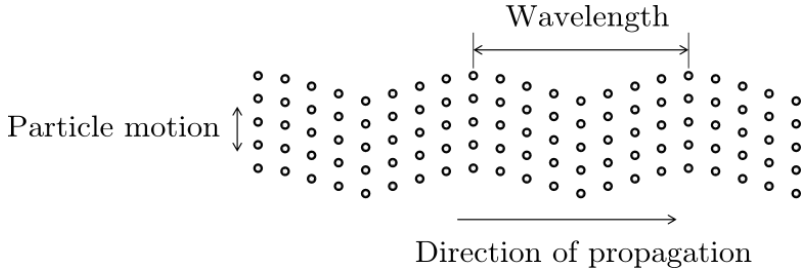

(b) Shear Waves

Figure 2.1: Particle motion and direction of propagation of a) the longitudinal wave and b) shear waves.

exist for anisotropic media [65] but they are not relevant here so will be omitted. A schematic diagram of the particle motion with respect to the direction of propagation in longitudinal and shear waves is given in Figure 2.1a and Figure 2.1b respectively.

2.6 Interactions with interfaces

Ultrasonic waves will propagate through a sample until a change in the properties of the medium is reached, upon which several things can happen such as transmission, reflection refraction and mode conversion. The extent to which these processes occur is dictated by the acoustic impedance of the medium and the medium into which the waves would propagate. The acoustic impedance is the product of the density of the material ρ and the acoustic wave speed v

$$z = \rho v \tag{2.20}$$

The different wave modes in bulk media react in different ways when incident on a change in media. Longitudinal modes, when incident on a boundary can be transmitted through the boundary, be reflected at the boundary, refract into the new medium or mode convert into Shear Vertical modes. The extent to which these processes occur depends on the angle of incidence and the wave speeds in the different media. This mode conversion complicates the received signals of these

modes and contributes to the generation of guided wave modes in the Lamb wave case.

By contrast, shear horizontal modes are polarised in the direction parallel to the material boundary, such that they do not mode convert into the other bulk wave modes when incident on a boundary. At a boundary such as that between metal and air, all of these waves are reflected with no loss in amplitude [69, 70] such that there is not transmission into the surrounding media [13, 65]. This is particularly attractive in ultrasonic inspection and with application in EMATs since the original signal amplitude is relatively low at generation. It is also a key advantage of using SH guided waves and allows inspection of welds [71, 72, 73, 74] and plates [75, 76] for defects and in the applications in this research since it means that energy is not lost into the product in an inspected pipeline or into the surrounding air/water in a topside or subsea inspection respectively.

2.7 Basic thickness measurement

Bulk waves are regularly used for thickness gauging due to the speed in a material only being defined by the properties of the material, so that the speed of sound of these waves is generally constant in a material at all frequencies, although some materials show a level of dispersion. This constant wave speed means that the time of arrival of a bulk wave that is excited in a known sample can be used to determine the thickness of the sample [12, 28, 13, 65]. The time of flight can be used from multiple back wall echoes or the initial pulse and back wall echo to give a very accurate measurement of the thickness of a sample and this is a method commonly used in industry for point thickness measurements.

The thickness of a sample in these measurements is found by using the following equation for thickness,

$$d = \frac{Ct}{2} \tag{2.21}$$

Where d is the thickness of the sample, C the velocity of the wave type used in the experiment and t the transit time of the ultrasonic wave between two echoes. A schematic diagram of the set up of a pulse echo measurement for sample thickness and defect detection is given in Figure 2.2, where there is an initial signal from the top surface of the sample, a defect signal caused by reflection from the defect in the bulk of the sample, and a back wall signal. The thickness of the sample can be determined using the first signal and the back wall echo or with the multiple back wall echoes that would occur further along in the scan. The time of arrival of the

defect signal can be used to determine the depth of the defect in the sample.

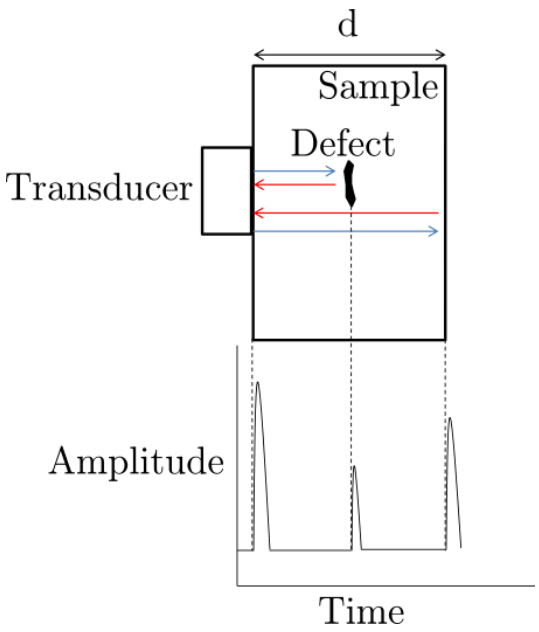

Figure 2.2: Schematic diagram for a thickness measurement and defect depth measurement of a simple sample. The time of flight would be taken from the arrival time at the transducer as shown in the graph and would be from a distance travelled determined by both the outgoing path (blue arrow) and the reflected path (red arrow).

The arrival time is often calculated using thresholding of the signal, determining the point in each waveform that the amplitude exceeds a certain value. This can be complicated in very thin materials where the travel time is very short, with back wall signals arriving within the dead time of the transducer or successive echoes merging with each other making thresholding an insufficient method to find the arrival times. Manipulation of the excitation signal used can help alleviate some of these issues by making the excitation signal broadband in frequency, which results in a smaller duration time signal and often ultrasonic inspections (particularly in guided wave cases as will be discussed later) are a delicate balance of a narrow enough band signal to excite a desired narrow frequency band, whilst being broadband enough to have a small time duration so as not to obscure different waveforms in the signal.

2.8 Phase velocity vs group velocity

The derivations in the previous sections allowed for the calculation of the propagation velocity of bulk waves. In the cases considered, the group velocity of the wave mode and the phase velocity of the mode are equal and not dependent on frequency. In these situations their velocity is dependent on the properties of the material in which they are propagating [8]. However, it is important to consider the difference between phase and group velocity since in the guided wave case, the phase velocity can be very different to the group velocity for a certain mode.

The phase velocity (c_p) of a wave can be expressed as,

$$c_p = \frac{\omega}{k} \tag{2.22}$$

Where ω is the angular frequency and k is the wavenumber. Its corresponding group velocity c_g is expressed as,

$$c_g = \frac{\partial \omega}{\partial k} \tag{2.23}$$

The different velocities as defined above, correspond to different properties of the received waveform. The group velocity is the propagation velocity of the wave, being the velocity at which energy is transferred by the wave. It is often defined as the speed of the envelope of the waveform and measured by the time of arrival of the wave by finding the peak of the envelope of a signal. The phase velocity of the wave is the rate at which a single feature in the waveform such as a peak or trough propagates, which can vary from the group velocity and result in parts of the wave travelling at a different velocity within the envelope of the wave. The phase velocity is often difficult to quantify as it requires tracking a particular feature through a waveform.

This becomes an essential distinction in dispersive waveforms where the peak of the signal may be travelling at a different phase velocity to the group velocity [8] and so is not a valid point to use to determine the group velocity of a waveform as may have been used before for a non dispersive waveform. Most guided wave modes show some degree of dispersion, especially in a pipe structure, so this distinction will be important when considering experimental data in this research. A diagram illustrating finding the group velocity of a waveform via the envelope if the signal is given in Figure 2.3.

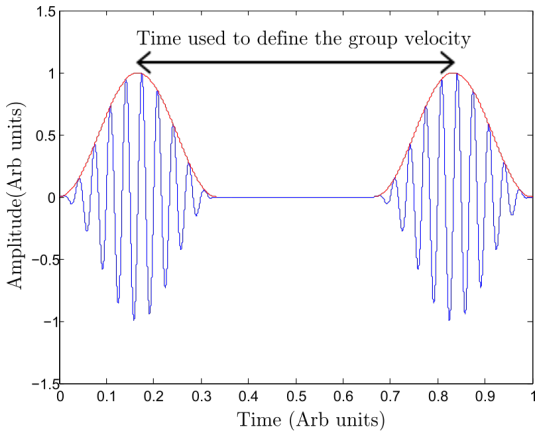

Figure 2.3: Schematic diagram showing the envelope of a waveform (red) over the waveform (blue) for determining the group velocity of waveforms.

2.9 Guided Waves and Surface Acoustic Waves

In addition to the bulk wave modes where ultrasound propagates into a material until it reaches an interface, there also exist other forms of ultrasonic waves, in the form of surface waves and guided waves. These are waves whose properties are affected by the boundaries of the medium in which they propagate [8]. Surface waves propagate at the interface between two different media and are often referred to as surface acoustic waves (SAW). Instead of simply propagating into the bulk of a material, these waves are confined to a surface in the case of surface waves or propagate away from the point of generation using the material's structure in the case of guided waves. In contrast to bulk waves, the velocity of a guided wave mode is usually dependent on the frequency at which the wave is generated, with the notable exception the lowest order shear horizontal guided wave in a plate.

Surface waves exist in a semi-infinite space, with their propagation constrained to the near surface of a sample, at the interface between two media. Much of the early research on surface waves was carried out in earth sciences, aimed at detecting waves generated by earthquakes, but the discipline has since found applications in the NDT field. A range of different surface waves exist including Rayleigh waves [8, 77], Stoneley waves [64] and head and creep waves [78]. The uniting factor in these waves is that their displacement decays exponentially with distance from the free surface, with the majority of the energy of these waves restricted to a depth equal to the acoustic wavelength [64, 8, 65].

$$A = A_0 e^{-d/2\lambda} \tag{2.24}$$

Where A is the amplitude, d is the depth and λ is the wavelength.

This behaviour means the waves follow the surface of the material, allowing for inspection of parts such as pipes, but also means that they are very sensitive to surface condition. They are highly dependent on factors such as surface roughness or surface impurities such as water, grease, oil and other substances, with these causing the wave to be scattered [12]. Due to this sensitivity to surface condition, they are particularly sensitive to surface breaking defects and have been used in NDT to detect defects remote from the generation position. Their use in remote inspection is aided by the concentration of the energy of the wave in the surface layer, which results in less attenuation than is seen in bulk waves. The type of wave that has seen most practical application in this family is the Rayleigh wave [64], which has an elliptical particle displacement on the surface as opposed to the bulk wave displacements seen earlier. As the thickness of a sample is decreased to become closer to the wavelength of the surface wave, these waves begin to travel a distance comparable to their own wavelength before encountering a surface of the sample and their elliptical displacements break down, eventually forming a superposition of longitudinal and shear vertical waves and becoming a Lamb wave mode [12, 28, 8].

2.10 Guided waves

Guided waves, in contrast to bulk waves and surface acoustic waves are constrained by the surfaces of the sample and hence are described as existing in a finite media. These wave modes are dependent on the boundary conditions of both sides of the sample, but due to their existence in samples of comparable thickness to that of the wavelength of the wave, they reach the entire thickness of the sample with ultrasound instead of being confined to one surface as in surface waves [8]. Due to these wave modes being constrained by the boundaries of the sample, they can be generated at one point and 'guided' to another point of interest by the waveguide (the plate or pipe sample they travel in) hence their name.

This is very useful in NDT and in the application of these modes in this work since they can be directed to inaccessible areas and their propagation used to show differences in the samples at that point as a replacement to methods such as bulk wave thickness gauging when the surface of interest is not accessible. Guided waves can be generated and propagate in a wide range of geometries such as plate [79, 80], pipe [56, 81, 82] and rail [54] structures, with the geometry of the waveguide, the material constants of the material and the boundary conditions all determining the propagation characteristics of ultrasound within the sample.

The different geometry samples and the direction in the structure along which the ultrasound is generated, as well as the polarisation of the wave modes generated will determine the guided wave solutions that are found. There are different guided wave modes in Lamb and Shear Horizontal modes, whose respective wave equation solutions lead to an infinite number of wave modes for each of these different types in a structure. The different solutions to the wave equation result in a dispersion relation for each mode that shows the phase and group velocity of a mode at a given frequency for a given thickness of sample.

These can be plotted as dispersion curves and used to determine the speed of a particular guided wave mode at a particular point in frequency [8]. Lamb waves and SH waves vary from each other in the ways in which they are generated, propagated and detected, with Lamb waves based in the longitudinal and shear vertical bulk wave modes discussed previously and SH waves based in the shear horizontal bulk wave modes. The difference in their particle displacements leads to their application in different situations and a difference in their sensitivities. The contents of this thesis will predominantly be concerned with Shear Horizontal guided waves propagating in the circumferential direction around a pipe. A brief overview of Lamb wave generation and propagation propagating in plates will also be given to illustrate the reasons why a circumferential SH wave system might be preferable to Lamb wave systems that are currently in use in industry [83, 84].

2.10.1 Lamb Waves

Lamb waves are a class of guided waves that are generated by the superposition of bulk longitudinal and shear vertical waves [8]. This superposition is achieved by the reflection of these waves off of the boundaries of the waveguide. This method of generation means that it is a system that is prone to 'losing' energy into the surrounding media through transmission. The dispersion relation of these modes leads to many modes that exist in the same frequency range especially for higher frequency waveforms. This multi modal appearance can result in extremely complex signals, with modes difficult to differentiate from one another.

Since their description by Lamb [85], they have been effectively applied in many non destructive scenarios for thickness measurement [79, 86] and defect detection [20, 58, 61]. Characteristic relations for the propagation of these modes can be derived from applying traction free boundary conditions to a sample with a thickness comparable to the wavelength of the ultrasonic signal.

The mathematical definition of Lamb waves [8] starts from the assumption of a thin plate that is considered infinitely large in all other dimensions than the

sample thickness, including the assumption that this sample is surrounded by a vacuum. This allows for all the energy to be contained within the plate due to the lack of coupling with the surrounding media and also negates the requirement to consider edge effects and reflections. The infinitely large thin plate assumption is illustrated in Figure 2.4.

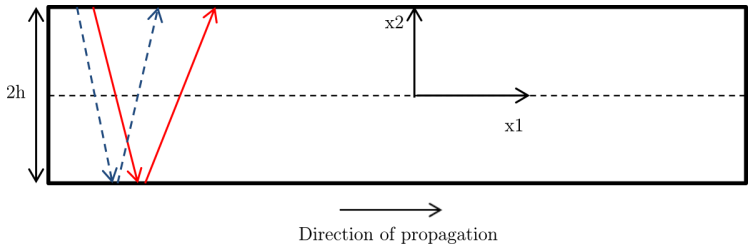

Figure 2.4: Schematic of the generation of Lamb waves by interference of Longitudinal (red) and shear vertical (blue dashed) waves in a plate of thickness 2h.

Lamb waves have been successfully used in a variety of different applications including detecting corrosion in pipelines [56, 55, 62] and plate [87, 88]. Typically a frequency of operation is chosen such that the generation of modes is limited in order to simplify the signal processing of the detected acoustic signals and to provide a large separation in arrival time between the modes due to their differences in velocity. The operation point on the mode is also chosen to be an area that shows low levels of dispersion so that the signals can travel long distances [89] along the pipeline without losing energy from the intended signal.

2.10.2 SH Waves

Shear Horizontal waves exist as a separate guided wave mode in the free plate situation, but here the particle displacement is polarised parallel to the surface of the waveguide [8, 64]. The guided wave is then generated by a superposition of up and down travelling bulk shear horizontal waves, with the conditions as in the Lamb case that the surfaces of the medium are traction free. This can be illustrated by considering the geometry in Figure 2.5 where the wave propagates in the x_1 direction, with the particle displacements polarised in the x_3 direction. The superposition of the modes occurs in the remaining x_2 direction through the thickness of the sample, here the thickness of the sample in the x_2 direction is twice the distance from the surface to the mid point of the sample, d=2h [8].

Where k is the wavenumber of the modes and is defined as

$$k = \omega / c_p = 2\pi / \lambda \tag{2.25}$$

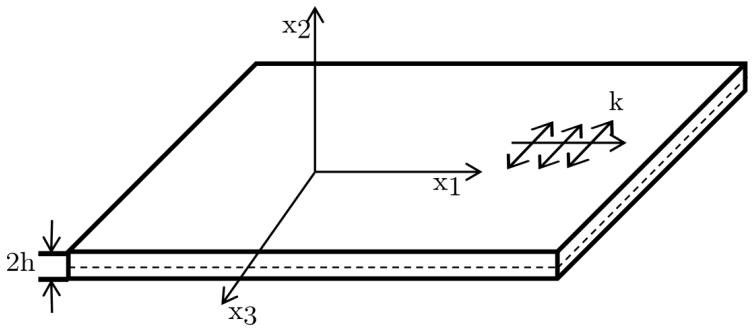

Figure 2.5: Schematic diagram showing SH wave mode propagation in a plate, with the propagation of the wave in the x_1 direction and the shear displacement of the particles along the x_3 axis.

The particle displacement field for an isotropic medium was given in equation 2.13, and this equation can be used for shear horizontal modes considering vectors with only an x_3 component such that the displacement in the other dimensions is equal to zero. This allows us to define the displacement vector for the wave as [8]:

$$u_3(x_1, x_2, t) = f(x_2)e^{i(kx_1 - \omega t)} \tag{2.26}$$

where ω is the circular frequency of the wave $\omega = 2\pi f$. It should be noted here that the displacement is independent of x_3 such that the wavefront of the SH wave is infinite in the x_3 dimension, travels in the x_1 direction and has a fixed distribution in the x_2 direction. Given the above conditions, the solution can be substituted into the equation in 2.13 and a general solution specified, such that the the general form of the displacement field is given by:

$$u_3(x_1, x_2, t) = [Asin(qx_2) + Bcos(qx_2)]e^{i(kx_1 - \omega t)} \tag{2.27}$$

Where q is defined as

$$q = \sqrt{\frac{\omega^2}{c_T^2} - k^2} \tag{2.28}$$

and A and B are arbitrary constants.

The total displacement field equation can then be separated into two different components relating to the symmetric and antisymmetric components with respect to x_2 :

$$u_3^s(x_1, x_2, t) = Bcos(qx_2)e^{i(kx_1 - \omega t)} \tag{2.29}$$

$$u_3^a(x_1, x_2, t) = Asin(qx_2)e^{i(kx_1 - \omega t)} \tag{2.30}$$

Where the superscripts s and a denote a symmetric and antisymmetric mode respectively. Now boundary conditions can be imposed on the modes that the surfaces of the layer at $x_2 = \pm$h are traction-free. This allows the dispersion equations for a traction free surface for the symmetric and antisymmetric modes to be defined as

$$sin(qh) = 0 \tag{2.31}$$

and

$$cos(qh) = 0 \tag{2.32}$$

Explicit solutions to these equations can be obtained using knowledge of the sine and cosine behaviour in that $sin(x) = 0$ when x is zero or an integer value of π and $cos(x) = 0$ when x is a factor of $\pi/2$. In other words

$$sin(x) = 0 \quad whenx = n\pi(n = 0, 1, 2, ...) \tag{2.33}$$

and

$$cos(x) = 0 \quad whenx = n\pi/2(n = 1, 3, 5, ...) \tag{2.34}$$

such that

$$qh = n\pi/2 \tag{2.35}$$

Where the symmetrical SH modes are defined by n=(0,2,4,...) and the antisymmetrical modes are defined by n=(1,3,5,...). By using the definition d=2h seen earlier and taking the real parts of the equation in equations 2.29 and 2.30, the displacement fields for the symmetric and antisymmetric modes can be respectively rewritten as:

$$u_3^s(x_1, x_2, t) = Bcos(n\pi x_2/d)\cos(kx_1 - \omega t) \tag{2.36}$$

$$u_3^s(x_1, x_2, t) = Asin(n\pi x_2/d)\cos(kx_1 - \omega t) \tag{2.37}$$

This is an important result, as the sine and cosine terms do not depend on the frequency and wavenumber of the mode. This means that the displacement field across the thickness of the sample does not vary with the frequency of the mode generated but only with the order of the mode generated. This provides a marked difference to the Lamb wave case where the displacement profile changes with the frequency and means that different SH modes should be more sensitive to different defects at all frequencies rather the sensitivity varying with frequency. An important aspect to note from the displacement profiles of the first few modes

in Figure 2.6 is that although the displacement is always maximum at the outer surfaces of the sample, it does vary throughout the sample, falling to zero at certain points for the higher order modes. This can pose a problem for inspections as it will be less sensitive to defects in these regions. As the order of the mode increases so does the complexity of these profiles, with more points of minimal displacement, which limits their use in NDT inspections.

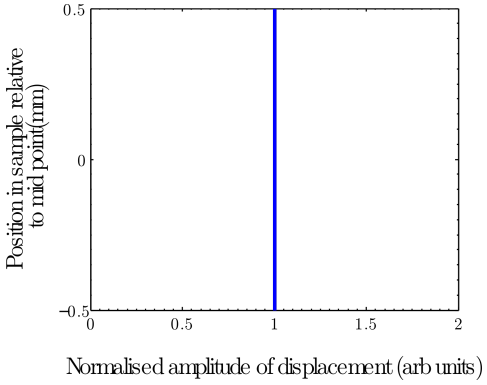

(a) SH0 displacement profile

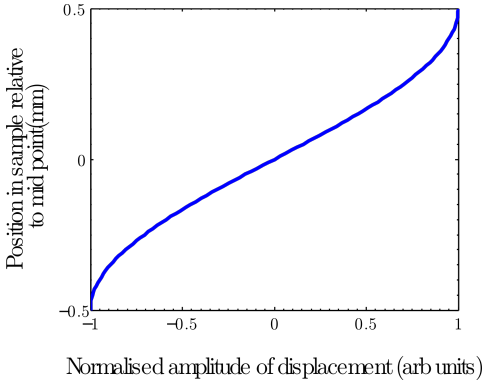

(b) SH1 displacement profile

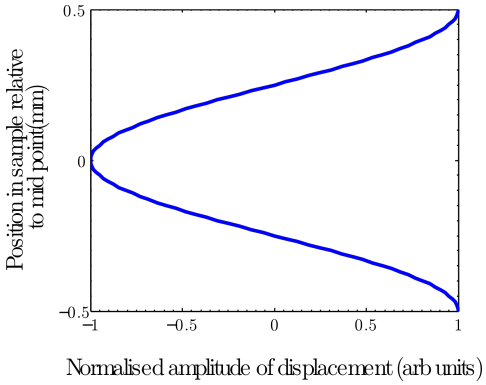

(c) SH2 displacement profile

Figure 2.6: Displacement profiles through the thickness of the plate for SH wave forces.

Explicit solutions to the phase velocity vs frequency thickness (fd) curves can be calculated from the solutions to the previous equations. This allows the generation of the dispersion curves for the shear horizontal modes that dictate the speed of wave generated for a particular frequency [8]. Using the definition of q, the solutions to the dispersion equations and the definition for k, the dispersion equation can be written as:

$$\frac{\omega^2}{c_T^2} - \frac{\omega^2}{c_p^2} = \left(\frac{n\pi}{2h}\right)^2 \tag{2.38}$$

Where the order of the SH mode in question is denoted by the integer number n. The phase speed can then be calculated using the equations set out for phase velocity where $cp = \omega/k$

$$c_p = \frac{\omega}{k} = \pm 2c_T \left(\frac{fd}{\sqrt{4(fd)^2 - n^2 c_T^2}} \right) \tag{2.39}$$

This develops the phase velocity curves for the infinite family of SH modes that can be generated in a plate. All of the modes in a plate show some dispersive nature except for the lowest order symmetric SH mode which is dispersionless and propagates with both a phase velocity and group velocity equal to the shear wave speed of the material. The group velocity of these modes is calculated from the definition of the group velocity seen earlier that $c_g = d\omega/dk$ such that:

$$c_g = \frac{d\omega}{dk} = c_T \sqrt{1 - \frac{(n/2)^2}{(fd/c_T)^2}} \tag{2.40}$$

The phase velocity curves are shown in Figure 2.7 and group velocity curves are shown in Figure 2.8, with the SH0 mode in blue, SH1 mode in red, SH2 mode in black, SH3 mode in green, SH4 mode in magenta, SH5 mode in cyan and SH6 mode in yellow. An important feature that can be seen is that in addition to the dispersive behaviour these modes show, all but the fundamental SH mode have a cut off where the phase velocity becomes infinite and the group velocity drops to zero at a certain value of frequency thickness.

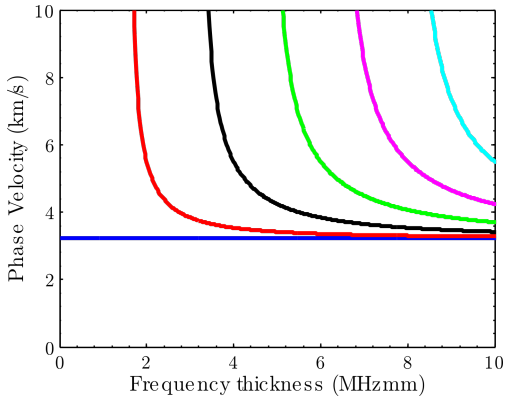

Figure 2.7: SH guided wave phase velocity dispersion curve for a steel plate

These are known as cut off frequencies, here the wavenumber of the propagating wave along the x_1 direction becomes imaginary and the wave becomes evanescent and nonpropagating [64]. The cut off frequency for the nth mode is:

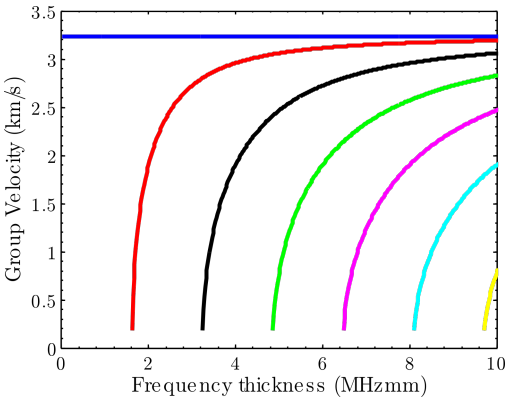

Figure 2.8: SH guided wave group velocity dispersion curve for a steel plate

$$(fd)_n = \frac{nc_T}{2} \tag{2.41}$$

When a higher order mode with a cut off frequency reaches a section of plate where the remaining thickness is less than the cut off thickness, then the mode is forced to mode convert and reflect at the interface. The extent to which these processes occur will be discussed later but it extremely important in guided wave inspections, being dependent not only on the thickness of the plate but the profile of the wall thickness change.

The area just before the cut off thickness in a sample is the most dispersive area of the curve, with the group speed decreasing for decreasing thickness which aids in identification of defects approaching the cut off thickness of the sample. As the frequency thickness product is increased, all modes tend towards the shear wave speed in the material, as the waves begin to propagate as if they were travelling in the bulk of a material.

2.11 Dispersion curves in different geometries

When guided waves are applied in a different structure to that of a plate, their behaviour is altered. The most common feature of this is in the use of guided waves in pipelines. Generally when experiments are carried out with pipelines, the difference between plate and pipe dispersion curves is accepted but assumed to be small so that the pipe dispersion curves are assumed to follow the pattern of that in the plate. However, there are some marked differences. Guided wave propagation in an annulus is dependent on direction, such that the dispersion curves differ depending on whether the waves propagate axially or circumferentially. Other

engineering structures such as rail track heads also have a distinctively different and more complex guided wave behaviour because of their geometry.

Much of the work on guided waves in a pipeline has been based on axially propagating Lamb like waves in order to provide long distance pulse-echo style detection of defects [90] via an amplitude drop of reflected signals. The waves generated axially can be referred to as longitudinal and flexural and are analogues to the symmetric and antisymmetric modes that are found in a plate [91, 58, 62]. The dispersion curves for Lamb-like modes can change quite drastically for axial travel and this change has to be taken into account when designing an inspection and a point of operation. With long distance scanning of pipelines in this application, the operation of probes is typically limited to areas of the dispersion curves that feature low levels of dispersion in order to simplify analysis and allow for the waveforms to travel long distances coherently. Lamb modes have also been successfully applied in a circumferential operation in theory [57] and experiment [83, 84] to provide a tool to locate wall thinning in pipeline, relying on a change of speed of the Lamb wave along a line to detect a defect and provide some quantification of the extent of wall thinning. Obstacles to these inspections can arise when the samples are thick as stronger single magnets are required in order to generate satisfactorily strong field to generate strong enough signals when using EMATs, and the type of waveform used can result in leaking of the wave's energy into the surroundings or the interior of a fluid filled pipeline.

The alternative to this is to use SH waves generated by EMATs which will be mentioned in detail in sections 2.13.2 and 2.13.8. The advantages here being that the SH wave energy doesn't leak into the internal media such as the liquid contents of the pipeline or the external surroundings in a subsea case due to the shear motion not being supported in liquid media. The interpretation of signals can also be simpler than some Lamb wave inspections [92]. SH waves have been shown to be able to travel round corners in plates [93] and can be used for axial propagation of SH waves along pipelines [82]. Their relatively simple behaviour compared to Lamb waves in terms of dispersion and mode conversion characteristics gives a better chance of being able to interpret received signals to obtain depth estimates for defects, but it has been shown that the geometry of defects [94, 82] as well as depths influences signals and the use of the circumferential dispersion curves [95, 96] is often neglected in favour of the more simple but less exact plate dispersion curves [97]. The validity of such an assumption has been studied and found that in cases this is indeed valid but in others the behaviour can be markedly different [96].

2.12 Dispersion curves in an annulus

The dispersion relations for SH waves in a plate, relating the frequency of a mode to its phase and group velocity were stated previously in equations 2.39 and 2.40 with the subsequent dispersion curves seen in Figures 2.7 and 2.8. When a pipe structure is involved, the governing equations become more complex and the derivation of these equations is possible following the procedure set out in [95]. The analytical derivation of guided circumferential SH wave modes can be started at equation 2.13. Assuming there is only displacement in the z direction along the length of the pipeline and changing to cylindrical coordinates, $u_r = u_\theta = 0$ and $u_z \neq 0$ so that equation 2.13 can be written as:

$$\rho \frac{\partial^2 u_z}{\partial t^2} = \mu \left(\frac{\partial^2 u_z}{\partial r^2} + \frac{1}{r}\frac{\partial u_z}{\partial r} + \frac{1}{r^2}\frac{\partial^2 u_z}{\partial \theta^2} \right) \tag{2.42}$$

Denoting the dimensions of the cylinder as having an inner radius of a and an outer radius b, and defining that the wave is time harmonic and propagates in the theta direction around the pipe circumference, the displacement in the z direction can be defined by:

$$u_z = \Psi(r) e^{i(kb\theta - \omega t)} \tag{2.43}$$

Where r is a value between a and b and the wavenumber k is defined by $k = \omega / c(b)$ and c(r) is the linear phase velocity for particles at a distance r from the centre of the cylinder. Using this value for the displacement allows the equation in 2.42 to become:

$$\Psi'' + \frac{1}{r}\Psi' + \left[\frac{\omega^2}{c_T^2} - \left(\frac{kb}{r} \right)^2 \right] \Psi = 0 \tag{2.44}$$

Where $\Psi'' and \Psi'$ are the second and first order derivatives with respect to r respectively and ω,k and c_T are the angular frequency, wavenumber and shear wave velocity as defined previously. This equation can be recognised as a Bessel equation and following the literature [57], non dimensional variables can be introduced such that:

$$\bar{r} = \frac{r}{b}, \quad \bar{k} = kh, \quad \bar{\omega} = \frac{\omega h}{c_T}, \quad h = b - a \tag{2.45}$$

$$\hat{k} = \frac{\bar{k}}{1-\eta}, \quad \hat{\omega} = \frac{\bar{\omega}}{1-\eta} = \frac{\omega b}{c_T}, \quad \eta = \frac{a}{b} \tag{2.46}$$

This allows the solutions to be written as:

$$\Psi(r) = AJ_{\hat{k}}(\hat{\omega}\bar{r}) + BY_{\hat{k}}(\hat{\omega}\bar{r}) \tag{2.47}$$

Where the $J_{\hat{k}}(x) and Y_{\hat{k}}(x)$ are Bessel functions of the first and second kind of order $\hat{k}$ and A and B are arbitrary constants.

Assuming the surfaces of the hollow cylinder are traction free so that

$$\sigma_{rz}|_{r=a,b} = \mu \left.\frac{\partial u_z}{\partial r}\right|_{r=a,b} = 0 \tag{2.48}$$

By substitution we can obtain the following equation:

$$AJ'_{\hat{k}}\left(\frac{\omega}{c_T}r\right) + BY'_{\hat{k}}\left(\frac{\omega}{c_T}r\right)\Big|_{r=a,b} = 0 \tag{2.49}$$

This can be written in an expanded form to find a set of linear homogeneous equations with A and B as unknown variables:

$$A\left[J_{\hat{k}-1}\left(\frac{\omega}{c_T}a\right) - J_{\hat{k}+1}\left(\frac{\omega}{c_T}a\right)\right] + B\left[Y_{\hat{k}-1}\left(\frac{\omega}{c_T}a\right) - Y_{\hat{k}+1}\left(\frac{\omega}{c_T}a\right)\right] = 0 \tag{2.50}$$

$$A\left[J_{\hat{k}-1}\left(\frac{\omega}{c_T}b\right) - J_{\hat{k}+1}\left(\frac{\omega}{c_T}b\right)\right] + B\left[Y_{\hat{k}-1}\left(\frac{\omega}{c_T}b\right) - Y_{\hat{k}+1}\left(\frac{\omega}{c_T}b\right)\right] = 0 \tag{2.51}$$

For non trivial solutions to these equations, the determinant of the coefficient matrix of this system must vanish. This gives a dispersion relation between the wave number and frequency of the system as:

$$\begin{gathered}[J_{\hat{k}-1}(k_T a) - J_{\hat{k}+1}(k_T a)][Y_{\hat{k}-1}(k_T b) - Y_{\hat{k}+1}(k_T b)] - \\ [J_{\hat{k}-1}(k_T b) - J_{\hat{k}+1}(k_T b)][Y_{\hat{k}-1}(k_T a) - Y_{\hat{k}+1}(k_T a)] = 0\end{gathered} \tag{2.52}$$

Where k_T is the shear wave wave number. For a given frequency value, the value of $\hat{k}$ can be obtained from this equation such that the phase velocity can be calculated:

$$c(b) = \frac{2\pi f}{\hat{k}(1-\eta)} \tag{2.53}$$

and the subsequent group velocity through equation 2.23. This allows for the generation of the phase and group velocity dispersion curves for SH waves in a hollow cylinder.

An example of the circumferential guided wave dispersion curves for the phase velocity is shown in Figure 2.9 with plate versions also provided for comparison and the group velocities shown in Figure 2.10. A few key differences are shown here in that the circumferential SH0 mode is no longer non dispersive at all frequencies and begins at above the shear wave velocity. The higher order modes also show some difference from the plate versions especially around the 'knee' areas of the curves, although the cut off frequencies remain the same as in a plate. It is apparent therefore that there are situations in which the pipe dispersion curves must be used instead of a plate approximation particularly if exact values of velocities are required.

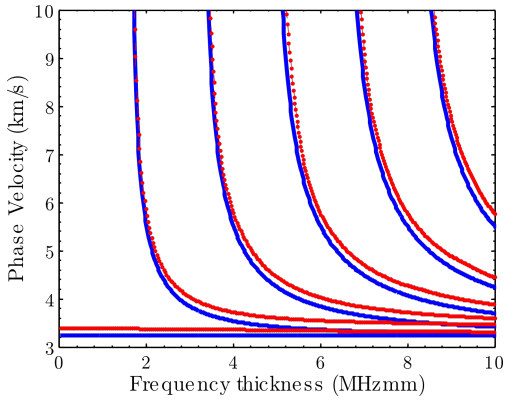

Figure 2.9: SH guided wave phase velocity dispersion curves for a 7 mm thick steel plate (blue) and circumferentially around a 7 mm thick, 86 mm outer radius pipe (red dotted).

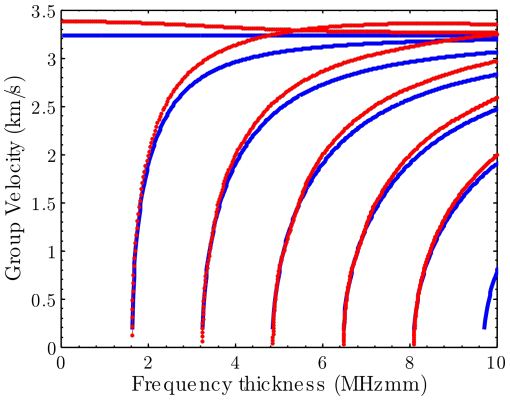

Figure 2.10: SH guided wave group velocity dispersion curves for a 7 mm thick steel plate (blue) and circumferentially around a 7 mm thick, 86 mm outer radius pipe (red dotted).

2.13 Ultrasonic Transduction

As mentioned in Chapter 1, a range of methods exist for generating and receiving ultrasonic signals. They have different strengths and weaknesses and are applied in different situations where they are appropriate [64, 12, 28]. The generation of ultrasound in different ways is explained subsequently, with particular focus on EMATs as that is the transducer type used in the experimental system here.

The most common transducer type in NDT is the piezoelectric transducer [64]. These are used all across the spectrum of NDT applications due to their high efficiency of generation and detection compared to other methods and the ease with which they can be applied to a wide range of materials including complex materials such as plastics and composites [98, 99]. However, they possess a distinct disadvantage in that they require contact with a sample and usually a couplant material to allow efficient transfer of energy from the transducer into the sample. The consequence of this is that they can be unsuitable for some uses such as when high temperature samples such as parts in constant use in power stations need to be tested, or when the part needs to be scanned continuously at a high speed (metres per minute) such as in the pipe screening implementation here. They can be used to generate a wide range of waveforms, but often are very sensitive to their positioning on the sample and of the transmitter relative to the receiver.

The advantage of non contact methods such as EMATs is clear in this case, as contact with the sample is not necessary and hence very fast continuous scanning systems (metres per minute) can be implemented, with less consideration of the surface condition of a sample and alignment of transducer to the surface. The EMAT also does not require the mechanical coupling to the surface [100] that is necessary in a piezoelectric transducer, removing the need for a coupling medium and ensuring measurements are more repeatable as there are no inconsistencies from the amount of couplant below a probe. It also makes them suitable for high temperature measurements [101] and means they can be applied for measurements through thin coatings and scanned tomography [102]. The trade off for these advantages is that the signal to noise ratio in EMAT scans is much less than in piezoelectrics [103, 104] due to the efficiency of generation and reception being much lower [105]. They also only work effectively on conductive samples, which limits their use in general to metals.

However, the use of EMATs is preferred in some cases for different wave mode generation due to the direction of the forces on the surface of the sample being defined by the orientation of the magnet and the coil. This allows for modes

such as the SH mode to be generated effectively by EMATs by simply using an array of magnets and a coil to generate the horizontal shear forces necessary for this wave mode [106].

In contrast to this, generation of shear waves by piezoelectric probes is more complex in that they require waves generated at a critical angle or with very high viscosity couplant which can make inspections more difficult. Shear vertical waves are often excited in a sample via an angled probe to achieve mode conversion of longitudinal waves at a critical angle in the medium [107], this works well for shear vertical modes but does not produce shear horizontal modes. Horizontally polarised shear waves can be generated in a sample using piezoelectric methods using zero degree angle of incidence probes [108] where the forces generated by the probe are designed to provide the shearing motion parallel to the surface as desired, but they require a much more viscous couplant than is used in the ordinary longitudinal or shear vertical generation such as a specialist high viscosity fluid or honey. This makes these transducers difficult to work with and limits their usage in the scanning of samples, with the use of such probes deemed unsuitable for the screening technique desired in this work.

2.13.1 Piezoelectric transducers

Although not considered in this work, it is prudent to give a summary of the piezoelectric effect in generating ultrasound due to its position as a major technology in ultrasound in NDT [12, 28, 13, 11]. Piezoelectric transducers can both generate and detect ultrasonic vibrations in a material to which they are coupled. The detection of ultrasonic waves is achieved via the direct piezoelectric effect where stress is applied to a crystal due to the ultrasonic vibrations in a sample, which produces a strain and a difference in potential between opposing faces of the crystal. The inverse effect can be used to generate ultrasound in a sample where a time varying potential difference is applied across the faces of the crystal to induce a strain at high frequency which results in mechanical deformation of the crystal, allowing ultrasonic vibrations to be generated and coupled into the sample material via a couplant substance. Hence it is possible to use these piezoelectric crystals to generate and detect ultrasound[12, 64, 11].

Piezoelectric materials do not have a centre of symmetry in the crystal, which is important as it separates positive and negative charge in the crystal [64]. Using the example of a quartz crystal, this effect can be illustrated. When no stress is applied, the positive and negative charges are balanced so that there is no molecular dipole moment. Once the crystal is exposed to a stress the distribution of positive

and negative charges becomes unbalanced, creating a molecular dipole moment and a polarisation, which leads to charge build up on the faces and a potential difference [64, 109]. The cut of a crystal and hence the axis along which the asymmetry of charge occurs, defines whether the longitudinal or shear modes are generated. Conventional piezoelectric transducers are commonly made from ceramics rather than a single crystal, with Lead Zirconate Titanate (PZT) and Barium Titanate (BaTi) common types.

The most common formulation of the constitutive equations for piezoelectricity that couple the elastic and electrical properties is [64, 28]:

$$D = d_p T + \epsilon^T E \tag{2.54}$$

and

$$S = s^E T + d_p E \tag{2.55}$$

Where D is the electric displacement, E is the electric field, S is the strain, T is the stress, ϵ^T is the permittivity of the piezoelectric under constant stress, s^E is the mechanical compliance for a constant electric field and d_p is the piezoelectric charge constant.

Piezoelectric transducers generally use the thickness oscillations across a plate of material a few millimetres thick. The operating frequency is set by the thickness of the piezoelectric material, with the thickness d_e of the element equal to half the wavelength, λ of the signal generated:

$$d_e = \frac{\lambda}{2} \tag{2.56}$$

giving a fundamental working frequency of the transducer f_0 of:

$$f_0 = \frac{c}{2d_e} \tag{2.57}$$

Where c is the velocity of longitudinal waves within the piezoelectric material. The element will also exhibit higher harmonics of the frequency.

In order to effectively transmit the oscillations in the piezoelectric into the sample to be tested, it is sometimes beneficial to add a matching layer in front of the piezoelectric material [110]. This is intended to minimise the acoustic impedance mismatch that occurs between the piezoelectric material and the sample and should have an impedance that is intermediate between the transducer impedance and the sample impedance. It has been shown that the ideal thickness of the matching

layer is $\lambda/4$ so that any reverberations in the matching layer occur in phase with one another allowing for constructive interference of the wave [64]. The general construction of a piezoelectric transducer with backing layer is shown in Figure 2.11. Often in NDT, a matching layer is not used and there is simply a wear plate in front of the piezoelectric element.

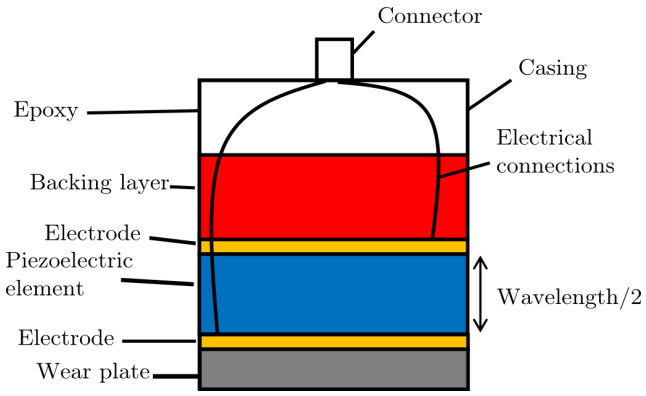

Figure 2.11: Schematic of a basic design of a piezoelectric transducer including an active element, backing and matching layers.

In addition to the matching layer to allow for more efficient transmission of the generated vibrations into the sample, piezoelectric transducers also generally require a gel or liquid couplant in order to provide satisfactory coupling of the signal into a sample. This can be prohibitive in high temperature applications and can prevent some modes from being generated. It also means that the coupling efficiency from one measurement to the next is not repeatable due to the liquid couplant not being a constant factor in every experiment.

2.13.2 Principles of EMATs

EMATs consist of a strong magnet and an electrically conducting coil of wire [9]. The magnet provides a biasing magnetic field to interact with the eddy currents that are induced at the surface region of a conductive material by an alternating electrical current that is pulsed through the excitation coil. EMATs couple their electromagnetic fields with the elastic fields generated in a sample in three ways. These coupling mechanisms are the Lorentz force, magnetisation force and magnetostriction.

The Lorentz force is caused by the interaction between the eddy currents that are induced in the sample and the static magnetic flux density generated by the permanent magnet. This force exists in any conductive sample and has been shown to be the predominant mechanism for ultrasound generation. The other

forces only effect samples that are ferromagnetic, with the magnetisation force between the oscillating magnetic field and the magnetisation of the material and the magnetostriction force being caused by the piezomagnetic effect.

The wave generation of an EMAT can be described as starting with the interaction of the electromagnetic fields within the sample, then calculating the body forces generated by the interactions between the electromagnetic and elastic fields in the sample and final calculation of the acoustic fields caused by the generated body forces.

The starting point for calculating the interaction between the electromagnetic forces generated by the EMAT and the electrically conducting sample is Maxwell's equations[111]:

$$\nabla \cdot D = \rho f \tag{2.58}$$

$$\nabla \cdot B = 0 \tag{2.59}$$

$$\nabla \times E = -\frac{\partial B}{\partial t} \tag{2.60}$$

$$\nabla \times H = \frac{\partial D}{\partial t} + J_f \tag{2.61}$$

Where D is the displacement vector, H is the magnetic field strength, J_f is the free current density, E is the electric field, B is the magnetic field and ρ_f is the free charge density. Any electromagnetic field must satisfy all of these equations. Also necessary here are the relations between the displacement and magnetic field strength vectors and the electric magnetic fields.

$$D = \epsilon_r \epsilon_0 E \tag{2.62}$$

$$H = \frac{B}{\mu_r \mu_0} \tag{2.63}$$

where ϵ_r is the relative permittivity of the material and μ_r is the relative permeability of the material.

2.13.3 Skin effect

The time varying excitation signal sets up an electric field in the sample which drives the eddy currents within the sample. These eddy currents act to oppose the propagation of the electromagnetic wave due to the action of Lenz's law [111],

which means that the eddy currents are only generated within a certain depth in the sample, in order for the boundary condition at the interface to be satisfied. The depth to which the eddy currents penetrate is known as the electromagnetic skin depth and is given for a conductor as [64, 32]:

$$\delta = \sqrt{\frac{2}{\omega\mu\sigma}} \tag{2.64}$$

So here the skin depth can be seen as inversely proportional to the angular frequency ω of the electromagnetic wave and the permeability, μ and conductivity σ of the sample.

The magnetic field then decays exponentially into the depth of the sample, by a factor of $1/\delta$.

The plane wave solution for the electric field can be represented by [111]:

$$E = E_0 e^{i(\omega t - \frac{z}{\delta})} e^{(-\frac{z}{\delta})} \tag{2.65}$$

Which shows that the amplitude of the electric field exponentially decreases with distance into the material. Since current density is represented by Ohm's law, it can also be stated that the current density decreases exponentially with penetration distance into the material:

$$J = \sigma E = J_0 e^{i(\omega t - \frac{z}{\delta})} e^{(-\frac{z}{\delta})} \tag{2.66}$$

So that the skin depth can be shown to be the depth below the surface at which the current density has fallen to 1/e of its original value at the surface.

The penetration depth for steel is around 0.01mm at ultrasonic frequencies of 1MHz [9], which means that this depth is much smaller than the ultrasonic wavelength of the types of EMAT probes that are used in NDT so that it can be assumed that the electromagnetic fields occur only at the material surface and subsequently that approximation of the forces that are applied by an EMAT can be assumed by approximating these forces on the surface of the sample.

The total current induced in a column of unit area through the semi-infinite, conductive medium can be found by integrating the current density through the depth:

$$I = \int_0^\infty J dz \tag{2.67}$$

$$I = J_0 e^{i\omega t} \int_0^\infty e^{-(1+i)\frac{z}{\delta}} dz \tag{2.68}$$

$$I = J_0 e^{i\omega t} \frac{\delta}{1+i} = I_k e^{i(\omega t - \frac{\pi}{4})} \tag{2.69}$$

Which shows how the induced current can be treated as a single image current, which has a phase lag of $\frac{\pi}{4}$ relative to the induced surface electric field defined in equation 2.65.

2.13.4 Lorentz force

As mentioned, the predominant force generated by an EMAT in a conducting material is commonly the Lorentz force[111]. This details the force experienced by a particle with charge q, as a result of electric and magnetic fields.

$$F = q(E + v \times B) \tag{2.70}$$

The magnetic field here contains both the static biasing magnetic field from the permanent magnet and the dynamic field produced by the excitation current. In a conducting material such as metals, the electrons are the charge carriers such that the Lorentz force equation becomes:

$$m\frac{dv_e}{dt} = -e(E + v_e \times B_0) - \frac{mv_e}{\tau} \tag{2.71}$$

Where m is the mass of an electron, e is the electron's charge and v_e is the mean electron velocity, with τ being the mean time between electron scattering events and being of the order of 10^{-14}s for metals such as steel at room temperature[9]. Assuming harmonic oscillation of the electric field with the angular frequency, this equation reduces to:

$$n_e\frac{mv_e}{\tau} = -n_e e(E + v_e \times B_0) \tag{2.72}$$

Where n_e is the electron density. The momentum is transferred from the electrons to the ions via collision processes, such that the body forces on the ions are approximated as [9]:

$$f = NZ_i(E + u \times B_0) + n_e\frac{mv_e}{\tau} \tag{2.73}$$

Where N is the ion density, Z_i the ion charge and u is the ion displacement. Assuming the volume has no charge such that $n_e e = NZ_i$ and that $v_e >> u$, the force per unit volume on the ions reduces to:

$$f = -n_e e v_e \times B_0 = J_e \times B_0 \tag{2.74}$$

where

$$J_e = -n_e e v_e \tag{2.75}$$

is the eddy current density. This has shown that the Lorentz force as above can cause an acoustic vibration. As mentioned previously, the magnetic field that is generated is made up of both the static field from the biasing magnet and the dynamic field from the excitation coil. It can be shown that the Lorentz forces due to the static field are proportional to the driving current and vibrate with the same frequency as the driving current, whereas those caused by the dynamic field vibrate at a frequency double that of the excitation current frequency [9]. Given that the static field is much larger than the dynamic field we can ignore the dynamic field in general, however, it does show that using a large driving current, the EMAT can generate ultrasound without the static field, which can be advantageous in some circumstances. The Lorentz force mechanism for the generation of ultrasound with EMATs is shown in Figure 2.12.

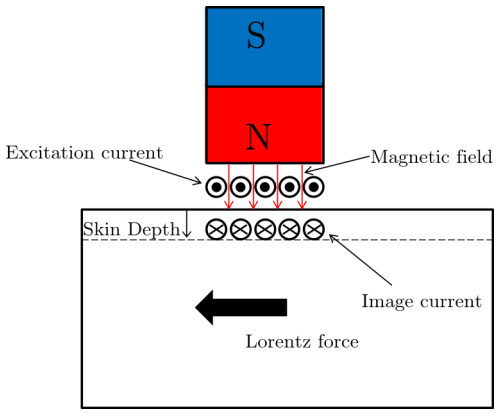

Figure 2.12: Schematic diagram of the Lorentz force mechanism seen in EMATs, the skin depth will typically be very small such that forces can be approximated as only affecting the surface of a sample.

The other methods that can contribute to the generation of ultrasound in a ferromagnetic material should be considered here since the material that is used in this research is steel. These as mentioned previously are the magnetisation force and mangetostriction. It has been the cause of much debate in the literature as to which transduction method dominates in steels, with some studies suggesting magnetostriction dominates [103]. However, it has been shown that the predominant effect in using EMATs on steels is the Lorentz force [112, 113, 114], with the

ferromagnetic effects only contributing a small amount to the forces exerted by the transducer. This is a particularly important issue here as it means the forces for the periodic permanent magnet array transducers used here can be approximated with the Lorentz force interactions as the magnet array generates the shearing forces on the surface via a Lorentz force interaction.

2.13.5 Magnetisation force

The magnetisation force [9] arises in a ferromagnetic material that is exposed to an external field, H. It is a function of the electromagnetic field that is generated by the transducer interacting with the internal magnetism in the material. It is composed of the body force per unit volume and a force on the surface of the material, which occurs due to the abrupt change of the electromagnetic fields at the surface and their related decrease into the material. These are defined as F_v and F_s respectively:

$$F = F_v + F_s = \int_v \nabla^*(M \cdot H)dv + \frac{1}{2}\mu_0 \int_S nM_n^2 dS \tag{2.76}$$

Where ∇^* denotes the gradient operating only on H, n is a unit vector normal to the material surface and M_n is the normal component of the magnetisation at the surface. The integrand in the first term of this equation is the mangetisation force, the body force per unit volume:

$$F^{(v)} = \nabla^*(M \cdot H) \tag{2.77}$$

The body force per unit volume can be rewritten when the biasing magnetic field is applied, the forces can be split into a force in x and a force in z:

$$F_x^{(v)} = M_{0x}\frac{\partial H_x^M}{\partial x} + M_{0z}\frac{\partial H_z^M}{\partial x} \tag{2.78}$$

$$F_z^{(v)} = M_{0x}\frac{\partial H_x^M}{\partial z} + M_{0z}\frac{\partial H_z^M}{\partial z} \tag{2.79}$$

The second terms here can be considered negligible since the external field in x is much larger than in z. Using this and the Lorentz forces in the material we can express the magnetisation and Lorentz forces in x and z:

$$F_x^{(M)} + F_x^{(L)} = B_{0z}\frac{\partial H_x^M}{\partial z} + M_{0x}\frac{\partial H_x^M}{\partial z} \tag{2.80}$$

$$F_z^{(M)} + F_z^{(L)} = (M_{0x} - B_{0x})\frac{\partial H_x^M}{\partial z} = -\mu_0 H_{0x}\frac{\partial H_x^M}{\partial z} \tag{2.81}$$

The biasing magnetic field in EMATs is normally less than a few Tesla and $|\mu_0 H_0| << |M_0|$

In the case of a tangential biasing magnetic field, the Lorentz and magnetisation forces in a sample act to oppose each other, with the magnetisation force cancelling a large part of the Lorentz force in the z direction so that EMATs are ineffective at generating longitudinal mode waves in a ferromagnetic material.

2.13.6 Magnetostriction

The third method of generation in an ferromagnetic sample such as steel is magnetostriction [9]. This occurs because the external magnetic field makes the magnetic domains within the sample want to align with the applied field, which causes a dimensional change within the sample, causing strain. In a polycrystalline material, the dimensional change has two steps, first the domains with a magnetisation orientated close to the orientation of external field increase in volume, causing an elongation along the field, then the magnetisation in this domain rotates about the easy axis within the domain to align exactly to the field direction. This method of changing the dimensions of the material can be used to generate an ultrasonic wave [115, 113].

The coupling between the elastic and magnetic fields can be assumed to take a similar form to that of a piezoelectric material:

$$S_I = d_{Ij}^{(MS)} H_J + S_{IJ}^H \sigma_J \tag{2.82}$$

Where I,J=1,2,...,6 and j=x,y,z, S_I is a component of the strain,S_{IJ}^H is a component of the compliance matrix at a constant field and σ_J the stress component. The piezomagnetic strain coefficients can then be written as

$$d_{Ij}^{(MS)} = \left(\frac{\partial S_I}{\partial H_j} \right) \Bigg|_{\sigma} \tag{2.83}$$

When a magnetic field is applied to the material the strain above appears. The stress to cause magnetostriction can be described as:

$$\sigma_K = c_{IJ}^H d_{Ij}^{(MS)} H_j \tag{2.84}$$

If the applied magnetic field changes quickly or vibrates with a high frequency, the strain will fail to respond simultaneously with the field and the stress field $-\sigma_k$ will occur inside the material. The magnetostriction stress is then given as:

$$\sigma_I^{(MS)} = -c_{IJ}^H d_{Jj}^{(MS)} H_j = -e_{Ij}^{(MS)} H_j \tag{2.85}$$

with the converse piezomagnetic stress coefficients

$$e_{Ij}^{(MS)} = c_{IJ}^H d_{Jj}^{(MS)} = -\left(\frac{\partial \sigma_I^{(MS)}}{\partial H_j}\right)\Bigg|_S \tag{2.86}$$

The constitutive equation between the stress, strain and field is then given by:

$$\sigma_I = -e_{Ij}^{(MS)} H_j + c_{IJ}^H S_J \tag{2.87}$$

The body forces caused by the magnetostriction stress are then:

$$f_x^{(MS)} = \frac{\partial \sigma_1^{(MS)}}{\partial x} + \frac{\partial \sigma_6^{(MS)}}{\partial y} + \frac{\partial \sigma_5^{(MS)}}{\partial z} \tag{2.88}$$

$$f_y^{(MS)} = \frac{\partial \sigma_6^{(MS)}}{\partial x} + \frac{\partial \sigma_2^{(MS)}}{\partial y} + \frac{\partial \sigma_4^{(MS)}}{\partial z} \tag{2.89}$$

$$f_z^{(MS)} = \frac{\partial \sigma_5^{(MS)}}{\partial x} + \frac{\partial \sigma_4^{(MS)}}{\partial y} + \frac{\partial \sigma_3^{(MS)}}{\partial z} \tag{2.90}$$

The acoustic fields generated by the magnetostriction forces can then be calculated when the piezomagnetic coefficients $d^{(MS)}$ and $e^{(MS)}$ are known.

Magnetostriction has been shown to have a smaller effect than the Lorentz force in the generation of ultrasound in materials such as steel [112]. There are specific applications however, where magnetostriction has a greater effect such as in high temperature applications where iron oxide scale (magnetite) has formed on the sample surface and greatly increases the effect of magnetostriction [116] .

2.13.7 Receiving ultrasound with EMATs

Both the Lorentz force and the magnetostrictive force are reversible [9], such that the process of detection can be considered to be the reverse of the generation process. This means that the acoustic wave generates dynamic electromagnetic fields in the conductive material when it's exposed to external bias field. This is caused by the ultrasonic wave forcing the ions and electrons to oscillate, with a Lorentz force felt by both charge carriers. The movement of electrons in the material gives rise to these electromagnetic fields which in turn induce a current in the coils of the detecting EMAT. This means that the receiving mechanism must consider the electromagnetic

fields in the material from the acoustic waves, the boundary at the surface where the fields pass into a vacuum and the electromagnetic fields in the vacuum where the coil is located.

The literature has shown that EMATs are velocity sensors [16, 117]. For a wave travelling to the surface of the sample, the displacement u(z,t) can be defined as:

$$u(z,t) = u_0 e^{[i(\omega t - kz)]} \tag{2.91}$$

At the surface of the sample, the displacement vector will be a sum of the wave travelling up to the surface and the reflected wave from the surface that travels away from it. This results in a displacement vector ξ that is defined as:

$$\xi = u_0 e^{[i(\omega t)]}(e^{[-ikz]} + e^{[+ikz]}) \tag{2.92}$$

which can be written as

$$\xi = u_0 e^{[i(\omega t)]} 2cos(kz) \tag{2.93}$$

Using Ohm's law, the current density can be defined as:

$$J(z) = \sigma \left(\frac{\partial \xi}{\partial t} \right) B \tag{2.94}$$

As ξ is perpendicular to the static magnetic field of the EMAT, the magnitude of the current density can be defined as:

$$\mid J(z) \mid = i\sigma\omega u_0 e^{[i(\omega t)]} 2cos(kz) \tag{2.95}$$

This can be integrated through the skin depth to give an average value of the current density through the skin depth.

$$J = \frac{1}{\delta} \int_0^{\delta} i\omega\sigma u_0 e^{i\omega t} 2cos(kz) dz \tag{2.96}$$

such that

$$J = \frac{i\omega\sigma}{k\delta} u_0 e^{i\omega t} [2sin(kz)]_{z=0}^{z=\delta} \tag{2.97}$$

As the eddy current density is confined within the skin depth, and the skin depth is much smaller than the ultrasonic wavelength in most cases, $\delta << k$ then the small angle approximation can be used to approximate that $sin(k\delta) \approx k\delta$ such

that these factors in the equation cancel and the expression simplifies to:

$$J = i\omega\sigma 2u_0 e^{i\omega t} \tag{2.98}$$

so that

$$J = 2\sigma \frac{\partial u(0,t)}{\partial t} \tag{2.99}$$

The current density here is what is detected by the EMAT coil, which has been shown in the temporal derivative of the displacement here (the velocity).

As mentioned, another method that can be used for ultrasonic wave generation in a ferromagnetic material is magnetostriction, this too is reversible, with the inverse magnetostrictive effect known as the Villari effect [13, 9]. The tensile stress in the material generates a change in magnetic flux and a corresponding current is induced in the detector coil.

In both generation and reception of ultrasound with EMATs, the efficiency is greatly reduced with lift off distance such that lift off is usually limited to a few millimetres [118, 119, 120], this is due to the exponential decay of the electromagnetic fields with distance. The lift off that is possible however, means that EMAT systems can be automated and detect defects through coatings, both aspects that are difficult for piezoelectrics due to the generation of the forces needing connection to the sample and a ringing effect seen in signals due to the coating layer.

2.13.8 The Periodic Permanent Magnet EMAT

The most common EMAT configuration for generating shear horizontal guided waves is the periodic permanent magnet (PPM) array design EMAT [121, 81, 106]. The PPM EMAT consists of an array of permanent magnets (usually rare earth magnets of the type Nd-Fe-B) with alternating polarities above a racetrack coil through which an excitation current is pulsed, a diagram of the structure is provided in Figure 2.13a.

In the case of a 10 mm wavelength array used in Chapter 3, the EMAT is comprised of 6 magnets, each 4 mm wide with 1 mm alumina ceramic spacers between the elements to provide a pitch of 5 mm for the array and hence a wavelength of 10 mm, a photo showing the array of magnets is provided in 2.13b onto which the racetrack coil would be placed.

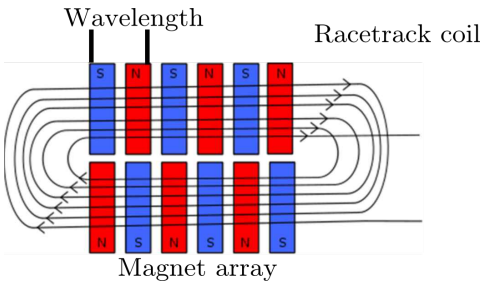

(a) Schematic plan diagram of the periodic permanent magnet array used in an EMAT that generates shear horizontal ultrasound via the Lorentz force.

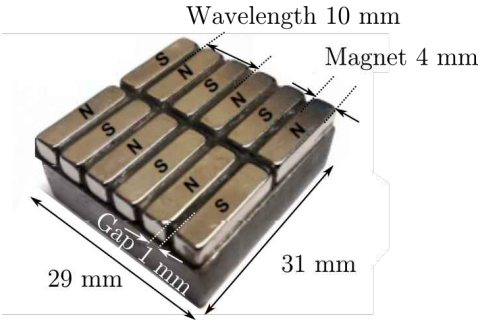

(b) Photo of the 10 mm wavelength PPM array with dimensions.

Figure 2.13: Construction of the PPM EMAT, schematic plan and photograph of the probe structure.

The alternating poles of the permanent magnets provide an alternating Lorentz force in the sample surface shown in Figure 2.14, giving the required shearing force parallel to the sample surface. Here a simplified view is provided, with a force in opposite directions below each magnet of opposite polarity as the shearing forces will reach a peak magnitude at the centre of each magnet, but in reality the structure generates a sinusoidal force profile, not a single maximum as will be seen in the next section covering the bandwidth of probes.

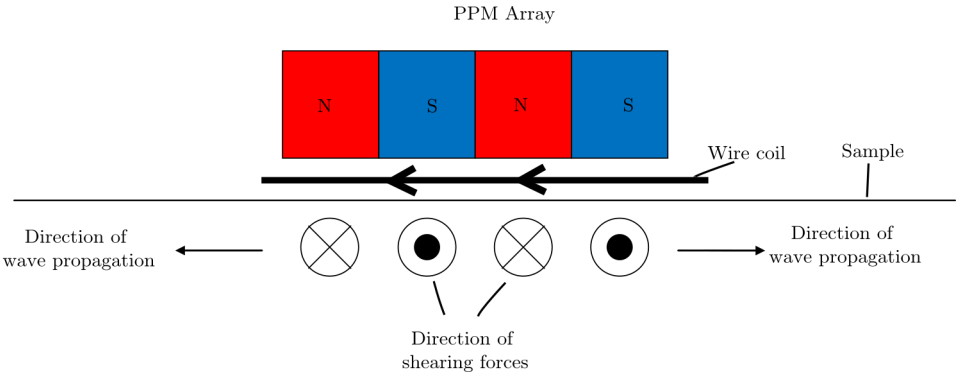

Figure 2.14: Schematic diagram of the PPM array from the side showing the direction of propagation of the generated waves and the forces produced by the array.

However, in order to utilise the whole of the racetrack coil, the probe is actually made up of six rows of two neighbouring magnets with alternating polarity. This alternating polarity in a row results in a Lorentz force being generated in the same direction by the elements, as the direction of the current reverses as the coil spirals around, this is illustrated in Figure 2.15.

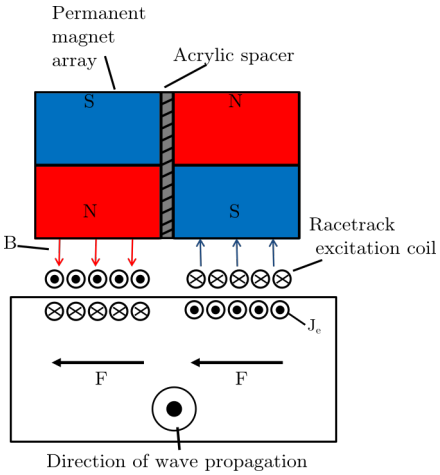

Figure 2.15: Schematic diagram of the generation of the Lorentz force in a sample by using the periodic permanent magnet array structure, with each row of magnets generating a Lorentz force in the material in the same direction due to the reversal of magnet polarity and excitation current direction. The magnetic force (B) induced eddy currents in the sample J_e and resulting Lorentz force (F) are illustrated in the diagram.

This nominal wavelength is set by the spacing between two magnets of the same polarity in the array, which is achieved by the application of alumina ceramic spacers. These spacers are also designed to improve the lift-off performance of the probe by reducing the magnetic field 'shorting' across to the neighbouring magnet and maintaining the magnetic field vectors perpendicular to the surface even with a degree of lift-off.

The wire used in the racetrack coil depends on whether the EMAT is designed as a transmitter or a receiver. For the EMATs used in transmission the diameter of the wire including the insulation layer was 0.28 mm. This is so that the wire is large enough to reduce the risk of overheating and thermal expansion caused by Ohmic heating from the high levels of current used in generation. The receiving EMAT can have a smaller diameter coil of 0.2 mm as the current levels are lower, allowing a greater number of turns of coil to be used, leading to better sensitivity.

The design of the probes used in this Thesis are provided in Table 2.1. The 10 mm wavelength probe was predominantly used in the preliminary tests in Chapter 3, whereas the 8.8 mm wavelength probe is applied in Chapter 5 and 6 as it is the probe that is predominantly used by Sonomatic.

The profile of surface forces that this creates can be examined and used to provide an approximation of the forces the EMAT exerts on the surface of the sample, which can be used as an input for finite element modelling of the transducer.

Probe	λ	Dims. (mm)	Tx wire (mm)	Rx wire (mm)	Coils	Magnets
1	10	31 x 29	0.28	0.2	140 Tx 200 Rx	Six magnets 4 mm wide 1 mm spacing 5 mm pitch.
2	8.8	40 x 35	0.28	0.2	110 Tx 155 Rx	Eight magnets 4mm wide 0.4 mm spacing 4.4 mm pitch.

Table 2.1: The design parameters for the two main wavelength of probes used to obtain data in this Thesis. With the wavelength (λ), dimensions of the active area, diameter of the transmitter (Tx) and receiver (Rx) coils including insulation, the approximate number of coils of the wire in each probe and the details of the magnets used in one side of the array.

The profile of the forces applied on the surface is important, as it sets the spatial bandwidth of the transducer. This concept arises because the nominal wavelength of the probe actually translates as a range of wavelengths at which the probe can operate such that the force profile is sine wave like on the surface of the sample. Knowledge of this profile for a probe is useful when modelling the transducer, as it allows for the generation of a model with a comparable range of possible wavelengths to approximate to the experimental transducer.

2.13.9 Bandwidth of Probes

The operation of this EMAT probe is controlled by setting the wavelength of the probe via the array of permanent magnets in the EMAT [17, 104] and by the temporal profile of the current that is pulsed in the coil. For this reason EMATs are often referred to by their wavelength as opposed to piezoelectric probes which are referred to by their peak frequency, although this is still set by the wavelength of the probe the form of the thickness of the piezoelectric material as seen in the Figure 2.11 previously [64]. An EMAT probe is constructed in order to excite guided wave modes at specific positions on the dispersion curves. Typical considerations for an inspection are the number of modes that are desired to be generated and the extent of dispersion, or lack thereof, that is desired to be present in the interrogating signals. When producing a PPM array probe, the desired nominal wavelength is achieved by appropriate choice of magnet width and by using acrylic spacing blocks in-between the magnets in the array to set the field profile and spacing between them if necessary [17]. If the wavelength of the probe is known, a line of constant wavelength can be superposed on the dispersion curves that gives an indication of the

optimum frequency for the generation of each mode, where the nominal wavelength line intersects with the mode of interest. The intersection points here also indicate the phase velocity for the mode at a certain frequency and wavelength. This can be seen in Figure 2.16, where the dotted line across the phase velocity dispersion curves indicates at what frequency these modes could be excited.

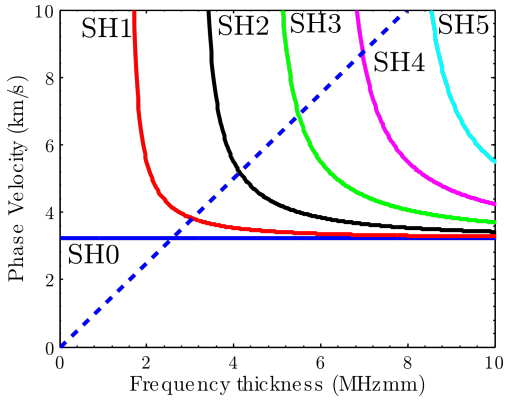

Figure 2.16: Example SH wave dispersion curves for a steel plate, showing a line of constant wavelength (blue dashed) which allows for excitation of the different modes where the line intersects with a mode.

Using the nominal wavelength of the probe to guide inspections is a useful tool, but in reality the generation of waves will depend on both the frequency bandwidth of the input signal and the spatial bandwidth set by the probe [122]. The spatial bandwidth occurs because of the finite size of the probe, and manifests as a range of possible wavelengths that can be used across the dispersion curves in contrast to the nominal wavelength excitation line. This is illustrated in Figure 2.17 where the nominal wavelength line is shown along with the highest and lowest wavelengths in the possible range.

It should be noted that this is for one probe, whereas if the receiving probe is taken into account, the wavelength range is reduced. The extent of the wavelength range can be reduced by adding more permanent magnets in the array, with the result of a more sharply defined wavelength at the expense of a the footprint of the transducer. The wavelength bandwidth is set by the alternating array of magnets, with the force generated by the array sine like on the surface. A fast Fourier transform can be taken of this profile to obtain a peak in the wavelength domain and a range of bandwidth that will also be possible. The frequency bandwidth of the excitation signal can be controlled by altering the number of cycles in the excitation signal to suit the inspection tasks. A greater number of cycles results in a smaller frequency bandwidth at the expense of a longer duration time signal, again an FFT

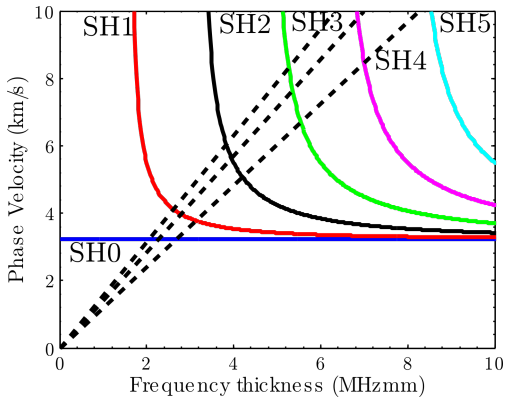

Figure 2.17: Phase velocity dispersion curve for a steel plate as before, with the wavelengths of the probe displayed by the black dashed lines. The middle of these lines is the nominal wavelength line, with the other two lines showing the upper and lower limits of the wavelength for the probe.

can illustrate the frequency bandwidth and peak frequency in the signal.

The spatial bandwidth and the frequency bandwidth results here and in the rest of this thesis are calculated using the Fast Fourier Transform function included in Matlab. This function returns the discrete fourier transform (DFT) [123] of the vector computed with a fast fourier transform (FFT) algorithm. In each application here, the vector is also padded with trailing zeros to a given length, which improves the appearance of the frequency representations, but doesn't improve the resolution of the results.

The transform used in the Matlab function is as follows:

$$X(k) = \sum_{j=1}^{N} x(j)\omega_N^{(j-1)(k-1)} \tag{2.100}$$

where $\omega_N = e^{(-1\pi i)/N}$ and N is the length of the vector.

It uses the Cooley Tukey algorithm like most FFT operations. This works by dividing the input signal into different components and performing the DFT on the separate inputs. By dividing the problem up in this way and taking advantage of symmetry and trivial operations that occur, the complexity of the operation can be changed from the order of N^2 operations to the order of Nlog(N) operations, making it much faster than calculating the DFT directly from the entire data set [124].

The frequency bandwidth and spatial bandwidth can be calculated by taking the Fourier transform of the time signal and the calculated forces on the sample surface from the probe. An example of the spatial profile of forces on the surface of

the sample is shown in Figure 2.18a with the Fourier transform of the approximate surface forces shown in Figure 2.18b. The inverse of the graph gives the wavelength of the probe and its bandwidth.

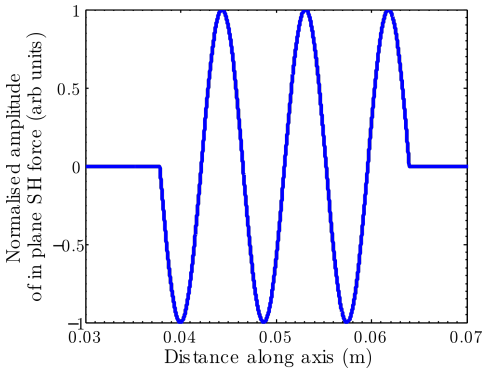

(a) Approximation of the in plane SH force generated by the 8.8mm nominal wavelength PPM EMAT.

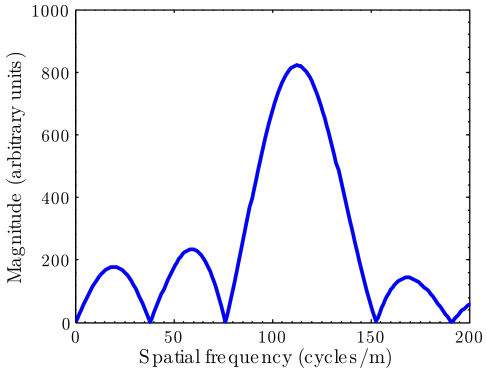

(b) FFT of the in plane SH force generated by the same EMAT.

Figure 2.18: Illustration of the in plane SH forces generated by the PPM EMAT and the corresponding spatial frequency. The use of a similar profile transmitter and receiver will narrow this bandwidth as will the addition of more magnets in the array.

The surface forces can be assumed to be sine-wave like, but the application of a probe will be dependent not only on the properties of the probe, but also on the sample properties. The surface forces are dependent on the sample used, with the profile on steel different to the profile on aluminium for example, due to their different physical properties and the ferromagnetic nature of steel. In order to determine the relevant profile for any situation in which a probe is applied, modelling of the situation is required. The modelling in this case would need to be of the static electric and magnetic fields generated by a transducer using a finite element program that can accommodate this. One such program is COMSOL Multiphysics [125] which is a finite element program specialising in the simulation of the underlying physics of problems such as interaction of electric and magnetic fields, heat flow and stress in components. Modelling of this form can confirm the realistic force profile on the surface and is necessary in order to input the correct force profile into the modelling of the ultrasound, which in this work is carried out in PZFlex [126]. PZFlex is another finite element program which is used for optimising the design of piezoelectric probes and to assess the propagation and interaction of ultrasound within a material, a more in depth description of the program will be provided in Chapter 4.

So the design of a probe and its interaction with the sample are necessary details required to identify the surface forces in a certain application of a probe. This information can be used with the frequency bandwidth with which the probe is excited to fully characterise the frequencies at which the probe can be operated. The temporal bandwidth and the spatial bandwidth can both be superimposed on the dispersion curves as in Figure 2.19, with the operation area of the probe given by the convolution of these two bandwidths.

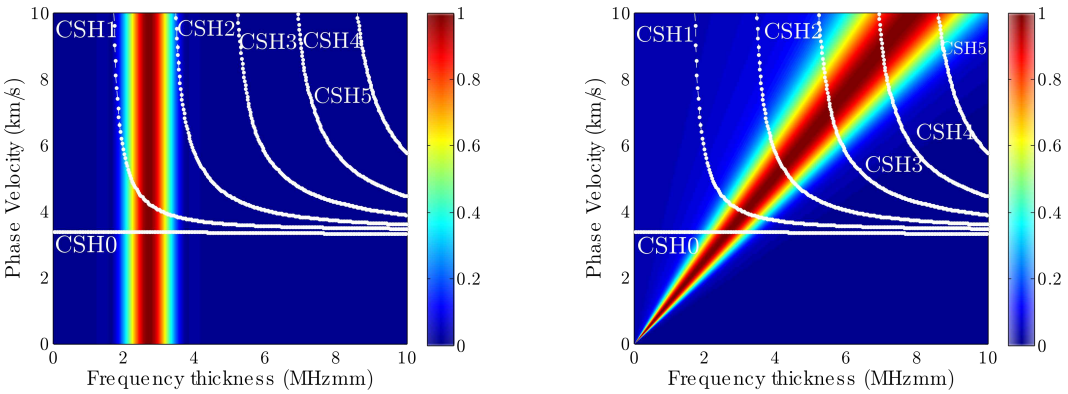

(a) Frequency bandwidth of excitation signal (5 cycle toneburst at 386 kHz).

(b) Spatial bandwidth of probe (8.8 mm PPM array).

Figure 2.19: Frequency and wavelength bandwidths of an 8.8 mm nominal wavelength probe excited with a 5 cycle tone burst at a frequency of 386 kHz onto a 7 mm thick 170 mm outer diameter pipe sample.

The convolution of the two different bandwidths gives the operator a full view of which modes may be generated in an inspection and the relative amplitude of both. Presented here are the areas of operation for the same probe and excitation signal on a plate (Figure 2.20a) and circumferentially around a pipe structure (Figure 2.20b). The dispersion curves show the different velocities at which the modes would be generated for the same frequency signal and also a shift in peak frequency between the two, although the relatively large frequency bandwidth means this is not generally a large effect.

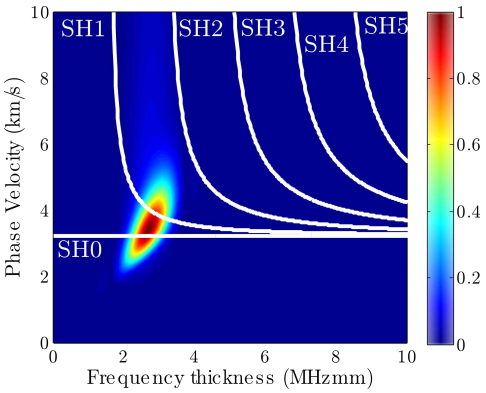

(a) Operation area of the 8.8 mm wavelength probe on a plate sample.

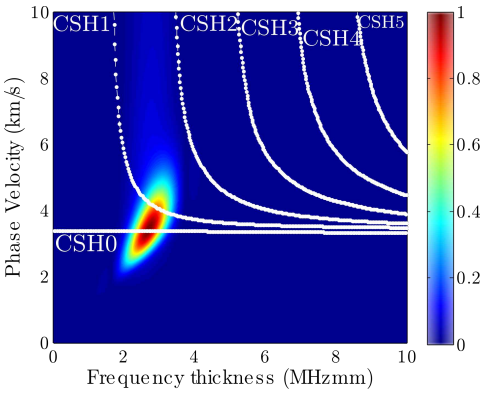

(b) Operation area of the 8.8 mm probe on a pipe sample of the same wall thickness.

Figure 2.20: Operation areas for an 8.8 mm EMAT probe with a 5 cycle excitation tone burst of centre frequency 386 kHz on a 7 mm thick plate and a 7 mm thick, 170 mm diameter pipe.

This assessment of operation areas can be carried out for each inspection if necessary, with the spatial bandwidth of the probe assessed and the excitation signal with the number of cycles used to identify what modes might be excited by a probe. It can also help to select signals that minimise the number of modes excited by a given signal.

To complete the assessment of the operation areas of the probes, the amplitude of the generated mode at each frequency can be plotted for both the plate and the pipe case, by taking the amplitude of the generation signal at the points where it intersects with the mode line in the dispersion curve. This illustrates the small differences in the peak frequencies of each mode for the plate and pipe cases. The amplitude profiles along the first two modes for the plate case is shown in Figure 2.21 with the pipe equivalent for the first two modes shown in Figure 2.22, with the frequencies shown as a product of the peak frequency and the thickness of the sample.

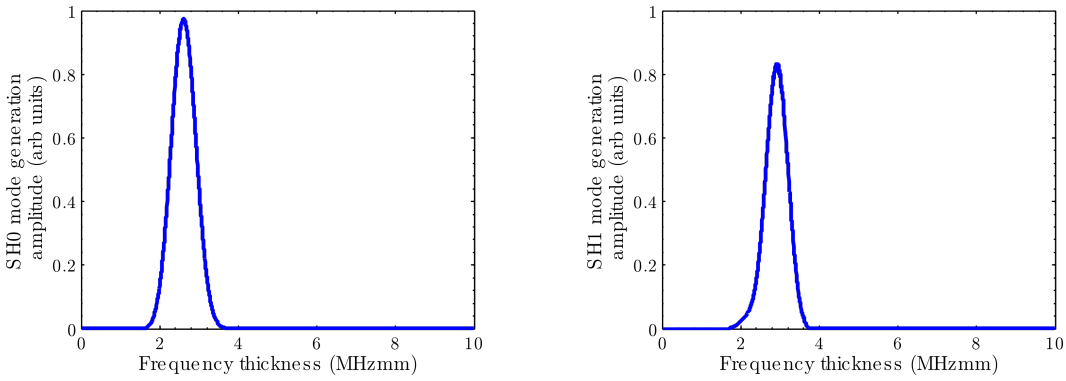

(a) (b)

Figure 2.21: Amplitude of the excitation signal where it intersects with a mode line, to illustrate the frequency thickness product where the optimum operation of the aforementioned probes on a plate sample is achieved, showing a) the SH0 mode and b) the SH1 mode.

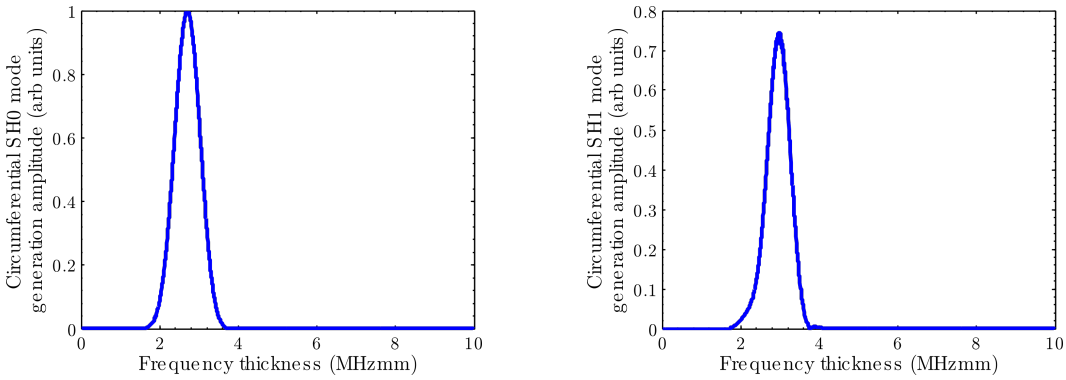

(a) (b)

Figure 2.22: Amplitude of the excitation signal where it intersects with a mode line to illustrate the frequency thickness product where the optimum operation of the aforementioned probes on a pipe sample is achieved, showing a) the CSH0 mode and b) the CSH1 mode. The optimum frequencies of operation are higher in the pipe case as for the application of the same probes.

2.13.10 Alternative Methods for the generation of ultrasound

Other methods than those described in detail here exist to generate and receive ultrasound in a sample, with laser ultrasonics and air-coupled ultrasound being two common ones included here for completeness. Laser ultrasonics [127, 128, 129, 130] is a promising area but is limited in its current applications by the cost, safety precautions and size of equipment required. It has the benefit that it can generate ultrasound in a sample remotely [128] using a focused pulsed laser beam to pro-

vide generation from a small spot size. The application of these lasers generates a broadband signal that can be used to generate surface or guided waves, but requires a second laser or other transducer to detect the generated ultrasound [131] or an EMAT can be used to generate and the laser used to detect [132], which can make it too complex and expensive a system for on site application. It has however, been successfully used to probe material microstructure using Surface Acoustic Waves (SAW), so has some good applications in material characterisation and flaw location [133, 134, 135, 136].

Air coupled ultrasonics involves using specially designed probes for operating into air which has a very low acoustic impedance. These have been applied in pipe but again need very specific properties of probe orientation to operate [137, 138, 139].

Chapter 3

Experimental system

This chapter considers the information that is necessary in order to plan the inspection of a pipe sample using the suggested SH wave screening technique. In particular, the properties of the sample that need to be found before the theoretical procedures mentioned in the previous chapter can be used to guide the operation of the probes. It continues to identify some of the differences that were highlighted in Chapter two between plate and pipe structures. In order to illustrate this, a system that allows for frequency sweeps to be carried out is used to characterise the optimum frequency of generation for different modes for a certain wavelength probe on a sample.

The preliminary testing shown here using a more versatile lab based system is used to validate a more limited industrial system, which while not as versatile, will be more portable and more suited to on site inspections in challenging environments. The capabilities of this industrial system provided to Sonomatic by Innerspec Technologies Inc. are then evaluated considering the advantages and disadvantages for the intended inspections.

The experimental system used here for the excitation and reception of waves has been developed with the intention of providing a robust method for pipe wall thickness screening that can be carried out rapidly, have the potential to be automated and allow easy identification of defects with a minimum of false calls and a high probability of detection of defects. This uses an inspection frame built in house at Sonomatic and the Innerspec Technologies Inc [140] pulser receiver.

The strengths and weaknesses of the system as a whole are considered in order to provide a background to the results presented in Chapters 5 and 6.

3.1 Basic sample measurements

When planning a guided wave measurement, several properties of the sample need to be known in order to guide the operation of the probes. These properties are namely the thickness of the sample, the outer diameter and the shear wave speed in the material.

In general these can be measured on the sample or a separate piece of piping that is the same specification as the sample to be tested. The outer diameter of the pipeline is usually easy to measure and the shear wave speed in the material will be addressed later, but the thickness of the sample is perhaps the most difficult of these to find. If the sample is well matched to its specification then the original specification of thickness can be used. Alternatively if an open section of the sample is available, the thickness of the sample can be measured by using vernier callipers, which would give a more precise measurement of wall thickness, this measurement is used where access is possible in this work. Even then, typically the thickness of the sample could vary by up to 10 percent from point to point and any measurement with callipers would also include the thickness of any coating on the pipeline.

If the coating is non conductive as is usually the case then the EMAT will generate guided waves in the sample at the surface of the pipeline, without being affected by the coating, so it would need to be discounted in any thickness measurement. Another method that is available to determine the thickness of the sample is to carry out a through wall thickness measurement at a point using ultrasonic thickness gauging as seen in Figure 2.2. Using a thickness gauge, the reflections from the coating layer will be distinct from the reflections within the sample such that the thickness could be determined from the time of flight measurements between successive back wall echoes, removing the effect of the coating on the signal.

These sample measurements are important in guided wave measurements, as the dispersion curves that have been illustrated in Chapter 2 that allow the operator to approximate the speed of a specific mode at an operation point, are dependent on all these factors. Choosing a probe appropriate for the nominal wall thickness of the sample is also important, as a different wavelength probe will change the frequencies at which the modes can be generated.

3.2 Optimising generation frequency

The Innerspec Technologies Inc system that will be described in detail later, only allows a maximum number of 5 cycles to be used in the excitation tone bursts used

to excite the ultrasound in a sample. In order to confirm that the operation of the industrial system fulfils the requirements for the guided wave inspections desired, initial tests were carried out to view the optimal frequency and bandwidth range for both the plate and pipe case. These tests are to confirm the assumption that a small number of cycles in the tone burst, and hence a relatively large frequency bandwidth is manageable in terms of the frequency bandwidth and time duration of the signal so that the desired modes are generated without obscuring signals in the time domain.

A preliminary experiment was carried out to illustrate the frequency bandwidth and optimum generation frequencies for the pipe and plate cases. In order to achieve this, a Ritec RPR 4000 pulser receiver system [141] was used with two EMATs of the PPM array design shown in Chapter 2, with a nominal 10 mm wavelength (probe number one in Table 2.1) operated in a pitch catch arrangement on the surface of a pipeline of 170 mm outer diameter and a wall thickness of 7 mm.

Initially the probes were arranged on top of the pipe, with probes orientated so that the wave was propagating in the axial direction along the pipe with a 200 mm spacing between the front of the EMAT cases as shown in Figure 3.1. (On this scale, at this point on the pipe, the dispersion relations for the SH waves should largely follow the plate behaviour, with the dispersion curves for the axially travelling guided waves being much more appropriate to approximate as having behaviour comparable to the waves in a plate.) A frequency sweep was carried out to determine the optimal frequency of operation for the 10 mm wavelength probes on the sample.The optimal frequency for a specific mode can be approximated by selecting the frequency that gives the largest peak-to-peak amplitude for the mode of interest.

The industrial system used in this thesis (described in detail later) can generate tone burst excitation signals with up to 5 cycle duration, in any application, the number of cycles that are used in the excitation signal defines the frequency bandwidth of that signal and the time duration of the received signals. In this particular application, the optimum signal is would be of a narrow enough frequency bandwidth that a small operation area is available on the dispersion curves (to minimise dispersion in the received signal) but also of a small time duration such that different modes in the signal can be differentiated from each other if their arrival time at the receiver is similar. In the application of the industrial system, a 3 cycle tone burst is used as an excitation signal such that both the CSH0 and CSH1 modes are generated with high amplitudes so that only a single scan is necessary (generally due to time constraints on the inspection). A total of 4 cycles is used in these preliminary measurements, this reduction in the frequency bandwidth from the 3 cycle

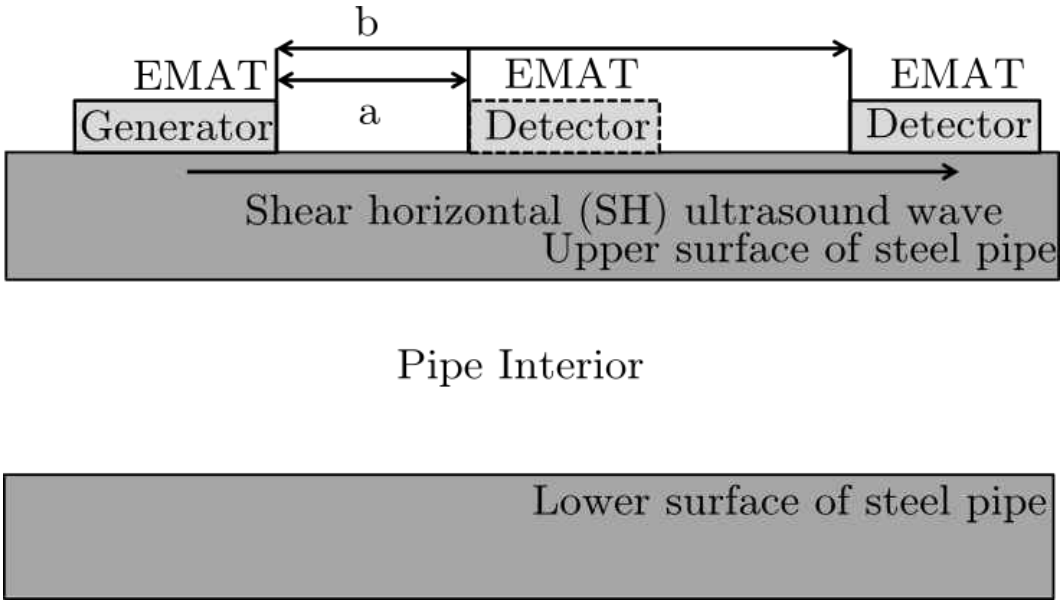

Figure 3.1: Experimental technique for carrying out frequency sweep measurements and shear wave speed measurements. Measuring axially allows the SH0 speed to be assumed to be equivalent to the plate case. Generator and detector are at a constant separation as the peak frequency is changed, this is 200 mm. For SH0 speed determination a=100 mm and b=200 mm.(Not to scale)

signal should allow more energy to be concentrated in the mode of interest at each frequency. The peak frequency of the generated tone bursts was swept from 0.25 MHz to 0.94 MHz with 0.01 MHz increments, with signals collected at each different increment in frequency. The data was collected via a computer, with 64 records taken at each generation frequency, with an average (mean) taken. The Ritec system applied a hardware bandpass filter to the data with a passband between 0.2 MHz and 2.5 MHz.

This allows the optimal frequency for the generation of each mode to be calculated, but due to the frequency bandwidth of the signal, several modes are likely to be excited at once (even with the reduced frequency bandwidth). The results of such a frequency sweep can be represented in the time (Figure 3.2a) or frequency (Figure 3.2b) domains and normalised to give the amplitudes of each signal relative to the other.

The presentation of the time of arrival of the waveforms with respect to the generation frequency shows how the maximum amplitudes in the signals change as the frequency is swept through the stated range. The different sections of signal that are seen arrive at different times due to the different speeds at which the modes travel for a given frequency. This representation shows the range of values that the

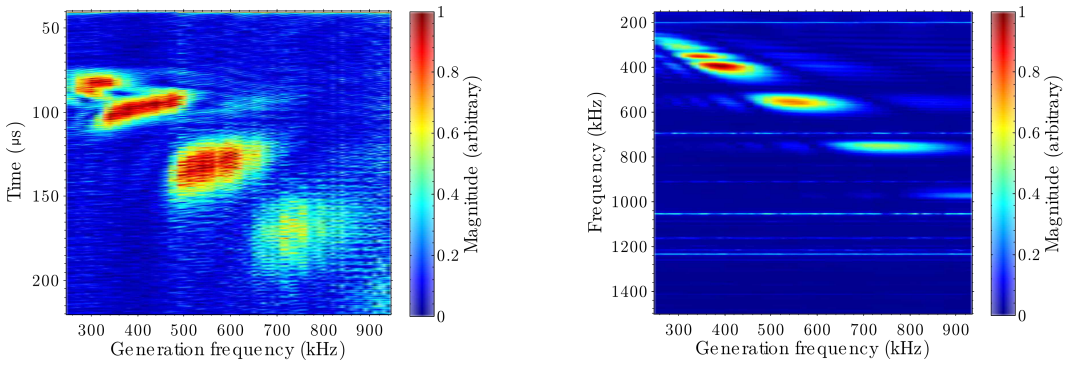

(a) (b)

Figure 3.2: A frequency sweep from 0.25 MHz to 0.94 MHz in 0.01 MHz increments of a 4 cycle tone burst on the surface of a pipe sample in the axial direction in a) the time domain and b) the frequency domain. The 10 mm wavelength EMATs were used, with a 200 mm separation between the EMAT cases, with the waves travelling in a purely axial direction, allowing the behaviour to be treated as plate like.

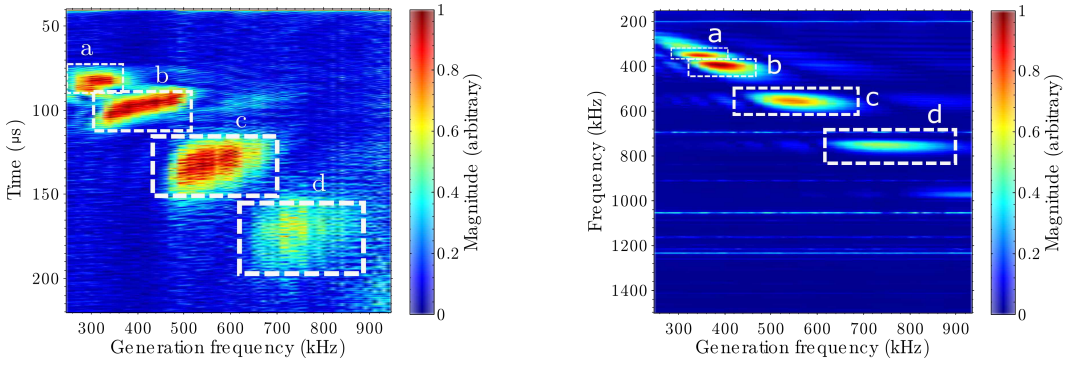

(a) (b)

Figure 3.3: The same frequency sweep as in Figure 3.2 in the axial direction in a) the time domain and b) the frequency domain, with boxes to show the approximate span of the signals in the time and frequency domain with areas labelled a,b,c and d relating to the SH0, SH1, SH2 and SH3 modes which peak at 330 kHz, 400 kHz, 560 kHz and 740 kHz respectively.

waveforms can take at different frequencies as a result of the relevant bandwidth of the signal, with different modes shown. The modes are shown in Figure 3.3a, with a,b,c,d, labels referring to the SH0, SH1, SH2 and SH3 modes respectively. To relate the generation frequency to the received frequency for the equivalent measurements, another figure can be mapped to show how the frequencies change with respect to the generation frequency. This is shown in Figure 3.3b labelled in the same way as Figure 3.3a. The concept of this graph is that if the axial and circumferential generation of modes with this technique were the same in terms of the relative amplitudes of

modes generated and detected and frequencies excited, then Figure 3.3b would look the same as the corresponding figure for the pipe sample, circumferentially (Figure 3.7b) as it shows the frequencies detected for given generation frequencies. The fact that Figure 3.7 looks different indicates that the generation of guided wave modes with this method is affected by the sample curvature. The time records and the FFTs of the data at the peak frequencies are shown in Figure 3.4a and Figure 3.4b.

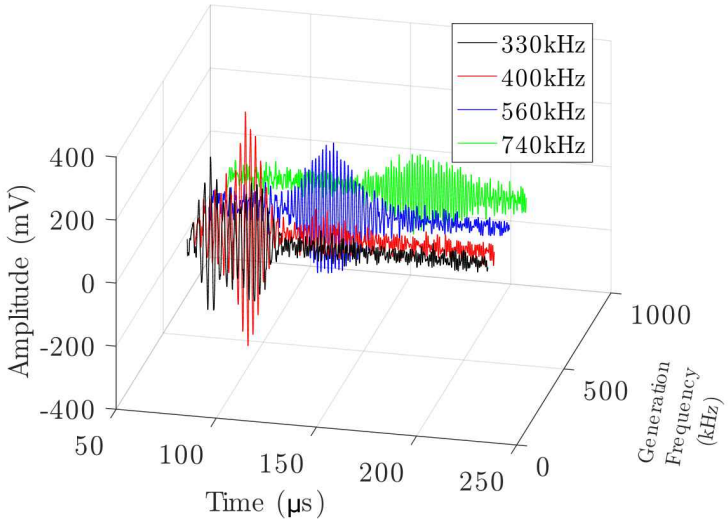

(a)

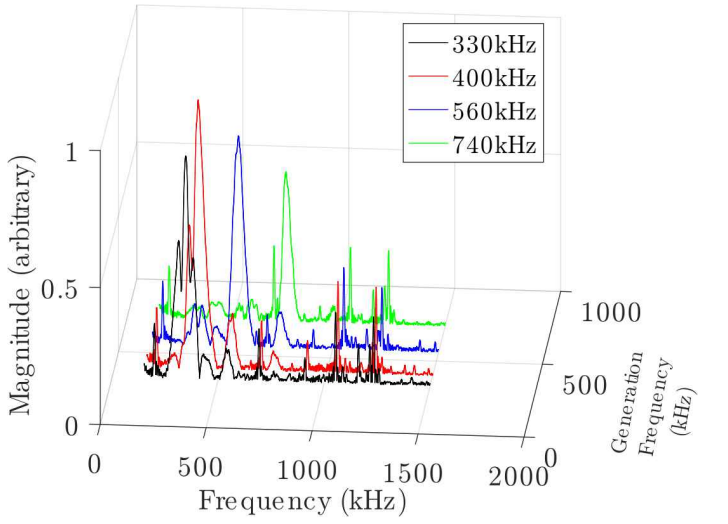

(b)

Figure 3.4: The data for the optimum frequency of operation for the different guided wave modes in a plate situation in a) the time and b) the frequency domain for the first four Shear Horizontal guided wave modes.

The peak frequencies here from the scan are identified as 330 kHz, 400 kHz, 560 kHz and 740 kHz for the SH0, SH1, SH2 and SH3 modes respectively. It should be noted that the optimum frequencies for generating the SH0 or SH1 modes also generate a portion of other modes, whereas the SH2 and SH3 excitation frequencies avoid exciting large proportions of the other modes due to the larger difference in excitation frequency between the two modes. However, due to the frequency range of operation of the SH2 and SH3 modes being situated on a more dispersive area of the dispersion curves, the received waveform will be subject to a larger variation in propagation velocity and hence a greater range in arrival time.

The same procedure can be carried out for waves travelling in the circumferential direction by rotating the transducers so that they are generating the waves in the circumferential direction of the pipe. The probes in this case were arranged to be touching each other as shown in Figure 3.5 so that the short path between the probes is minimised to reduce measurement error of the distance between the probes and the signals are received after travelling almost a full circumference of the pipeline.

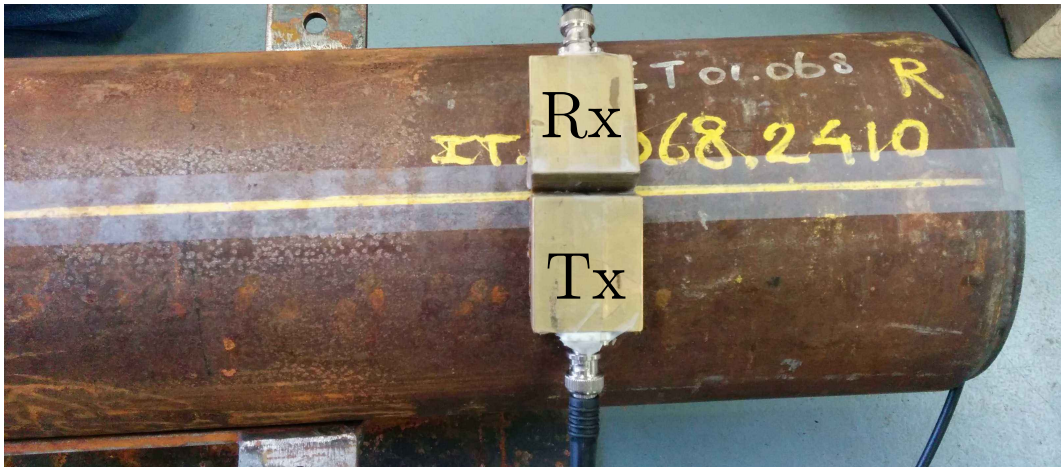

Figure 3.5: Orientation of probes for the frequency sweep carried out in the circumferential direction of the pipeline.

This will result in the short path in the clockwise direction (from the transmitter to the receiver) and the long path in the anticlockwise direction being very close to each other in terms of distance travelled and time taken to travel that distance. The original short path will be in the dead time of the transducer and the first long path will be the circumference of the sample minus the length of the transducer(to the mid point of the probe) and the second short path signal will be the length of the transducer plus a circumference. This will result in some overlap

of modes travelling in the opposite directions, leading to identification of different modes being more difficult. This emphasises the need for positioning of probes such that their separation is enough to differentiate the different circumferentially travelling modes, in order to be able to use this approach as a diagnostic tool.

An important point to note here is that the SH3 mode that was obvious in the plate orientation is not seen in this arrangement on the pipe, and the SH2 mode has a much weaker amplitude compared to the other modes than that in the axial case. This is thought to be due to the differences in generation and reception between the flat plate and pipe cases, with the increase in lift off of the different sections of the probe due to the curved surface of the pipe believed to reduce the efficiency of generation and reception of the higher order modes. The lift off here can be up to 1 mm greater at the edges of the probe than it is at the centre of the probe. This is minimised in the case of the experimental rig as the probes are held in a more secure way at a distance away from the surface. The change in lift off will affect all the modes but appears to have a greater effect on the higher order modes making them unsuitable in general to use for giving information about the presence of defects in a sample. This effectively limits the application to the two lowest order circumferential modes of the SH0 and SH1 type.

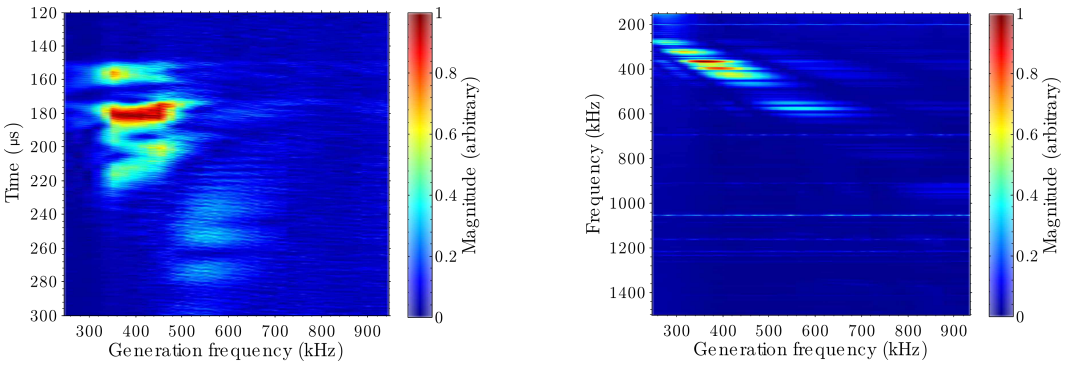

(a) (b)

Figure 3.6: A frequency sweep from 0.25 MHz to 0.94 MHz in 0.01 MHz increments of a 4 cycle tone burst on the surface of a pipe sample in the circumferential direction in a) the time domain and b) the frequency domain. The 10 mm wavelength EMATs were used, with the cases touching and the waves travelling in a purely circumferentially direction. The peaks for the SH0, SH1 and SH2 modes are seen, but due to the waves travelling in both directions around the pipeline, the long path SH1 mode overlaps with the SH0 short path plus a circumference signal. The SH3 mode cannot be seen in the signal and the other modes show different frequency peaks at 350 kHz, 390 kHz, and 570 kHz for the SH0, SH1 and SH2 modes.

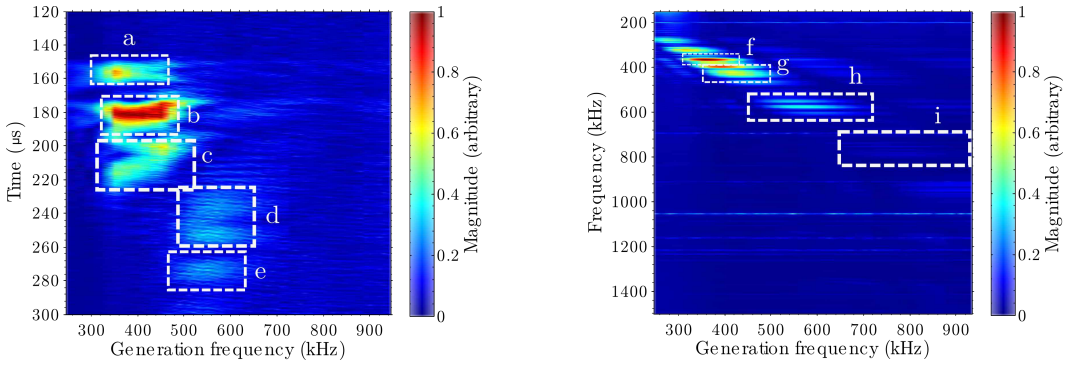

(a) (b)

Figure 3.7: The data for the optimum frequency of operation for the different guided wave modes in a circumferential pipe situation in a) the time and b) the frequency domain for the first three Shear Horizontal guided wave modes that are visible, with a box added for the fourth mode position if it could be detected.

The frequency sweeps shown in Figure 3.6a and 3.6b are the figures obtained in the time and frequency domains respectively for the circumferentially travelling guided waves. It is important to note here that the signal is more complicated than in the plate like case due to the propagation of the waves in both the clockwise and anticlockwise directions of the pipe. It is also different to that of the plate like case as the distance travelled between the transducers around the circumference of the pipe is almost a full circumference of 540 mm, whereas in the plate like case this was limited to 200 mm such that a different scale is necessary in order to show the same modes. As before, a labelled version of the frequency sweep data is provided to make it clear where the different SH modes arrive in the time and frequency domain. The modes are highlighted with boxes in Figure 3.7, with some modes overlapping due to the coincidence of waves travelling in opposite directions around the pipe circumference.

For ease of reference, the different modes that can be seen in Figure 3.7a are described here. The area of signal shown in box a of Figure 3.7a represents the CSH0 mode travelling the long path distance between the transducers in an anticlockwise direction around the pipe circumference. It differs to the SH0 mode detected in the plate-like case in that its peak excitation frequency is higher and its group velocity is greater than the plate like case.

The signal seen in box b of Figure 3.7a is more complex to interpret as it is a combination of the anticlockwise travelling CSH1 mode and the clockwise travelling CSH0 mode which has travelled a full circumference of the sample and the short path. The difference in group velocities of these modes results in the two modes

arriving at the receiver with very similar arrival times despite the different distances they have travelled.

A clearer representation of the CSH1 mode where it arrives without overlapping with the other generated modes is seen in Figure 3.7a in box c. This is the CSH1 mode that has travelled the short path distance and a full circumference of the sample. The remaining signals that can be seen in Figure 3.7a are the anti-clockwise and clockwise travelling CSH2 modes seen in boxes d and e respectively. These show a marked decrease in relative amplitude to that of the CSH0 and CSH1 modes which is believed to be due to the inefficient generation and detection of the higher order modes due to the different profile that the probes generate on the pipe's surface because of the variation of lift off of the probe along the axis of the probe where the magnetic array varies.

The propagation of the respective modes in both the clockwise and anti-clockwise directions around the pipe circumference results in the representation of the maxima of the received frequency for each generation frequency being less clear than in the plate-like case, but they can still be highlighted in Figure 3.7b, with the CSH0 mode shown at f, the CSH1 mode at g and the CSH2 mode at h. The CSH3 mode is not seen in the signals, with a box placed on Figure 3.7b at i to show where it would lie if it could be seen.

The time and frequency domain signals for the peak frequencies of the circumferentially travelling ultrasound are shown in Figure 3.8a and 3.8b. The difference in the selected peak frequencies here from the plate case illustrates that the peak frequencies that can be generated change with the different geometry and the arrival time will be different due to the different velocities of the modes when travelling in a circumferential direction on the pipeline.

The frequency sweeps here showed that there is a change in frequency of operation between the plate and pipe samples and that there is a range of frequencies at which the probes can be operated at, illustrating the need to find the optimum frequency at which to operate the probe. It has also shown that the use of a limited cycle tone burst (as will be necessary with the industrial system) is valid if the inspection is planned beforehand in terms of the excitation frequencies that are used. When considering the difference between these two orientations of the probe, there are other factors that also must be taken into account. Namely these are the lift off of the probe from the sample surface and the spatial bandwidth of the probe on the sample. The spatial profile of the probe on the surface will be different for the two probe orientations due to the curvature of the sample in the pipe case. Whereas the plate like use of the probes has the variation in the magnetic array of the EMAT

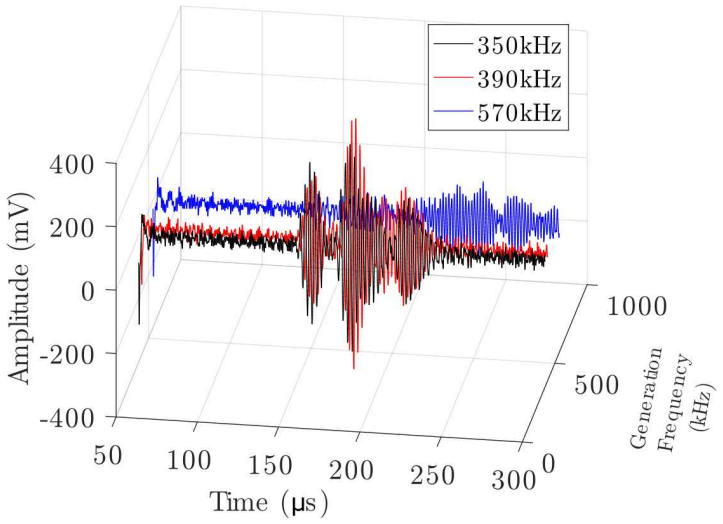

(a)

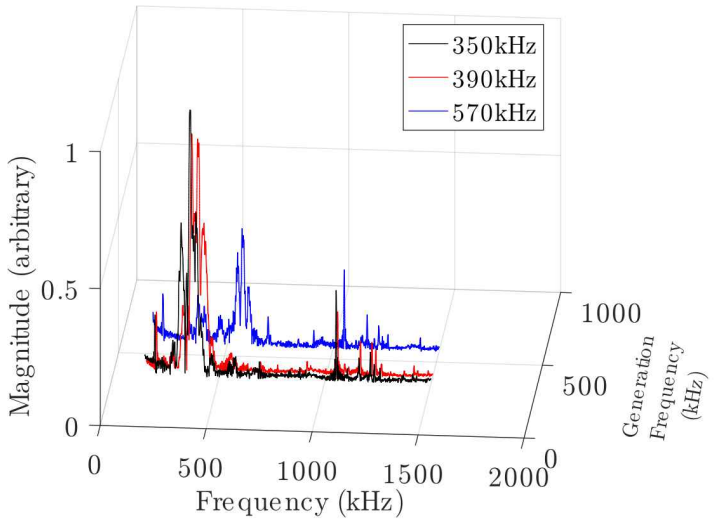

(b)

Figure 3.8: The data for the optimum frequency of operation for the different guided wave modes in a plate situation in a) the time and b) the frequency domain for the first three Shear Horizontal guided wave modes in a pipe.

along the axial direction of the pipe, which will result in the sinusoidal behaviour of the profile as mentioned previously, the circumferentially travelling wave has the variation in the PPM array in the circumferential direction. This leads to different amplitude responses to the applied fields in the sample at the edges of the probes because if the probe is attached to the sample at its centre point, the amplitude

of the fields in the sample will be less further away from the centre due to the increase in lift off. This means that both the nominal wavelength of the probe and the bandwidth of the signal will be different in the two cases and will likely behave differently with increased lift off, which could account for some of the change in signal in the experiments.

A basic COMSOL model was constructed to show the spatial profile that the probes generate on the surface for both the axial case and the circumferential case. These were set at a lift off of 1 mm from the centre of the array to the sample and the in plane spatial force profile approximated, with FFTs taken of the subsequent profiles to ascertain the nominal wavelength and bandwidth of the signals. The results are shown in Figure 3.9a for the spatial profiles and in Figure 3.9b for the bandwidths of the signals. It can be seen that at this size of probe and sample, the circumferentially travelling waves show a small change of nominal wavelength and an increase in bandwidth of the transducer compared to the transducer in the axial direction. The change however is small and will be largely neglected here, with the profile for the flat plate case used to generate simulations as the bandwidth of the simulation is likely to already be greater than in experiment, with further details on this in chapter 4.

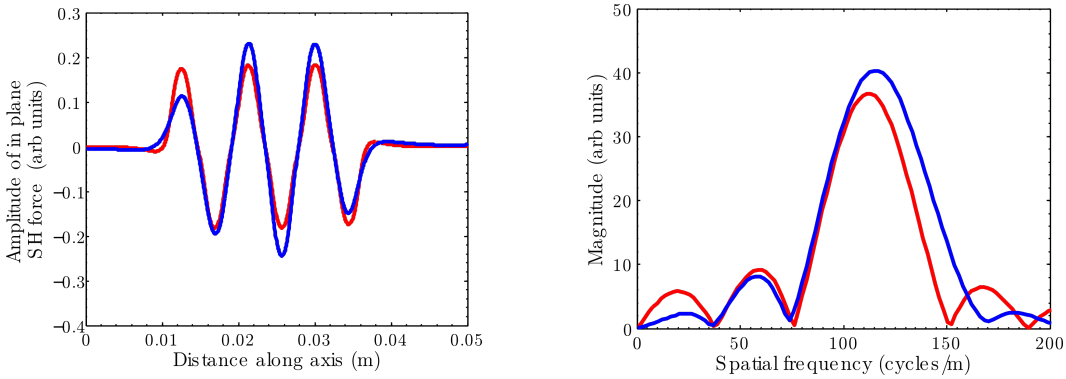

(a) (b)

Figure 3.9: Illustration of the in plane SH forces generated by the same EMAT probe a) as a force profile both axially(red) and circumferentially (blue) at 1 mm lift off showing the profile change. b) The in plane spatial frequency for the axially (red) and circumferentially (blue) orientated probes, showing a small change in nominal wavelength and spatial bandwidth of the probe.

3.3 Confirming Shear wave speed in sample

Another factor that was listed that can affect the accuracy of generated dispersion curves for a given sample is the shear wave speed in the material. Typically the steel samples will have a shear wave speed that is close to the standard shear wave speed for mild steel, but significant deviation from this would result in alteration to the dispersion curves generated. Therefore it is recommended that the shear wave speed in the sample is determined before carrying out an inspection, in order to adjust the dispersion curves accordingly. This can be achieved by taking measurements for the time of flight in the axial direction for different transducer separations. Here 100 mm and 200 mm separations have been chosen for recording signals, and the transducers moved to allow the measurement to be repeated 3 times using the peak frequency for the SH0 mode calculated from the frequency sweep. An average of the recorded signals for the two different positions is shown in Figure 3.10.

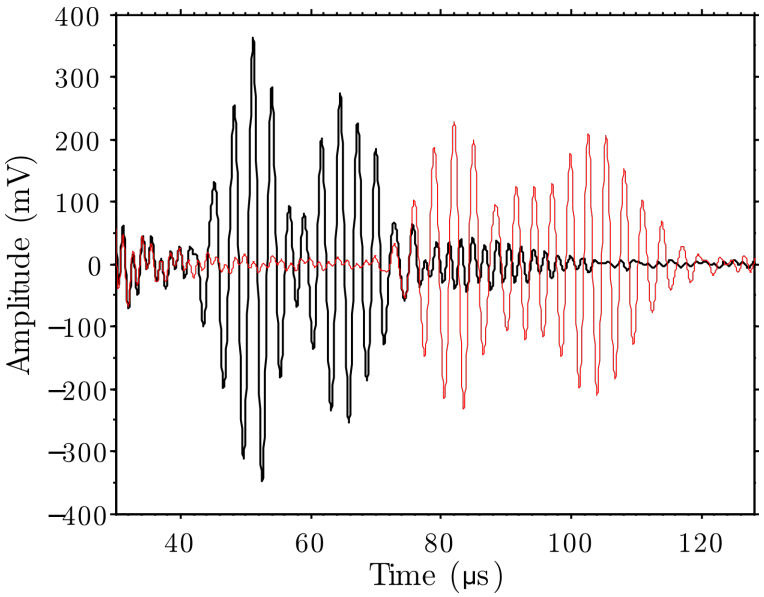

Figure 3.10: Waveforms generated from an excitation frequency of 330 kHz for 100 mm separation between EMAT cases (black) and 200 mm separation between the EMAT cases (red), cross correlation of the SH0 modes gives the shear wave velocity in the sample.

Using the knowledge that at this point of operation, the guided wave should travel with a constant speed equal to that of the shear wave speed in the sample, the shear wave speed can be calculated. The difference between the two positions in distance and the two waveforms in the time domain can be used, as a differential measurement removes errors due to the uncertainty in when the wave can be said

to have arrived at the detector.

The difference in arrival time of the SH0 wave packet for the 100 mm separation and 200 mm separation can be calculated using a cross correlation on the waveform, which allows the speed of the mode in the sample to be measured as (3234 ± 21)m/s which is very close to the standard value of 3235 m/s expected for the SH0 mode [142].

The same procedure can be carried out for the circumferentially travelling modes in order to determine the wave speed of the CSH0 mode when travelling circumferentially around the pipeline, but the phase velocity and group velocity of the CSH0 mode are no longer equal and the wave mode shows dispersion, so taking velocities directly from the data is less straightforward and becomes more of an estimate.

3.4 Planning an inspection

3.4.1 Procedure for setting up an inspection

Using the information from above and the applicable guided wave theory, a procedure for planning an inspection with the minimum of calibration can be written. First the shear wave speed should calculated in the sample if possible by carrying out a differential wave speed measurement of the fundamental shear horizontal mode in the axial direction of the pipe. Secondly, the nominal thickness and outer diameter of the sample should be obtained and the speed and sample dimensions used to generate the dispersion curve for the sample.

The nominal wavelength of the probe or the full representation of the operation area of the probe can then be used to determine the frequency of operation for the various modes that are desired to be generated. The inspections focus on the lowest order symmetric and antisymmetric modes and the bandwidth of the system means these are usually generated simultaneously. The choice is then whether to choose a frequency that suits the generation of both modes or different frequencies that are optimised for each different mode. A single frequency that lies in between the maxima of the modes would allow for a single scan of the sample but compromises on the energy into each mode. A set of measurements that excite the probes at the peak frequency for each given mode means more sweeps are needed by but the energy is more concentrated into the mode of interest.

3.4.2 Probe positioning

Once the parameters of the sample have been determined and the frequencies of operation obtained from the dispersion curves, the application of the probes should be considered. The system that has been used here involves two PPM EMATs of either 8.8 mm or 12 mm nominal wavelength operated in a pitch catch arrangement, mounted on a wheeled trolley, equipped with an encoder wheel. When these probes are applied to the sample, the system is designed to saddle the top of the pipeline so that there is around 200 mm separation between the probes on the surface of the pipeline (depending on the diameter of the pipeline), with half of this distance to either side of the centre line of the pipe. This places the transducers at approximately the ten and two o'clock positions on the pipe surface.

This inevitably takes some calibration each time in order to make the probes lie at the appropriate lift off from the surface, and at the desired separation. It is important to know the circumferential separation of the probes so that if there is a change in the arrival time of signals, the distance travelled by the waveform is known and information about the severity of the defect can be extracted.

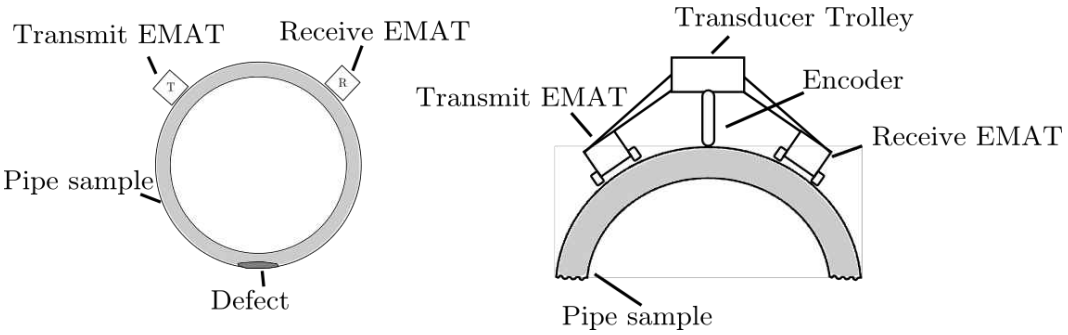

Figure 3.11: Schematic diagram of the positioning of probes on the pipe surface and of the EMAT rig used to carry the probes.

The method of operation of the EMAT probes results in the propagation of guided waves in both directions around the pipeline, both clockwise and anticlockwise. This allows for the separation of the received signals into these two categories, with the first signals detected being the short path signal that goes between the two transducers along the top of the pipeline and the second signal being the long path signal, which travels between the transducers along the bottom of the pipeline. The set separation of the EMATs is designed to provide a different propagation distance for the short path compared to the long path, so that they appear at different times.

The different times of arrival for the different paths allows categorisation of any defect into being between the transducers on the top of the pipe or on the

base of the pipe by seeing which set of signals are different from the clear area. The propagation of the waves in the circumferential direction means that multiple signals will be seen in the time records, corresponding to the multiple loops that the waves travel around the pipeline. These multiple loop signals can be used to determine wave speeds in areas that are defect free without knowing the separation between the probes. If the signal that has travelled the short path distance and the signal that has travelled an entire circumference plus the short path distance are considered, the time taken for the constant distance that is the circumference of the pipeline is found and hence speeds can be calculated without any errors in distance.

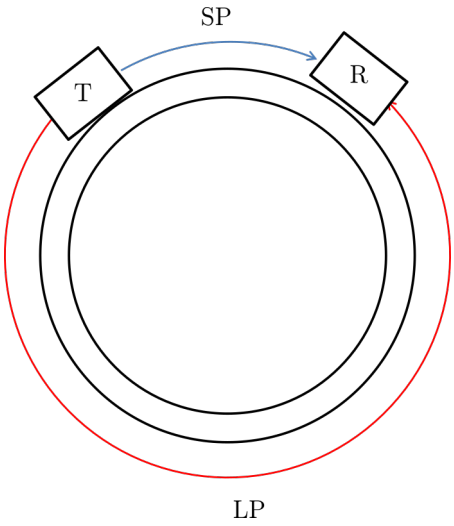

Figure 3.12: Schematic diagram of the positioning of probes on the pipe surface and the short (SP) and long path (LP) along the pipe surface that arises due to the generation of waves in both directions by the transmitting probe (T), detected by the receiving probe (R).

Knowledge of the positioning of the probes with respect to each other and the pipeline centre circumferentially allows any reflections of waves from the defect to be used to provide further information for the inspection. The position of these reflections with respect to the short and long path signals can be used to provide further characterisation of the circumferential positioning of a defect, if the defect allows for coherent reflection of the waves from the defect edge. This can happen if the edge of the defect is abrupt and relatively uniform, but is unlikely to be able to be used if the defect is varied in shape and depth such as would be the likely case with an in-service corrosion patch.

3.5 Characterisation of Pulser Receiver system

With the inspections optimised in terms of the frequency of operation and the placement of the probes, the final factor to be considered in terms of inspection is the pulser receiver system that is used to generate the excitation signal and to record the time signal data. The tone burst excitation signals and data capture were provided by an Innerspec Technologies Inc pulser box (Innerspec "PowerBox"), this has been referenced previously, but the following describes in more detail some of its advantages and disadvantages.

This system has been designed by Innerspec on the basis of portability, user interface and power restrictions, so that it can be used on site using only battery power with the minimum of user input. This means that the industrial system has various limitations as compared to a laboratory based system. The most relevant of these limitations for the user are the limits on the full data sets that can be recorded, and the bandwidth and temporal duration of excitation signals that can be generated.

3.5.1 Pulser receiver considerations

The time signals recorded by the system are limited to a full time record of 600 microseconds. This could lead to issues on large diameter samples due to the time that it takes for the guided wave modes to propagate around the circumference of the pipeline. It could also pose a problem when trying to detect reflections from the defect that arrive later on in the time signal, or any attempts to gain further information from signals that have travelled multiple loops of the pipeline. The acquisition of information from multiple loop signals in the data will be considered later, but tests have been carried out with this system on a sample that has an outer circumference of almost 2 metres, so this time restriction is deemed to not be damagingly limiting for obtaining signals.

The system also has a maximum number of five cycles in the excitation signals that can be generated. This determines the level to which the frequency content of the signals can be controlled. The frequency sweep with the more versatile lab based system has shown that this limitation of the frequency should not prove too disruptive in terms of obtaining signals of relevant frequency content from the system. It is however likely to mean that multiple wave modes are generated simultaneously, which can cause problems if the modes overlap with each other, making it difficult to separate the two modes for travel time measurement.

The final factor that should be taken into account when applying the system

in an in-situ measurement is the limitation in the power settings that can be used to generate the excitation signals. The system only features two power settings of 600 of 1200 Volt excitation signals. This can cause issues, in that the lower power setting can lead to unsatisfactory amplitude of signals due to the poor transduction efficiency of the EMAT probes. The higher power setting on the other hand can lead to a saturation of the receiver such that the amplitude information can be lost from a signal in terms of being able to compare amplitudes between clear areas and areas where a defect is present.

These limitations have been assessed with regard to the quality of data that is recorded in a particular sample. The frequency restrictions can be dealt with by careful consideration of the excitation frequencies used and the time restrictions have been considered and deemed adequate for the majority of samples that will be examined. The saturation of the received signal can be avoided by viewing an initial A-scan of the sample before an encoded scan is carried out. This allows for confirmation that the signal does not saturate and the application of a lower power setting if it does. If there is time when carrying out the inspections, the saturated signal can still be recorded and used to show differences in areas where a defect is present for a screening style measurement, as an immediate indication of the present of a defect.

3.5.2 Experimental rig considerations

The experimental trolley that holds the transducers is designed to move across the surface of the pipe with minimal disruption. It consists of wheeled carriages for the EMAT probes, holding them at a fixed lift off from the sample which can be adjusted but is set here at 0.3 mm lift off and an adjustable arm that holds these carriages in order to set them on the pipe surface at a given separation. A photograph of the trolley with dimensions is shown in Figure 3.13 [143].

This arrangement is effective for securing the probes to the surface at the desired point, but has its own inherent drawbacks. Different surface conditions of the sample can lead to the frame not moving smoothly over the pipe surface and can lead to missed data or poor quality data axially. This can occur if the shaft encoder doesn't move when the rig is moved over a particular section, which leads to rescanning of areas to compensate for the missing data. Obtaining this missing data is achieved by rescanning an area but unless this is done very carefully, keeping the encoder position for each time record correct, errors can occur in the encoder position, which could lead to over or underestimation of a defect's size by an encoded distance step (here 1 mm). Errors could also occur given the risk of circumferential

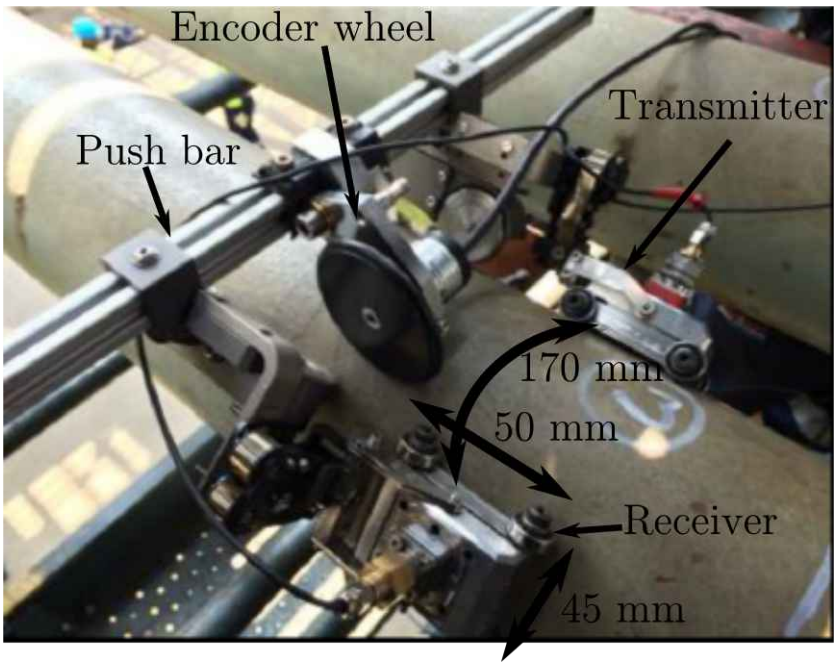

Figure 3.13: Photograph of the experimental rig used for scanning topside pipe samples with EMATs in this Thesis.

slippage of the transducers, changing the positioning of the scanning system with respect to any defect.

These limitations in positioning are solved in the subsea case by allowing location tracking for the rig, such that it remains on the top of the pipe and compensates for any change to positioning that might occur. A photograph showing the subsea unit on a pipe is given in Figure 3.14. At present this is only used in the subsea version due to the necessity of getting the measurements correct on the first sweep of the sensors due to limited inspection times due to weather limitations in a marine environment. However, this approach could be applied in the topside application of the system if necessary. In general the encoded scans are recording a time record every 1 mm, such that any inconsistencies in the encoded data are on a much smaller scale than the size of the defects that are encountered. This should not affect the screening capability of the system, but would affect the fine measurements that may be required such as defect positioning circumferentially or defect extent in the axial direction.

Due to the uncertainties involved in the measurements with regard to the application of the experimental rig and the application of the pulser receiver system, it will be necessary to assess the interaction with defects in a modelling situation as well as taking the experimental data. Finite element modelling of the system will

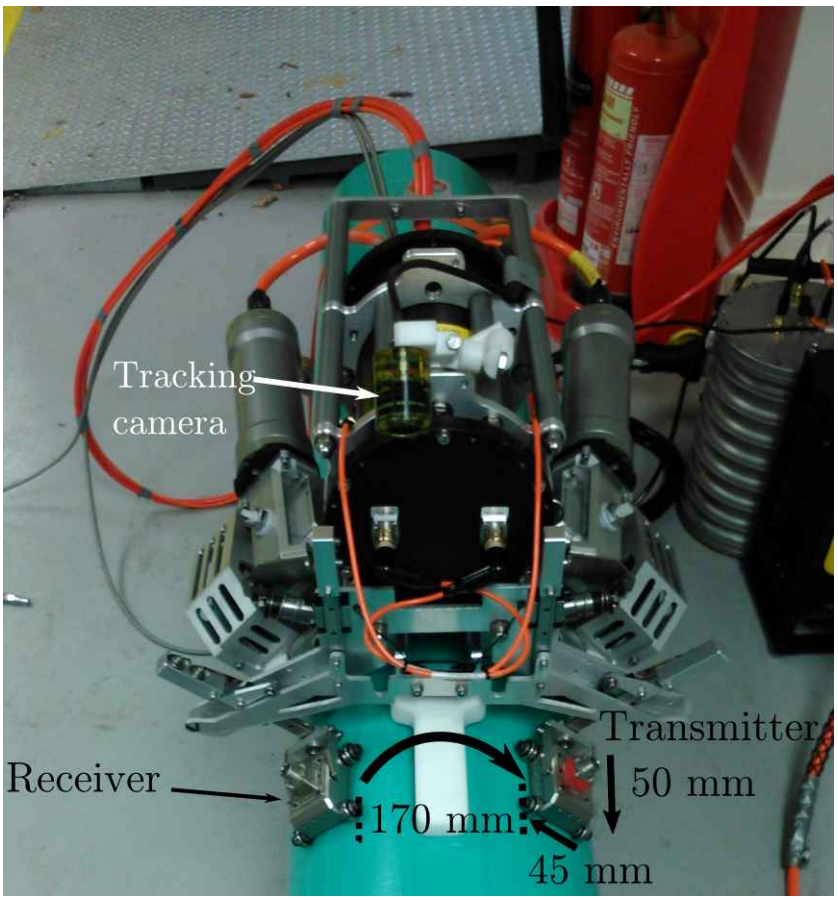

Figure 3.14: Photograph of the experimental rig used for scanning subsea samples with EMATs.

allow for any uncertainties in distances and the recording of data to be considered separately to the actual data and provide a deeper understanding of what happens to the different wave modes when they interact with a defect. An introduction to finite element modelling is provided in Chapter 4 along with some of the processes that have been carried out in order to establish a representative model of the experimental system.

Chapter 4

Finite Element Analysis

In order to gain a better understanding of a system at all stages of development, computer modelling of the system is often used. In the case of ultrasonic inspection techniques, this can take several forms. One form of modelling is to carry out finite element modelling of the wave propagation [61, 58], another is to carry out modelling of the wave propagation in an analytical sense using Huygens principle type models [106]. Modelling of the generation mechanisms that lead to ultrasound being generated by a transducer can also be carried out such as in the determination of forces caused by the electromagnetic interactions in an EMAT [144]. Modelling can be used to give further information on the processes that happen at all points of the inspection process, from the generation of ultrasound by the EMAT, through to the propagation of ultrasound in the sample and interaction of the ultrasound with a defect to the reception of the ultrasound by the receiving transducer.

Finite Element Analysis (FEA) is a useful tool for understanding complex experimental signals and separating effects that are seen experimentally in order to assess their contribution to the situation as a whole. It can also be used to visualise complex interactions such as how waves behave when incident on a defect [60, 61, 58] and can be used to generate a range of different scenarios that may not be available to experimentally. FEA is used in this thesis to determine the profile of forces generated by an EMAT transducer in an electromagnetic model. The forces determined here can then be used as an input to a model of the generation and propagation of ultrasonic guided waves in a pipe sample. The purpose of this being to confirm the hypothesis of what happens to different SH guided wave modes when they interact with defects of different sizes and shapes, to provide a tool to interpret the complex signals received and to give an opportunity to visualise these interactions.

The process of finite element modelling can be computationally expensive and certain simplifications may have to be made in order to make the acquisition of data from the model possible in terms of the computational load of a model and reasonable in terms of the amount of time that a simulation takes to complete. This section gives a brief introduction to finite element theory and the steps taken to make sure that the model that is generated is suitable to compare to the experimental data.

Finite element modelling of wave behaviour is carried out here with the commercial package PZFlex developed by Weidlinger Associates Inc. This is a package that has been developed to investigate amongst other things, the behaviour and optimal design of piezoelectric style probes and arrays and their ultrasonic wave propagation. In this thesis, the focus is on the propagation of ultrasound in a sample that is generated by an EMAT. This is achieved by using an excitation signal and transducer force profile that represent that which is seen in experiment for both the transmission and reception of guided waves. Initially an electromagnetic model of the EMAT was generated using COMSOL Multiphysics, to confirm that the profile of forces on the surface is approximately sinusoidal and to obtain a realistic excitation force that is seen in experiments, that can be used for the excitation force in the PZFlex model. Once a model for the transducer's generation and detection of guided waves is created and verified against experimental data, the model can be used to create more complex scenarios or data for defect geometries that are not available experimentally.

4.1 Finite Element theory

FEA is commonly used to investigate the behaviour of complex systems that change over time. The complexity in these systems could be in the geometry, the wave interaction behaviour such as the level of scattering, reflection or mode conversion, or in the changes that such a system sees with time such that an analytical solution to the problem is unavailable. For example in the problem that is presented here, the phase and group speeds of the different modes are given by the respective dispersion curves as in Chapter 2, but the extent to which waves are reflected or mode converted can't be derived from these dispersion curves.

The finite element method is based on building a structure out of a series of discrete elements such that a large sample is constructed from many small elements, this is known as building a mesh [145], and an example of this is shown in Figure 4.1. This mesh has to be fine enough to allow for a good approximation of the overall

structure to be achieved. The small elements that the sample is split into allows for the wave equation for the situation to be solved for each individual element and the results propagated into the next element, whilst also ensuring global boundary conditions are met. In modelling processes for NDT tasks, a chronological solution to the problem is found usually employing a time stepping solution. Breaking the problem down in this way allows for very complex systems to be examined due to the calculations for each element being simple and easy to calculate but the combination of all these solutions making up the more complex global solution.

Numerically solving the wave equations for the mesh of elements provides a self consistent series of solutions for each element, which is used to obtain a global solution to the wave equation for the whole model of which the elements are a part, and this is then used to calculate the wave displacements, velocities or pressures, as is required for a given situation.

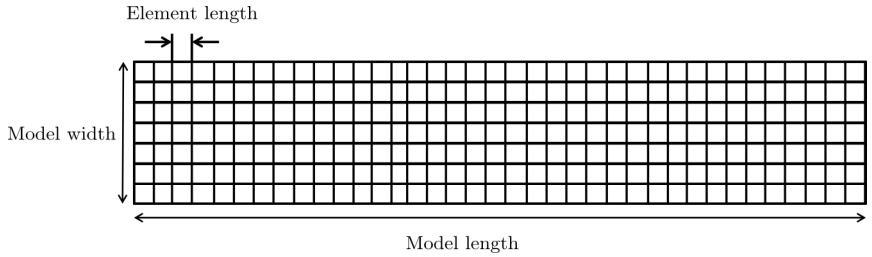

Figure 4.1: Illustration of the concept of meshing in finite element methods, with many small elements making up a larger model. The solutions for the wave equation are found for each element allowing the propagation of waves through the model.

When designing a finite element simulation, care must be taken that the small errors that can be inherent in building a large model out of smaller elements do not add up to make the output of the model non representative of the experimental situation. These errors are generally introduced by rounding errors or mistakes that are made when discretising the model. If the mesh is not fine enough then a propagating wave will experience numerical dispersion [146, 147]. The mesh density that is required for a given situation in order to accurately represent the sample is generally found through convergence of the solution. Although various suggestions for the number of elements that are required can be seen in the literature, in reality a convergence test is the only method that will provide a definitive answer [145, 148, 149].

The convergence of a model is the concept that as the size of the elements is reduced, hence increasing the density of the mesh for a given distance, the solution to the finite element problem becomes closer to the actual experimental results. For

example in an ultrasonic case, the speed of the ultrasonic waveforms in the simulation should approach the analytical value for that type of wave. A common way of confirming the convergence of the solution is by doubling the mesh density and investigating whether the output of the model changes significantly. Here convergence was tested by testing the arrival time of the modes to check whether they were close to the theoretical values. If the theoretical arrival time value wasn't reached, then the number of elements was doubled and the model rerun. This procedure continued until the solution converged. This is illustrated in Figure 4.2 where the number of elements that make up the distance represented by one wavelength of the ultrasound generated is doubled from one case to the next, with the extra elements in that distance providing a more representative solution to the problem.

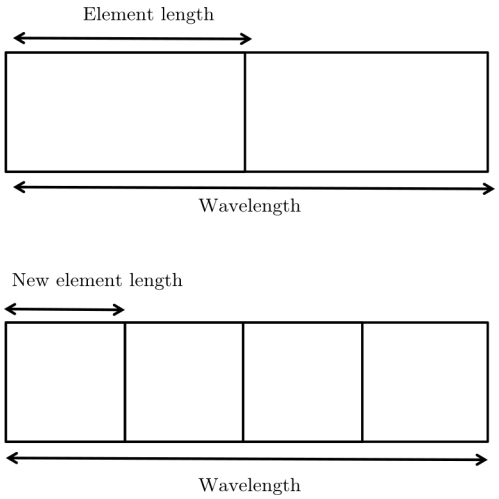

Figure 4.2: Illustrative example of doubling the number of elements in a model for the distance given by one wavelength of the ultrasound in the model. Convergence is achieved when the signal representation in the model doesn't improve when the number of elements is increased.

The convergence test is easy to carry out on a flat plate style geometry due to the simplicity of the propagation of the waves between the elements but becomes more complex when a pipe structure is considered. This is because PZFlex as a finite element analysis tool doesn't provide the user with a choice of element geometries, it limits the mesh choice to that of square or cubic elements. This can cause issues with generating geometries that are more complex such as curved surfaces as the number of elements will have to be increased to bring the approximation of the surface closer to the real situation, the issue of a square mesh for a circular sample is illustrated in Figure 4.3. This limiting factor is avoided in other finite element programs where a choice of the mesh type is allowed so that a suitable element shape

can be chosen to suit the geometry and a variation in mesh density is possible such that areas of interest can be finely meshed and areas that are not as relevant to the solution can be more broadly meshed. This allows for the mesh to provide a closer approximation to complex geometries such as curved surfaces by using elements that can be distorted to match the desired surface or allowing shapes such as triangles that may be more suitable to fill the area desired. Even in programs where a choice of mesh is provided, it is usually recommended for time stepping procedures to provide elements of identical size and shape for the mesh.

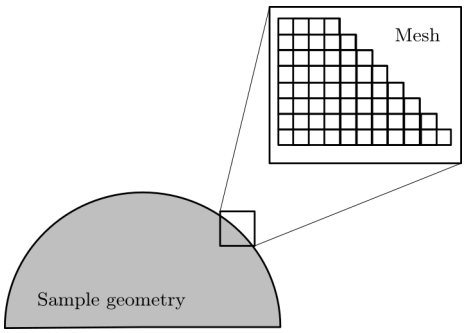

Figure 4.3: Illustration of the difficulty of representing a curved surface with square elements.

When carrying out modelling of ultrasonic wave propagation, a chronological simulation is used [150]. The most common is to perform a time step solution such as PZFlex uses. PZFlex uses an explicit time stepping approach, in which the values such as displacements and velocities at any time are used to extrapolate a new set of values a certain time later. This procedure is followed as many times as is necessary until the desired end time is reached. Using this method, the element size and time step size have to be within certain limits to ensure the accuracy and stability of the model. As such the program limits the size and shape of elements in the mesh to be the same to improve solution efficiency and to prevent wave reflections from boundaries in mesh regions with different element sizes. The time step is set to be less than the time taken for the fastest wave to travel the shortest distance between adjacent nodes, which will correspond to the element length. This ensures the stability of the simulation and also ensures that when the convergence test is carried out, it is not only the size of the elements that is changed but also the time step, so that the solution becomes more precise in both distance and time as the number of elements per wavelength is increased.

Despite the restrictions in PZFlex on the shape of the elements, it is a useful tool to use for the propagation of ultrasound due to the ease with which a model

can be established and the reduction in parameters that need to be specified by the user.

Although increasing the mesh density increases the accuracy of the resulting data, it also increases the size of the model as more elements have to be included in the structure. This will lead to increased memory usage and computation times. A balance is therefore required between the number of elements in the system and computational cost of the simulation. If the number elements is too low then the mesh density will not be adequate to represent the sample and so the model will not converge to the desired value. Conversely if the element size is too small, then the simulation will be impractical in terms of memory usage and computation time.

A common technique for reducing the number of elements and hence reducing the computational load and time of a finite element simulation is to use knowledge of boundary conditions and symmetry to reduce the size of the model. Symmetry can be used in some cases to allow for half or even a quarter of the overall structure to be representative of the whole model for example, which would reduce the computational time [151].

Absorbing boundary conditions can also be used to limit the computational load by shortening the sample in a direction that isn't important and removing reflections and scattered signals that are not desired. PZFlex implements the MINT condition (Material Independent Non-reflecting Treatment) that can be found in the literature [151, 152], which makes no assumptions regarding the boundary geometry, angle of incidence of scattered waves or material constitutive properties so that non linear effects can be accommodated.

In the cases considered here, the computational load can be reduced by using the SH wave feature in PZFlex that makes a 2D model with an arbitrary thickness in the 3rd dimension so that a shearing force can be applied in this dimension without having to generate a full representation of this dimension in the model. This allows for simpler models to be generated to determine the behaviour of the waves in the propagation direction circumferentially, but is unable to give any axial information, so 3D models are needed for such an analysis.

4.2 Spatial profiles as an input

PZFlex can input its excitation signals to the model in different ways; it can either be used to model piezoelectric probes with voltage inputs to piezoelectric materials as is used in probe design, or use a pressure to excite the face of an element of the mesh in order to mimic the forces produced by a transducer, known as pressure

loading. This causes the element to distort and transmit the forces onto the next element and so on, allowing the disturbance to propagate through the material as it would in the experimental case.

Here the probes used were PPM EMATs, (the structure of which was shown in Chapter 2) to generate an alternating shearing force in an orthogonal direction to that of the propagation direction of the wave. It was also shown previously that the waves are generated in the skin depth of the sample, and that in the steel samples that will be considered, this means that the forces generated by the transducer can be approximated as forces on the surface. Therefore in generating the shear horizontal forces here, the pressure loading to generate the desired guided wave will be an alternating pressure load on the surface elements of the sample. The pressure loading will be provided by a tone burst signal that is modulated by this spatial profile along a length that is matched to the size of the experimental transducer.

Getting a representative distribution of these forces on the surface of a sample is the key to generating the modes with spatial and frequency bandwidths that are similar to that seen in experiment. This works well in a plate sample where the number of elements on the flat surface for the given length of the transducer on the surface is more than adequate to provide a representation of the probe, even with a low mesh density. However, when the same forces are desired to be used on the surface of the pipe, the profile must be adjusted to account for the fact there are less element faces directly facing out from the sample, which means less faces onto which the forces can be directly applied.

The effect of this is that in order to obtain the same quality of results as the flat plate case in terms of narrowing the spatial bandwidth that is produced, the number of elements per wavelength for the pipe must be greater in order to provide a surface that is more realistic. This is an example where the propagation of the ultrasound in the sample is not limited by the size of the elements in terms of being small enough to represent a material but in the ability to apply the force profile effectively on the surface. The disadvantage of the increase in the number of elements per wavelength required is that the computational load of the model increases as well as the processing time. A new pattern of the respective amplitude of forces on the surface is then necessary in order to produce a nominal wavelength that is comparable to the experimental probe. This is separate but connected to the issue that arises from trying to generate a curved surface with cubic elements in that the number of elements representing the surface must be large enough in the first place to give a good representation of the curved surface geometrically. It must then have enough elements representing the surface for the force profile to be

generated on the surface with enough points of operation to suitably represent the forces that are seen experimentally.

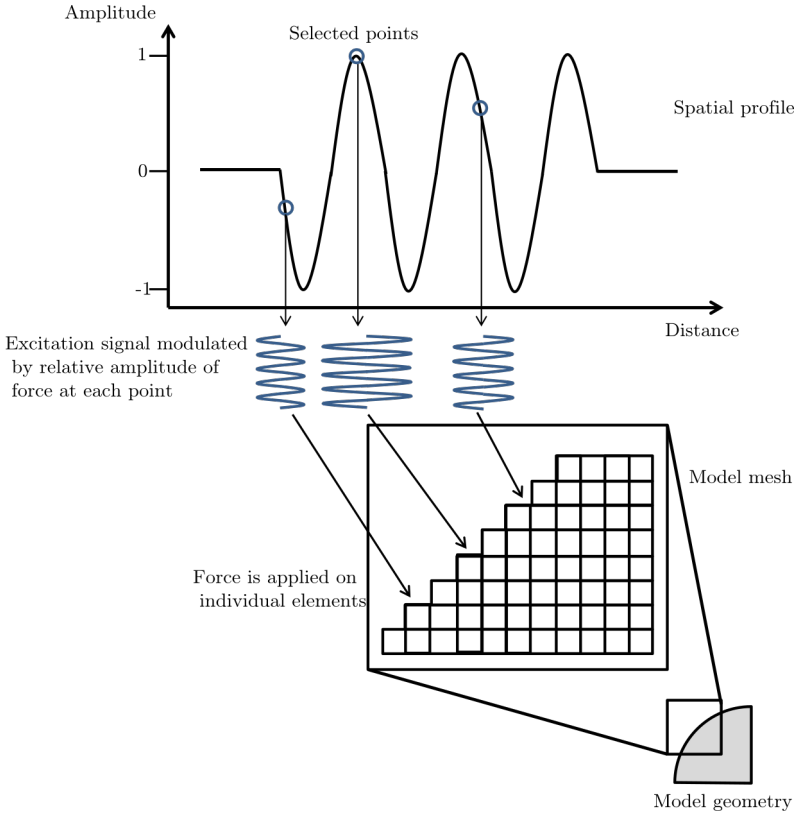

Figure 4.4: Illustration of how the spatial profile of the probe is applied to the excitation signal in order to generate signals of the correct relative amplitude and the application of these signals to the relevant elements in the mesh of the finite element model with a curved surface.

The practical application of this concept is illustrated in Figure 4.4. Here the spatial profile that determines the amplitude of the forces on the surface of the sample is used to modulate the excitation signal that is input by the pulser system, this is done for every element under the active area of the transducer, so that the effect on the surface is a periodic series of excitation points with the amplitude of the excitation signal at each point different. The number of points in the profile is adjusted to match the number of elements in the mesh on which the forces can be applied in order to effectively apply the forces on the surface that approximate the transducer forces. Figure 4.4 shows a simplified version of this with only a few forces and elements selected, the full application would consider forces applied at every element on the surface.

Given that the EMAT is a velocity sensor, as discussed previously, the data

that will be considered from these simulations is the velocity of the nodes in the direction of the shearing forces, so that an approximation of the velocities detected by the receiver can be achieved. In order to ensure that the simulation matches the experiment as much as possible, this value is taken from the surface elements of the pipe that approximate the size of the transducer used in the transmission. These outputs are then modulated by the spatial profile of the transducer in the same way as the signals were generated for the transmitter and an average over the area of the transducer taken in order to mimic the reception mechanism over the entire footprint of the transducer. This should give the best approximation of the generation and reception mechanisms that take place due to the forces in the material that are induced by the interaction of the electric and magnetic fields that the transducer generates.

In much of the work here, the model was used in two dimensions to approximate the wave interaction with defects. Two dimensions were used to limit the computational load and calculation time of the model. This approach is taken to be valid because the defects of interest are often of a scale that is larger than the transducer, such that the two dimensional model is representative of the propagation through a defect. This means that the effect of a transducer being entirely over a defect in the axial direction will be effectively modelled by having a defect in two dimensions blocking the passage of the ultrasound around the pipe circumference. This will clearly give no axial information on sizing of defects as the scanning rig travels along the pipeline, but can be used to accurately model the interaction of the ultrasound with defects and reflection from defects in the circumferential direction around the pipeline.

From this basis of the finite element theory and its application to the situation that is presented in this study, it should be possible to model the interaction of the SH guided wave ultrasound with defects as the waves travel circumferentially around the sample. This should be comparable with the experimental situation in terms of the proportions of the different modes that are generated and should give a facility to assess the signals that are seen experimentally by knowing how they are generated and behave in the simulation.

Chapter 5

Experimental results

The previous chapters have set out the preparation that is required before an inspection is attempted with the SH guided wave screening system specified and the theoretical basis of these measurements, including the limitations of the experimental system that have to be accommodated. This chapter will illustrate the information that can be extracted from a measurement of a defect of known dimensions using the experimental technique set out previously and how finite element modelling of the defect can provide a greater understanding of how the ultrasound interacts with defects. This can be extended to other cases of in service corrosion patch defects, where the depth of the defect is not necessarily known, in order to assess what depth information can be gained without prior knowledge of the defect structure or depth.

5.1 Samples of interest

The samples considered in this Thesis are taken to be representative of oil and gas pipelines that would be used in industry. As such, a range of sample circumferences and thicknesses are considered and presented. In addition to the samples tested here, a wider range of samples have been tested in blind trials to assess the detection capabilities of the system. The main focus in this Thesis is on samples of the lower wall thickness range and circumference that are seen in industry, as these are the types of samples that are more prone to failure due to external corrosion. The samples considered in the general work here ranges from a wall thickness of 5 mm to 12.5 mm (although not all of this range is provided here). Further blind trials have seen the technique used on samples up to 19 mm thick wall thickness for defect detection. The pipe circumferences tested range from 540 mm to 863 mm, with application to circumferences of over 2.2 metres in further lab tests. As mentioned

previously in Chapter 3, the main limiting factor with scanning large circumference pipelines would be the length of the time signal that can be recorded by the receiver. Clearly if the circumferential distance between the transducers is too great, then the arrival time of the ultrasonic waves will be beyond the maximum time that can be recorded.

The samples vary in surface condition and preparation, with some featuring a layer of protective coating such as paint or fusion bonded epoxy. This layer is designed to protect the underlying metal from external corrosion and can in general be anything up to 1 millimetre thick. As long as this coating is non-conductive, as in the case of the two materials mentioned, this should not present a problem for inspection by EMATs, since the electromagnetic fields generate the shearing forces in the underlying conductive material, effectively bypassing the coating thickness. The main effect that the coating layer will have on the generation of ultrasound in the sample is in the increased lift off of the EMAT probes from the surface of the pipe. It will also affect the dispersion curves [153] but this is neglected in this Thesis for simplicity. This lift off will lead to an inefficient generation of ultrasound due to the strength of the electromagnetic forces decreasing with distance from the probe [118, 119, 154]. This can present a major problem for inspection with EMATs, since the signal transduction is inefficient compared to other ultrasonic methods.

A table detailing the specific samples tested in this Thesis is provided in Table 5.1. This table labels the pipe samples and identifies which chapter contains the scan data for each sample. The pipe samples tested here had a range of different circumferences and pipe wall thicknesses as shown in the table but were focussed on the lower pipe wall, smaller circumference pipes as mentioned. Some of the samples had a coating layer present which was no thicker than 1 mm although the thickness is unlikely to have been uniform at all points. The dimensions of any single defect in the sample are recorded if they were known and are provided in Table 5.1 as a measurement of a bounding box that encompasses the full defect. The maximum depth of the defect is shown if it is available but in several cases it was not and is provided elsewhere (Table 6.1) for samples with multiple defects. For the blind trial cases in Chapter 6, no information was available on the defects, but for the rest of the samples at least the approximate extent of the defect on the pipe surface was known. Finally a brief description of the defects in the sample is given.

Sample	Chap.	OD (mm)	WT (mm)	Coating (mm)	Def. Dims. (mm)	Depth (mm)	Description
1	5	170	7	1	48.6 circ 44.2 ax	4.8	One artificial corrosion patch style def.
2	6	170	7	none	75 circ 145 ax	n/a	Single in-service corrosion patch, varied depth.
3	6	275	9	none	n/a	n/a	Blind trials with pipe support defect.
4	6	274	6.4	1	Multiple	Multiple	Multiple with varied morphology. Details in Fig. 6.10, Table 6.1.
5	6	171	7.5	none	Diam. 20 Diam 30	3.8	Flat-bottom -hole style defects, int, ext and varied size and depth. See Fig. 6.15.
6	6	222	8.18	none	100 circ 100 ax	2	Wrapper welded on exterior inc. 25% depth defect. See Fig. 6.17.

Table 5.1: Summary of dimensions of the pipe samples for which data is shown in this Thesis. Columns represent sample number, which chapter the sample features in, outer diameter, wall thickness, coating thickness, dimensions of the defect, maximum depth of defect and brief description of the defects.

The attachment of the probe to the pipe surface is shown in Figure 5.1, with

the coating thickness shown to illustrate how this increases probe lift off. It should be noted as from the COMSOL modelling before in Chapter 3, that the lift of the probe for a circumferential measurement varies across the transducer such that the signal generation could be efficient at the centre of the probe but less efficient for the ends of the probe. The extent to which the system is affected by lift off is hence dependent on the curvature of the pipe sample inspected.

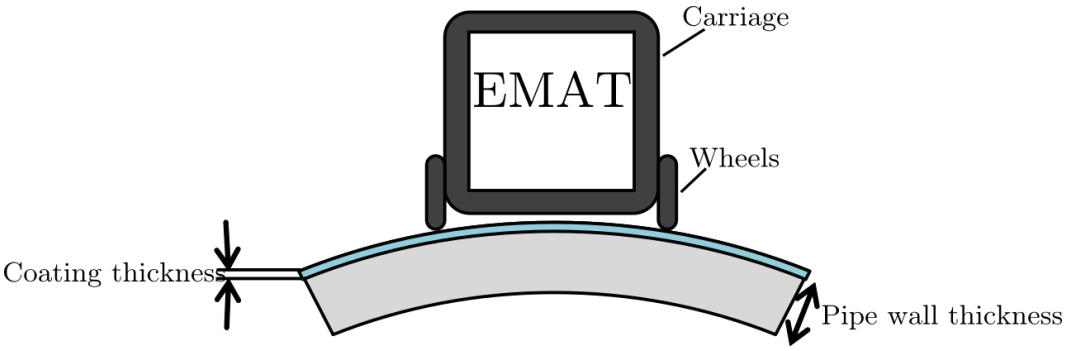

Figure 5.1: Diagram showing how the EMAT is held against the pipe in its wheeled carriage to allow it to be moved along the surface of the pipe and showing the extra lift off that the coating layer introduces for the EMAT, (not to scale).

The change of lift off of probes is a particularly important factor when considering defects that can be at any position around the pipe's circumference. The presence of defects will make the surface of the pipe uneven, which could lead to a change in lift off of probes if the circumferential position of the defect area is directly underneath the EMAT. This will cause the probes to lift further away from the surface and decrease the efficiency of generation of ultrasound in the sample, changing signals without providing any wall thickness information. The lift off of the probes from the surface is maintained in the experimental rig by the arms that hold the transducers and can be adjusted in each case to have the lift off of the probe at a fixed distance from the surface.

5.2 Defects

The defects of interest in this Thesis are considered to be corrosion patch defects that have been generated by external corrosion of the pipe surface as shown in Figure 5.2. In the topside case, corrosion patch style defects are most likely to be located at pipe support locations as noted in the original problem description, but their location is not limited to these positions. Corrosion patch style defects are usually irregular in shape and depth, this presents a challenge for any inspection as they are likely to

cause significant scattering of signals [155, 156]. The defect is also likely to change in depth throughout its area in both the axial and circumferential directions, which makes exact defect sizing difficult. Given that the methods here involve detecting the ultrasound after it has been transmitted through a defect, this means that any thickness measurement that can be achieved will only be an estimate of the average thickness. The complicated nature of in-service corrosion patches also presents a problem in determining the depth in order to assess results from the system.

Figure 5.2: Photograph showing an in-service corrosion patch in a non-coated sample. The corrosion patch is of irregular size and shape, with the wall thickness variable throughout the defect.

Artificial defects that are induced in samples struggle to replicate the behaviour of the in-service defects due to the inherent complexity of a real defect. The introduction of an artificial defect into a sample is generally limited by the tool that is used to make the defect, with flat bottomed and straight sided defects the easiest type to generate using techniques such as electrical discharge machining. A range of artificial defects are considered in this Thesis, with different shapes and sizes and the system has been tested on in-service defects. A study on the different defect profiles is provided in Chapter 6, with straight sided flat bottomed holes situated internally and externally generated by electrical discharge machining, but these are not very representative of a corrosion patch defect, being more representative of the type of pitting corrosion that may be an initial progenitor of further corrosion. As the straight sides of the defects don't compare well with the gradual change in depth

found in in-service corrosion patches.

An artificial defect that is a more suitable representation of a corrosion patch is a gouged hole in a sample, where the depth profile can be more easily fitted to the sort of profile seen in in-service samples. In generating these defects, a gradual change of thickness to the full depth is employed as would be seen in real corrosion patches, but unless the profile is considered in detail, the edges of the defect in the circumferential direction will be relatively uniform. This will result in coherent reflections from the edges that may not be seen with more complex real defects.

5.3 Pipe Screening

Before an inspection is carried out, the preparation steps given in Chapter 3 can be used to generate the dispersion curves for a sample and determine the operation points in terms of frequency-thickness and velocity. Once the operation points on the dispersion curves are known, the frequency of operation for each mode can be set for an inspection. If the sample is the same thickness along the circumference, then the arrival times of the different modes will correspond to the circumferential distance travelled by the mode divided by the speed at which the mode travels. The introduction of a defect in the form of wall thinning in the propagation path of the guided wave will alter the arrival time of the different modes at the receiver.

5.3.1 Defect effect on the circumferential SH0 mode

As the thickness of the curved sample decreases from the nominal thickness, the operation point on the dispersion curve will change. The change in the boundary conditions caused by the thinning of the pipe wall results in a change of the velocity of the wave in order to satisfy the new parameters of the sample. With the excitation frequency constant and the thickness decreasing, the frequency-thickness product of the mode changes such that its new velocity can be determined from the dispersion curve.

When the circumferential SH0 (CSH0) mode is considered, a reduction in the thickness will result in the CSH0 mode travelling at a higher speed whilst propagating through the defect. This change in speed in the thinner region is shown as the operation point of the guided wave moving to a lower frequency-thickness value on the dispersion curve. The overall change in the arrival time of the signal will not be a large change, as the mode only travels at the higher speed when propagating through the defect. This means that for the vast majority of the distance that the wave propagates around the circumference, it will travel at the original velocity de-

termined by the nominal thickness. The effect of this change in operation area is shown in Figure 5.3 for the phase velocity in Figure 5.3a and the group velocity in Figure 5.3b.

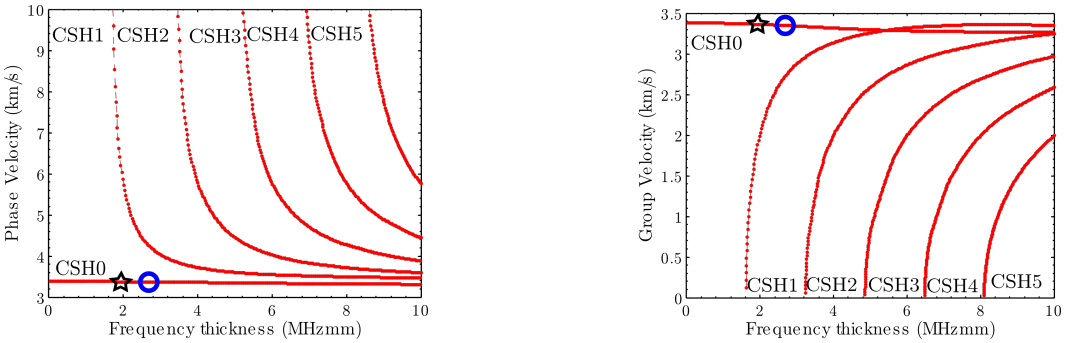

(a) (b)

Figure 5.3: The phase and group velocity dispersion curves for the first 5 SH modes in a 7 mm thick 86 mm radius steel sample with the nominal operation point set by the nominal wavelength of the probe circled in blue and the resulting operation point for a thickness that is reduced by 2 mm to a thickness of 5 mm shown by the black star. (It is clear here that the small change in thickness results in a change in velocity in the CSH0 mode, with a greater change in thickness resulting in a greater change in velocity.)

Here the change from the excitation point for a 7 mm thick sample to a thinner area is shown. The blue circle represents the original excitation point and the black star represents the operation point of the wave that would be expected if the thickness of the pipe is reduced to 5 mm. This shows the velocity the circumferential SH0 mode would travel at in the section of the sample that is at this reduced thickness.

The result of this change in wave propagation when a defect is reached is a waveform that is essentially a sum of the wave travelling in the full thickness for the majority of the path and the faster speed at the defect. In the case of a real defect, the change of the velocity will be gradual as it will not possess an abrupt edge, with the tapered depth defect gradually gaining its maximum value and then decreasing again as the shallower part of the defect is encountered. This leads to a low level of reflection, as the boundary conditions change at a rate that the wave can adjust to. The change in velocity of the SH0 mode in the circumferential application here presents a distinct difference to that of shear waves in a plate, where the velocity of the SH0 mode remains constant at all frequency-thicknesses.

The low level of dispersion of the circumferential SH0 mode means that the change in velocity of the CSH0 mode will be small compared to the higher order

modes. The amount of difference in arrival time that is observed between the arrival time of the CSH0 mode for the case of no defect and the case of a defect depends on the depth profile of the defect and the circumferential extent of the defect. The depth profile of the defect will determine the waveform received, as it will change the depth of the defect at each point, determining how long the mode travels at the particular speed that is defined by the new boundary conditions. The circumferential extent will also alter this, as it will change what proportion of the total distance the wave propagates to the different speeds.

Although the mode will show some disruption from the presence of a defect, the small changes in velocity make it more difficult to use the CSH0 mode for defect depth gauging than other modes that show a greater change with depth of a defect such as the CSH1 mode that will be considered subsequently.

5.3.2 Defect effect on the circumferential SH1 mode

When a defect is encountered by a higher order mode than the fundamental shear horizontal mode, its interaction is more complex. The higher order modes have a cut-off frequency-thickness below which the waves cannot propagate within a sample as was considered in Chapter 2.

The existence of a cut-off frequency of the mode results in different behaviour when a sample is reduced to a remaining wall thickness that is below the cut-off value. When the frequency-thickness product of the CSH1 mode for example falls below its cut-off at a defect, the propagating ultrasound is partially reflected away from the edge of the defect and partially transmitted through the defect as a mode converted CSH0 waveform. This mode conversion to the CSH0 mode allows the CSH1 mode energy to be transmitted through the defect area as the lower order mode, with the wave mode converting back to the higher order mode as it reaches an area where the full thickness of the sample is restored. This mode cut-off can be used to determine a thickness range that the defect must fall into in order to have caused a cut-off of the CSH1 mode.

For higher order modes such as the CSH2 mode, there are more options to mode convert into lower order modes, with both the CSH0 and CSH1 modes available depending on the remaining thickness in the defect area. However, as was determined in the mode propagation tests in the original data in Chapter 3, the higher order modes that can be excited with the EMATs considered here are not suitable for defect detection, so will not be considered in detail here.

The other scenario for the interaction of the CSH1 mode with a defect is if the defect is shallow enough for the remaining wall thickness to be above the cut-off

thickness. If the section of wall thinning in the pipe is above the cut-off thickness, then the CSH1 mode travels at a slower speed under the defect corresponding to the new frequency-thickness value, with the velocity increasing to the original value when the defect is passed. This different speed is illustrated in Figure 5.4 for the phase and group velocity, where the change of velocity is shown for the thinning of a 7 mm thick section of pipe to a 5 mm thick remaining wall thickness.

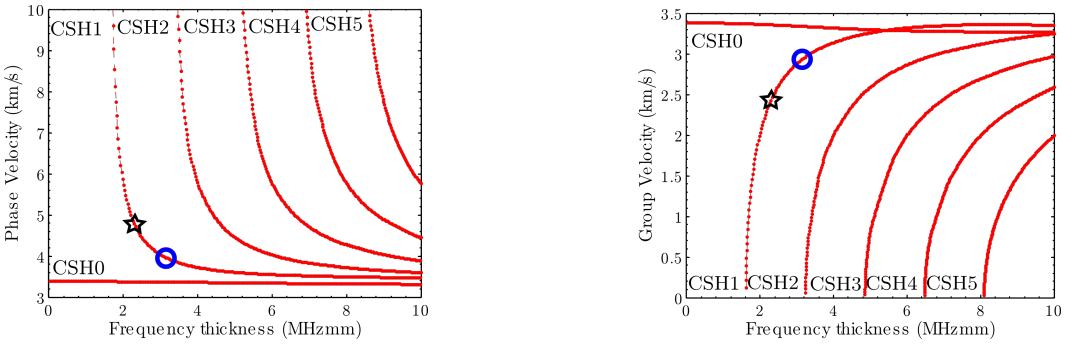

Figure 5.4: The phase and group velocity dispersion curves for the first 5 SH modes in a 7 mm thick 86 mm radius steel sample with the nominal operation point set by the nominal wavelength of the probe circled in blue and the resulting operation point for a thickness that is reduced by 2 mm to a thickness of 5 mm shown by the black star.

The change in the propagation velocity as the wave propagates through the defect area results in a later arrival time of the mode in the received signal, which can be compared against the circumferential SH1 mode in a clear area of pipe to show the presence of a defect. In the case of the CSH1 mode, the effect of the change of the frequency-thickness product means that the wave is operating at a more dispersive section of the dispersion curve, which will result in a greater spread of velocities for the different frequency components of the signal. This will result in a greater spread in the arrival time of the different frequencies in the mode, altering the appearance of the received mode. It is clear here that the small change in thickness results in a change in velocity in the CSH1 mode, with a greater change in thickness resulting in a greater change in velocity.

As with the CSH0 mode, the defect profile and circumferential extent will determine how much of the mode transmits through the defect region as the mode converted waveform and how much is reflected. The important issue here is the point at which the remaining wall thickness of the defect reaches a value below the cut-off thickness and how abrupt a change occurs between the area of full thickness and the area below the cut-off thickness. The change in the CSH0 and CSH1 modes

can be used to give an indication of the severity of the defect, with scans put into three categories:

- Category one is defined as having no defect present in the sample and is characterised by having both the CSH0 and CSH1 modes arriving at the same time and amplitude throughout an axial scan of the sample.
- Category two is indicative of having a defect in the sample that reduces the wall thickness but leaves a remaining wall thickness that is greater than the cut-off thickness. This is characterised by the slowing on the received CSH1 mode such that the arrival time of the mode is later than in the case where there is no defect present.
- Category three is that of a defect that reduces the remaining wall thickness in the defect area to below the cut-off thickness of the CSH1 mode. This results in a mode conversion of the CSH1 mode into an CSH0 mode in the area beneath the defect, with the mode converting back the CSH1 mode when the defect area is passed. This defect is identified by having some of the energy that was expected in the CSH1 mode arriving as a faster waveform in between the CSH0 mode for the path and the expected arrival of the CSH1 mode for the path.

5.4 Initial measurements

The experimental system described in Chapter 3 using the Innerspec pulser receiver and the EMAT rig was assessed in terms of its capabilities for detecting an area of external wall thinning on a pipe sample and the sizing information that this provides. A further assessment of the effect of defect geometry and depth is given in Chapter 6.

5.4.1 Sample Parameters

Preliminary measurements were carried out on a steel pipe of 534 mm circumference with a wall thickness of 7 mm, and a full axial length of 700 mm (Sample number one in Table 5.1). This sample had a painted surface of approximately (1 ± 0.5)mm thickness to mimic a coating that might be seen in industrial applications. The sample contained a single artificial defect in the form of a gouged defect where material has been removed from the pipe surface to leave a maximum remaining wall thickness of 2.2 mm.

The defect was designed to mimic a basic wall thinning area in the sample, with several simplifications compared to an in-service defect. The defect structure as shown in Figure 5.5 featured a gradual slope down to the area of greatest depth, such that the change from the full thickness of the sample to the cut-off thickness was gradual. However, the defect had a uniform shape along its axial length such that it is roughly rectangular in shape to remove any complexities inherent in the interactions of the guided waves with a complex shape.

The defect was situated in the centre of the pipe axially on the external surface. It had a measured axial length of 48.56 mm and a circumferential extent of 44.22 mm. The intention is to represent a defect that has a depth profile and size comparable to a simple corrosion patch without representing the complex shapes that are often generated by in-service corrosion patches. The controlled knowledge of the size of the defect can then be used to interpret the results and a finite element model generated that represents this type of defect. The size and positioning of the defect is intended to represent a defect that could occur in a pipe support area. The defect is shown at the side of the diagram for visibility in Figure 5.5, but the sample is free standing so the initial tests will be carried out with the defect centred at the 6 o'clock position on the pipe to represent a pipe support style defect. Figure 5.5 shows all the relevant dimensions of the pipe and a representation of the defect, although the profile here is simply an approximation of the likely style of the defect.

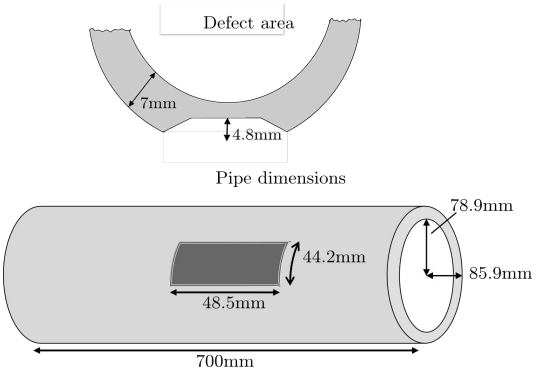

Figure 5.5: Schematic diagram showing the dimensions of the pipe sample with the artificial defect.

Before the inspection is carried out, the sample dimensions can be used to determine the optimum frequencies that the modes can be operated at for the specific wavelength probe used. Here an 8.8 mm nominal wavelength probe is used for generating and detecting the guided waves which gives an approximate frequency of operation of 380 kHz for the CSH0 mode and 450kHz for the CSH1 mode.

5.4.2 Recorded data and experimental setup

An encoded scan of the pipe can then be carried out, by exciting the transmit probe with a 5 cycle tone burst in order to generate guided waves in the circumferential direction of the pipe. The experimental rig is then moved axially along the pipeline in order to achieve an encoded scan of the pipe. The scans can be carried out at a high speed, (approximately 2 metres per minute) with the main limitation being the smooth movement of the rig along the pipe in order for the encoder to work appropriately.

The Innerspec Technologies Inc Powerbox provides the A-scans of the waves received at the receiver and presents the encoded scan data on screen so that an immediate assessment of the presence of a defect can be made. This sort of immediate response for the presence of corrosion is extremely useful for on-site inspection. However, in order to provide more quantitative information about the depth and positioning of the defect, more in depth off-line processing needs to be carried out.

The experimental rig was adjusted to fit the sample, with the EMAT carriages set to a 0.3 mm lift off from the pipe surface to maintain the lift off distance as a constant and the separation of the EMATs circumferentially across the top of the pipe was set to 170 mm The relatively low number of cycles in the excitation signal will mean that the signals span the operation areas for both the CSH0 and CSH1 modes such that both modes will be generated simultaneously.

5.4.3 Filtering

When collecting data, the digital software filters in the Innerspec system are used, as the system generates unwanted low frequency content. Applying the software filters in the system to remove the content below 200 kHz appears to be sufficient to remove such signals, but more extreme filters are often used in the industrial application of the system in order to make the initial data presentation adequately clear. This frequency content appears to be due to the generator receiver behaviour, as the content is present in a received signal even if the receiver is not attached to the sample and is predominantly the same even when a different wavelength probe is used in the system.

This suggests it is a consequence of insufficient shielding between the generation and reception sections of the equipment in this application, with a low amplitude signal at the desired frequency and signals at a half and quarter the frequency of the excitation frequency. These signals are not from propagating wave modes that are generated and detected by the transducers and so are not relevant

to the defect detection performance of the system. They are easily filtered out if the digital software filters on the receiver are used and at any rate appear at much lower amplitude than the signals of interest in the sample and so can be largely discounted. Appropriate filtering of these additional signals is used when collecting data in order to remove this noise and present a clear view of the received modes in the collected time signal. Detailed analysis can then be carried out with the appropriate application of software filters in processing of the data off-line.

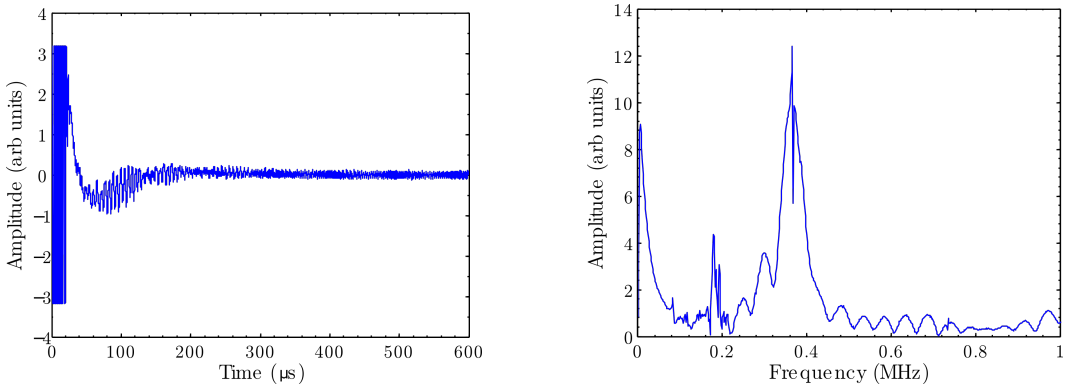

(a) (b)

Figure 5.6: Time and frequency records for the transmitter pulsing at 375kHz but the receiver not attached to the sample, showing the low frequency leakage from within the experimental system.

A filter can also be introduced to remove any high frequency noise content in the signal, but any noise in the higher frequency regime is generally of low amplitude. The time record for the transmit EMAT attached to the sample but the receiver removed from the sample is provided in Figure 5.6a showing the periodic nature of the signals that are generated, suggesting that they are leakage from the operation of the pulser. The frequency content of the signal is presented in Figure 5.6b, illustrating that the majority of the signal is low frequency content that can be filtered out from the signal.

5.4.4 Circumferential scan raw data

The frequency bandwidth of the excitation signals and the separation of the probes on the surface of the pipe will result in the appearance of several different wave modes in the received signal. The received waveforms in a circumferential scan were briefly described previously for the frequency swept case, but will be presented in detail here along with the way these waveforms can be manipulated to extract quantitative data from the scans.

The encoded scan is composed of Amplitude (A) scan data taken at 1 mm intervals in the axial direction of the pipe as the guided waves propagate around the circumference of the pipe. The A-scan data contains numerous waveforms due to the frequency bandwidth of the excitation signal spanning both the excitation points for the CSH0 mode and for the CSH1 mode. It also features waveforms travelling in both directions around the pipe due to the EMAT generating waves in both the clockwise and anticlockwise directions, knowledge of the operation of the probe and the circumferential distance between the probes can be used to determine what each waveform corresponds to. In the operation of the probes in this application, the theoretical peak frequency for a mode is used as an initial estimate of the optimum excitation frequency, with a small range around this frequency searched in order to find the optimum frequency for the specific sample. This leads to a peak frequency of 380 kHz for the CSH0 mode and 420 kHz for the CSH1 mode for this sample.

The filtering mentioned in the previous section can be applied to remove unwanted disruptions to the signal. The Innerspec system allows filtering of the received data through digital bandpass filters implemented on the system. There are different filters available with 64, 128 and 256 taps which represent the quality of the filter, with an increased number of taps relating to an increase in filter coefficients and a better quality filter in terms of tightness of the passband and the amount of attenuation of the signals outside of this band. An example of the filter is shown in Figure 5.7 from the manual for the Innerspec system [140] in order to illustrate the shape of the filter.

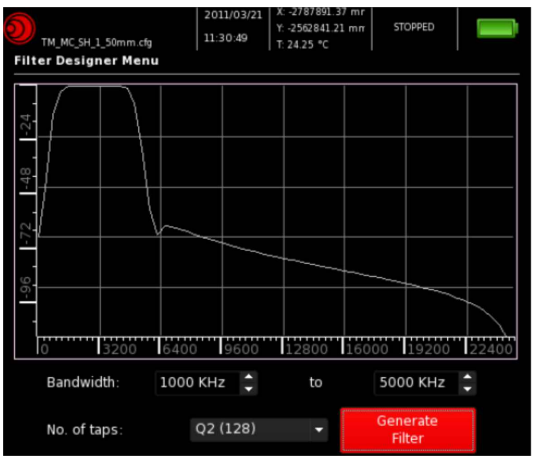

Figure 5.7: Image of the filter application screen for the Innerspec system used in this Thesis to illustrate the shape of a bandpass filter applied. The data presented here was taken with a higher number of taps of 256, but the shape of the filter will still be representative.

In the data presented in this thesis the highest order filter of 256 is used allowing for a narrow transition from pass to stop band and a variety of levels of filtering have been tested for their suitability. The change in the recorded signal when different levels of filtering are applied is shown in Figure 5.8. The original unfiltered signal is shown in Figure 5.8a, which shows a noisy initial signal due to the extra signals in the data as referred to in Figure 5.6. The effect of applying the filters in a wide passband between 200 kHz and 1 MHz is illustrated in Figure 5.8b this removes any low and high frequency noise that is not related to the generated signals but that could be disrupting the recorded data. A final figure is provided in Figure 5.8c that illustrates the use of a tight passband around the excitation frequency used to excite the EMAT, this is a filter with a passband between 320 kHz and 480 kHz for an excitation frequency of 380 kHz. The use of this tight filter removes most of the extra signals from Figure 5.6, leaving only the signals of interest.

This tight passband of frequencies around the excitation frequency is the way the filters have been employed in the industrial application of the screening method. This allows for the intended modes to be presented more clearly and removes any excess noise from around the intended modes. The danger here is that information may be lost if it lies outside this frequency range once a defect is encountered. This means the excitation frequency and likely changes in the received signal need to be known to a high accuracy in order to prevent the loss of information due to these severe filters.

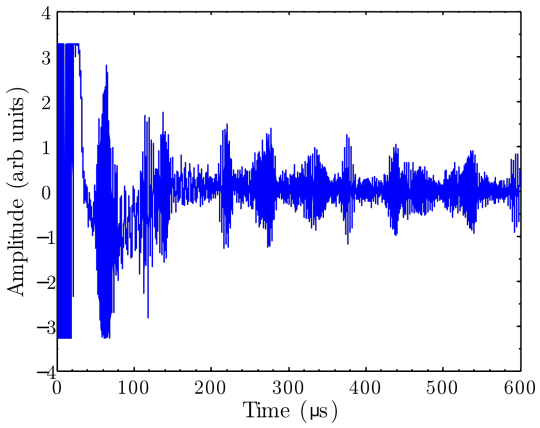

(a)

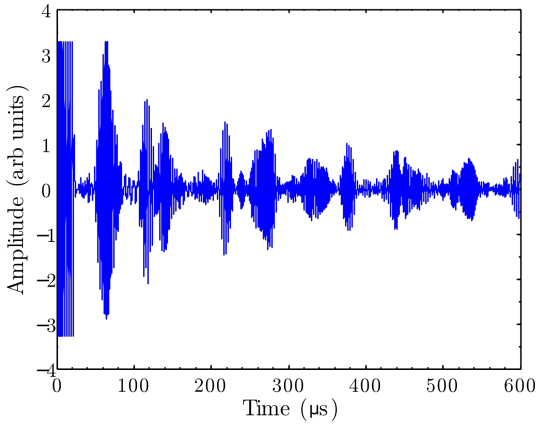

(b)

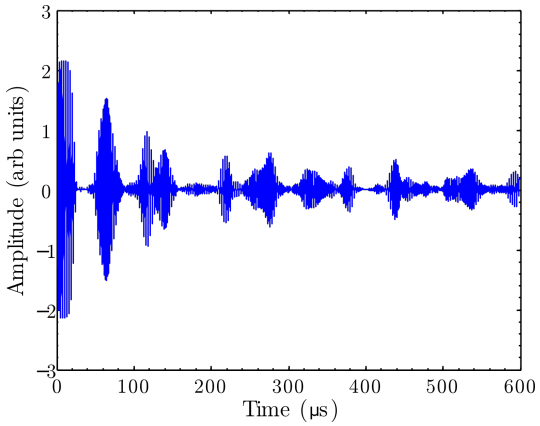

(c)

Figure 5.8: Time records for circumferentially travelling SH modes showing the effect of different frequency filtering ranges in order to obtain clearer signals. The initial raw data suffers greatly with unwanted noise, caused by the system as mentioned previously and filtering can make the signals clearer to interpret.

With the appropriate filters set for the collection of data, an assessment

of the different sections of the waveform can be made in order to determine the different modes that are detected. The signal for a defect free section of the pipe is shown in Figure 5.9 with the different wave modes circled. The first signal that will be detected, (labelled as number 1), will have travelled the short path distance between the two transducers across the top of the sample. With the small transducer separation distance in the short path in this example, both the CSH0 mode travelling the short path distance and the CSH1 mode travelling the short path distance arrive with similar arrival times. Due to the time duration of the signals and similar arrival times at the receiver, the two modes are indistinguishable from each other in the time domain although they should be able to be partially separated in the frequency domain.

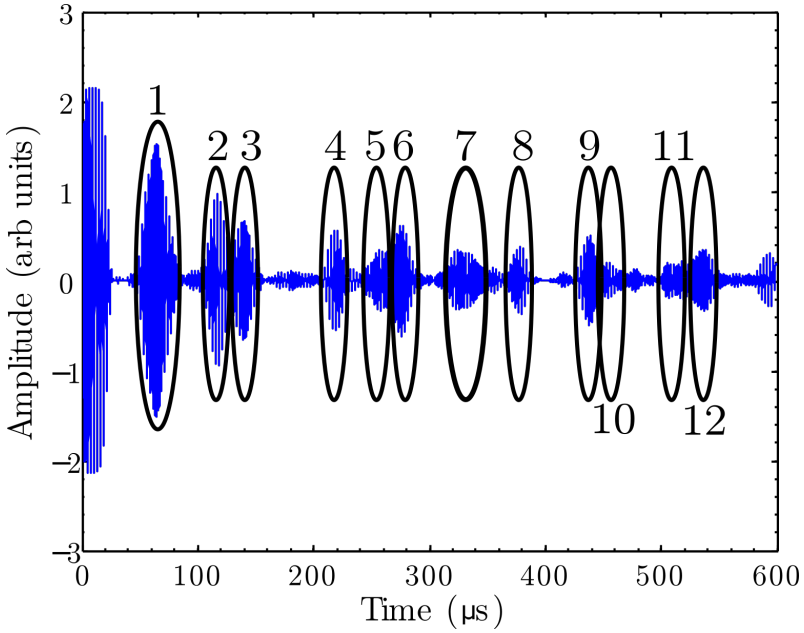

Figure 5.9: Time record for a defect free section of pipe showing the different wave modes that are detected as the waves propagate around the pipe circumference. Both the CSH0 and CSH1 modes are observed with waves propagating in both directions around the pipe circumference.

As the waves travel a greater distance around the pipe circumference, the different modes will separate in arrival time and become distinct from one another. The waveform corresponding to the CSH0 mode travelling along the long path distance (labelled number 2), will be the next to arrive, followed by the long path from the CSH1 mode (labelled as number 3). This pattern is repeated for the multiple loops of the pipe, with waveforms corresponding to CSH0 and CSH1 modes travelling the short path plus a circumference seen (labelled 4 and 5), followed by the

same modes travelling the long path plus a circumference (labelled 6 and 7). The CSH0 mode always arrives first in these cases due to its greater group velocity, but the different speed of the two modes means they separate in time in the received signal, with the CSH1 mode increasingly likely to arrive at a similar time to the CSH0 mode travelling in the opposite direction around the pipe. This is observed in the sections 9 and 10 and 11 and 12 especially, where the slower CSH1 modes arrive at similar time to the CSH0 modes and complicate the recorded signals.

The knowledge of what the different waveforms relate to is essential in extracting circumferential defect positioning information from the data. If there is a defect that occurs in the path of the transducer, then the amplitude and arrival time of the CSH1 mode will change, as mentioned previously. This change from the behaviour seen in the clear area can be used to indicate the presence of a defect and the waveform in the signal that it affects can indicate whether the defect is located within the short path between the transducers or the long path. If the defect is located in the short path, then the short path CSH1 mode will show a change from the clear area and similarly for the long path waveform as shown in Figure 5.10.

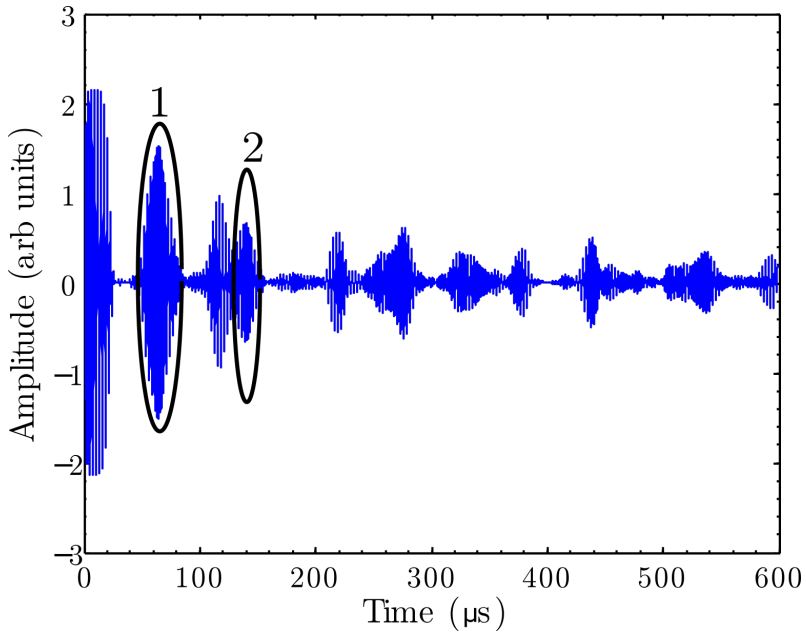

Figure 5.10: Time record for the defect free area of pipe. If a defect is located between the transducers on the short path around the top of the pipe, then the waveform labelled 1 will see a change, whereas if it is located between the transducers on the long path around the bottom of the pipe, the waveform labelled 2 will be affected.

The presence of a defect can also lead to distinct reflections from the edge

of the thinning region if it is uniform axially. If the experimental rig is positioned correctly, any reflections from the defect edge will allow for the approximate positioning of the defect circumferentially. If the defect is positioned at the base of the pipe then any reflections are likely to travel further than the long path in order to reach the detector, which will mean that they are received after the long path signals in a time record. If the defects are located at positions that are not at the base of the pipe, for example at the 3 and 9 o'clock positions on the pipe, then any reflections will be detected between the short path and the long path signal and so can be used for circumferential positioning. This will be considered in more detail in Section 5.4.8. The arrival time of each mode distinct by its frequency content and speed can be visualised using a Short time Fourier transform (STFT) of the signal as in Figure 5.11.

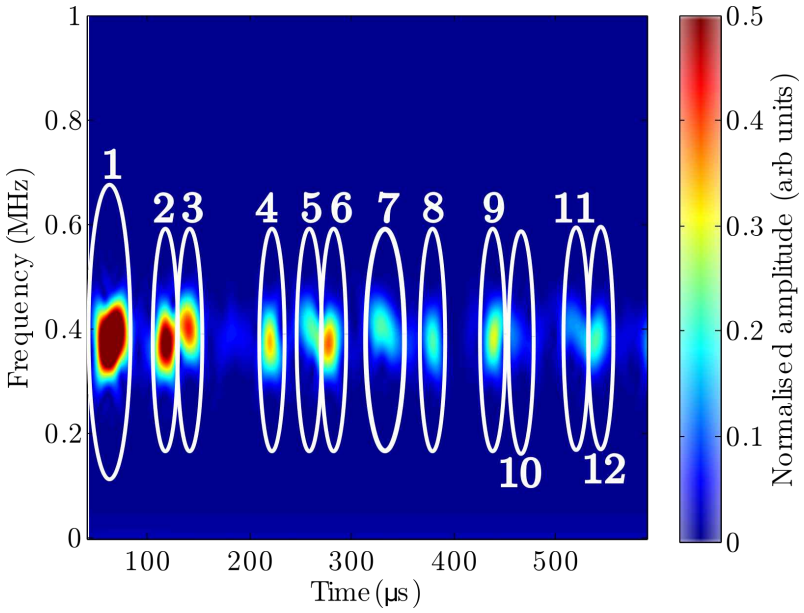

Figure 5.11: Short time Fourier transform of the received signal for the clear section of the pipe, with the modes detected as described earlier in Figure 5.9. Data is normalised to the amplitude of the short path CSH0 mode, but the colour scale adjusted to allow all the signals to be visible.

The STFT is a form of time frequency analysis [157, 158] of which there are many available [159] that allows the different waveforms in a signal to be characterised in both the time and frequency domains [160]. It consists of applying a window function that can be moved through the data. This splits the signal into sections of a specified equal size which can then be Fourier transformed to give the frequency content of each window. Due to time frequency duality, an increase in

the time resolution results in a decrease in the frequency resolution and vice versa. This means that the result of a STFT is a balance between the resolution of these two factors and is dependent on the windowing function used.

In this work the Hann function in Matlab is used which imposes a Hanning window on the data [123], this was chosen as a window as it reduces the appearance of frequency band side lobes. The window is a symmetric window given by:

$$w(n) = 0.5\left(1 - cos\left(2\pi\frac{n}{N}\right)\right), 0 \leq n \leq N \tag{5.1}$$

The STFT gives an indication of the frequency of a waveform and its arrival time which is very useful for mode decomposition here and for showing dispersion that is present in signals. It also helps separate the different modes in the visualisation of the signal, which can be difficult when just looking at the A-scan signals. The different wavemodes are labelled as in Figure 5.9, with the colour map showing the amplitude relative to the maximum value in the signal. The STFT representation allows the different modes to be identified by their operation frequencies and arrival times [161, 99].

The speed of the different modes can be estimated in order to provide a baseline for velocity changes and confirm the operation on the dispersion curves at the intended area. The most accurate way of doing this is to compare the waveforms that have travelled multiple loops of the pipe with the ones that travel just the long or short path separation between the transducers. This removes the need to know the long or short path distance accurately, as the time of arrival of the envelope of the direct paths can be subtracted from the time of arrival from the multiple loop signal to obtain a time of flight for the waves travelling the circumference of the pipe. This means that only the circumference of the sample needs to be known, which is a much more readily available and measurable parameter to use.

The velocity can be calculated in several ways, but it is complicated compared to general ultrasonics due to the dispersive nature of the waveforms, which means that finding the phase velocity of the wave by locating the same point on the waveform is difficult and the group and phase velocity are not equal. Finding the speed of a specific mode is also complicated by the interaction and overlap of the CSH0 and CSH1 modes that can make it difficult to sufficiently separate the two modes to make reliable speed measurements. A variety of methods are then available to assess the group velocity of the modes, with the CSH0 mode the easiest to assess due to its low levels of dispersion. An estimate of the group velocity can be found by carrying out a cross correlation of the waveforms from multiple loops to find the time lag between the detection of the different signals and using the

circumference of the sample as the distance to determine a speed for the waveform.

Alternatively, the envelope of the waveform can be approximated and the maximum of the envelope of the waveform found and compared for each part of the signal to obtain a group velocity of the signal. These methods have their inherent advantages and disadvantages, with the cross correlation method relying on using the same shape and frequency signals for identification, which can be complicated when the modes interact with other modes in the signal and interfere with each other. Obtaining the peak of the envelope of the signal requires selecting the correct section of the signal to fit the curve over and is subjective as to what fitting techniques are used.

By time gating the relevant signals out from the rest of the time record (in this case the CSH0 signals are considered) and comparing the multiple loop signals for each path, the average (mean) velocity of the wave from these two methods is calculated to be (3356 $\pm$ 21)m/s and (3355 $\pm$ 30)m/s for the cross correlation and peak of the envelope methods respectively. If the method is repeated after removing waveforms that show considerable interference from the CSH1 mode, (in this case the first mode and last mode in the signal), then an average velocity for the CSH0 mode is calculated to be (3349 $\pm$ 21)m/s for the cross correlation method and (3348 $\pm$ 30)m/s for the peak envelope method. The method taking the peak of the envelope of the signal is found by time gating out the CSH0 signals, obtaining the Hilbert transform of the data, and then fitting a Gaussian peak to the data, to obtain the peak of the envelope of the mode, giving an arrival time that can be used with the known circumference. This speed is close to the expected value of 3348 m/s from the dispersion curves shown in Chapter 3.

5.4.5 Encoded scan data

Any quantitative data from the scans will be obtained from looking at the individual time records for each encoded distance step. However, for the qualitative screening application where it is used to detect the presence of a defect, the colour map of the encoded scan can be used. As the scanning rig is moved axially along the pipe, the transmitting probe is excited and guided waves generated that propagate circumferentially around the pipe. The encoder is set to record a time record every 1 mm step along the pipe length. A colour map of the amplitude of the received signal at each distance step is generated, building up an image of how the signals travelling around the circumference behave. A range of different representations of the data are possible, but the most appropriate way to highlight the different modes in the signals is to use the absolute value of the time record. An encoded scan is presented

in Figure 5.12 for the sample considered previously, with a centre frequency of 386 kHz and tight bandpass filters applied around the excitation frequency of 326 kHz to 486 kHz, with the different modes labelled.

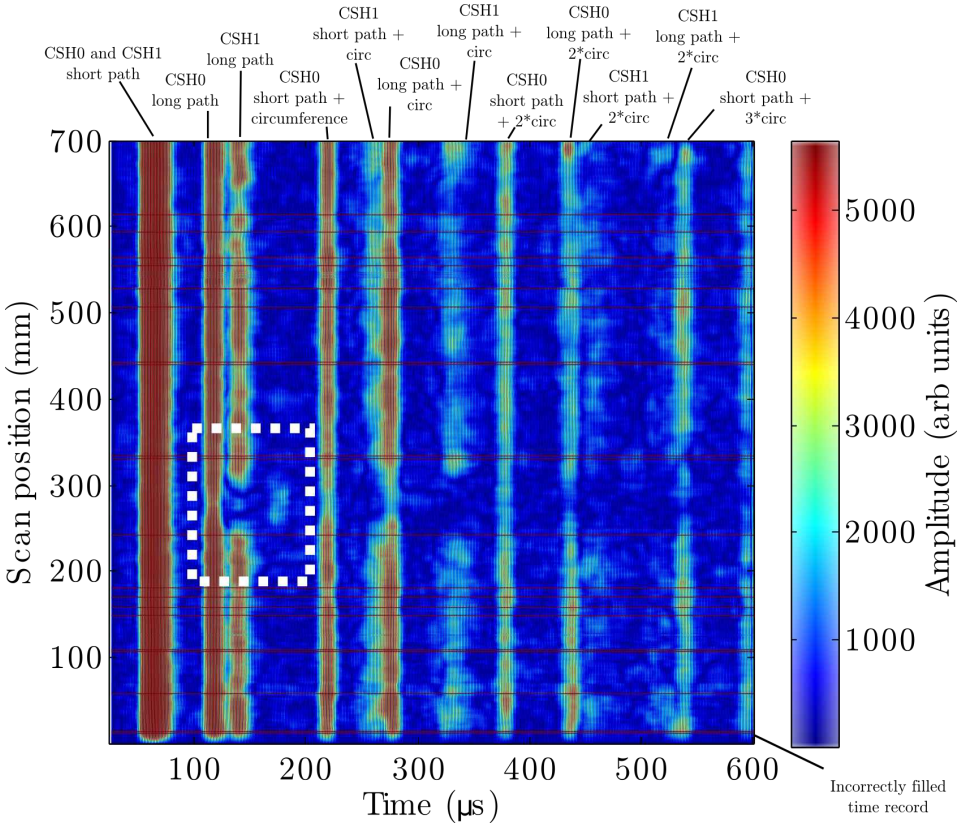

Figure 5.12: Encoded scan of the pipe sample with a single wall thinning defect, with the different modes labelled and the defect area highlighted

The different modes in the signal can be highlighted as in Figure 5.12 and the presence of any defect in the sample identified by the difference of the amplitude or arrival time of the CSH1 mode compared to the clear areas. This is shown with the defect area bounded by the white box. The colour map can be made more relevant to the received signal by gating out the initial signal of the transducer, as has been done in the scans presented here. This ensures that only the propagating modes contribute to the colour scale so that the amplitude levels are more relevant.

When viewing the encoded scan, the presence of defects becomes clear, but what happens to the energy of the CSH1 mode that doesn't arrive at the expected time is less clear. This is partly because the received modes in the clear area dominate the colour map, such that further processing of the signals is required in order to locate the different signals that are generated by the mode's interaction

with a defect. The amplitude of the wave will also decrease with distance travelled (in this case with greater number of loops around the pipe). This is due to material attenuation, which makes it more difficult to see the 'extra' signals that are of lower amplitude to the largely unaffected signals such as the CSH0 modes. The improvement of the appearance of the encoded scan will be shown later in section 5.4.7.

A further obstacle for viewing the encoded scan is the presence of time records that haven't recorded data due to the encoder not recording a value as it moves more than one increment at once. This can either be ignored if the records are not in a critical position or fixed in the processing of the scan by making the record an average of the data to either side. It can however pose a problem if the surface is rough, as it may be difficult to run the scanning rig along the pipeline smoothly, In these cases the surface roughness may be abruptly overcome, with the rig then moving further than expected, such that the encoder doesn't record a value for a particular distance step. The solution to this being to perform an initial scan to locate the defect area then a scan of smaller axial extent at this area to ensure the recording of all time histories.

An axial scan with this smaller axial extent centred around the defect position is shown in Figure 5.13 with the defect area highlighted again, the modes are as labelled in Figure 5.12.

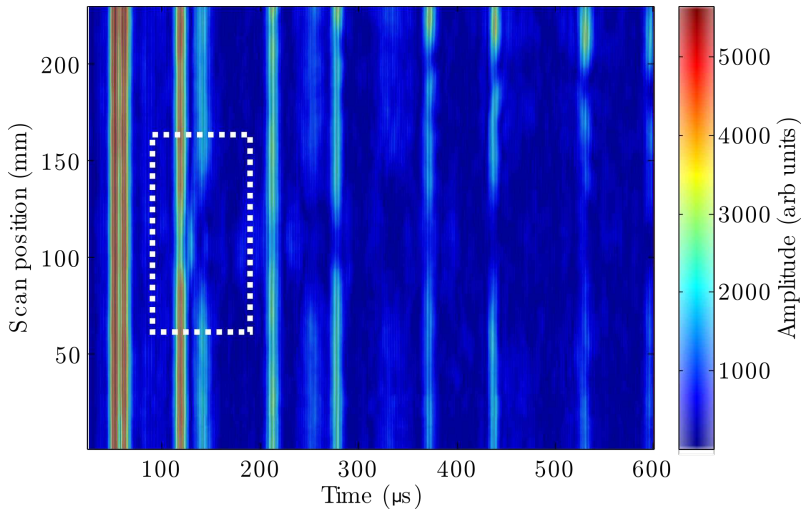

Figure 5.13: Encoded scan of the pipe sample with a single wall thinning defect. The position of the defect is highlighted by the white dotted box. At this position the CSH1 mode is much different to the mode seen in the rest of the axial length of the sample. A small disruption to the modes is also seen above 200 mm in the scan, which may be to small internal defects in this sample that weren't mapped.

The encoded scans presented previously have been for the excitation signal frequency centred at 386 kHz for the full axial length and 380 kHz for the smaller axial extent, with this change in frequency to better suit the peak frequency of the received CSH0 modes. The scans can also be carried out at a higher frequency to match the CSH1 mode frequency, which will see a change in the energy in the signal to be more concentrated in the CSH1 modes.

However, much of the other behaviour of the signals should be the same due to the bandwidth of both of these excitation signals being sufficient to excite both the CSH0 and the CSH1 modes in the sample. The encoded scan for the higher frequency, showing the shift of energy into the CSH1 mode is shown in Figure 5.14. Here the CSH0 mode shows a more similar amplitude to the CSH1 mode and the mode converted waveform in the defect area becomes clearer due to the greater proportion of energy that is put into this mode. The modes are as labelled in Figure 5.12.

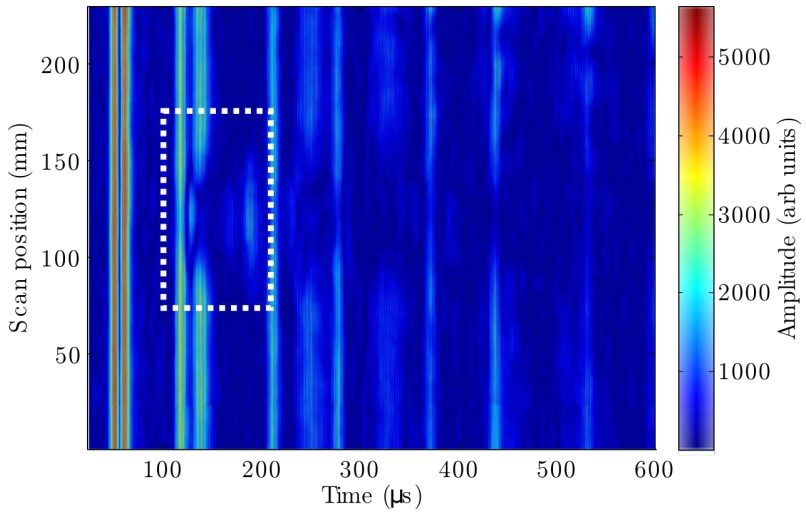

Figure 5.14: Encoded scan of the pipe sample at 420 kHz (in order to concentrate more of the wave energy in the CSH1 mode.) with a single wall thinning defect. The defect is again highlighted by the white dotted box.

5.4.6 Axial sizing of defects

The encoded scans of the pipe sample can be used to show the presence of a defect, but further processing of the data is required in order to extract sizing data for the defect. From the colour maps of the encoded scans of the sample, the clear areas of the pipe can be identified by the constant wave velocity and amplitude of both the CSH0 and CSH1 modes. If these values are constant throughout the length of the sample then it can be said to be defect free in terms of the corrosion patch style defects that the system here is designed to locate.

As shown in the encoded scans, the most convenient way of locating whether a defect is present in the sample is to look for an area where the amplitude and arrival time of the CSH1 mode differs from its normal value. The mode that is affected by the defect can be extracted from the rest of the signal using time gating. This allows the affected signal to be considered separately for all of the axial distance steps, as shown in Figure 5.15.

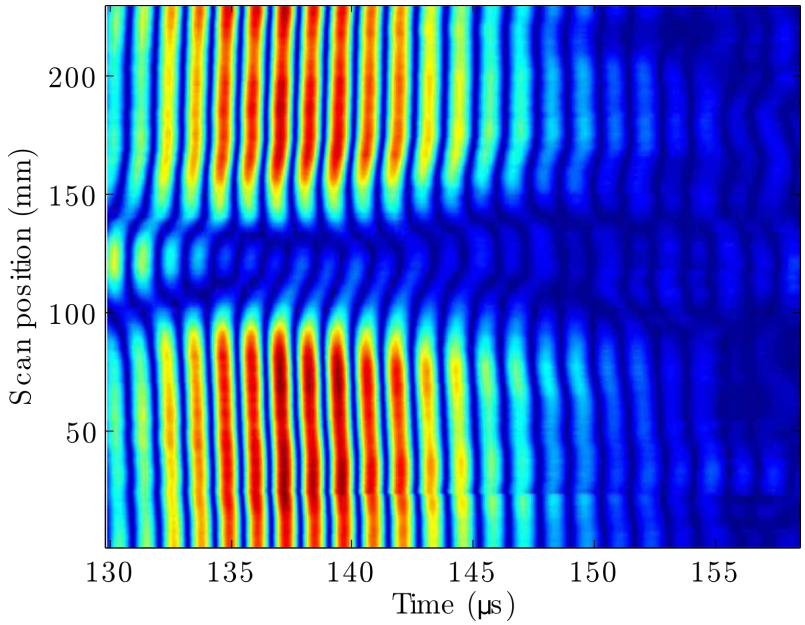

Figure 5.15: Presentation of just the long path CSH1 mode section from the encoded scan, showing the mode at all distance points. Here the change in amplitude at the defect becomes more obvious.

The reduced time signal here for all distance steps can be manipulated to present the relative amplitude of the mode at each distance step by calculating the Root Mean Squared level (RMS) of the waveform. This is the value of the square root of the average of the squares of the waveform values:

$$X_{RMS} = \sqrt{\frac{1}{N}\sum_{n=1}^{N}|X_n|^2} \tag{5.2}$$

This yields an RMS value for every distance step in the scan, which effectively generates an amplitude profile of the CSH1 mode for each distance point in the axial scan.

Changes in the amplitude of the CSH1 mode will indicate that a defect is present that has redistributed the CSH1 mode energy, due to the mode interacting with the defect. This will manifest as a drop in amplitude of the CSH1 mode as the probe is moved past the defect area. The change in amplitude of the CSH1 mode along the length of the sample will be a valid method of detecting the defect whether the remaining thickness is above or below the cut-off thickness of the sample due to the difference that will be seen in the selected time gate. The raw amplitude profile from this data can be presented as in Figure 5.16, highlighting the axial size and position of the defect.

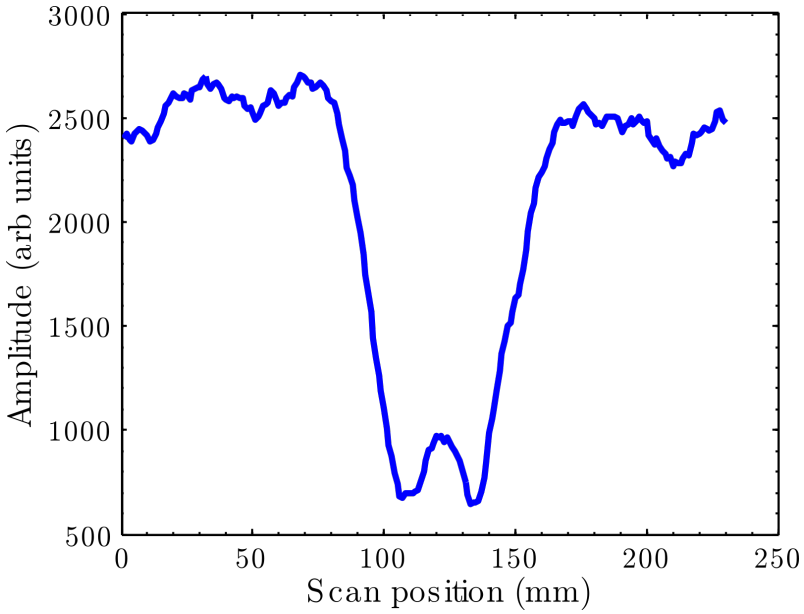

Figure 5.16: Amplitude profile of the long path CSH1 mode through the axial length of the pipe, showing a decrease in amplitude as the probes pass the axial position of the defect.

Taking into account the width of the transducer in the axial direction, the length of the defect in the axial direction can be calculated. If a single defect is assumed in the pipe then this process can be carried out with minimal user input. This is achieved by normalising the value of the RMS at each axial point to a baseline

value by taking an average of a section that is assumed to be defect free. The minima of the profile along the length of the pipe can then be found, which will correspond to a point where the path of the ultrasound is centred over the defect so that the guided wave energy is unable to travel around the pipe without interacting with the defect. The value of the amplitude at a point is then compared to the average value of the non defective area and when the value reaches this average value the full extent of the defect's effect on the signal is acquired.

Subtracting the active area of the transducer from this defect extent then gives the axial length of the defect. This is an effective method for finding the axial extent of a single defect in the sample, as the minima of the profile will be easy to find, with the amplitude of the profile returning to the average value as the probe passes out of the defect area. The procedure would become more complex for multiple defects in the sample axially due to the presence of several minima, with the accuracy of the measurement of the axial extent likely to decrease if the defects are close together axially. If the defects are close to each other axially, then the amplitude profile would not be able to return to its maximum value after passing over the first defect due to the signal still being affected by the other defect, which would complicate the extraction of information from the profile, the effect of this is illustrated in more detail in Chapter 6.

The furthest extent of the defect effect is shown in Figure 5.17, with the full extent of the defect being this value minus the active area of the transducer, giving an approximate axial extent of (47 $\pm$ 1)mm. This is in reasonable agreement with the measured value of (48.6 $\pm$ 0.1)mm.

This technique can be applied for either the long path signals or the short path signals, depending on where the defects are expected to lie around the circumference. The mode that is affected can be found from the colour map, allowing the relevant area of the signal to be gated out of the full signal for further consideration. If this information is not known, both can be tested to check for the presence of defects in the signal. The use of the quantitative A-scan data rather than relying on the qualitative appearance of the encoded scan is important, as the appearance of the defect in the colour map is likely to be different than the actual data due to the limited number of colour levels in the map. However, when the defects are very shallow (below 10%) or have a small circumferential extent, a combination of the two methods may be necessary as the drop in amplitude for the CSH1 mode may be minimal as the mode will be only affected by a slowing of the wave in the case of the CSH1 mode so the energy will still be contained in the window. The minimum detectable defect will be considered in Chapter 6.

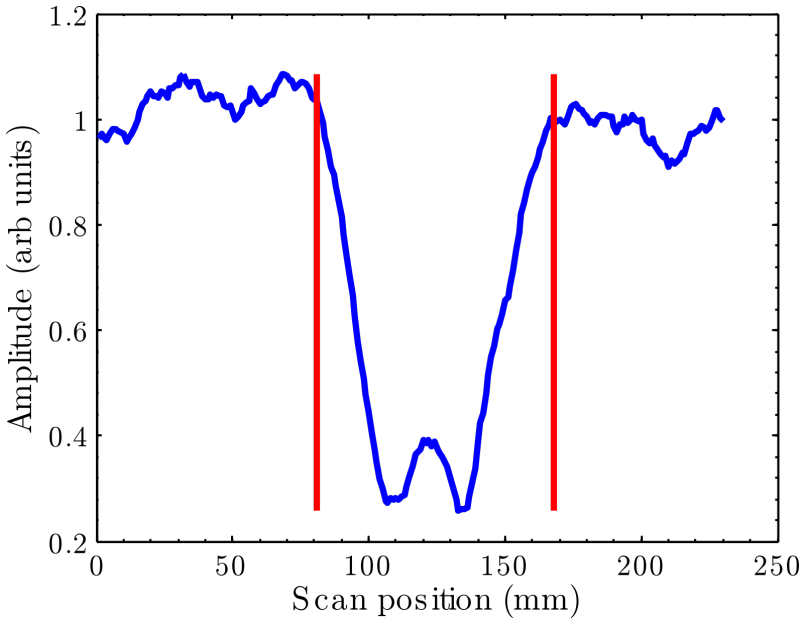

Figure 5.17: Amplitude profile of the long path CSH1 mode through the axial length of the pipe, normalised to an average value of the defect free section of pipe, with the outer extent of the defect's effect shown by the red lines.

5.4.7 Presentation of encoded scans

When the CSH1 mode interacts with the defect as is seen in the encoded scans, the amplitude of the waveform at the expected time of arrival decreases. This decrease in amplitude means that the energy is redistributed throughout the sample via processes such as reflection, mode conversion and scattering.

In the case of the defect presented here, where the edges of the defect are uniform, the amount of scattering should be minimal. This should mean that the receiver is able to detect the reflections from the defect at the point where the boundary conditions change due to the thinning of the sample, in the tapered defect case here, that is not necessarily the start of the defect but depends on the thickness at each point. This can be seen in the individual time records, but is less obvious in the encoded scans of the data due to all of the data being on the same colour scale. This results in the lower amplitude signals, such as reflections or waveforms that have travelled a further distance being more difficult to see due to their amplitude relative to the other modes.

In order to provide a colour map that allows all the different waveforms to be visible in a single figure, the amplitude values can be manipulated. The encoded scan is split into different sections along the time axis, with a high amplitude CSH0 mode

included in each section. The rest of the data in the section is then normalised to the maximum value of the CSH0 mode, such that the other waveforms in the section have an amplitude that is more visible within the colour map. This representation can be made clearer if a low level of smoothing is applied to highlight the areas of coherent signal. This is a very useful method for improving the visibility of the different waveforms in the signal but means that the different sections of the signal can only be compared relative to the amplitude of each maxima, as the absolute amplitude information is lost. However, the raw data can still be retained and the new colour map used to locate the areas in which the different signals are seen in order to select these time records for further analysis. An example of this processing of the image data is shown in Figure 5.18, where the extra signals that were not visible in the original scan because of their lower amplitudes are visible in the processed scan.

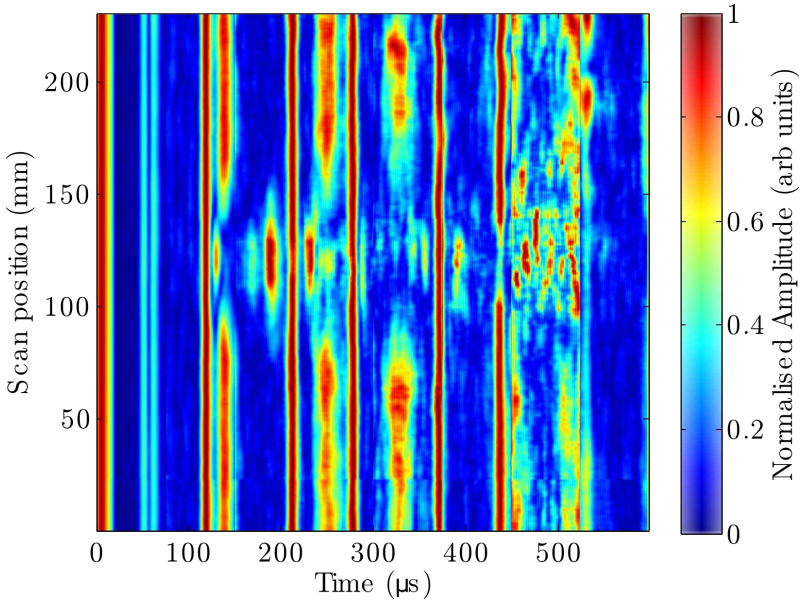

Figure 5.18: Adjusted colour map of the sample around the defect area showing the wave modes that become more obvious when the colour scale is manipulated.

This is a useful precursor to extracting more information from the extra signals that occur when the ultrasound that is generated in the pipe interacts with a defect. It works especially well in this case because the sides of the defect are uniformly straight such that most of any energy reflected from the defect will travel directly around the pipe and be received by the receive transducer. This allows for the reflected energy to be recorded by the transducer and the positioning of these signals to be used to define where the defect lies circumferentially.

5.4.8 Reflections and mode conversion

With a defect structure that generates coherent reflections from the defect, the circumferential positioning of the defect area can be approximated. It has been mentioned previously that the position of the defect in the short or long path between the transducers determines which portions of the received signal are affected by the presence of the defect, but information can also be extracted from any reflections seen. With the defect centred at the base of the pipe and the transducers saddling the top of the pipe centred at the 12 o'clock position, the reflected energy from the defect will arrive after the signal that represents the modes travelling the long path between the transducers. This is because the total distance travelled by the reflected waves in this case is greater than the long path distance between the signals. Due to a proportion of both the CSH0 and CSH1 modes being reflected, two waveforms should be generated, but due to the distances between the defect and probes, the clockwise and anticlockwise modes should coincide.

If the defect is between the transducers at the top of the pipe, then the reflected signals would be seen after the long path signal, but the effect on the modes would be observed in the short path. Again as long as the defect is centred at the top of the pipe and the transducers are equally spaced away from its edges then the reflections travelling clockwise and anticlockwise should arrive at approximately the same time. Changes to the arrival time of reflections that travel in different directions around the pipe would be introduced if the defect has a different depth profile at each edge.

If the defect is at another position on the pipe such as the 3 or 9 o'clock positions, then the reflected signal will occur between the short and long path signals. This can be used to further characterise where a defect lies circumferentially on a pipe sample, whilst maintaining the information that is provided by the wave that propagates through the defect area. It would not necessarily give any indication as to which side of the pipe the defect is on due to the travel distance for the reflected waves in these two cases being equal. However, if the dimensions of the sample are well known, the arrival time of the reflections at different times for each position could give an approximate position of the defect.

The sample used here is free standing, such that it can be rotated to have the defect at any of these positions, so the effect of having a defect at different positions around the pipe circumference can be investigated. The change of time of arrival of the reflected signals can then be used to show this circumferential positioning capability of the system.

In the case of the transducers saddling the top of the pipe and the defect

being centred at the base of the pipe at the 6 o'clock position as shown in Figure 5.19, the different modes can be identified.

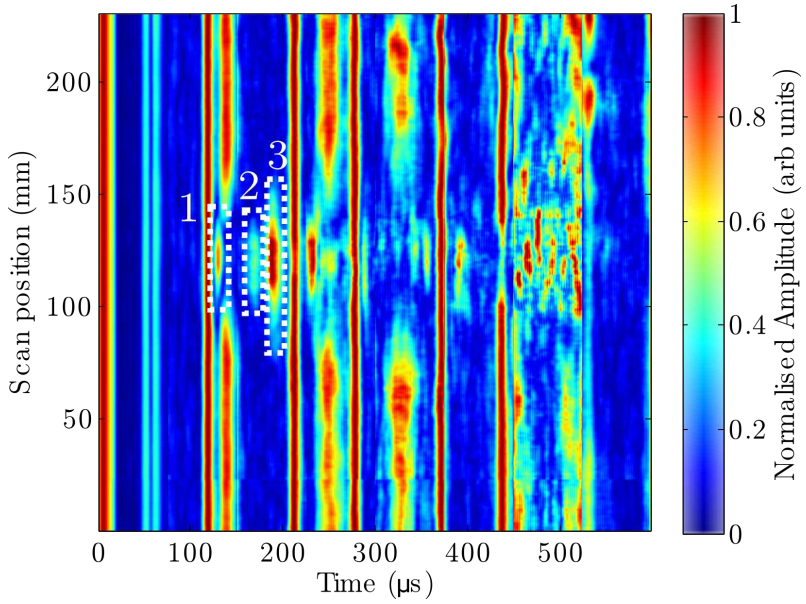

Figure 5.19: Adjusted colour map of the sample around the defect area for a defect at the base of the pipeline, showing the new waveforms that become more obvious when the colour scale is manipulated. These defects are labelled 1,2 and 3 corresponding to the mode converted CSH1 mode, reflected CSH0 mode and reflected CSH1 mode respectively.

Here a mode converted wave mode is seen at the position labelled 1, instead of the CSH1 mode, because the remaining thickness of the sample in the defect area is less than the cut-off thickness. This results in the CSH1 mode travelling towards the defect, mode converting to the CSH0 mode at the defect area in order to propagate through the defect area and then mode converting back to the CSH1 mode as the full thickness of the sample is regained after the defect.

Portions of the CSH0 and CSH1 signals that are reflected from the defect edge are seen at positions 2 and 3 respectively. These are portions of the signal that have reached the defect and reflected back due to the change of boundary conditions for the wave. They travel back in the direction they came from, being detected at the receiver. This can be observed in the raw data if the A-scan data from the centre of the defect is selected from the distance steps as in Figure 5.20b, the signals due to interaction with a defect can be seen labelled 1,2 and 3 as in Figure 5.19, with the respective travel paths shown in Figure 5.20a.

If the different wave modes were to travel as a beam directly to the defect, then the through propagating signals at the defect would not change if the defect

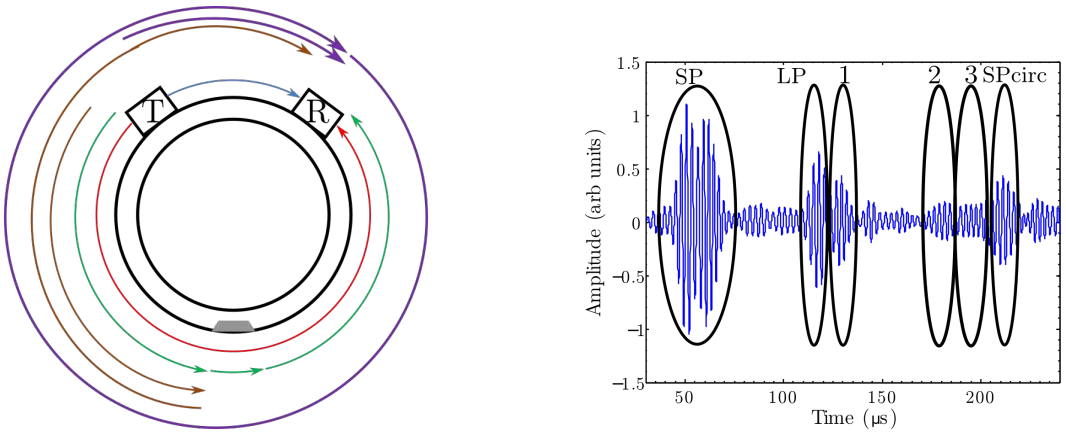

(a) (b)

Figure 5.20: A-scan output from experimental scans, with the associated paths of the different signals. a) Schematic showing the paths the guided waves can take around the pipe circumference through the defect and after reflecting off of the defect (shown in grey). b) The associated A-scan signal from the centre of the defect area in the axial scan. The different modes are highlighted and labelled, with the mode at SP the short path CSH0 and CSH1 signal (blue in schematic), LP the long path CSH0 signal (red), 1 a signal generated from the original CSH1 signal mode converting to CSH0 under the defect and back again at the other side of the defect (green), 2 and 3 reflections of the CSH0 and CSH1 modes from the defect edge (brown) and SPcirc the CSH0 mode that has travelled the short path plus a circumference (purple).

was at a different circumferential position. This is because the times at which these modes are detected depends not on the position of the defect, but the separation of the probes on the pipe surface. As long as the short and long path travel distance was kept constant, the arrival times of the through propagating modes should be constant. In a real three-dimensional situation however, there will be beam divergence as the waves propagate away from the transducer and attenuation of the wave modes as they travel a longer distance to the defect. This will result in a change in the received signal as a different proportion of the wave energy will be able to interact with the defect depending on how far away the defect is from the transmit transducer.

Changing the position of the defect relative to the probes in the long path will also affect any reflections from defect that are seen, by changing the distance that the reflections have to travel before they are detected. The same treatment of the results as in Figure 5.19 is shown here for a change of the orientation of the defect circumferentially compared to the probe position. The results for having the defect at the 3, 9 and 12 o'clock positions on the pipe are shown in Figure 5.21,

with the corresponding effect on the reflected waveforms shown.

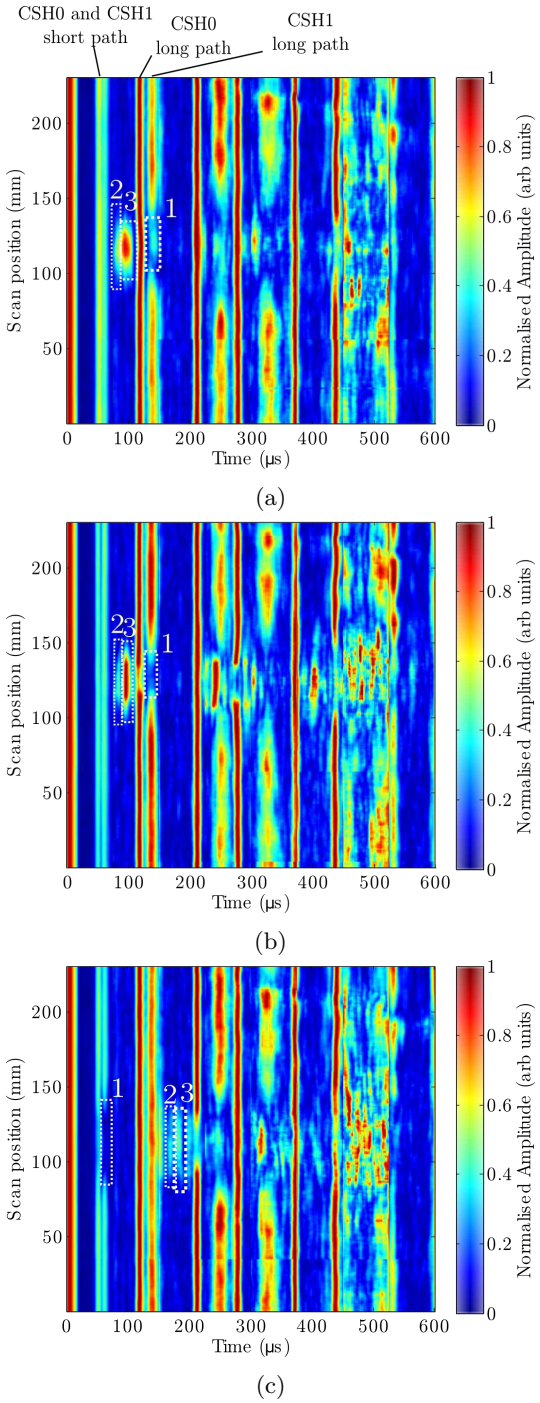

Figure 5.21: Axial scans of the sample with the defect positioned at the 3, 9 and 12 o'clock positions in (a), (b), and (c) respectively. Mode conversion of the CSH1 mode is highlighted at 1, with the reflected CSH0 mode shown at 2 and the reflected CSH1 mode at 3. The modes are labelled in a), with the same applying for all figures.

It has therefore been illustrated that the axial length of the defect can be found by monitoring the amplitude of the CSH1 mode and that the circumferential positioning of a defect can be characterised by the mode which it affects and the reflections that it generates. In order to confirm the nature of the different waveforms in the received signal and in particular what happens to these modes when they interact with a defect, finite element modelling can be carried out.

5.5 Finite element modelling of the artificial defect

It should be possible to construct a valid finite element model for this sample, given that the dimensions of the sample and defect are well known. Using the finite element theory set out in Chapter 4, a model can be constructed with an excitation and reception mechanism that represents the structure and operation of the EMAT probe used in experiment.

The use of finite element modelling here will allow the different modes in the sample to be visualised graphically and provide the A-scan data that is seen in experiment in order to confirm the behaviour of the different guided wave modes as they interact with a defect. Generating a model that correlates well with the experimental data for the non defective area of pipe and generating a defect profile that gives a received signal that matches well with the recorded data will allow the simulation to be validated as a tool for predicting the behaviour of the different modes as they are incident on a defect.

The model can then be used for more complex defect profiles and different depths of defect. This will allow the interaction of the waves with the defect to be estimated without having the range of defects available for testing experimentally, allowing for a more thorough analysis of the method with sample models of exact parameters.

A two dimensional model was constructed in PZFlex showing the circumference of the sample. Since the predominant aspect of interest in this case is the guided wave interaction with defects when travelling in the circumferential direction around the pipe, the axial extent of the sample is neglected apart from a one element section onto which the shearing forces can be applied. This is achieved using a function in the program that is specifically designed to allow for the creation of SH waves in the two dimensional model without having to introduce a third dimension. Using the program to generate and deal with the arbitrary length in the axial direction of the pipe eliminates any extra signals that might occur due to the introduction of an arbitrary extent by the user. The ability to essentially treat the situation as

a two dimensional problem is important, as it cuts down the computational load of the model without invalidating any of the physics of the model.

The model is constructed to be the same dimensions as the experimental sample, with a 7 mm thick pipe wall and the same outer radius, with the material properties of a steel pipe. The excitation profile is set as a series of pressure loads on the outer radius with a profile that represents the 8.8 mm nominal wavelength transducer. This is calculated using the techniques discussed in Chapter 4, where the force profile of the transducer is mapped onto the surface of the model. The data is then extracted from the equivalent surface extent at the receiver position, modulated by the transducer profile again and averaged to represent the signal that would be recorded from the probes in experiment.

The signal that is obtained from the model without a defect is comparable to the clear area signals obtained from the experimental system. Similarly, the defect signals for the model are comparable to the areas of the scan where the probe is directly above the defect axially, such that no energy from the waves is able to travel around the defect. The scans that are obtained in the simulation will have an arbitrary amplitude such that they cannot be directly compared to the experimental data in terms of amplitude, but the relative amplitude of the different modes in the experimental and simulated signals should be generally comparable. The two dimensional nature of the model will mean that all the signal is retained in the model situation. This is different to the experimental situation where signal energy can be lost in several ways including reflections occurring at angles that do not return the signal to the receiver position and other phenomena such as scattering from the non-uniform shape of the defect, as well as diffraction of the ultrasonic beam meaning that not all of the transmitted energy reaches the defect.

Another point of note for the simulation is that the effect of material attenuation has been neglected such that the amplitude of the different modes does not decrease with distance due to the material. This was chosen to restrict the changes in the simulated signal amplitude to the changes in the signal from phenomena such as dispersion of the signal and in order to remove any uncertainties in the simulation generated by frequency dependent damping.

A 5 cycle tone burst that is modulated by the spatial profile of the transducer is input at the appropriate element faces at a frequency that matches that used in experiment, with the peak frequency of the excitation signals here being 386 kHz. The transducers are set at a spacing of 170 mm short path distance along the outer circumference of the sample. The modelling of the transducers and samples in this way should give scan data that is representative of the experimental data with an

improvement in the knowledge of the dimensions in that they are known exactly in the simulation data. It will also have the added benefit of the ability to visualise the modes as they propagate around the circumference of the sample if the velocity in the axial direction of the sample is plotted.

The 5 cycle tone burst was used in the simulation to compare against the initial measurement that used a 5 cycle tone burst experimentally. This signal was chosen for comparison as the probe separation on the surface was measured exactly in this case and so was deemed the best result to set up the simulation to represent. A measurement with the 3 cycle tone burst was also carried out, but the separation of the probes wasn't identified as consistently, leading to a drift in arrival times due to different travel distances. Therefore the data from the 5 cycle case is considered here with the experimental and simulated waveforms compared in Figure 5.22 but the same will be applicable for the three cycle case.

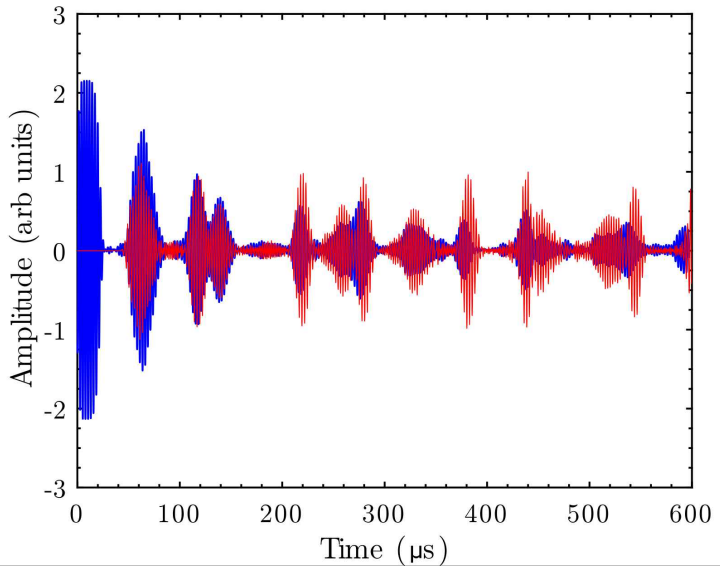

Figure 5.22: A-scan data from the experiment in blue and the simulation in red of the non defective area of the sample showing the good correlation between the arrival times and relative amplitudes of the modes. The amplitudes cannot be directly compared between the two and the amplitude of the simulation data has been scaled to show on the same scale as the experimental data.

The data from the simulation can be seen to match well with the experimental data gained from the encoded scan, with the different waveforms in the data correlating to the waves seen in Figure 5.9. The main difference that is seen here is a slight change in arrival time of the modes from the simulated to the experimental data, this could be due to the accuracy of the nominal wavelength that is generated

in the sample and the circumferential distance that the mode travels being slightly different. However, the general behaviour of the modes including the relative amplitudes appears to correlate well and the speed for travelling a full circumference of the sample as discussed earlier matches well between the two cases and to theory, with the simulated waves travelling at a group speed of 3347 m/s for the cross correlation method and 3356 m/s for the peak of the envelope values method. This confirmation of the behaviour of the simulation without a defect present will allow the simulation to be adapted to have a defect present, in order to confirm the behaviour of the mode at the defect area.

The other benefit of the simulation as mentioned, is that the different modes can be visualised in the scan. A basic example of this is shown where the amplitude of the velocity can be approximated to the shearing forces through the thickness; first for a single transducer at the top of the pipe as the wave is being established in Figure 5.23 and then for the different modes as they propagate around the pipe circumference as seen in Figure 5.24.

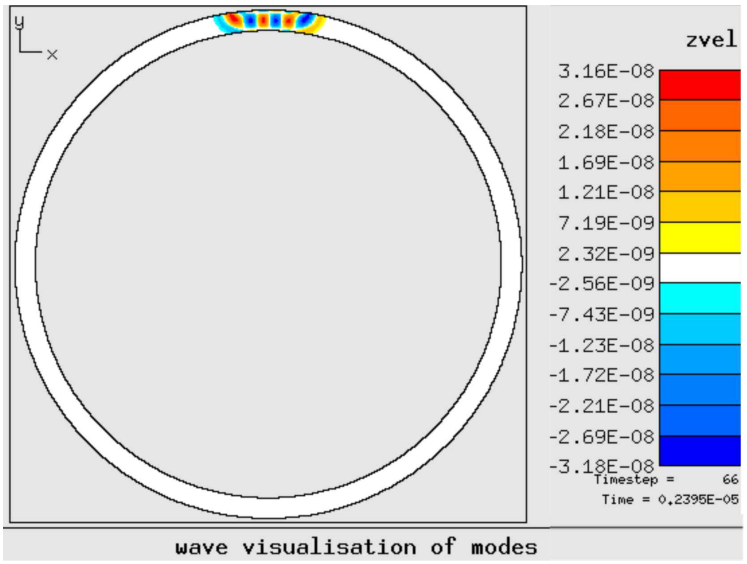

Figure 5.23: The in-plane velocity generated by the transducer in the simulation a short time after starting the excitation, with the waves not yet established.

By plotting the velocity of the mode into the plane of the sample, an approximation to the relative amplitude of the shear wave displacements through the thickness is achieved, allowing the differentiation between the modes seen. This is possible, as the displacement profiles through the thickness of the sample will match the theoretical displacement profiles as seen in Chapter 2. In summary these are: a constant displacement through the sample for the CSH0 mode, a maxima at the

top and bottom surfaces with opposite sign for the CSH1 mode, with zero displacement in the centre of the sample and maxima at the top and bottom surfaces of the sample with the same sign for the SH2 mode.

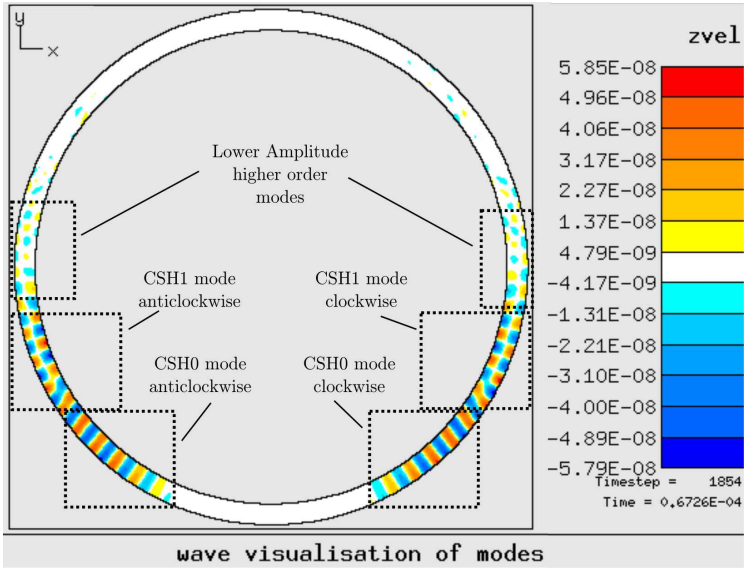

Figure 5.24: The in-plane velocity of the waves once an amount of time has passed, with the different wave modes established and travelling circumferentially in both directions around the pipe structure. The different modes can be differentiated from each other by their profiles through the thickness of the sample.

This tracking of the modes at each point allows the reflection and mode conversion behaviour to be visualised at the defect area. Here for simplicity the transducer is placed at the top of the pipe such that the propagation in both directions around the pipe is symmetrical around the mid-point. This is altered for the A-scan data acquired where the transmitting probe is placed at a position such as would be seen in the experimental system.

With the experimental measurements, the dimensions of the pipe sample are able to be measured and the simulation can be generated to closely represent the non defective area situation. However, the defect structure in terms of the shape and profile of the defect, the depth through the defect and degree of roughness of the defect circumferentially is not well defined in the experimental case. Although the defect is artificial and designed as a wall thinning patch that removes material to make the nominal depth below the cut-off thickness of the CSH1 mode, the specific structure is unknown.

In order to model the defect appropriately therefore, assumptions need to be made about the structure of the defect. An assessment was carried out on different

defect geometries, taking into account calibration style defects such as flat bottomed holes and constant depth defects in a pipe (the two are not equivalent in a pipe as they would be in a plate) and more representative corrosion patches.

The modelling carried in this study involved the generation of defects of the same circumferential extent as the artificial manufactured defect in the experiments, but with a different structure, which affects the results that are obtained. Modelling of the calibration style defects is presented in Chapter 6, but the abrupt nature of the beginning and end of the defect circumferentially means that a greater proportion of energy from the different modes is reflected from the edges of the defect than would be seen in a real corrosion patch. This is because the thickness of the sample goes from full thickness to a large depth of defect almost immediately which causes a greater degree of reflection.

By contrast, the defects used for modelling in this Chapter had a more representative structure to that of a corrosion patch style defect by tapering the thickness down from the full thickness of the sample to a minimum value before tapering up to the full thickness of the sample again as the end of the defect is encountered. The effect of this is that the change of depth is more gradual, which allows for more of the higher order modes energy to be transmitted through the defect. This is because the tapering of the plate allows for the frequency-thickness product of the defect area to reduce to its minimum value for the CSH1 mode before it mode converts to the CSH0 mode under the defect. If this change from the full thickness to the cut-off thickness is abrupt, then a greater degree of reflection of the mode occurs. The slope of the tapering area also defines the arrival time of the received modes since it determines how long the CSH1 mode spends at the lower velocity as the defect develops and the higher CSH0 velocity in the mode conversion area under the deepest section of the defect. It has a similar effect on the arrival time of the reflected signals, as the modes can travel into the defect area before being reflected when the remaining thickness approaches the cut-off thickness.

A range of different tapering angles for the defect were assessed in the model, with the most appropriate angle to represent the experimental data chosen. In this case that is a slope of ten degrees to the horizontal for the defect modelled here, with a circumferential extent of 44.2 mm and a maximum defect depth of 4.8 mm out of an original 7 mm wall thickness. This defect structure gives a relatively long length of the defect where it is tapering down to its maximum depth. The structure of the defect can be seen in Figure 5.25a, with the depth of the defect plotted in Figure 5.25b to show the depth profile and allow the cut-off thickness to be seen so that the point at which modes will be reflected and mode converted can be found.

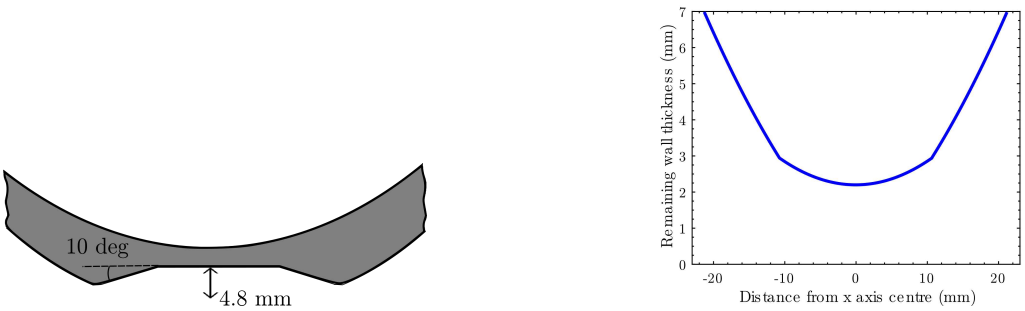

(a) (b)

Figure 5.25: Illustration of the structure and depth profile of the defect. a) Schematic showing the defect used in the simulation with the maximum depth and tapering angle of the defect labelled. The model continues to the full circumference of the pipe, but only the defect section is shown here. b) Plot of the depth profile of the defect.

The origin of different parts of the signal can be identified by matching the likely paths to the sections of simulated signal as in Figure 5.26.

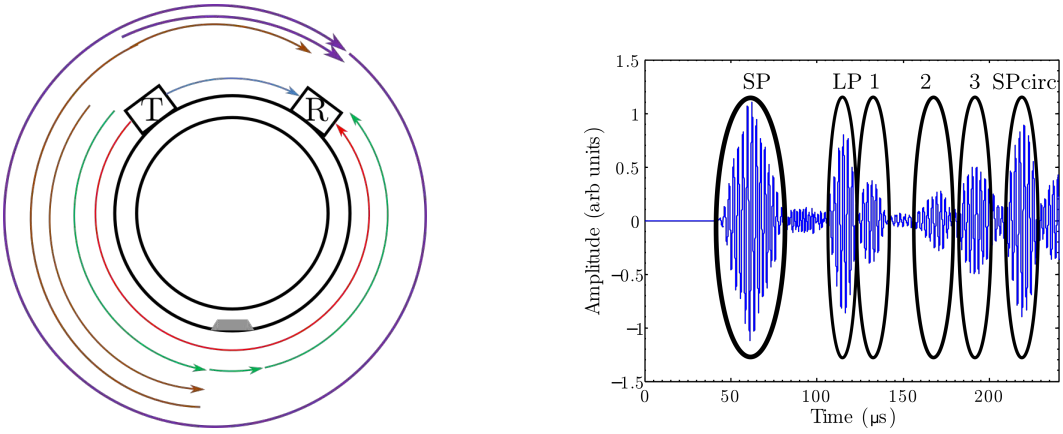

(a) (b)

Figure 5.26: A-scan output from the simulation, with the associated paths of the different signals. a) Schematic showing the paths the guided waves can take around the pipe circumference through the defect and after reflecting off of the defect (shown in grey). b) The associated A-scan signal from the simulated defect data. The different modes are highlighted and labelled, with the mode at SP the short path CSH0 and CSH1 signal (blue in schematic), LP the long path CSH0 signal (red), 1 a signal generated from the original CSH1 signal mode converting to CSH0 under the defect and back again at the other side of the defect (green), 2 and 3 reflections of the CSH0 and CSH1 modes from the defect edge (brown) and SPcirc the CSH0 mode that has travelled the short path plus a circumference (purple).

It can be seen that the simulated signal exhibits the same behaviour as the experimental signal. The first signal received is the short path signal in which the two modes appear very close to each other labelled as SP in Figure 5.26b. This is followed by the long path CSH0 signal at LP and a mode converted signal at 1 where the CSH1 mode has travelled to the defect and mode converted to the CSH0 mode in order to propagate underneath it, with further mode conversion back to the CSH1 mode on the far side of the defect. Reflections of both the CSH0 and CSH1 modes are then seen at 2 and 3. These are signals that have travelled towards the defect and reflected from the part of the defect that has reached the cut-off thickness, to be detected later at the receiver. The CSH0 signal from travelling a full circumference and the short path separation is then shown at SPcirc.

This can be compared to the experimental signal by overlaying the simulated data onto the experimental data as in Figure 5.27, with the amplitude of the simulated data adjusted to fit the experimental signal amplitudes.

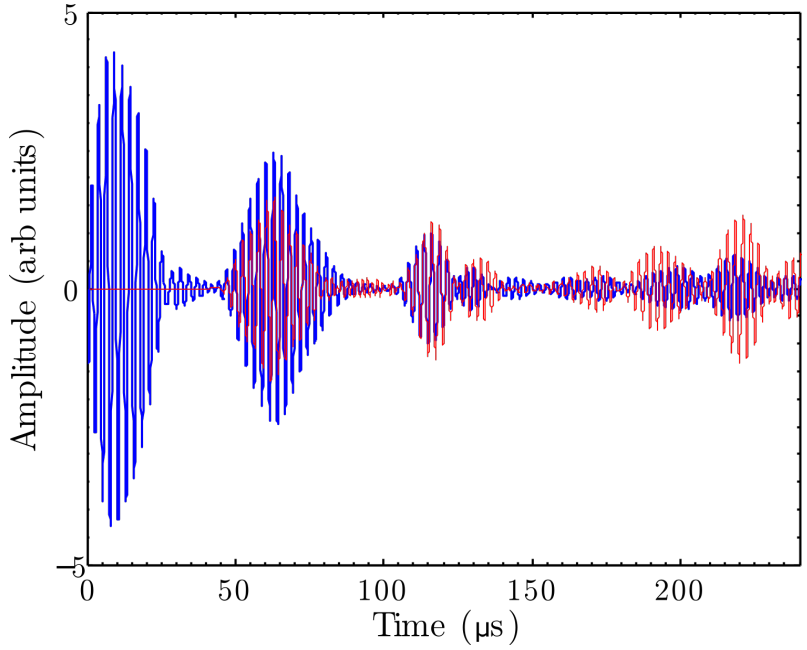

Figure 5.27: Simulated (red) and experimental (blue) data from a single wall thinning defect of maximum depth of 4.8 mm out of 7 mm. The behaviour of the two signals correlates well with only small deviations in arrival time due to the difference in the exact positioning of the probes on the pipe surface in the experimental scans.

The experimental and simulated data are found to be in good agreement in terms of the relative amplitudes of the different signals and arrival times of the different modes, with small discrepancies in arrival time due to the less exact spacing

of the probes in the experimental situation resulting in a slightly different travel distance between the two. This illustrates that the defect has been well modelled by the simulation in this case. Given this good agreement, the model could be altered to predict what would happen if it was a different depth or had a different circumferential extent and should be valid as the simulation is a good approximation to the experimental data.

5.5.1 Graphical representation of mode behaviour.

The physical behaviour of the waves in the sample can be confirmed by viewing the graphical representation of the wave propagation generated by the simulation. The modes are identified in the same fashion as previously, where the representation of the signals in the simulation is compared to the theoretical displacement profiles of the modes through the sample thickness. Here the propagation of the CSH0 mode can be seen in Figure 5.28a, with the transmission of the CSH0 mode through the defect, as well as the CSH1 mode approaching the edge of the defect seen in Figure 5.28b).

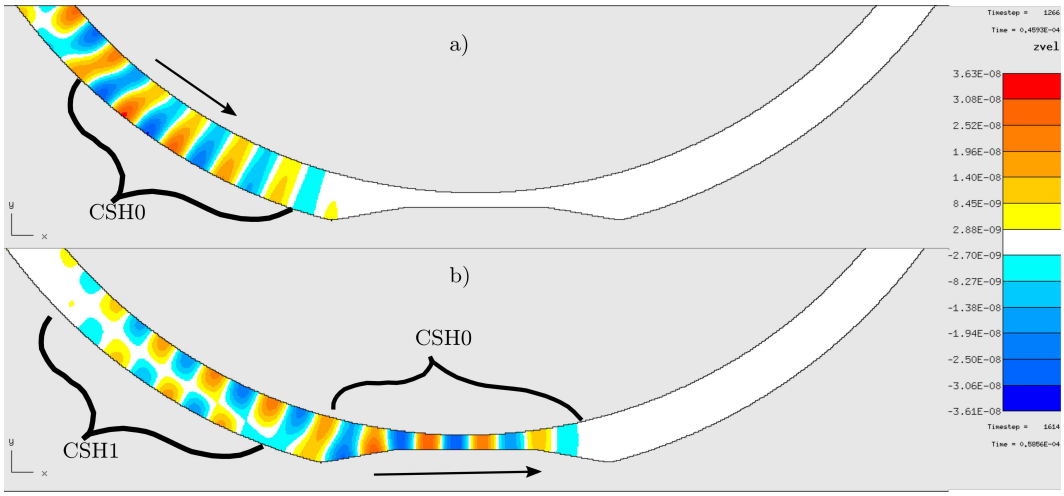

Figure 5.28: a)Wave propagation in the model at 46 μs showing the CSH0 mode approaching the defect area and b) Wave propagation in the model at 59 μs, showing the CSH0 mode transmitted through the defect area and the CSH1 mode approaching the defect.

The CSH0 mode is shown emerging from the defect in Figure 5.29a), with the CSH1 mode interacting with the edge of the defect, causing some of the energy of the CSH1 mode to reflect from the edge of the defect and some to propagate through the defect as a mode converted CSH0 mode. The position at which this behaviour begins to occur is also highlighted in Figure 5.29a). The image in Figure 5.29b

shows the CSH0 mode propagating away from the defect area, having propagated through the defect. The CSH1 mode can be seen mode converting in the defect area in order to propagate through the defect, with reflections of the CSH1 mode from the defect seen to move in the opposite direction around the pipe.

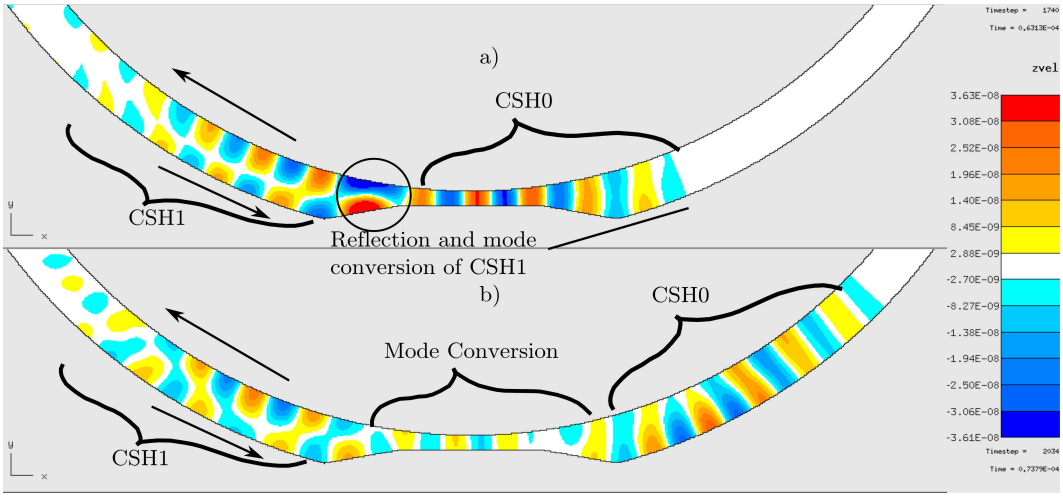

Figure 5.29: Wave propagation in the model at 63 μs, showing the CSH0 mode emerging from the defect area and the CSH1 mode encountering the defect, where some of the energy is reflected and some mode converted into the CSH0 mode as it travels through the defect area. b) Wave propagation in the model at 74 μs, showing the reflected CSH1 mode now travelling away from the defect in the direction it came and the rest of the signal mode converting underneath the defect.

The final images shown in Figure 5.30 show the behaviour after the CSH1 mode has interacted with the defect. Figure 5.30a) shows a snapshot where the CSH0 has propagated further around the pipe circumference, moving out of the image. The CSH1 mode is seen re-establishing itself after mode converting under the defect and the reflected CSH1 mode seen propagating further away from the defect area. The final image shown in Figure 5.30b) shows the reflected CSH1 mode moving further away from the defect along with some of the higher order CSH2 mode that is generated due to the different bandwidth of the signal in the simulation. The CSH0 mode that propagates in the opposite direction around the pipe structure is shown appearing in the image.

The graphical representation presented here has been for the case analogous to the experimental sample, with a remaining wall thickness below the cut-off thickness of the CSH1 mode. This results in the mode conversion of the CSH1 mode in the defect area, with this mode unable to propagate through the defect area. The same images can be generated for a defect that doesn't reach the cut-off thickness,

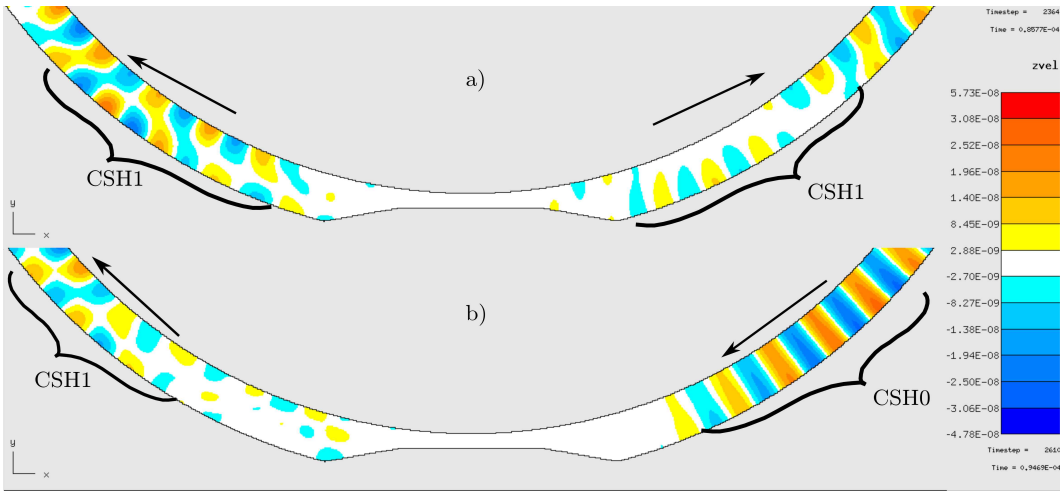

Figure 5.30: Wave propagation in the model at 86 μs, where the CSH1 signal has mode converted to travel through the defect and is now re-establishing itself on the far side of the defect area, with the reflected CSH1 mode moving further away from the defect. b) Wave propagation in the model at 95 μs, with the CSH0 mode travelling in the opposite direction around the pipe entering the graphics from the opposite direction.

where the CSH1 mode can be seen to be transmitting through the defect as the CSH1 mode instead of mode converting.

So in summary, the modelling of a sample with a defect carried out here produces accurate time records, which match the behaviour seen in the experimental case. The arrival times and relative amplitudes of the modes correlate well with the experimental data and the graphical representation of the modes allow for the visualisation of the physical processes that occur at each point. Given the good correlation between the two sets of data, the model can be extended to other situations for which the experimental data is not necessarily available.

5.5.2 Different defect depths.

In order to further investigate the defect effect on the ultrasonic signal, the depth of the defect can be adjusted. By keeping the circumferential extent of the defect constant and altering the minimum remaining thickness of the sample in the defect area, the effect of different defect depths on the signal can be examined.

A particularly useful feature here is the ability to examine the thickness range where the cut-off thickness is reached for a higher order mode in order to ascertain what happens at this point. As mentioned previously in this chapter, if the remaining thickness in the cut-off area is greater than the cut-off thickness, then

the CSH1 mode will be able to propagate through the defect area, but the speed at which it propagates will be lower than the speed at which the mode propagates in the area of full thickness. There will also be a greater range of speeds for the mode in the defect area due to the frequency range of the mode spanning more possible velocity values on the dispersion curves, due to the dispersive nature of the wave. In practice this means that the CSH1 mode will arrive later than expected and elongated in the time domain. As the defect becomes deeper, the amount of energy that is reflected at the edge of the defect will become greater, with a smaller proportion of the mode propagating through as the altered CSH1 mode.

A range of different defect depths were considered to assess the effect on the ultrasonic signals. The data shown previously was for the full depth of the defect in experiment of 4.8 mm depth out of a wall thickness of 7 mm. The frequency-thickness product of the excited frequency in the defect area is therefore around 0.9 MHz mm which is below the CSH1 frequency cut-off, which is at 1.62 MHz-mm. The maximum depth of the defect can then be altered to give an indication of what happens to the signal above and below the cut-off thickness of the CSH1 mode, whilst maintaining the general structure of the defect. The depth of defects considered are 2.9 mm, 3 mm, 3.5 mm and 4 mm deep defects in addition to the original defect depth. The first two of these depths generate a frequency-thickness product in the defect region above the cut-off thickness or near to the value, with the last three including the original depth showing what happens after the cut-off thickness is reached. These signals are shown in a STFT format to illustrate the arrival times and frequencies of the received modes.

The simulated data presented here therefore shows the difference between a measurement taken with the remaining wall thickness above and below the cut-off thickness of the CSH1 mode. These plots can explain how the remaining wall thickness in these samples can be estimated and all contain both the short path signal, the long path signals and at least the CSH0 mode that has travelled a distance of the short path plus a whole circumference of the sample. The graph in Figure 5.31a shows the simulation of a sample without a defect present, showing the short path at 1, the long path CSH0 at 2 and the long path CSH1 at 3, along with the signal that has travelled the short path plus a circumference at 4. Since there is no defect, the signals travel unimpeded around the pipe circumference, at the velocity set by the operation area on the dispersion curves.

The images in Figure 5.31b and Figure 5.31c then show the result of the scan when the remaining wall thickness is above the cut-off thickness of the CSH1 mode. These show the CSH1 mode arriving later, as the mode travels at a slower

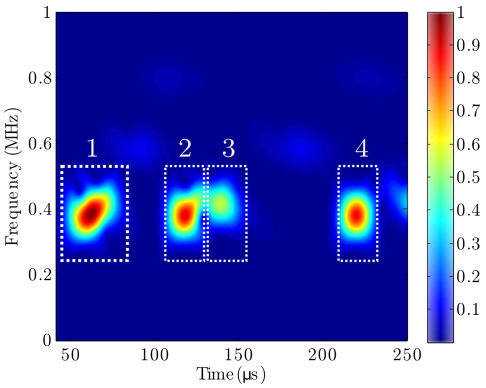

(a) STFT of the defect free simulation, with a wall thickness of 7 mm.

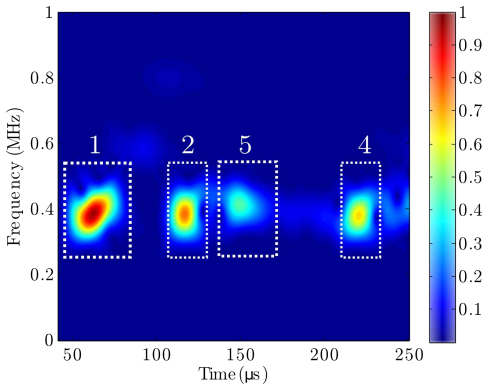

(b) STFT of a simulated defect of 2.9 mm depth out of 7 mm.

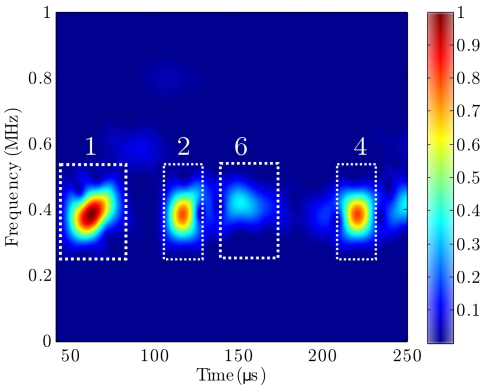

(c) STFT of a simulated defect of 3 mm depth out of 7 mm.

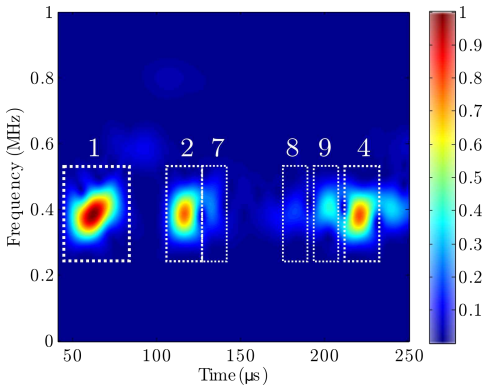

(d) STFT of a simulated defect of 3.5 mm depth out of 7 mm.

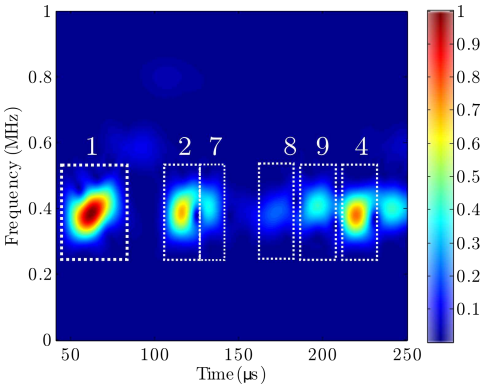

(e) STFT of a simulated defect of 4 mm depth out of 7 mm.

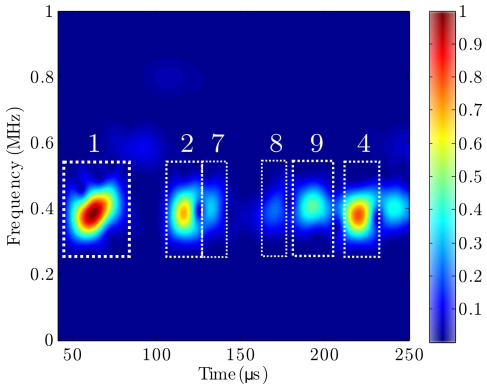

(f) STFT of a simulated defect of 4.8 mm depth out of 7 mm.

Figure 5.31: STFT data for defects of the same circumferential extent and profile but different maximum depths. Colour scale is the amplitude normalised to the maximum signal received.

velocity whilst in the defect region. As the depth of the defect deepens but remains above the cut-off thickness, the CSH1 mode (as labelled at 5 and 6) arrives later

and with a greater spread of velocities due to the operation area spanning more possible speeds in the more dispersive area of the mode. In contrast to this, once the thickness of the sample goes below the cut-off thickness of the CSH1 mode, the CSH1 mode can no longer propagate as this mode under the defect and is forced to mode convert to the CSH0 mode under the defect, before converting back to the CSH1 mode once the full thickness of the sample is regained. The mode converted waveform is illustrated in Figure 5.31d, Figure 5.31e and Figure 5.31f, labelled at 7 and shows an earlier arrival time than that of the pure CSH1 mode due to travelling as the faster CSH0 mode under the defect.

After the cut-off thickness is reached, the opportunity to gain more information on the depth of defect is minimal. As the depth of the defect goes below the cut-off, reflections can be seen arriving from the CSH0 mode and the CSH1 mode from near the defects edge. As the defects become deeper, the reflections will have an earlier arrival time, as the depth at which the mode conversion of the waves occurs will be earlier in the circumferential extent of the defect. The amplitude of the mode converted waveform will grow as the depth becomes deeper, as will the amplitude of the reflected CSH0 mode. This is because as the remaining wall thickness becomes less, the likelihood that some of the CSH0 energy will reflect, as opposed to travelling through the defect area increases.

The reflections labelled at 8 and 9 in the Figure 5.31d, Figure 5.31e and Figure 5.31f can be characterised as the CSH0 and CSH1 reflected waves respectively due to their different arrival times and frequencies. Given that in a real corrosion patch style defect, the reflections will not necessarily reflect directly back to the receiver due to scattering, the use of the different amplitude reflections would not necessarily be possible as a tool for assessing depth and or positioning of the defect in an actual corrosion patch measurement. This will be investigated further in Chapter 6 when real corrosion patches are considered.

In all of the above cases, Figure 5.31a to Figure 5.31f, the arrival time of the CSH0 mode that propagates through the defect also changes, here the pattern is consistent in that as the defect gets deeper, the arrival time of the CSH0 mode becomes earlier as the mode will travel faster in the area of the defect. However, due to the low level of dispersion of the mode, the change in arrival time for different depths is minimal.

In summary, the modelling of a defect with a range of different depths, both above and below the cut-off thickness of the CSH1 mode has been carried out and the difference in behaviour between the two cases illustrated, to show the ability to distinguish between different remaining wall thicknesses for the same structure

of defect. The complex nature of the defect has been shown by the variety of different thicknesses that will be presented to the through propagating guided wave mode, which will mean a range of different speeds are possible at each point in its propagation through the defect. The outcome of this is that the circumferential size and structure of the defect affects the speed of propagation of different modes and limits the opportunities for gaining more information about the remaining wall thickness, as the circumferential size and structure of the defect are unlikely to be known.

5.5.3 Different circumferential extent defects.

In order to expand this study, the other parameters of the corrosion patch can be adjusted. Modelling was carried out to examine the difference between the large circumferential size corrosion patch viewed up until this point and corrosion patches of different circumferential extent, using circumferential extents of 10, 20 and 30 mm. These different circumferential size defects were tested with a depth above and below the cut-off thickness of the CSH1 mode in simulations, using depths of 3 mm and 4.8 mm. In order to generate these defects with a specific depth and circumferential extent, the angle at which the defect tapers down to its full depth will have to be adjusted. This will complicate the behaviour of the modes as the mode behaviour will then be affected by the distance spent in each different depth part of the defect and the different defect structure caused by the change in tapering angle. A range of different angles were tested for the tapering angle of the defect, but the lowest angle of slope to the horizontal is used each time in order to maintain the structure of the defect as being close to the original defect structure.

The simulation of the smaller defects here is carried out with the same assumption as before that they are part of a larger size defect axially, such that the two dimensional representation is equivalent to the results from the transducer being directly over the defect area. This may not be a valid assumption in some cases since the style of the defect could vary to have smaller axial extent than the circumferential extent. In these cases, the received waveform will be a combination of both the signals received from propagation through the defect, reflection from the defect and from portions of the beam that travel from the transmitter to receiver without interacting with the defect or that diffract around it. Therefore, the simulated data presented here represents only the 'ideal' interaction of all of the wave interacting with the defect and not the case of a small axial size defect, the effect of which is considered briefly in Chapter 6.

With the defects considered here, although the maximum depth of the defect

is the aspect that has governed the design, the structure of the corrosion patch on a pipe results in the varying depth of the defect throughout the circumferential length. The waves therefore travel for a variable amount of time as the slower CSH1 modes and the mode converted CSH0 modes in the different depth defects and in the different circumferential extent defects. In the case of defects that are above the cut-off thickness of the CSH1 mode at all points, this does not complicate the inspection, with the arrival time of the CSH1 mode increasing with increasing circumferential extent due to travelling at a lower velocity underneath the defect. These waves will always have an increased arrival time with respect to the CSH1 mode from the area without a defect present and so can be differentiated from the more extreme defects where the CSH1 is forced to mode convert in order to propagate through the defect area.

The different modes in the signals are highlighted in Figure 5.32 for a sample with a remaining wall thickness in the defect area greater than the cut-off thickness and length of 10 mm, 20 mm and 30 mm respectively for figures a,b,and c. The signals that are seen will depend on the tapering angle as well as the extent of the defect, with the reflections from the larger defects appearing more coherently and at a different arrival time due to the angle of the defect edge. The short path signal which is unaffected by the defect is labelled at 1 in Figure 5.32a, Figure 5.32b and Figure 5.32c. This is followed by the CSH0 that travels the long path distance, labelled as 2. A partial mode conversion waveform is shown at 3 in Figure 5.32b and Figure 5.32c due to the bandwidth of the signals and the tapering angle.

The slowed CSH1 modes are shown at 4 in Figure 5.32a, 5.32b and 5.32c, with the increasing arrival time and dispersion of the mode due to the greater amount of time spent as the slower mode under the defect. The reflected waves are shown at 5 with the differences here predominantly determined by the angle of the tapering slope, which is 50 degrees in the 10 mm circumference case and 20 degrees in the 20 mm and 30 mm case. This leads to a family of reflections in the 10 mm case due to the more abrupt nature of the defect edge leading to a reflections from within the defect. The CSH0 mode that has travelled an entire circumference plus the short path distance is shown at 6.

In the case of varying the circumferential length of the defect when the depth is below the cut-off thickness of the CSH1 mode in the sample, the arrival time still increases with increasing circumferential length of the defect, this is due to the complex nature of the defect.

If the CSH1 mode were to purely mode convert at the edge of the defect directly from the CSH1 in the full thickness, to the CSH0 at the defect area, then

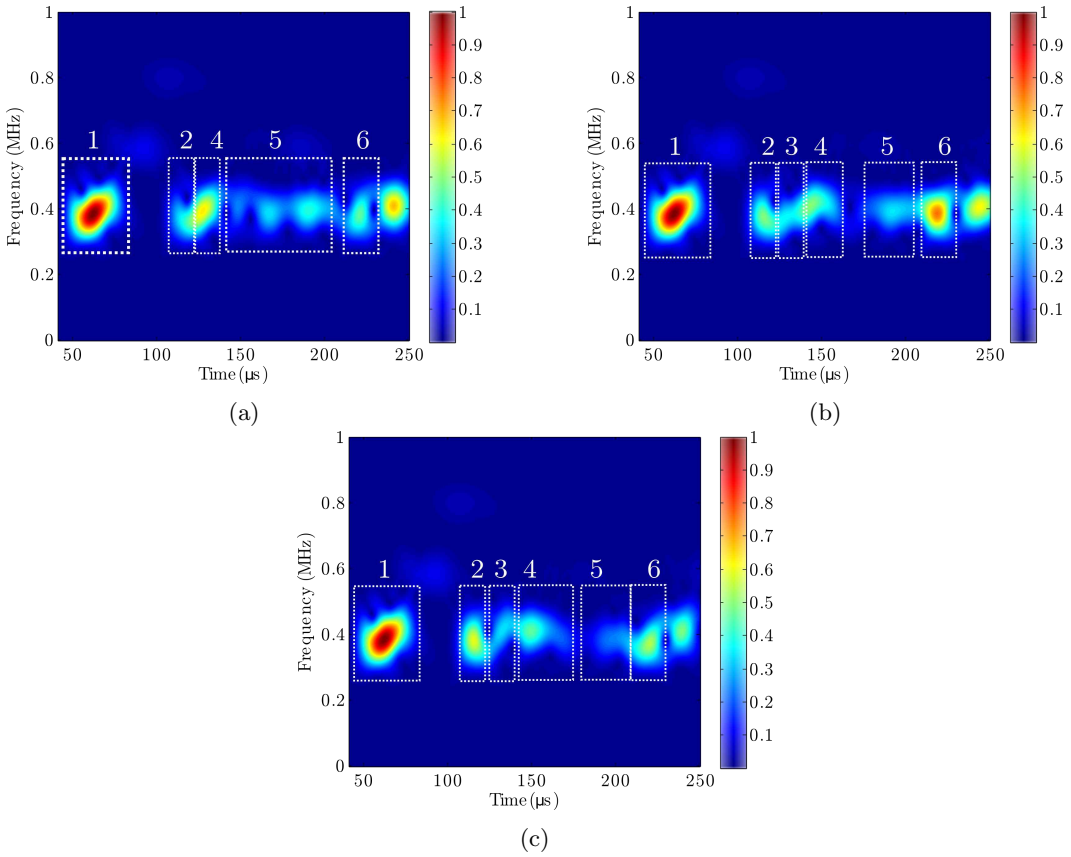

Figure 5.32: STFT's of the simulated data for a remaining wall thickness of 4 mm in the defect area with a) 10 mm circumferential extent, b) 20 mm circumferential extent and c) 30 mm circumferential extent. Colour scale is the amplitude normalised to the maximum signal received.

the arrival time would be expected to decrease for a greater circumferential extent due to the greater amount of distance travelled as the faster mode converted mode. However, this does not happen due to the more complex nature of the defects, with a varying thickness down to the cut-off thickness ensuring the wave travels some distance as the slower CSH1 mode and some distance as the faster CSH0 mode under the defect. This leads to an increase in arrival time of the mode converted waveform as the circumferential extent of the defect is increased. However, due to the increase in speed in the defect area, the waveform will still arrive faster than the CSH1 mode from the clear area.

This effect is observed in Figure 5.33, for defects of the same depth but different circumferential extents of 10 mm, 20 mm and 30 mm in the figures labelled a,b and c respectively. Here the same behaviour is seen in Figure 5.33a, Figure 5.33b and Figure 5.33c for each of the extents. The unaffected short path signal

seen at 1, and the long path CSH0 mode seen at 2. This is followed at 3 by the mode converted waveform that gradually separates from the CSH0 mode in time by arriving later but still has a earlier arrival time than the CSH1 mode in the clear area of the sample. The reflections of the CSH0 and CSH1 modes from the edge of the defect are shown at 4, with varying arrival times due to the circumferential extent of the defect. The CSH0 mode that has travelled the circumference and the short path distance of the sample is then seen at 5.

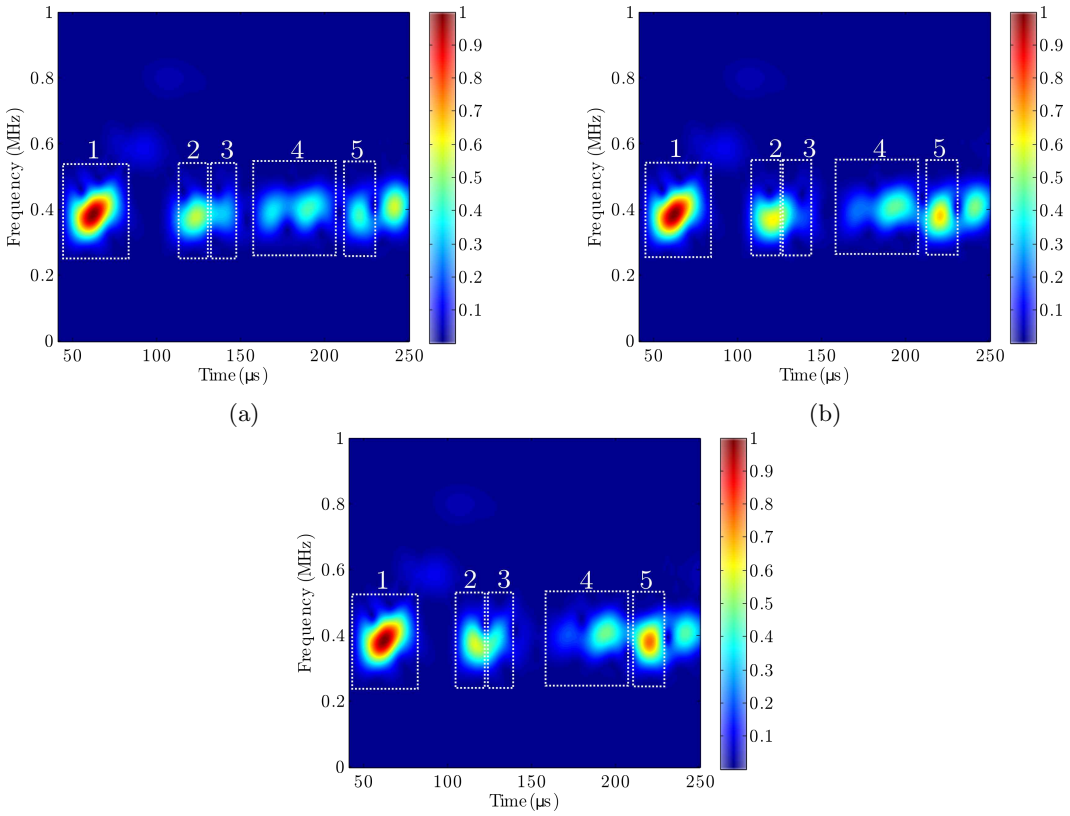

Figure 5.33: STFT's of the simulated data for a remaining wall thickness of 2.2 mm in the defect area with a) 10 mm circumferential extent, b) 20 mm circumferential extent and c) 30 mm circumferential extent. Colour scale is the amplitude normalised to the maximum signal received.

From the simulation data presented, the remaining wall thickness of a defect can be characterised by whether a slowed CSH1 waveform is detected or whether a mode converted wave is detected. The level of dispersion of the CSH1 mode can be used to indicate a shallow or deeper defect up to the cut-off thickness of the CSH1 mode. As the cut-off thickness is approached, the mode conversion behaviour starts to occur in the signal suggesting that a signal that shows both the CSH1

slowed mode and the mode converted mode will be from a defect that has a mean thickness that is close the cut-off thickness of that mode in the sample. If the entirety of the frequency range of the CSH1 signal goes below the cut-off point for the new frequency-thickness product that the defect generates, then the mode converted waveform is what will be seen, with no appearance of the slowed CSH1 signal. This can be used to identify areas of more severe corrosion, that have involved the mode conversion of the entire signal in order to propagate through the defect area. These defect areas are also characterised by high amplitude reflections, with differing arrival times due to the thickness profile of the defect.

The circumferential size of the defect alters the behaviour of the modes, with an increase in arrival time for increasing circumferential size of defects due to the complex depth profile of the defect. For a defect above the cut-off thickness, increasing the circumferential extent leads to a more dispersive CSH1 waveform with an increase in arrival time. The arrival time also increases for the mode converted wave in a sample whose defect is below the cut-off thickness as the circumferential extent is increased. The results here suggest that there is not the possibility to separate the effect of depth and circumferential extent satisfactorily with this method without prior knowledge of the defect depth structure, limiting its potential for more exact wall thickness measurements.

5.6 Conclusions

This chapter set out the changes that the CSH0 and CSH1 modes would experience in terms of frequency and level of dispersion when they interact with a defect in the form of a section of pipe wall thinning. This was shown with reference to the dispersion curves for the specific sample of interest for a defect that leaves a remaining wall thickness that is greater than the cut-off thickness of the CSH1 mode. Experimental scans using the Innerspec pulser receiver were then shown and differences between non-defective and defective areas highlighted to show how this method can be used to detect defects and categorise their severity into one of three categories. Axial sizing capabilities of the system were illustrated, showing that the method gives a reasonable approximation of the axial size of a defect. More complex processing methods to present the encoded scans in order to highlight different signals in the scans were shown to allow for reflections and mode converted waveforms to be highlighted. The physical origin of reflections and mode converted waveforms in this method were assessed in order to provide circumferential positioning of any defect present in a sample.

The results from the experimental data and the corresponding information that can be gained from it as listed above were used in conjunction with a finite element model to confirm the underlying physics in the inspection. This was achieved by the development of a model with behaviour matching that seen in experiment in terms of the data sets received. Images of the propagation of the ultrasound in the model were obtained to confirm where in the structure of the defect area processes such as reflection and mode conversion were taking place. The close correlation of the modelling behaviour with that of the experimental data allowed the model to be extended from the known defect case into different defect depths and circumferential sizes.

The results from changing the depth of the defect allowed the change from a defect that is above the cut-off thickness of the CSH1 mode to below the cut-off thickness of the CSH1 mode to be considered. It was shown that the defects that leave a remaining wall thickness above the CSH1 mode cut-off thickness cause a decrease in the speed of CSH1 waveform as it moves to a lower velocity position on the dispersion curves and showed the corresponding increase in dispersion seen at these points in the dispersion curve. The modelling illustrated the change of the CSH1 mode to a CSH0 mode underneath a remaining thickness of pipe of below the cut-off thickness, with a conversion back to CSH1 once the defect is passed. It also confirmed that the presence of both a mode converted waveform and a slower CSH1 mode in the signals is due to the remaining thickness being close to the mode cut-off, causing some but not all of the CSH1 mode to mode convert in the defect area. It illustrated the greater proportion of the signal that is reflected from the defect once the remaining thickness in the defect area is below the cut-off thickness of the CSH1 mode.

The modelling of defects of different circumferential extent showed that there is a difference between defects of the same depth but differing circumferential extent. The range of reflections that are seen are different as the circumferential extent is increased, as the reflections travel different distances. The slope of the defect also has to be adjusted to generate these different defects however, so the level of reflection will be affected by this. The CSH1 mode is seen to arrive later in the time record for these different circumferential extents because the waves spend more of their travel time in the defect area and hence more time travelling as the slower velocities. Once the remaining wall thickness is below the cut-off thickness of the CSH1 mode, these different circumferential lengths don't show a decrease in time as would be expected, but an increase in arrival time as the circumferential length increases. This is due to the complex structure of these defects causing the CSH1 mode to spend more

time as a slower CSH1 mode, as well as its longer period as the faster CSH0 mode under the defect.

This chapter has illustrated the method and clarified the underlying physics involved in an inspection with this method, making it clear that the depth and circumferential extent of a defect can't be separated satisfactorily without prior knowledge of the geometry of the defect, as the structure of the defect defines the behaviour of the CSH1 mode in conjunction with the maximum depth.

Chapter 6

In-service corrosion patches, calibration defects and welds

Following on from the presentation of data from the known depth defect and the corresponding simulated data in the Chapter 5, this chapter will consider the system's operation on samples with in-service corrosion patches. Due to the nature of the corrosion in these cases, the generated defect will be of an irregular shape, size and depth, so the behaviour of the guided wave modes will be different, but the basics of the interaction of the waves with the defect will be used to identify a range of remaining wall thicknesses.

These inspections will be used to assess the applicability of the system on real samples that have more complex defects, and on a range of different sample circumferences and wall thicknesses.

The chapter will also briefly consider the different structures of defects that are used as calibration defects in industry, illustrating the differences that are seen between these calibration defects and the signals received from the real corrosion patches. A sample with straight sided flat bottomed holes is used to compare these defects with corrosion patch data and illustrate the differences between internal and external defects.

Further studies will be presented of defects with known dimensions in a more complicated pipe structure, with features such as welded areas on the external surface of the sample, which can mask defects and complicate the received signal as the circumferential signals interact with the welded area.

6.1 In-service defects

In order to ensure the technique is valid for a range of different samples, it has been tested on in-service defects, both in laboratory conditions and on site with the sample in situ. These samples have real corrosion patches that can have a very variable depth and shape throughout the length of the defect and the detection of external defects has been focussed on. The shape and size of the defects will not be obvious and may not be visible or measurable in terms of circumferential and axial size and defect depth. A range of samples have been tested, with defects both in the pipe support position and at various positions around the pipe circumference, with different coating conditions.

For the type of corrosion considered to be relevant here, the evolution of the defect goes through several stages [2]. The corrosion of the pipe material starts from a position of damage in the coating layer, which allows water to come into contact with the steel and begin to corrode it. This water can then spread under the coating later and cause the corrosion patch to expand. As this process continues, the patch becomes larger and the structure more complex, forming different layers and corrosion products such as scabs.

An initial sample with a single corrosion patch defect with known axial and circumferential extent but unknown depth is considered, which has the same sample dimensions as the sample with an artificial defect. Several samples with unknown defect dimensions at the pipe support position that were measured in blind trials are then presented, which were found to have varying defect depths and axial extents. A further sample is presented with a range of defects around the pipe circumference, in order to show the ability to gain information from defects at any circumferential position, and the effect of corrosion products being present in a sample.

In each of these cases, the pipe circumference and thickness is different and the theoretical operation points of the probe on the sample is calculated before an encoded scan along the axial length of the pipe is carried out. The axial size and the depth of the defect are then estimated. Interpretation of these real corrosion patches is more complicated, as the irregular shape of the defect will cause a greater degree of scattering [162] when the guided wave modes reach the defect area and the reflections from the defect will not necessarily reflect directly back to the receive transducer. This effectively means that the reflected signals seen in the artificial defect case are not expected to arrive at such high amplitude as in the artificial defect data in these real corrosion patch situations.

An initial example is shown here of the system operating on a pipe sample

with a single defect centred in the pipe support position. This sample has the same dimensions as the sample with the artificial defect considered in Chapter 5, with a circumference of 534 mm and a 7 mm wall thickness (Sample 2 in Table 5.1). It has a single corrosion patch style defect at the pipe support position, and is tested while resting in a saddle support such that the defect is not visible. Before being placed in the support, the defect's extent on the surface is measured and found to be 145 mm long at its maximum axial extent, with a circumferential extent of 75 mm. This is only an estimate for the dimensions of the defect, as the defect is irregular in shape as shown in Figure 6.1 where the sample, defect and stand are shown.

Figure 6.1: Photograph showing the sample with corrosion patch defect, with the pipe stand in the background.

Encoded scans were taken of the sample at different frequencies with an 8.8 mm nominal wavelength probe (probe number two in Table 2.1) and the sizing techniques discussed in the Chapter 5 used to characterise the defect. Measurements were also taken without the scanning rig, by moving the transducers manually and recording A-scans at 5 mm steps. This was carried out with a 10 mm nominal wavelength probe (probe number one in Table 2.1).

The defect is variable in depth throughout the axial length of the sample, with a large circumferential extent area that is approximately 30 mm in axial extent, followed by a deeper area that is approximately 60 mm in extent, and a following shallower area that decreases in circumferential extent of approximately 55 mm. The transducer active area size is approximately 32 mm for the manual scan and 40 mm for the encoded scanner scan, due to a different design of probe being used.

6.1.1 Manual Scan

A manual scan with a 5 mm axial step was carried out with the probes touching, to minimise any errors related to the separation of the probes, since a rig wasn't used to keep the separation between the transmitter and receiver constant. This means that the different modes in the signal will not be separated as before, but will arrive very close to each other, making the analysis of the effect of the defect on different modes more complex. The scans using this technique will show the change in the CSH1 modes in the signal, but due to the relative position of the defect and the probes, any reflections from the defect area will not be distinct from the original signals. The close proximity of the short and long paths in the time domain also means that the tracking of the RMS of the CSH1 mode will be carried out on both the CSH1 modes. Closer inspection of the A-scans will be necessary to ensure the correct area for the defect is selected. The scan of the sample is shown in Figure 6.2, clearly showing the area where the amplitude and arrival time of the CSH1 mode is changed by the presence of the defect in the path of the ultrasound.

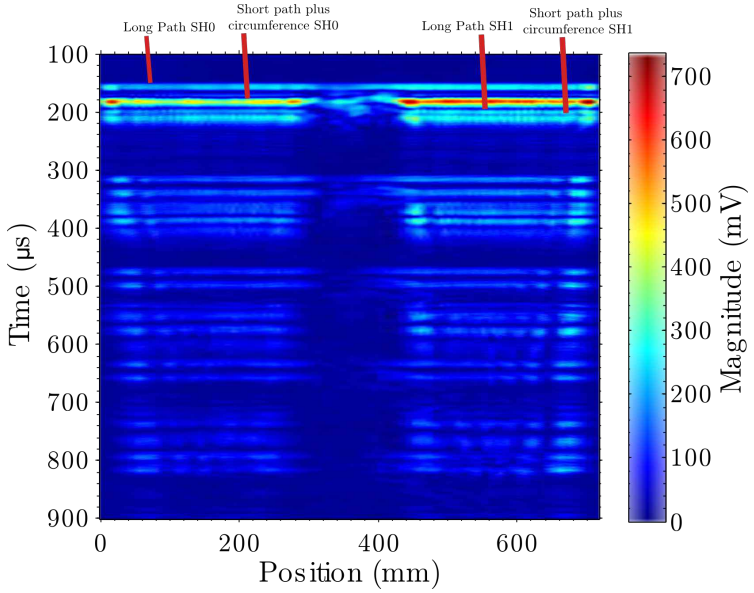

Figure 6.2: Scan of the sample shown in Figure 6.1, using transducers that are aligned with their edges touching each other, this results in the short and long path signals arriving at similar times. The short and long path signals are labelled for their first arrival and the defect area is seen in the removal of signal from the CSH1 mode in the defect area.

The 5 mm step for the scans will mean the scan is of a low axial resolution as compared to the encoded scans, which record scans at 1 mm intervals. The axial

length of the defect can be determined as 143 mm although this value has more of an error attached to it of ±5 mm due to the distance step used. This agrees with the measured value of 145 mm.

The scan shows consistent arrival times of the different modes outside of the defect area, but some variation in the amplitude of the modes. These changes are predominantly caused by the difference in lift off at each point, due to the manual application of the transducers to the surface of the sample rather than being the effects of other defects in the sample. A sample time record for the clear area of the sample is provided in Figure 6.3, where the CSH0 and CSH1 modes for the short and long paths are very close to each other in the time domain, due to the minimal circumferential separation of the transducers.

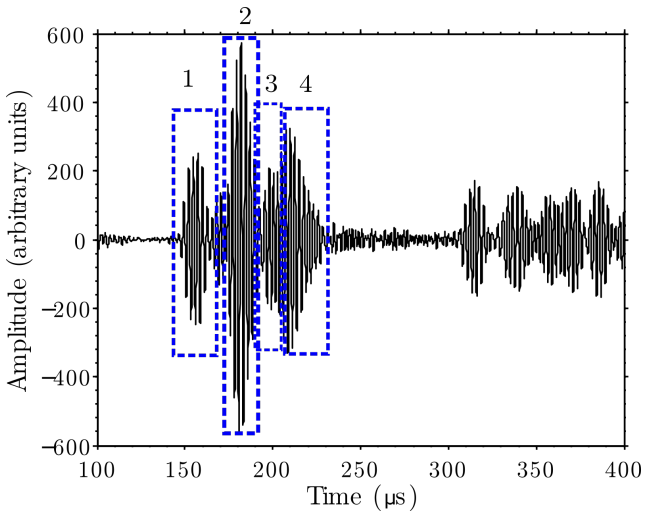

Figure 6.3: Raw data for the clear area of the sample showing the arrival of the CSH0 and CSH1 modes that have travelled the long path distance (at 1 and 3 respectively) and the CSH0 and CSH1 modes that have travelled a full circumference and the short path (at 2 and 4 respectively). The remaining waveforms in the data are the received signals that have travelled another circumference of the sample, they are not considered in detail here.

Different sections of the time records can be identified that show how the interaction with the defect differs throughout the axial length. The length of the axial step here, limits the resolution such that the initial scans for the less extreme area are mostly dominated by the section of the transducer that is outside of the defect. This results in a gradual decrease in amplitude of the CSH1 mode before the transducer is wholly over the defect, and the arrival time of the modes becomes later, as in Figure 6.4a. This area is approximately 50 mm in axial length. The deeper part of the defect is then encountered, giving a scan with some reflections and mode

conversion, giving a faster arrival time for the CSH1 modes. As the transducer is centred over the deepest section, the mode converted signals dominate as in Figure 6.4b, which extends for approximately 60 mm before the signal becomes a mixture of the mode converted waveforms and a slowed CSH1 mode, which is approximately 65 mm long. These lengths are taken from the first change in the signal due to the defect, so the defect appears larger due to the axial size of the transducer.

As the path of the ultrasound then goes through the area of small depth and passes the defect, the signal becomes dominated by the clear area signal, returning to its original value. It is expected that these areas of the defect will be able to be differentiated from each other more clearly in the encoded scan, because it has a smaller axial distance step.

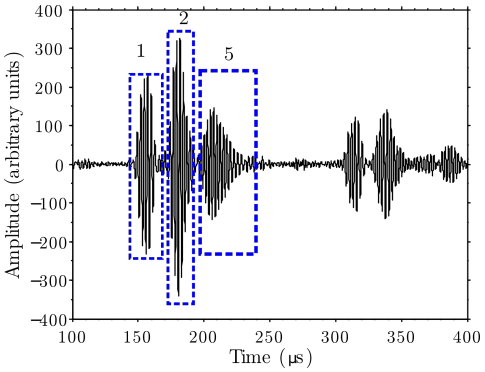

(a) Raw data from the initial thinning area showing the two CSH1 modes slowing and becoming more dispersive in the waveform labelled 5.

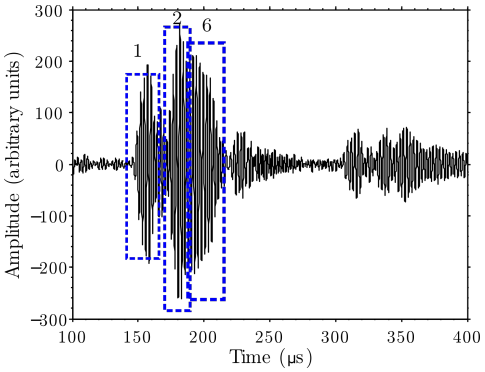

(b) Raw data from the mode converted waveforms, when the transducer is centred over the deeper section of the defect, with the two mode converted signals arriving earlier than the CSH1 modes at the section labelled 6.

Figure 6.4: A-scan signals for the lower level of wall thinning and the more extreme area of wall thinning.

6.1.2 Encoded Scan

The encoded scan shows similar behaviour to that of the manual scan. Here the distance step is 1 mm and the probes are separated from each other in the short path by 170 mm, with the probes situated at the 10 and 2 o'clock positions on the pipe. In this case, the scan has only been taken from a small distance away from the pipe support area, as the position of the defect is known, resulting in a much smaller axial extent of the scan. The scan was also taken in the opposite direction along the pipe to the manual scan, such that the behaviour arising from the different depths of the defect will be reversed in the scan. This will result in the larger area

of smaller depth being encountered first, before the deeper section is reached and then the smaller low depth area at the other end of the defect. This change has resulted in the amplitude profile technique that was used for the axial sizing of the defect underestimating the axial length of the defect. The area where the CSH1 mode is significantly affected by the defect is found as 131 mm, suggesting there is some change in the interaction with the defect at one end of the defect that causes the underestimate. This is a function of the increase in distance step resolution, as previously the 14 mm underestimate would be covered by 3 measurements, instead of the 14 measurements now used for the same axial extent.

The reason for this change can be identified when the structure of the defect is compared to the raw data. It can be seen that one end of the defect has a much longer shallower section, with a small circumferential extent. On examining the raw data, the beginning section of the defect can be seen to not have a large effect on the CSH1 mode, but the CSH0 mode changes in arrival time. Once this change in the signal is considered, the axial extent of the defect can be seen to be longer, extending it to 143 mm, which agrees with the measured extent of the defect. A schematic diagram of the defect is shown in Figure 6.5.

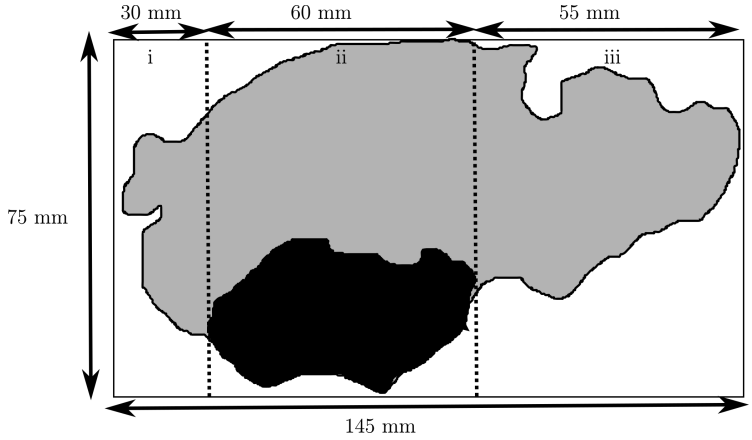

Figure 6.5: Schematic diagram of the in-service corrosion patch considered here. It shows a complex structure with varying depth and shape throughout but a noticeably deeper section shown at ii and large area of small defect depth, small circumferential extent at one end. The manual scan of the defect is performed from left to right, whereas the encoded scan is carried out from right to left, (not to scale)

The encoded scan can be sectioned as before, to show the extra signals in the data record in a more obvious way. This shows reflections and slowed CSH1 sections due to the defect, as well as the central section of mode converted waves due to the area of deeper defect depth, the encoded scan is shown in Figure 6.6.

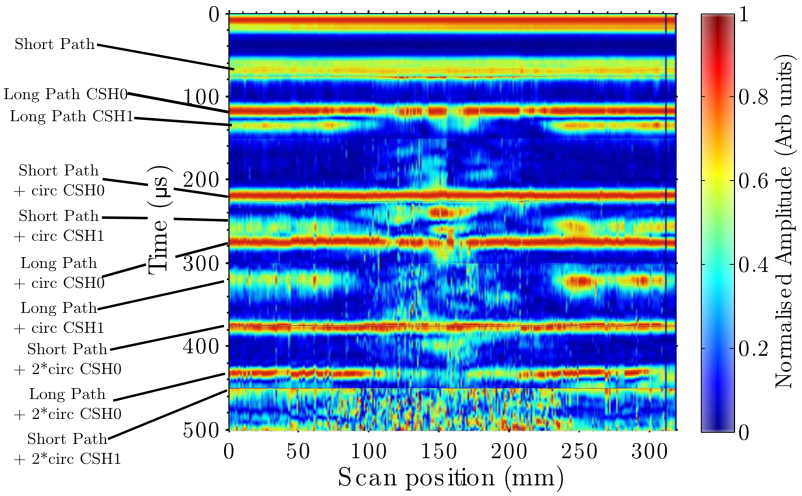

Figure 6.6: Encoded scan of the defect with the amplitudes adjusted to see all the modes. The short and long path signals are labelled, and the defect area is seen where the long path CSH1 mode behaviour changes.

The structure of the defect can be followed as in the manual scan case from the area without a defect shown in Figure 6.7a, through where the amplitude of the CSH1 drops as the defect is reached until the transducer is directly over the defect in Figure 6.7b. In this case the resulting waveform should be a slowed CSH1 mode, but it is seen that the reflections dominate the signals here. As the scan continues, the mode converted waveforms then dominate, as the deeper section is encountered, that goes below the cut off of the CSH1 mode as seen in Figure 6.7c. An area of smaller defect depth is then encountered, showing a slower speed CSH1 mode and reflections in Figure 6.7d, before the sample thickness returns to the original thickness. Again the resolution of the different areas within the defect will be limited by the axial size of the transducer, as the transducer overlaps with the various different sections of the defect at different points in the axial scan.

So in summary, the techniques described before that allowed the artificial defect to be characterised are applicable to the case of a real defect, but may not provide full quantitative information when the defect depth changes rapidly due to the footprint of the transducer and the complex profile of the defect. However, the information can be used to locate defect areas that are deeper by tracking the behaviour of the CSH0 and CSH1 modes and determining where mode conversion occurs compared to areas that show just the more dispersive CSH1 modes. The appearance of areas that have a small change in thickness and a small circumferential extent are more difficult to detect in the data, and may need additional examination of the A-scans that are acquired in order to establish their effect on the received

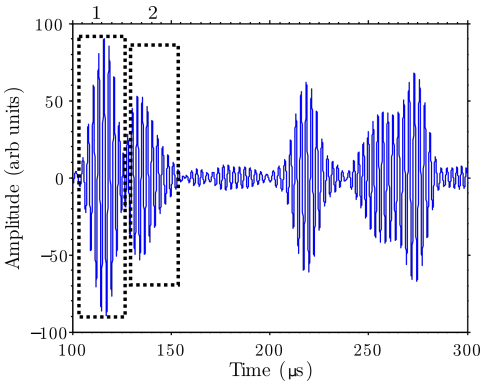

(a) Raw data for the area without a defect in the path of the guided waves. The long path CSH0 signal is highlighted at 1 and the long path CSH1 highlighted at 2.

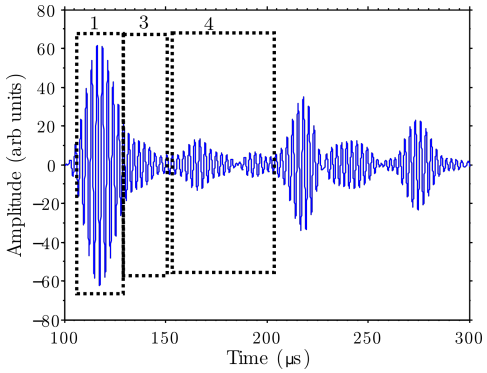

(b) Raw data for the initial section of the defect, much of the ultrasound here is reflected, with a small amount of CSH1 signal transmitted through the defect area. The long path CSH0 signal is highlighted in 1, with a slowed CSH1 mode at 3 and reflections at 4.

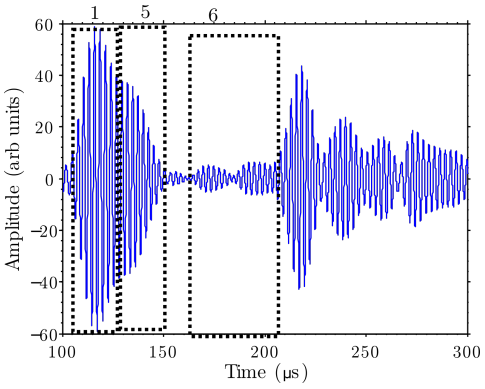

(c) Raw data for the mode converted waveforms, when the transducer is centred over the deeper section of the defect. Showing the long path CSH0 mode in 1, a mode converted waveform at 5 and reflections at 6.

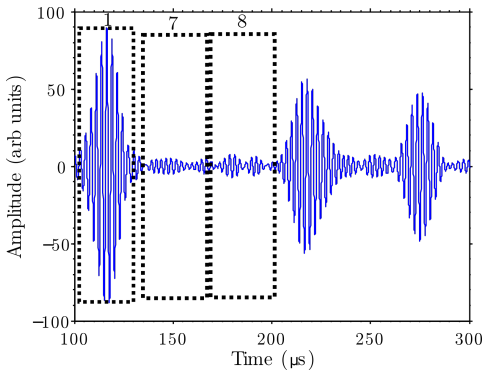

(d) Raw data for the final section of the defect showing a slowed CSH1 mode and reflections from the edge of the defect. The long path CSH0 mode is shown at 1, with the slowed CSH1 mode at 7 and reflections at 8.

Figure 6.7: A-scan results for different positions in the axial scan to show the difference in behaviour as different parts of the defect are encountered.

signal which may be minimal. Therefore it is suggested that the amplitude of the CSH1 mode is used as a guide to indicate the axial length of the defect, but that further inspection of the surrounding data should also be taken into account to avoid underestimating the axial length of the defect.

The technique works very well for the screening of samples in order to determine the presence of defects by the changing behaviour between a defect free area and an area in which a defect is present. Exact measurements of the change of speed of the mode in order to provide further information on the depth of the defect

is limited, due to the path of the ultrasound and the axial size of the transducer. It is deemed unfeasible with this method, without knowing the defect structure a priori. This suggests that the most appropriate method for assessing the different behaviour with a defect may be to develop a catalogue of different defects, and their effect on signals instead of a single method that draws out a remaining thickness value.

6.2 Blind trials

A range of different pipe support style defects were also examined in blind trials, where a sample has a defect present at the pipe support position but no information is provided about the defect. A subset of these blind trials is presented here for samples where only the dimensions of the pipe sample are given. An assessment of the axial length of the defect and the remaining wall thickness is provided as in the previous case. The sample tested here was of a much larger circumference than the previous samples, having a circumference of 864 mm and a pipe wall thickness of 9 mm (Sample 3 in Table 5.1). The samples had a long axial length (many metres), but only the area around the defect was scanned, as the defect was at a known position on the pipeline. The A scans recorded in this case have saturated the receiver such that the signals for each distance step can be compared in terms of amplitude, but the different waveforms in the same time signal cannot be compared directly due to the initial signals exceeding the amplitude scale and removing amplitude information. However, the arrival time information for the modes shouldn't be affected. The encoded scans are shown in Figure 6.8a to Figure 6.8e.

An assessment of the likely wave behaviour at these defects and a corresponding estimate of the likely depth of the defect was carried out. This has been carried out using the physical behaviour of the CSH1 mode and the experimental operation of the method in Chapter 5. The dispersion curve for the sample is generated and the operating frequency of the CSH1 mode calculated for the full pipe wall thickness of 9 mm. Using this operation frequency and the frequency thickness product of the CSH1 mode at its cut off point, the cut off thickness of the sample for the peak frequency of the CSH1 mode can be calculated. This is found to be at the point at which the sample has a remaining wall thickness of approximately 4 mm. This will be a different thickness than the cut off thickness that is observed in the 7 mm wall thickness sample previously due to the thickness and outer radius of the sample altering the operation point of the CSH1 mode on the dispersion curves.

The blind trial samples showed behaviour that was consistent with the thick-

ness being near to the cut off thickness of the CSH1 mode. The results showed both the slowed CSH1 mode propagating in the sample and the signal that travels to the defect as the CSH1 mode, mode converts to the CSH0 mode under the defect and then converts back to CSH1 after propagating through the defect. Both of these waveforms being detected is thought to be due to the bandwidth of the signals used. Some of the lower frequency content of the signal falls below the cut off thickness of the CSH1 mode and travels as a mode converted wave under the defect, whereas some of the signal doesn't reach this cut off point and still propagates as the slowed CSH1 through the defect area. This behaviour is different to that which is seen when the CSH1 modes frequency range falls entirely below the cut off value, where all the energy of the mode is mode converted. It is suggested therefore, that this provides another category in testing where the thickness has decreased enough for some mode conversion to take place, but not enough to cause the entirety of the wave to mode convert. The balance of what proportion of the energy is mode converted compared to travelling as the slowed CSH1 mode can be used to compare each defect to the other in terms of severity.

In the case of the sample in Figure 6.8a, the defect contained two separate areas where mode conversion from the CSH1 mode to the CSH0 mode under the defect, back to CSH1 after the defect has occured, along with a high amplitude slower velocity CSH1 mode throughout. This suggests that the defect is deep enough to make some of the signal mode convert at two positions, but that it is not deep enough to cause the entire signal to mode convert under the defect. There are minimal reflections seen from the defect, suggesting the transition of wall thickness in the defect is either a smooth slope or the shape of the defect scatters the reflected amplitude. However, the amplitude of the through propagating signals recorded is similar to the clear area amplitude which suggests a low level of scattering is taking place. The defect has a 203mm axial extent as determined by the signal amplitude method described previously.

The encoded waveform amplitude data of Figure 6.8b shows an almost complete removal of the CSH1 mode in the defect area. Closer inspection shows a small mode converted signal is received along with a range of reflections, suggesting a deeper defect than before with an uneven shape that removes most of the reflection energy from the direct path between the transducers. The axial extent of the defect is much smaller than the previous scan with a length of approximately 64 mm. The encoded waveform amplitude data in Figure 6.8c shows a strong mode converted waveform suggesting a deep defect that forces the CSH1 mode to mode convert almost entirely, leaving only a small signal from the slowed CSH1 mode. It also

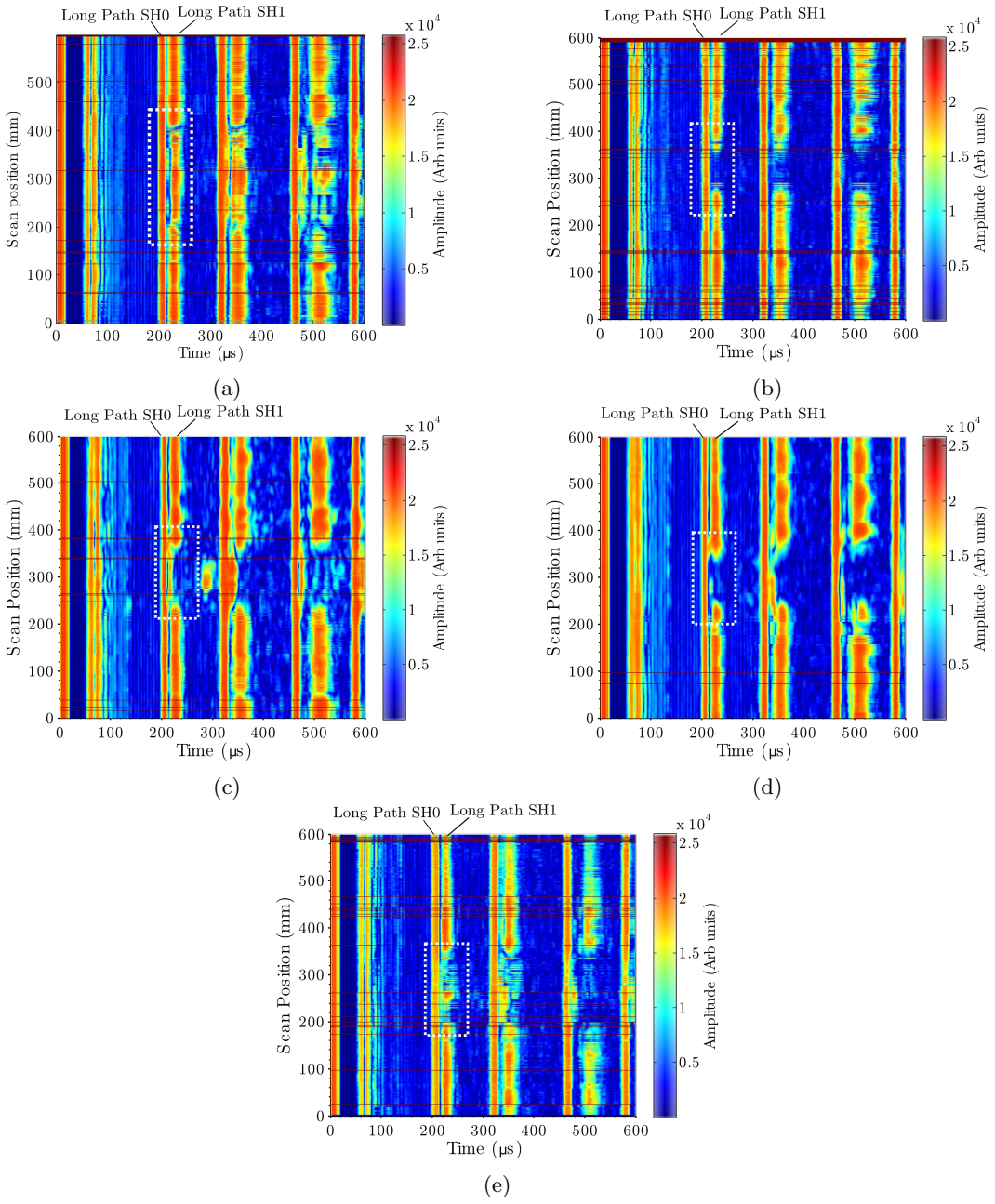

Figure 6.8: Encoded scans of blind trials undertaken with the experimental system featuring different size defects with a varying level of defect depth. The behaviour in each case is estimated based on the previous simulated behaviour and from the previous scans on the known defect sample.

features strong reflections, suggesting the change to full depth of the defect could be abrupt and straight, forcing much of the energy to reflect directly back to the receive transducer. The axial extent of the defect is approximately 112 mm. The encoded

waveform amplitude data in 6.8d shows an area with strong mode conversion, along with a separate section showing just the slowing of the CSH1 mode, suggesting the defect has a deep section and a less deep section axially. It also features a range of reflections from the defect edge; it has an axial extent of approximately 140 mm. Finally the encoded waveform amplitude data in Figure 6.8e shows a defect that is dominated by the slowing of the CSH1 mode, with a smaller amplitude and extent mode converted signal, which suggests the defect is predominantly above the cut off thickness but may have some parts that are slightly below the cut off thickness, allowing some part of the CSH1 mode to mode convert to the CSH0 mode in the defect area and back to the CSH1 mode after the defect. The axial extent of the defect is approximately 150 mm.

Another comparative technique that could be used in the case of blind trials is the use of a longer wavelength probe. The effect of using the longer wavelength probe is that the operation frequencies for the modes become lower for the different modes. Given that the dispersion curve is determined by the sample itself, the use of a longer wavelength probe will mean that the cut off thickness for the CSH1 mode will occur at a different point. The longer wavelength probes will cut off at a higher remaining thickness such that the same defect will cause different behaviour for the two transducers. The issue that is encountered here is that the fine detail of the behaviour in the defect area can be lost due to change in resolution caused by the use of lower frequencies and the desire for rapid single sweep scanning where there may not be time available to scan with multiple probes as in the subsea application.

The blind trial results for this system were found to be effective in detecting and axially sizing the defects and categorising the defects in terms of severity using the three tier system mentioned earlier. All the intended defects were detected, suggesting a high probability of detection and low false call rate for this type of defect. Scanning took considerably less time than some of the other methods in the trials and required no surface preparation or minimum length of sample that were required by other methods taking part in the trial. The results put the system at the forefront of detection capability for these samples however, detailed comparisons with the other methods involved were not made available at the time of writing.

6.3 Multiple variable sized defects

In addition to the pipe support area defects, samples with a range of defects around the pipe's circumference were tested, these defects had different axial positions but some of them overlapped with one another in the axial direction. An example of

such a sample is presented here with a circumference of 861 mm, a nominal wall thickness of 6.4 mm, and an approximately 1 mm thick coating of paint on the external surface (Sample 4 in Table 5.1). The sample had 12 real corrosion patch style defects of varying size, shape, depth and circumferential positioning that had developed in-service. The defects had a range of levels of corrosion, from initial corrosion after a coating breach, to extreme corrosion levels with corrosion products visible as scabs on the outer pipe surface. This is illustrated in the images provided of the defects, where Figure 6.9a shows the initial defect that can only be identified by a small hole in the coating, to a corrosion patch that has expanded underneath the coating in Figure 6.9b, to a severe corrosion patch where considerable pipe wall material has been removed from the sample resulting in a large irregular defect in Figure 6.9c.

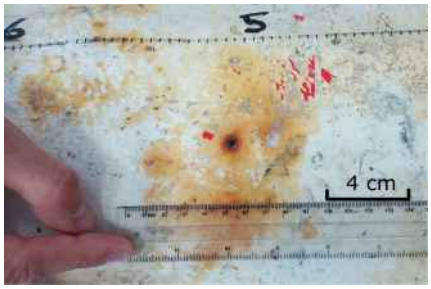

(a)

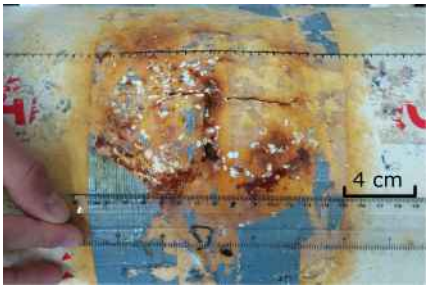

(b)

(c)

Figure 6.9: Examples of the range of defects present in the multiple defect sample, from an initial small defect in a), to a larger corrosion patch with the corrosion product in place in b), to a more severe corrosion patch in c).

The approximate sizing and positioning of the defects on the sample surface are shown in Figure 6.10 along with the positioning of the transmitter and receiver probes on the pipe surface.

The circumferential extent of the sample, probe separation (200 mm) and the wavelength of the probe used on this sample allows the CSH0 and CSH1 modes for the short and long paths to be clearly temporally separated from each other,

which gives more clarity to the defect indications. This sample shows how defects can be detected in the short and long path of the circumferentially travelling guided waves, with the defects labelled at 4,5,6,7,8,10 and 11 in Figure 6.10 and Figure 6.11 affecting the short path signal between the transducers, whereas defects 1,2,3,9 and 12 can be said to be affecting the long path of the waves.

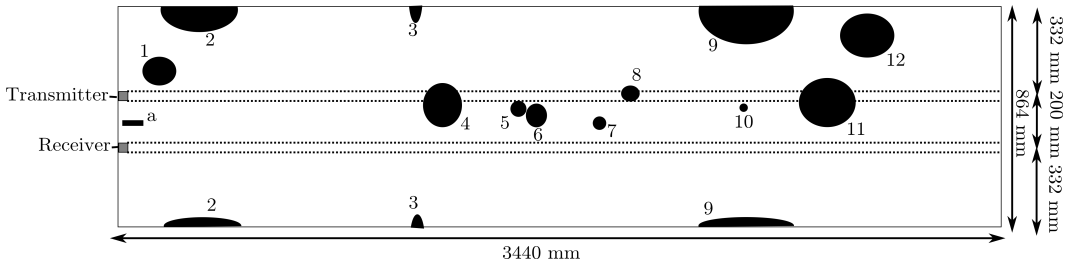

Figure 6.10: Schematic diagram of the 'unwrapped' pipe to illustrate the axial and circumferential positioning of the defects in the 864 mm circumference sample. The different features are to scale but the shape of the defects is not intended to be representative. The circumferential extent of the defect at a is unknown.

This also illustrates one of the weaknesses of the technique when real defects are encountered, as a closer inspection of the defect positioning shows that the defects at 1 and 2 overlap with each other in the axial direction but have different positions circumferentially. Both are in the long path of the signal at different positions circumferentially, but as the indicative defect signals are due to transmission through both areas, they cannot be differentiated from each other. These defects would have a chance of being distinguished using the reflections in the smaller samples, but the reflected signals that are caused by the defects in this longer circumference case are too low amplitude to be used in such a way here. This is in contrast to the defects at 3 and 4 and the defects 9 and 10 that overlap with each other axially but their effect on the signals can be separated since 4 and 10 affect the short path signal and 3 and 9 affect the long path signal.

The scan shown in Figure 6.11 illustrates the difficulty that was stated earlier in having a defect develop directly underneath the path of the transducer on the surface of the sample. The indications at 4, 8 and 11 show that signal is removed due to the defect being situated underneath the receiving transducer, increasing its lift off. This effect is smaller at defect 8, as the defect scab has a lower profile and hence the lift off is reduced, but the defects at 4 and 11 increase the transducer stand off to a larger extent and remove the signal almost entirely. This effect of the removal of any signal is dominated by the change in lift off, instead of the depth of the defect. This results in the signals in this area providing inconclusive information

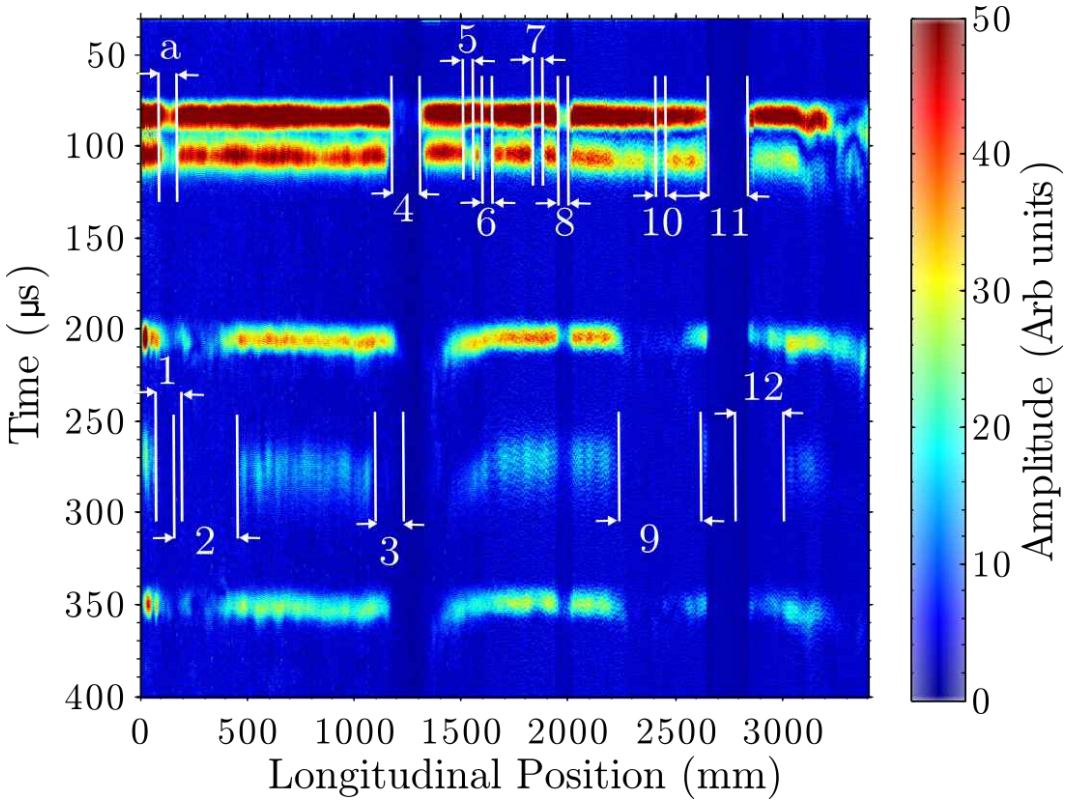

Figure 6.11: Scan of a long axial extent sample with multiple in-service defects spread around the pipe circumference. An unmarked defect in the short path (no measurement data available) is labelled a, with various in-service corrosion patch defects in the short path at 4,5,6,7,8,10 and 11. Defects situated in the long path are labelled 1,2,3,9 and 12. The removal of signal by the change of lift off from the sample is seen at defects 4, 8 and 11.

about the severity of the defect, but allowing the area to be highlighted for further analysis.

The axial sizing method used previously becomes more difficult in this instance, as some of the defects overlap in their axial extent and are in the same path between the transducers. The change of lift off caused by the defects being underneath the transducers also makes it difficult to probe for defects in the long path at these points, as no energy is available for such signals. This leads to varying accuracy of the axial sizing of the defects, which is achieved by comparing the image of the scan amplitudes and the amplitude of the RMS of the CSH0 and CSH1 modes, taking into account that the axial step here is 5 mm. The results for the axial sizing along with the measured extent on the sample are presented in Table 6.1.

So by identifying the mode that is affected by the interaction with the defect

and by tracking the amplitude of the CSH1 mode for the affected mode, the axial position and size of the defect can be estimated and the circumferential position localised to being in the short or long path between the transducers. In this case the defects can be seen and their level of corrosion assessed, with the defects labelled 3, 5, 6, 7, 8 and 10 having a small axial and circumferential extent, with small depths, whereas defects 1, 2, 4, 9, 11 and 12 are large corrosion patches, with and without the corrosion scabs still in place.

However, the different defects can be characterised in terms of their severity without having this prior knowledge of the defects, by using knowledge of the dispersion curves for the sample and how the different modes interact with defects as considered in Chapter 5. The defects at 3, 5 and 6 show through propagating CSH0 modes that increase in velocity, arriving earlier than the clear area CSH0 mode. This is due to the decrease in thickness at the defect area, causing the frequency thickness product at that point in the sample to decrease, resulting in the operation of the mode at a higher velocity section of the CSH0 mode on the dispersion curve. The defect at 5 then can be seen to have a CSH1 mode that arrives later than in the clear area, which suggests that the defect in this area has a depth that is above the cut off thickness of the CSH1 mode, as a mode converted waveform is not seen in the A-scan data. The defect at 6 experiences the same behaviour as defect 5 in that the CSH1 mode slows in the defect area, suggesting a defect of a depth that is not as extreme as would be necessary to reach the cut off thickness of the CSH1 mode as there is no mode converted wave detected.

Defect	Measured Axial length (mm)	Scan Axial length (mm)	Comments
a	-	78	Unmarked, no measured length available.
1 + 2	420	418	Overlapping axially, with all CSH1 mode removed.
3	50	58	Small defect seen on surface, testing hampered by the effect of defect 4.
4	150	155/263	Large defect with corrosion product in place. Extent on scan gives 155 mm but effect on the CSH1 amplitude extends much further due to general pipe condition.
5 + 6	140	138	Small defects too close to be measured separately using the amplitude of the CSH1 mode, however combined extent is as expected.
7	50	58	Small defect on the sample surface that extends further under the coating.
8	70	63	Small defect on the surface with larger corrosion patch under coating.
9	370	433	Extreme defect, adjusted amplitude scan gives 373 mm but CSH1 amplitude scan overestimates to 433 due to pipe condition.
10	25	30	Small axial extent, small depth defect, only visible due to slight changes in the arrival time of the CSH0 and CSH1 modes in the scan.
11	220	223	Large corrosion patch with change of lift off, axial size matches, but only gives an idea of how far the surface is uneven for with the defect present.
9 + 11 + 12	760	778	Part of defect 12 overlaps with defect 11 where the signal is removed, combined extent of 9,11 and 12 is correct.

Table 6.1: Summary of the measured (with a tape measure) axial length of defects and the approximated length from scan data.

However, the amplitude of the slowed CSH1 mode at defect 6 is much lower than the amplitude seen at defect 5, which suggests that there is considerable reflection and scattering of the CSH1 mode when it interacts with the defect. Characterisation of the defect seen at 3 is difficult as it overlaps with defect 4 axially, which as has been mentioned removes some of the signal from the received signal due to a change in lift off of the probes. However, it shows the CSH0 mode being able to propagate into the defect area as mentioned and then an almost complete removal of the CSH1 mode from the signal suggesting that there is considerable reflection and scattering of this mode when it interacts with the defect.

The defect labelled at 7 exhibits the same behaviour as the defect at 6, suggesting it has a depth that is above the cut off thickness of the CSH1 mode, but causes a large degree of reflection and scattering of the CSH1 mode such that the through propagating mode has a low amplitude. The defect labelled at 8 removes the signal from the receiver due to the increase in stand off of the transducers, which makes it difficult to obtain any quantitative information about the defect. The transducers could be realigned to straddle the defect such that the lift off returns to the normal levels for the rest of the sample in order to gain information about the defect, but due to the rig not being used here, this type of scan was not recorded. From the visual appearance of the defect, it is suggested that it would give similar results to that seen in defect 5. The defect labelled at 10 is an area of corrosion that has a small axial and circumferential size, with a small amount of wall thinning occurring. It is only obvious with careful inspection of the amplitude profile and the encoded waveform amplitude data, so it would be difficult to detect the presence of the defect if it had not been found in the visual survey of the sample.

The more extreme defects that are seen at 1, 2, 4, 9, 11 and 12 can be differentiated from the less extreme defects seen as they affect both the CSH0 and CSH1 modes to a larger extent. In the case of defects 1, 2, and 9, the CSH1 mode is entirely removed from where it would be expected to be detected if there was no defect. This is not accompanied by a mode converted waveform, as would be expected from the other defects that have been investigated, suggesting that the energy of the CSH1 mode cannot propagate as the CSH1 mode through the defect but instead is reflected and scattered when it interacts with the defect due to the depth of the defect and its irregular structure. The more extreme nature of the defect here is confirmed by the fact that the CSH0 mode that should propagate through the defect area is either entirely removed in the case of defect 9, or has a very low amplitude in the case of defects 1 and 2. This suggests that the depth of the defect is extreme, as it was observed in Chapter 5 that the reflection of the

CSH0 mode increases with the depth of the defect, and this is the predominant mechanism by which the expected amplitude of the CSH0 signal would decrease. It also suggests the structure of the defect is irregular, as the reflected energy from both the CSH0 and CSH1 modes is not received, suggesting that it is scattered and does not return to the receive transducer as a coherent waveform.

The defects at 4 and 11 exhibit a removal of signal due to the increase in stand off of the probes, so quantitative information about the depth of the defect is not available, however, a visual inspection of the defects would suggest that the behaviour would be similar to that seen in defects 1, 2 and 9 if a scan at a different angle was carried out. The defect at 12 is partially overlapping with the area of defect 11 where the stand off of the probes is changed, which makes the assessment of the defect difficult. The section of the defect that can be seen however, shows the removal of the CSH1 mode, with a CSH0 mode that increases in velocity but with a smaller amplitude than in the clear area of the sample. This suggests that the defect is extreme enough to cause a large amount of reflection of the CSH0 mode and the CSH1 mode, but still allows for some propagation of the CSH0 mode through the defect area, suggesting it is less extreme than defects 1, 2 and 9.

In summary, the application of this method to detect in-service corrosion patches is very effective as a screening technique, showing the defects clearly as a change in the received signals. The method works best as the axial size of the defect is increased and where the depth of the defect is increased or the abruptness of the defect is extreme, such that the most difficult defects to detect are those that are of a small axial size and have a small defect depth. The removal of the energy of a mode completely suggests a complex defect with a rough profile and therefore usually a more severe defect, with the removal of the CSH0 mode from the signal suggesting a very severe defect. Any defect that causes the mode conversion of the CSH1 mode or total reflection of this mode is severe enough to warrant further investigation.

6.4 Modelling different geometries, other calibration defects.

It was stated earlier that a range of different defect geometries were tested before deciding on the most appropriate geometry of defect to represent the experimental structure. In the corrosion patch case, the main consideration was the slope of the defect at the beginning and end of the defect, such that the extent of reflection from the defect matched that of the experimental case. However, it is also noted that there are a range of calibration defects that are considered in industry and have been

used previously in the flat plate case. These machined defects are quite unrealistic in terms of the behaviour they exhibit compared to real corrosion patches and are presented here in order to emphasise these differences.

The original modelling of a defect therefore started from the desire to generate an equivalent defect in a pipe to that of a flat bottomed hole in a plate [163, 164, 165]. The flat bottomed hole in a plate generates a defect that abruptly moves to its full depth and then back again after the defect. The equivalent defect in the pipe situation is one that follows the curvature of the pipe, but this type of defect is difficult to machine into a sample. In practice this sometimes leads to calibration defects being made by machining flat bottomed holes into a pipe, which will result in a defect that is not a constant depth throughout the pipe wall, but whose depth changes in a similar way to that of the corrosion patch defect considered previously. The difference between this defect and the one chosen for modelling in Chapter 5 is that the defect in Chapter 5 exhibits a controlled tapering of the depth down to the full thickness of the defect. This is in contrast to the flat bottomed hole case which shows a varying depth, but still features an abrupt start and end to the defect, which affects the behaviour of the guided wave interaction with the defect. The geometry of these defects is shown in Figure 6.12, with the constant depth defect shown at a) and the flat bottomed hole at b).

Figure 6.12: Diagrams of a) the constant depth defect and b) a flat bottomed hole defect that were simulated to show the difference between the two situations and the difference from defects in a plate.

This distinction between a flat bottomed hole in a plate compared to a flat bottomed hole in a pipe brings another consideration to the testing of defects in a pipe. In a plate structure, the generation of the same depth defect in either side of the plate should be identical in terms of the geometry of the defect and the effect that the defect has on the guided wave, with the SH waves as sensitive to internal defects as they are to external defects. However, due to the curvature of the pipe, an equivalent depth flat bottomed hole on the internal and external surface of the sample is different in terms of the structure of the defect and how it will affect the

wave propagation. The difference being that the external defect will move from a maximum remaining depth through a minimum wall thickness and back to the original depth, whereas the internal defect of the same dimensions will increase its remaining depth at the centre of the defect, which will produce different results. This distinction is important as it greatly affects the signals received from the defective areas.

To illustrate the differences that are seen with the range of different defects, both the flat bottomed hole case and the constant depth defect case have been modelled in PZFlex, with the same circumferential extent as the experimental defect but with the different defect structures and depths to illustrate being above and below the cut off thickness. Some of these cases show markedly different behaviour to the corrosion patch style defect that has been studied in both experiments and simulations, due to the distance in which the transition from the defect to the full thickness of the sample is found. In the flat bottomed hole case, the defect is a reasonable analogue to the corrosion patch when the depth of the defect is low, as the transition to the full depth of the defect is gradual in this case although not as gradual as the corrosion patch style case.

The problem with using this type of defect arises when the defect falls below the cut off thickness of the CSH1 mode in the sample. Above the cut off thickness at a 2 mm depth the defect simply slows the CSH1 and speeds the CSH0 mode up in the received signal. When the value gets closer to the cut off thickness at 3 mm depth, the signal received shows some mode conversion as a portion of the signal falls below the cut off thickness, but most of the signal is still above the cut off, so propagates as a slower, more dispersive CSH1 waveform. As the frequency of the CSH1 mode goes entirely below the cut off thickness, the behaviour diverges from the corrosion patch style defect in terms of the reflection behaviour of the modes.

For the case where the maximum defect depth matches that of the experimental defect, the A-scan data with labelled waveforms is presented in Figure 6.13a, with the corresponding STFT of the signal in Figure 6.13b. Here the reflected portion of the CSH0 mode converts into the CSH1 mode, there is also considerable reflection of the CSH0 mode from the far edge of the defect, which again mode converts into the CSH1 mode when it leaves the defect. The equivalent behaviour also occurs from the wave travelling in the opposite direction, although due to the different time spent as the different wave modes, the arrival times are different to the original reflected signals. In addition to this is, the reflection of the CSH1 mode from the initial interaction with the defect and with the far edge of the defect results in reflected CSH1 modes from the edge and the far edge respectively after

mode conversion to the CSH0 mode in the defect area. The effect of all this is a range of reflections from the edge of the defect that will not occur in general for the more realistic corrosion patch style defect.

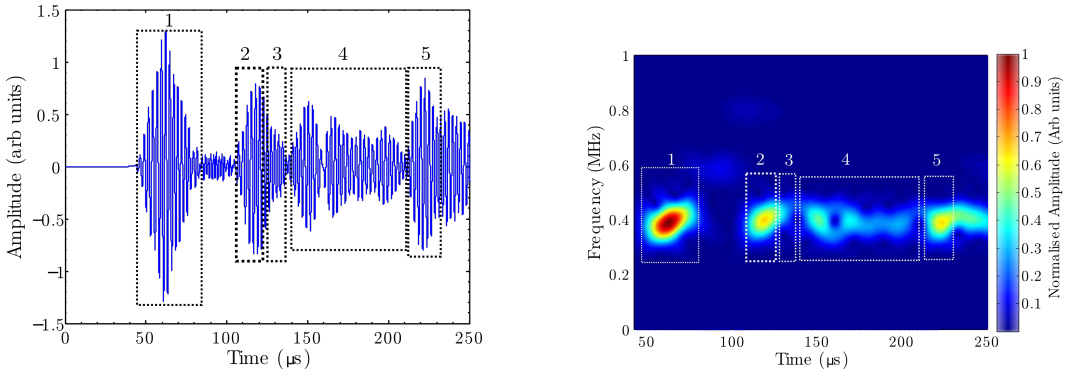

(a) (b)

Figure 6.13: Simulated flat bottomed defect of depth 4.8mm out of a pipe wall thickness of 7mm with a circumference of 534 mm, the structure of which is shown in Figure 6.12b. The short path signals are labelled at 1, with the long path CSH0 mode at 2, the mode converted CSH1 mode at 3 and a family of reflections from the defect at 4 that arrive predominantly as CSH1 modes. The CSH0 path having travelled the circumference plus the short path is labelled at 5.

The constant depth defect suffers similar problems with reflections due to the structure of the defect, the A-scan data for this defect is shown in Figure 6.14a, with the corresponding STFT in Figure 6.14b. Here there are a range of reflections from the edge of the defect and the further defect edge, although in this case there is not mode conversion of the reflected waves at the defect, with the modes remaining as their original mode when reflected. Reflections from inside the defect still exist in this case. The main difference compared to the flat bottomed hole case here is that the CSH0 mode appears to mode convert to the CSH1 mode after it propagates under the defect due to the short distance in which the sample goes from the full depth of the defect to the full thickness of the pipe. The CSH1 mode, as in the other cases, is forced to mode convert to the CSH0 mode under the defect and so arrives faster than the original CSH1 mode, this leads to the through propagation modes appearing close to each other in arrival time and at similar frequencies.

The identification of the origin of these modes has been achieved using a combination of both the A scan data acquired from PZFlex and the visualisation of the modes through the thickness of the sample at defect depths of 2 mm, 3 mm and 4.8 mm for both cases. Visualisation of the behaviour of the CSH0 only was also achieved by applying symmetrical forces on both the internal and external surface

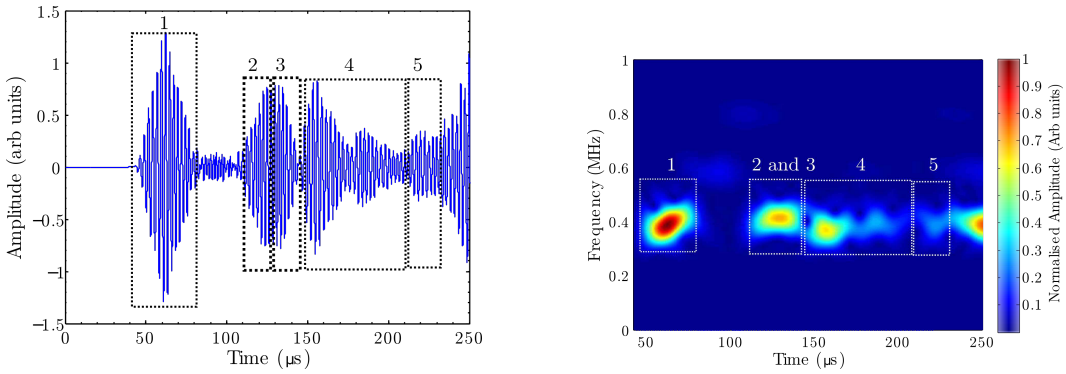

(a) (b)

Figure 6.14: Simulated constant depth defect of the form shown in Figure 6.12a, with a depth of 4.8 mm out of a thickness of 7 mm, and a circumference of 534 mm. The short path signals are labelled at 1, with the long path CSH0 mode that mode converts into an CSH1 mode after the defect, and the CSH1 mode that mode converts to CSH0 under the defect and then back to CSH1 after the defect shown at the section labelled 2 and 3. Section 4 shows the reflected waves from the defect edge and far edge, with the signals remaining as their initial mode type as they reflect and travel around the circumference to the receiver. The waveform labelled at 5 is what would be the CSH0 path having travelled the circumference plus the short path, but the earlier mode conversion affects its behaviour.

of the pipe, in order to suppress the generation of antisymmetric modes. This allowed the more complex mode conversion behaviour of the mode in the straight sided defect to be defined. An important distinction between these defects and the corrosion patch style tapering defect, is that the reflection occurs at different positions along the defect length. This is due to the abrupt nature of the edges causing reflection at the edge, whereas the tapered ends allow propagation into the defect before reflection occurs.

6.5 Flat bottomed holes experimentally

Scans were carried out on a sample with internal and external flat bottomed hole style defects and are presented here to illustrate several points. Firstly they are presented to show that the same size flat bottomed holes in a sample are not equivalent if they are on the internal and external surfaces. Secondly it shows that small defects of an axial length of 20 mm are detectable in general with the system, and thirdly it illustrates again the difficulty of sizing defects when they are close to each other axially.

A 535 mm outer circumference sample with a 7.5 mm thick pipe wall was

considered (Sample 5 in Table 5.1). One scan with the 8.8 mm wavelength EMATs (probe number two in Table 2.1) was carried out on an area with circular flat bottomed holes of 20 mm circumference, that had a 3.8 mm deep external defect followed by a 1.9 mm deep external defect, then a 3.8 mm deep internal defect and finally a 1.9 mm deep internal defect as illustrated in Figure 6.15a. The regions over which these defects occur are indicated by the areas numbered 1 to 4 on the ultrasonic waveform scan respectively in Figure 6.16a.

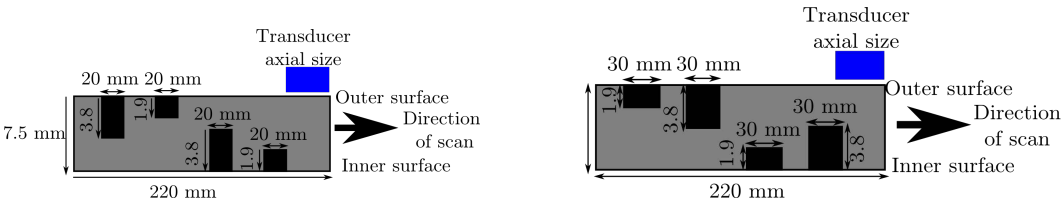

Figure 6.15: Schematic diagrams of the axial position of the flat bottomed hole defect (all measurements in mm) for a) the 20 mm circumference defects and b) the 30 mm circumference defects. The axial size of the transducer is also provided in blue (to scale).

The other half of the sample had circular flat bottomed holes of 30 mm circumference, starting from a 1.9 mm deep external defect, a 3.8 mm deep external defect and then a 1.9 mm deep internal defect and a 3.8 mm deep internal defect as illustrated in Figure 6.15b. These are labelled 1 to 4 respectively in Figure 6.16b.

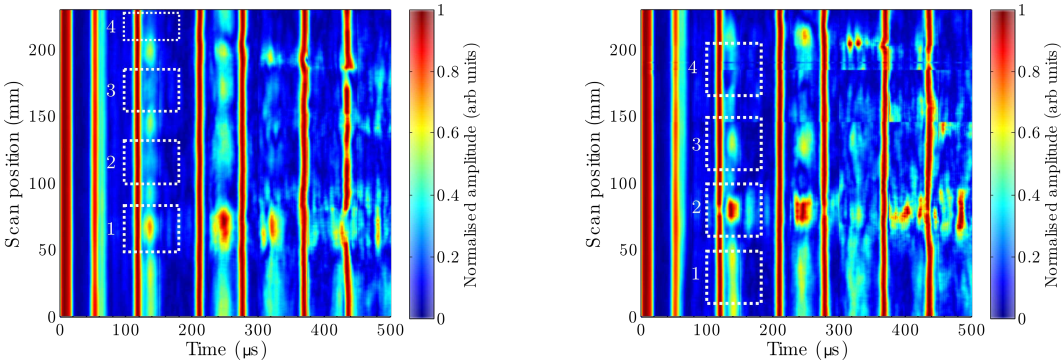

Figure 6.16: The effect of closely spaced flat bottomed hole defects on the internal and external surface of a sample to illustrate the detectability of the defects. Precise depth gauging for the separate defects and axial sizing would not be possible due to the close axial positioning of the defects.

Axial sizing of these defects would be difficult as the axial size of the active

area of the transducer is 40 mm and the separation between the defects is small, such that the transducer beam will interact at least partially with the defects at most positions. The 20 mm diameter defects are less obvious, as more energy in the ultrasonic beam can travel from the transmitter to the receiver without encountering the defect, resulting in a waveform that is a combination of the clear path signal and the signal affected by the defect. However, the defects can still be identified and it shows that the defects have a different effect on the signal due to the curvature of the pipe if they are internal or external. This would not be the case if they were truly identical defects in terms of depth from the inner and outer surface. This indicates that the method is sensitive to both internal and external defects but that they can't necessarily be differentiated from each other.

6.6 Welded areas

Another factor in the inspection of real samples is the presence of more complicated pipe areas such as bends and welded areas. It has been shown previously that SH waves in a plate can be transmitted around corners [93], so it is thought that the presence of the much more gradual bends in the samples will not hamper this technique, although samples weren't available to test this. Of more interest in the cases considered here are the presence of welds in a sample [166]. A weld will present an area of increased thickness to the guided wave and an area that is heat affected, which could change the behaviour of the guided waves. If the welds connect two sections of pipeline, then the effect that is likely to be seen is the change in thickness as the probes are scanned past the weld. Given the small axial extent of the weld, this shouldn't disrupt the signal too much, but runs the risk of masking any defects in the weld area due to the overarching behaviour of the weld obscuring any defect signals.

Another issue for this method would be if the pipe is held in a support which is welded to the pipe. Some of the experiments carried out in blind trials by Sonomatic have shown the effect of welds on these scans by having a wrapper plate stitch welded onto the pipe in order to cover the defects that have been artificially induced in the sample. The samples tested here had a circumference of 695 mm with a wall thickness of 8.18 mm (Sample 6 Table 5.1) and had a range of defects induced varying from large wall thinning patches to small diameter holes. The wrapper plate is welded to the sample at the ends and at two patches along the length of the plate, the dimensions and positions of the weld are shown in the schematic in Figure 6.17.

Encoded scans are carried out on these samples with the 8.8 mm wavelength

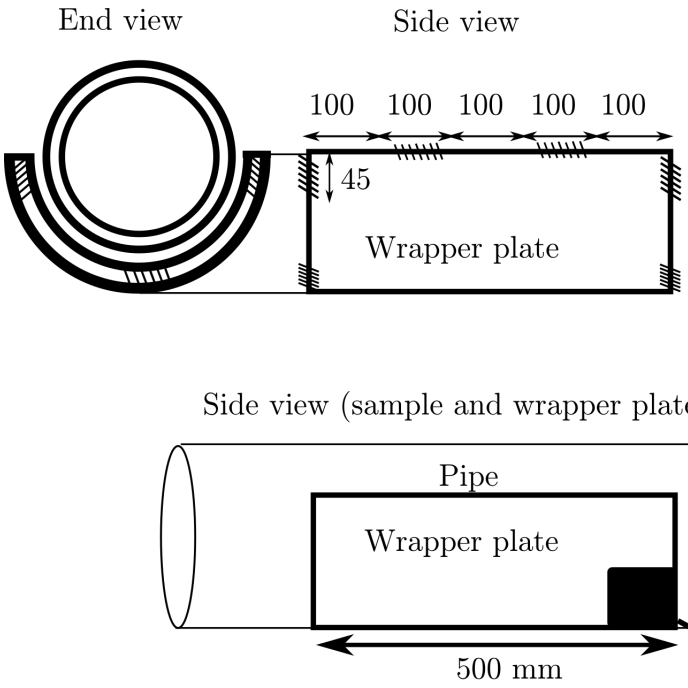

Figure 6.17: Dimensions of the sample with the wrapper plate and the position of the welds, the encoded scan extends slightly further to either side of the wrapper plate area.

probes (probe number two in Table 2.1) and the results assessed to see the effect of the welds on the received signals to investigate the difference between an area with a weld, a clear area and an area with a defect. The welds at the beginning and end of the wrapper plate can be seen in the scans as sections where the clear area is disrupted, with a small axial extent, these are labelled at 1 and 7 in Figure 6.18. The scan then goes through a 100 mm section of clear area shown at 2, followed by a length of 100 mm where there is a weld shown at 3, another 100 mm of clear area at 4, followed by a weld area at 5 and a non welded area with a 25 percent wall loss defect present at 6. These different sections can be highlighted in the scans, with the areas where the weld is present showing different behaviour to the clear areas.

The non defective areas show the expected CSH0 and CSH1 behaviour with a constant constant arrival time and amplitude of the two modes generated. The areas with the axial welds show a range of reflections predominantly appearing to be from the CSH1 mode, where it has reached the weld and been reflected, with signals from the mode travelling in either direction around the pipe and arriving between the long path and the short path plus the circumference. Reflections also appear between the short and long path for the welded areas but are of low amplitude.

The defect area shows considerably higher amplitude reflections due to reflection from the edge of the defect, which has a greater effect on the guided wave modes, with a clear waveform seen before the long path and after the long path due to the positioning of the defect closer to the transmitter rather than at the 6 o'clock position. Since this defect is artificial it represents an abrupt change so much of the energy reflected. The effect of the welds on the received data can be illustrated in the encoded scan shown in Figure 6.18, with the low amplitude reflections seen from the weld area having much less effect on the signal than the defect.

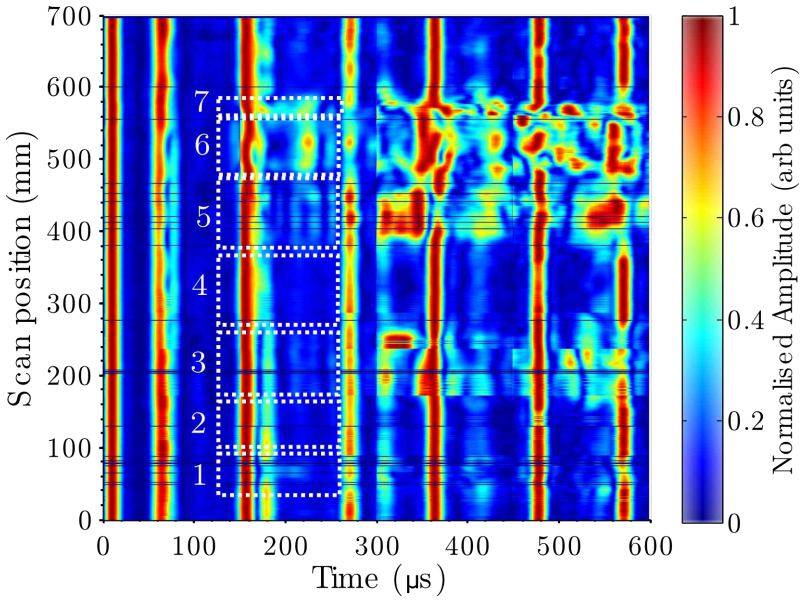

Figure 6.18: Encoded scan of a sample with a plate wrapped around the bottom half and welded onto the surface of the pipe at the axial ends of the plate and at two positions along the axial length of the wrapper plate. The welds at each end of the pipe are labelled 1 and 7, with the areas in which there is no weld affecting the signal labelled 2, 4 and 6, with a 25 percent wall loss defect at 6 and two weld areas at 3 and 5. The main difference being the multiple reflections seen in the weld areas between the long path and the signal that have travelled a circumference and a short path.

The scans carried out here showed that welded areas will have an effect on the signals in terms of the extent of reflection that will occur and it is likely to have an effect on the through transmitted waveforms. However, due to the short circumferential extent of welds, this effect is not thought to be significant compared to the effects that a corrosion patch style defect has on the CSH0 and CSH1 signals. It appears that the weld signals could give a characteristic response, with the reflections seen in the areas labelled at 3 and 5 in 6.18 being very similar.

However, further study of this would be necessary to come to more firm conclusions of the effect due to the artificial defects used here not being representative of real corrosion patches.

6.7 Conclusions

This chapter has been concerned with the application of the methods established in Chapter 5 to pipe samples with in-service corrosion patches. It has illustrated the advantages of scanning with a small axial step and having a set separation between probes. It has featured some quantification of sections of defects with different depths and circumferential extent using in-service defects. The use of the method on blind trials has illustrated the ease of detection of defects, giving axial sizing and defect severity data for samples with unknown defects. The method was applied to a sample with a range of defects at different axial and circumferential positions, with a range of severity in terms of defect depths. These defects were characterised in terms of severity and their length estimated in terms of axial extent, as well as the position of the defects around the circumference inferred. This sample illustrated the method working on a range of complex defects and showed its strengths at defect detection and characterisation but also its weaknesses in terms of defects that overlap in their axial extent, which can hamper defect depth sizing and axial sizing. It also illustrated the effect of a greater degree of lift off of the probes, which makes them more inefficient in terms of the ultrasound they can generate and receive in the sample, which can cause issues if the defective area is situated underneath the path of the probes on the surface.

In addition to this usage on more complex defects, the chapter also considered the modelling of different calibration defects and has identified the weaknesses of these defects in that the thickness of the sample rapidly goes from the full thickness to the full defect depth thickness. This causes much more reflection than is seen in corrosion patch cases and changes in behaviour of the through-propagating modes, which can make these artificial calibration defects non representative of an actual corrosion patch. Following on from the modelling of these situations, flat-bottomed-hole style calibration defects are scanned experimentally. The experimental scans of these samples are used to illustrate the change in the profile of a defect if it is on the internal or external surface of a sample and are also used to illustrate the difficulties of measuring the axial length of defects when they are not well separated in the axial direction. The defects in question had either a 25% remaining wall or 50% remaining wall thickness and a diameter of 20 or 30 mm, but all were able

to be detected in the scans. However, the smaller diameter, smaller depth defects were approaching the limits of detectability here, as much of the signal bypasses the defect on the way to the receiver and the effect of the depth on the CSH1 mode is minimal. The behaviour of the internal defects was different to the external defects due to the curvature of the sample.

The chapter concluded with an assessment of the effect of welded material onto the outer surface of the sample, with a small axial length welded area easy to identify in a scan as having a small effect on the signal in that area. The longer axial extent welds had much more of an effect on the data, with considerable reflections seen compared to a normal section of the pipe. A defect of 25% depth can be seen in the data as it has a long axial extent but smaller defects or less severe defects in welded areas may be difficult to identify against the background of the differences caused by the welded area.

Chapter 7

Conclusions

7.1 Main Conclusions

There are a range of NDT tools available to industry to test pipeline integrity that operate at various levels of accuracy and are applicable in different situations. The tool presented in this Thesis was designed to solve the problem of screening large areas of pipeline, with a limited access to the pipe, as an alternative to PIG inspections. It was also designed as an alternative to the commonly used guided wave tools in industry that perform long range guided wave measurements axially along the pipe, which require full circumferential access. Tools exist that used mid range guided waves from the exterior of the pipeline as is implemented here, but little information was found relating to their performance on real samples, and very few treat the situation in the circumferential way, often resorting the estimation of an unfolded plate for simplicity.

The work presented in Chapter 3 considered the optimum frequencies of operation of EMATs on a pipe sample. This illustrated the differences between a plate sample and a pipe sample, showing that the different geometry of a sample leads to different peak frequencies of operation for the probes and similar (but different) force profiles on the surface of a sample leading to similar (but different) spatial bandwidths and nominal wavelengths. The efficiency of generation and detection of different order modes in a sample was considered, showing that in a plate sample modes up to the SH3 mode can be seen and possibly used for defect detection (although the higher order modes are more dispersive and less likely to be useful in experiment). In contrast when the circumferentially travelling modes are considered, the CSH2 is of low amplitude and the CSH3 mode is not detectable in a pipe sample of 534 mm circumference. This is thought to be because of poor generation

and detection efficiency of these higher order modes in the pipe sample due to the different lift off conditions that are experienced by the flat probe on the curved surface. This initial work therefore restricted the useful modes for inspection to the CSH0 and CSH1 modes and provided information on how to find the optimum frequency at which to operate these modes. The use of an industrially viable pulser receiver signal was considered in this chapter, giving a procedure for carrying out effective scans and illustrating the equipment used to take these measurements.

The remaining work in the Thesis in Chapters 5 and 6 was concerned with addressing what happens when circumferentially travelling shear horizontal waves interact with a defect in the form of a corrosion patch in a pipe wall. A range of samples of varying wall thickness, coating condition and pipe circumference were studied to be representative of the different samples that are in use in industry, with an emphasis on the thin walled carbon steel pipeline that is more prone to catastrophic failure. These samples featured a range of artificial defects and real in-service generated corrosion patches in order to demonstrate the system operating not only on a sample with known defect dimensions and severity but also on the sort of corrosion patch style defects that are likely to be encountered when applying this method in industrial applications.

Chapter 5 introduced the samples that were considered in this Thesis and gave a brief introduction to the effects that are expected on the guided wave modes when they interact with a defect of a certain depth, namely the increase in velocity of the CSH0 mode when a thinner area is encountered, and the decrease in velocity or mode conversion of the CSH1 mode when encountering an area that has a remaining wall thickness above or below the cut-off thickness of the mode. It continued to address the filtering requirements of the system when used in industry, illustrating the possible leakage from the industrial system and effective close filtering around the generation frequency in order to achieve a good quality signal for an inspection. For application in industrial contexts where time may be a critical factor, the single frequency between the CSH0 and CSH1 peak frequencies was identified as optimal, with tight filters around the generation frequency to generate an initial indication of where defects are located. Although this provides an almost instant idea of the defect and its severity, it risks losing data such as reflections with the filtering applied if the frequency is altered significantly from the generation frequency. The effect of an artificial defect with known dimensions and depth was used to investigate the behaviour of the CSH0 mode and CSH1 modes when they interact with a defect that has a remaining wall thickness below the cut-off thickness of the CSH1 mode, with the mode converted waveforms and reflected waveforms from interaction with the

defect shown. The experimental data was used to evaluate the axial and circumferential sizing capabilities of the system, showing that for a single defect axial sizing can be very effective with this method, but circumferential positioning remains an estimate based on reflections.

A finite element model of this defect and the ultrasonic waves that are generated by the EMATs was developed and used to investigate this mode conversion and reflection behaviour. This model is expanded to defects of different depths to show the changes when the thickness of a sample is reduced to below the cut-off thickness of the CSH1 mode at a defect. Important to note here was that once the frequency thickness at the defect area is below the cut-off thickness, all of the CSH1 mode mode converts under the defect in order to propagate through it, which results in a single mode converted signal. However, if the full bandwidth of the signal is not below the cut-off of the mode then some mode conversion can be seen along with a slowed, more dispersive mode that is related to a change in thickness to a level above the cut-off thickness of the CSH1 mode.

The modelling is also extended into changing the circumferential extent of the defect both above and below the cut-off thickness of the CSH1 mode. When above the cut-off thickness the CSH1 signals received will increase in arrival time as the defect becomes longer in circumferential extent, as the mode travels for a greater proportion of time as the slower CSH1 mode expected in a thinner section of pipe. However, once the cut-off thickness of the mode is reached, the received CSH1 modes, although arriving where a mode converted signal would be expected, travel slower when the defect's circumferential extent is increased due to the increased proportion of time they propagate as the slower CSH1 mode in addition to the faster CSH0 mode under the defect.

This result and those presented in the rest of the experimental and modelling sections in Chapter 5 suggest that the profile of a defect, (in terms of its structure and where in the profile it reaches its maximum depth) has a large effect on the arrival time of different wave modes using this method, which suggests that the remaining wall thickness cannot be calculated exactly using this method without prior knowledge of the defect profile. This limits the technique to a method for screening for severity in its current form, as the thickness cannot be calculated sufficiently accurately without prior knowledge of the defect depth profile.

Chapter 6 applied the results from the basic analysis and modelling of a defect in Chapter 5 to more complex situations such as in-service corrosion patches. Initially a single corrosion patch was chosen to illustrate the axial sizing and circumferential positioning capabilities of the system with some consideration of how

to identify more severe parts of the same defect. The importance of a small axial distance step and probe separation on the surface was illustrated through comparison of manual scans and those with an experimental rig to hold the transducers. The use of the system to identify the presence of defects and provide axial sizing and defect depth severity information in blind trials was shown, with 100% detection rate of defects. These blind trials have been extended within Sonomatic to a greater range of samples and in various different environmental conditions, proving its effectiveness in this screening application.

A sample with multiple defects, with varying severity and positioning was tested to illustrate the range of different defects for which the method is applicable and to highlight some of the strengths and weaknesses of the method. The strengths of the method were shown in the ability to detect the defect and categorise in terms of severity and to separate the circumferential positioning of the defects into lying in the short path or the long path between the transducers. Weaknesses in the method were highlighted where different defects lie at the same position axially but different positions circumferentially (within the same path) as these cannot be differentiated from each other. The issue of a defect directly underneath the transducers was also highlighted, as this alters the lift off of the transducers in transmission or reception and will remove information about the defects from a scan.

The weaknesses of some types of calibration defects were considered with reference to a corrosion patch style defect, with both a constant depth defect and a flat-bottomed-hole style defect considered. The artificial defects investigated all showed a much greater level of reflection than in the more realistic corrosion patch style defect examined due to the abrupt changes in thickness they featured. These abrupt changes in thickness were shown to change the behaviour of the through-propagating modes and make their results less representative of the experimental data. These issues are mitigated if the defect has a gradual change in thickness towards the maximum depth and therefore a move to defects more representative of this style is suggested. Experimental measurements of flat-bottomed-hole style defects were included to illustrate the difficulties in measuring the axial size of defects when they are not well separated in the axial direction, but also illustrated the capability to see the minimal effects from a small diameter, small depth defect of 20 mm diameter and 25% wall thickness defect.

The effect of welds on the ultrasonic signals has been briefly studied since this is a factor that will be seen in industrial samples if large lengths of pipeline are desired to be scanned. Welds were found to have some effect if they are in the axial direction of the pipe when panels are welded to the exterior of the pipe but

the effect of circumferential welds is minimal in these studies and not apparent in the experimental data.

The result of this Thesis has been a robust screening system for detecting and partially quantifying corrosion patch style defects, with underlying physics of these inspections illustrated. The system can provide defect sizing and positioning information and can give an indication of the range in which the minimum remaining wall thickness will lie for the sample. More in depth measurement of the remaining wall thickness of the sample is not possible in its current iteration, as it was shown that the defect structure plays an important role in affecting the arrival time of the through propagating signals. The defect structure was shown to have a large influence on the extent of time that the different wave modes propagate at different speeds. This means that in order to have a more precise measurement of the remaining pipe wall in the defect area, the operator would need prior knowledge of the defect structure.

It is well suited as a screening method to indicate where damage has occurred and reached a safety critical point in the pipeline, and to carry out fast measurements on long sections of pipe. The work in this Thesis has explored the current limitations of the system and provided explanations for the signals seen in the application of the system industrially. Separately to the results presented in this Thesis, the system has been validated in blind trials in various countries with the sponsor company Sonomatic. In laboratory tests, the techniques have been able to be used on a wider range of pipe wall thicknesses, up to 19 mm thick (with the appropriate wavelength transducers) and on samples with an outer circumference of 2.2 metres, illustrating the versatility of the system and the testing procedures.

7.2 Further work

This Thesis has described and explained the capabilities and limitations of a circumferential guided wave screening system both theoretically and in practice for simulated and real corrosion patches. The use of the circumferential dispersion curves has made this study more relevant to the pipe case than those that assume it to be equivalent to a plate, but in order to fully characterise the coated pipes, a further step would be to investigate the effect of the coating layer on the dispersion curves and the changes that occur to the displacement profiles of the modes due to the curved structure. These factors have been neglected for the sake of simplicity in this work, but in reality will affect the dispersion curves and a full characterisation would be necessary if more accurate speed measurements for wall thickness are to

be attempted.

The limitation of the axial sizing of the defect by the axial size of the transducer could be mitigated by developing probes with a smaller axial extent in order to maximise the axial resolution of the scan. This would involve decreasing the axial footprint of the active area of the probe perhaps by using different types and arrangements of magnets. The difficulty here would be in ensuring the magnetic fields are still of a satisfactory strength to excite the waves at a measurable amplitude and that the forces generated are those desired. This would allow for more accurate measurement of small axial extent defects and the differentiation between closely spaced defects in the pipe axially.

The circumferential sizing and positioning of the defects provide another opportunity for further study, as these are still low accuracy in this study. If coherent reflections from the edge of the defect can be found in the received signal, the circumferential positioning and sizing could be improved by using two receivers at different circumferential positions, in order to take advantage of the different times of arrival of the reflections. However, as was shown, the position at which the signals reflect depends on the structure of the defect, which is likely to be unknown, so this would remain an estimate of the size and position.

The coating thickness through which adequately high amplitude signals for defect testing are generated and received is around 1 mm in the current system. This is a clear area for improvement, as coating thicknesses in real samples are often quite variable. Further development of transducer design could improve this limitation of lift off, as transducer design was not considered in detail here. Further modelling of the full electrodynamic system of the transducer and sample in COMSOL could be carried out to further probe the theoretical limits of lift off from the pipe surface.

A relatively straight forward way of testing this technique on the real corrosion patches would be to map the defect depths and compare this against the results that are obtained. This information was not made available for the defects considered here, primarily as they were considered in a series of blind trials for the detectability of the defects over the depth sizing capabilities. However, for many of the results, the defect surface would have been available for corrosion mapping techniques if these had been available.

Obtaining the accurate depth profiles of these defects would have allowed the modelling of these more complicated defects in PZFlex, to assess the behaviour in a complex situation, with differing depths through the profile of the defect, so this is another area that could be considered. The depth profiles could have been obtained by corrosion mapping of the sample in order to obtain a shape and depth

profile of the defect which could then be approximated in the modelling by inputting the design of the defect into PZFlex. This could be carried out along with the full three dimensional modelling of the defects, which is not carried out here due to the computational load and real time duration proving impractical for the computing facilities available in this work.

Development work on a full subsea version of the system is ongoing at Sonomatic, with the main difference between the topside and subsea versions being the design of the probes, such that they can withstand high pressures and remain functional. Measurements otherwise should be predominantly similar and provide a preferable scanning technique to methods that use Lamb like waves for example, due to the shear waves not propagating in the liquid medium, which will result in less problems associated with energy leakage.

References

[1] A. S. H. Makhlouf and M. Aliofkhazraei. *Handbook of Materials Failure Analysis with Case Studies from the Oil and Gas Industry*. Elsevier Science, 2015.

[2] E. McCafferty. *Introduction to Corrosion Science*. Springer New York, New York, 2010.

[3] International ASM. *Corrosion in the Petrochemical Industry, Second Edition:*. A S M International, 2015.

[4] HSE. Evaluation of the effectiveness of non-destructive testing screening methods for in-service inspection(HSE research report) [Online]. Available: http://www.hse.gov.uk/research/rrpdf/rr659.pdf [Accessed: 24-Aug-2015]., 2009.

[5] A. Cosham, P. Hopkins, and K.A. Macdonald. Best practice for the assessment of defects in pipelines Corrosion. *Engineering Failure Analysis*, 14(7):1245–1265, 2007.

[6] D. Mukherjee, S. Saha, and S. Mukhopadhyay. Inverse mapping of magnetic flux leakage signal for defect characterization. *NDT & E International*, 54:198–208, 2013.

[7] K.F. Bainton. Characterizing defects by determining magnetic leakage fields. *NDT International*, 10(5):253–257, 1977.

[8] J. L. Rose. *Ultrasonic waves in solid media*. Cambridge University Press, Cambridge; New York, 1999.

[9] M. Hirao and H. Ogi. *EMATs for science and industry: noncontacting ultrasonic measurements*. Kluwer Academic Publishers, London, 2003.

[10] B. Hull and V. John. *Non-destructive Testing*. Springer, 1988.

[11] W. J. McGonnagle. *Nondestructive testing*. Gordon and Breach, 1966.

[12] D. E. Bray and D. McBride. *Nondestructive Testing Techniques*. New Dimensions In Engineering Series. Wiley, 1992.

[13] J. Blitz and G. Simpson. *Ultrasonic Methods of Non-destructive Testing*. Non-Destructive Evaluation Series. Springer Netherlands, 1995.

[14] P. E. Mix. *Introduction to Nondestructive Testing: A Training Guide*. Wiley, 2005.

[15] K.A. Fowler, G.M. Elfbaum, K.A. Smith, and T.J. Nelligan. Theory and Application of Precision Ultrasonic Thickness Gauging. *Insight-Non-Destructive Testing*, 38:582–587, 1996.

[16] S. Dixon, C. Edwards, and S. B. Palmer. High accuracy non-contact ultrasonic thickness gauging of aluminium sheet using electromagnetic acoustic transducers. *Ultrasonics*, 39(6):445–453, 2001.

[17] S. Dixon, P. A. Petcher, Y. Fan, D. Maisey, and P. Nickolds. Ultrasonic metal sheet thickness measurement without prior wave speed calibration. *Journal of Physics D: Applied Physics*, 46(44):445502, 2013.

[18] R. J. Smith, W. Li, J. Coulson, M. Clark, M. G. Somekh, and S. D. Sharples. Spatially resolved acoustic spectroscopy for rapid imaging of material microstructure and grain orientation. *Measurement Science and Technology*, 25(5):55902, 2014.

[19] D. P. Almond and S. G. Pickering. An analytical study of the pulsed thermography defect detection limit. *Journal of Applied Physics*, 111, 2012.

[20] A. Demma, P. Cawley, M. Lowe, A.G. Roosenbrand, and B. Pavlakovic. The reflection of guided waves from notches in pipes: a guide for interpreting corrosion measurements. *NDT & E International*, 37(3):167–180, 2004.

[21] M. J. Lovejoy. *Penetrant Testing: A practical guide*. Springer Netherlands, 1991.

[22] M. J. Lovejoy. *Magnetic Particle Inspection: A practical guide*. Springer Netherlands, 1993.

[23] D. P. Almond and S. G. Pickering. Analysis of the defect detection capabilities of pulse stimulated thermographic NDE techniques. *AIP Conference Proceedings*, 1581(33):1617–1623, 2014.

[24] S.R. Baughman. Application for thermal NDT on advanced composites in aerospace structures. *Proc. SPIE 3361, Thermosense XX*, 3361:311–319, 1998.

[25] K. Kim, K. Kim, H. Jung, and H. Chang. Measurement of defect thickness of the wall thinning defect pipes by lock-in infrared thermography technique. *International Conference on Experimental Mechanics*, 7522:1–6, 2009.

[26] P. Bison, S. Marinetti, G. Cuogo, B. Molinas, P. Zonta, and E. Grinzato. Corrosion detection on pipelines by IR thermography. In Morteza Safai and Jeff R. Brown, editors, *Proc. SPIE*, volume 8013, page 80130F, 2011.

[27] J. W. Kim, K. W. Yun, and H. C. Jung. Investigation of optimal thermal injection conditions and the capability of IR thermography for detecting wall-thinning defects in small-diameter piping components. *Nuclear Engineering and Design*, 262:39–51, 2013.

[28] D. E. Bray and R. K. Stanley. *Nondestructive Evaluation: A Tool in Design, Manufacturing and Service*. Taylor & Francis, 1996.

[29] B. Lebrun, Y. Jayet, and J.-C. Baboux. Pulsed eddy current signal analysis: application to the experimental detection and characterization of deep flaws in highly conductive materials. *NDT & E International*, 30:163–170, 1997.

[30] A. McNab and J. Thomson. An eddy current array instrument for application on ferritic welds. *NDT & E International*, 28(2):103–112, 1995.

[31] R. Halmshaw. *Non-destructive Testing*. Metallurgy and materials science. Edward Arnold, 1991.

[32] H.A. Wheeler. Formulas for the Skin Effect. *Proceedings of the IRE*, 30(9):412–424, 1942.

[33] D. G. Park, C. S. Angani, and Y. M. Cheong. Differential Pulsed eddy current probe to detect the sub surface Cracks in a Stainless Steel Pipe. In *18th World Conference on Nondestructive Testing*, Durban, 2012.

[34] P. W. van Andel, M. Lorenz, and R. E. R. Meyer. Eddy current inspection technique (patent), 2001.

[35] J. E. Lenz. A review of magnetic sensors. *Proceedings of the IEEE*, 78(9036163):973–989, 1990.

[36] Z.D. Wang, K. Yao, B. Deng, and K.Q. Ding. Quantitative study of metal magnetic memory signal versus local stress concentration. *NDT & E International*, 43(6):513–518, 2010.

[37] Z.D. Wang, K. Yao, B. Deng, and K.Q. Ding. Theoretical studies of metal magnetic memory technique on magnetic flux leakage signals. *NDT & E International*, 43(4):354–359, 2010.

[38] M. Roskosz. Metal magnetic memory testing of welded joints of ferritic and austenitic steels. *NDT and E International*, 44(3):305–310, 2011.

[39] H. Y. Wei and M. Soleimani. A magnetic induction tomography system for prospective industrial processing applications. *Chinese Journal of Chemical Engineering*, 20(2):406–410, 2012.

[40] B. J. Darrer, J. C. Watson, P. Bartlett, and F. Renzoni. Toward an automated setup for magnetic induction tomography. *IEEE Transactions on Magnetics*, 51(1):18–21, 2015.

[41] R. Halmshaw. *Industrial Radiology: Theory and practice*. Non-Destructive Evaluation Series. Springer Netherlands, 2012.

[42] U.K Government. The Ionising Radiations Regulations, 1999.

[43] HSE. HSE information sheet: Industrial radiography - managing radiation risks[Online]. Available: http://www.hse.gov.uk/pubns/irp1.pdf [Accessed: 25-Mar-2013]., 2000.

[44] K. Marstboom. Computed radiography for corrosion and wall thickness measurements. *Insight-Non-Destructive Testing*, 41(5):308–309, 1999.

[45] F. Benmeddour, S. Grondel, J. Assaad, and E. Moulin. Experimental study of the A0 and S0 Lamb waves interaction with symmetrical notches. *Ultrasonics*, 49(2):202–5, 2009.

[46] D. Marioli, C. Narduzzi, C. Offelli, D. Petri, E. Sardini, and A. Taroni. Digital time of flight measurement for ultrasonic sensors. In *IEEE Instrumentation and Measurement Technology Conference*, number 2, pages 198–201. IEEE, 1991.

[47] BSI. Specifcation for acceptance levels for internal imperfections in steel plate, strip and wide flats, based on ultrasonic testing, 1999.

[48] M. G. Silk and B. H. Lidington. The potential of scattered or diffracted ultrasound in the determination of crack depth. *Non-Destructive Testing*, 8(June):146–151, 1975.

[49] L. W. Schmerr. *Fundamentals of Ultrasonic Phased Arrays*. Solid Mechanics and Its Applications. Springer International Publishing, 2014.

[50] F. Ravenscroft, R. Hill, C. Duffill, and D. Buttle. CHIME-A new Ultrasonic Method for Rapid Screening of Pipe, Plate and Inaccessible Geometries. In *7th European Conference on Non Destructive Testing*, page 103, 1998.

[51] P. Wilcox, M. Lowe, and P. Cawley. The effect of dispersion on long-range inspection using ultrasonic guided waves. *NDT & E International*, 34(1):1–9, 2001.

[52] D. N. Alleyne and P. Cawley. Optimization of lamb wave inspection techniques. *NDT & E International*, 25(1):11–22, 1992.

[53] P. D. Wilcox. A rapid signal processing technique to remove the effect of dispersion from guided wave signals. *IEEE transactions on ultrasonics, ferroelectrics, and frequency control*, 50(4):419–27, 2003.

[54] R. S. Edwards, S. Dixon, and X. Jian. Characterisation of defects in the railhead using ultrasonic surface waves. *NDT and E International*, 39:468–475, 2006.

[55] D. N. Alleyne and P. Cawley. The excitation of Lamb waves in pipes using dry-coupled piezoelectric transducers. *Journal of Nondestructive Evaluation*, 15(1):11–20, 1996.

[56] M.J.S. Lowe, D.N. Alleyne, and P. Cawley. Defect detection in pipes using guided waves. *Ultrasonics*, 36(1-5):147–154, 1998.

[57] G. Liu and J. Qu. Guided Circumferential Waves in a Circular Annulus. *Journal of Applied Mechanics*, 65(June 1998):424, 1998.

[58] A. Demma, P. Cawley, M. Lowe, and A. G. Roosenbrand. The reflection of the fundamental torsional mode from cracks and notches in pipes. *The Journal of the Acoustical Society of America*, 114(2):611, 2003.

[59] D. Alleyne. Guided Wave Testing for touch point corrosion. In *18th World conference on NDT*, number April, pages 16–20, Durban, 2012.

[60] S. E. Burrows, B. Dutton, and S. Dixon. Laser generation of Lamb waves for defect detection: experimental methods and finite element modeling. *IEEE transactions on ultrasonics, ferroelectrics, and frequency control*, 59(1):82–9, 2012.

[61] D. N. Alleyne and P. Cawley. The interaction of Lamb waves with defects. *IEEE transactions on ultrasonics, ferroelectrics, and frequency control*, 39(3):381–97, 1992.

[62] A. Galvagni and P. Cawley. The reflection of guided waves from simple supports in pipes. *The Journal of the Acoustical Society of America*, 129(4):1869–80, 2011.

[63] K. R. Leonard and M. K. Hinders. Lamb wave tomography of pipe-like structures. *Ultrasonics*, 43(7):574–83, 2005.

[64] J. D. N. Cheeke. *Fundamentals and Applications of Ultrasonic Waves, Second Edition*. CRC series in pure and applied physics. Taylor & Francis, 2012.

[65] J. D. Achenbach. *Wave Propagation in Elastic Solids*. Applied mathematics and Mechanics, vol. 16. North-Holland Publishing Company, 1975.

[66] A. P. French. *Vibrations and Waves*. M.I.T. introductory physics series. Taylor & Francis, 1971.

[67] W. S. Slaughter. *The Linearized Theory of Elasticity*. Birkhauser Boston, 2012.

[68] K. F. Riley, M. P. Hobson, and S. J. Bence. *Mathematical Methods for Physics and Engineering: A Comprehensive Guide*. Cambridge University Press, 2006.

[69] M. Fukuhara and Y. Kuwano. Propagation characteristics of {SH} ultrasonic waves through the surface depth of an isotropic medium. *NDT & E International*, 31(3):201–210, 1998.

[70] R. B. King and C. M. Fortunko. Determination of inplane residual stress states in plates using horizontally polarized shear waves. *Journal of Applied Physics*, 54(6), 1983.

[71] C. M. Fortunko. Nondestructive evaluation of planar defects in plates using low-frequency shear horizontal waves. *Journal of Applied Physics*, 53(5):3450, 1982.

[72] J .A. Ogilvy. Ultrasonic beam profiles and beam propagation in an austenitic weld using a theoretical ray tracing model. *Ultrasonics*, 24(6):337–347, 1986.

[73] C. M. Fortunko and J. C. Moulder. Ultrasonic inspection of stainless steel butt welds using horizontally polarized shear waves. *Ultrasonics*, 20(3):113–117, 1982.

[74] J. A. Ogilvy. Ultrasonic reflection properties of planar defects within austenitic welds. *Ultrasonics*, 26(6):318–327, 1988.

[75] J. J. Ditri. Some results on the scattering of guided elastic SH waves from material and geometric waveguide discontinuities. *The Journal of the Acoustical Society of America*, 100(5):3078, 1996.

[76] A. Demma, P. Cawley, and M. Lowe. Scattering of the fundamental shear horizontal mode from steps and notches in plates. *The Journal of the Acoustical Society of America*, 113(4):1880, 2003.

[77] M.H. Rosli, R.S. Edwards, and Y. Fan. In-plane and out-of-plane measurements of Rayleigh waves using EMATs for characterising surface cracks. *NDT & E International*, 49:1–9, 2012.

[78] J. P. Charlesworth and J. A. G. Temple. *Engineering Applications of Ultrasonic Time-of-flight Diffraction*. Ultrasonic inspection in engineering series. Research Studies Press, 2001.

[79] F. Jenot, M. Ouaftouh, M. Duquennoy, and M. Ourak. Corrosion thickness gauging in plates using Lamb wave group velocity measurements. *Measurement Science and Technology*, 12:1287, 2001.

[80] Nurmalia, N. Nakamura, H. Ogi, and M. Hirao. Detection of shear horizontal guided waves propagating in aluminum plate with thinning region. *Japanese Journal of Applied Physics*, 50, 2011.

[81] M. Hirao and H. Ogi. An SH-wave EMAT technique for gas pipeline inspection. *NDT & E International*, 32(3):127–132, 1999.

[82] N. Nakamura, H. Ogi, and M. Hirao. Mode Conversion and Total Reflection of Torsional Waves for Pipe Inspection. *Japanese Journal of Applied Physics*, 52(7S):07HC14, 2013.

[83] WD Wang. Ultrasonic Lamb wave technique for measurement of pipe wall thickness at pipe supports (Patent), 1999.

[84] L Scrantz. System, method and apparatus for the ultrasonic inspection of liquid filled tubulars and vessels (patent), 1997.

[85] H. Lamb. On waves in an elastic plate. *Proceedings of the Royal Society A*, 93:114–128, 1917.

[86] W. Luo and J.L. Rose. Guided wave thickness measurement with EMATs. *Insight-Non-Destructive Testing*, 45(11):1–5, 2003.

[87] P. Cawley and D. Alleyne. The use of Lamb waves for the long range inspection of large structures. *Ultrasonics*, 34(2-5):287–290, 1996.

[88] R. P. Dalton, P. Cawley, and M. J. S. Lowe. The potential of guided waves for monitoring large areas of metallic aircraft fuselage structure. *Journal of Nondestructive Evaluation*, 20(1):29–46, 2001.

[89] M. H. Park, I. S. Kim, and Y. K. Yoon. Ultrasonic inspection of long steel pipes using Lamb waves. *NDT & E International*, 29(1):13–20, 1996.

[90] M. G. Silk and K. F. Bainton. The propagation in metal tubing of ultrasonic wave modes equivalent to Lamb waves. *Ultrasonics*, 17(1):11–19, 1979.

[91] A. Løvstad and P. Cawley. The reflection of the fundamental torsional guided wave from multiple circular holes in pipes. *NDT & E International*, 44(7):553–562, 2011.

[92] Y. Cho. Estimation of ultrasonic guided wave mode conversion in a plate with thickness variation. *IEEE transactions on ultrasonics, ferroelectrics, and frequency control*, 47(3):591–603, 2000.

[93] P.A. Petcher, S.E. Burrows, and S. Dixon. Shear horizontal (SH) ultrasound wave propagation around smooth corners. *Ultrasonics*, 54(4):997–1004, 2014.

[94] N. Nakamura, H. Ogi, M. Hirao, and K. Nakahata. Mode conversion behavior of SH guided wave in a tapered plate. *NDT & E International*, 45(1):156–161, 2012.

[95] X. Zhao and J. L. Rose. Guided circumferential shear horizontal waves in an isotropic hollow cylinder. *The Journal of the Acoustical Society of America*, 115(5):1912, 2004.

[96] W. Luo, X. Zhao, and J. L. Rose. A Guided Wave Plate Experiment for a Pipe. *Journal of Pressure Vessel Technology*, 127(3):345, 2005.

[97] N. Andruschak, I. Saletes, T. Filleter, and A. Sinclair. An NDT guided wave technique for the identification of corrosion defects at support locations. *NDT & E International*, 75:72–79, 2015.

[98] E. Moreno and P. Acevedo. Thickness measurement in composite materials using Lamb waves. *Ultrasonics*, 35(8):581–586, 1998.

[99] Z. Su, L. Ye, and Y. Lu. Guided Lamb waves for identification of damage in composite structures: A review. *Journal of Sound and Vibration*, 295(3-5):753–780, 2006.

[100] E. R. Dobbs. Electromagnetic generation of ultrasonic waves in metals. *Journal of Physics and Chemistry of Solids*, 31(8):1657–1667, 1970.

[101] F. Hernandez-Valle and S. Dixon. Initial tests for designing a high temperature EMAT with pulsed electromagnet. *NDT & E International*, 43(2):171–175, 2010.

[102] K. S. Ho, D. R. Billson, and D. A. Hutchins. Ultrasonic Lamb wave tomography using scanned EMATs and wavelet processing. *Nondestructive Testing and Evaluation*, 22(1):19–34, 2007.

[103] H. Ogi. Field dependence of coupling efficiency between electromagnetic field and ultrasonic bulk waves. *Journal of Applied Physics*, 82(8):3940, 1997.

[104] K. Mirkhani, C. Chaggares, C. Masterson, M. Jastrzebski, T. Dusatko, A. Sinclair, R. J. Shapoorabadi, A. Konrad, and M. Papini. Optimal design of EMAT transmitters. *NDT & E International*, 37(3):181–193, 2004.

[105] L. Kang, S. Dixon, K. Wang, and J. Dai. Enhancement of signal amplitude of surface wave EMATs based on 3-D simulation analysis and orthogonal test method. *NDT & E International*, 59:11–17, 2013.

[106] S. Hill and S. Dixon. Frequency dependent directivity of periodic permanent magnet electromagnetic acoustic transducers. *NDT & E International*, 62:137–143, 2014.

[107] Olympus. Olympus angle-beam transducers [Online]. Available: http://www.olympus-ims.com/en/ultrasonic-transducers/angle-beam/ [Accessed : 24-Aug-2015]., 2015.

[108] Olympus. Olympus shear-wave transducers [Online]. Available: http://www.olympus-ims.com/en/ultrasonic-transducers/shear-wave/ [Accessed : 24-Aug-2015]., 2015.

[109] T. R. Meeker. Thickness mode piezoelectric transducers. *Ultrasonics*, 10(1):26–36, 1972.

[110] G. Kossoff. The Effects of Backing and Matching on the Performance of Piezoelectric Ceramic Transducers. *IEEE Transactions on Sonics and Ultrasonics*, 13:20–30, 1966.

[111] I. S. Grant and W. R. Phillips. *Electromagnetism*. Manchester Physics Series. Wiley, 2013.

[112] R. Ribichini, P.B. Nagy, and H. Ogi. The impact of magnetostriction on the transduction of normal bias field EMATs. *NDT & E International*, 51:8–15, 2012.

[113] R. B. Thompson. Generation of horizontally polarized shear waves in ferromagnetic materials using magnetostrictively coupled meander-coil electromagnetic transducers. *Applied Physics Letters*, 34(2):175, 1979.

[114] R.B. Thompson. Physical Principles of Measurements with EMAT Transducers. In R N Thurston and ALLAN D Pierce, editors, *Ultrasonic Measurement Methods*, volume 19 of *Physical Acoustics*, pages 157–200. Academic Press, 1990.

[115] L. Laguerre, J.-C. Aime, and M. Brissaud. Magnetostrictive pulse-echo device for non-destructive evaluation of cylindrical steel materials using longitudinal guided waves. *Ultrasonics*, 39(7):503–514, 2002.

[116] Olympus. Olympus boiler tube thickness measurments [Online]. Available: http://www.olympus-ims.com/en/applications/thickness-boiler-tubes-emat-transducers/ [Accessed : 24-Aug-2015]., 2015.

[117] K. Kawashima. Quantitative Calculation and Measurement of Longitudinal and Transverse Ultrasonic Wave Pulses in Solid. *IEEE Transactions on Sonics and Ultrasonics*, 31:83–93, 1984.

[118] S. Huang, W. Zhao, Y. Zhang, and S. Wang. Study on the lift-off effect of EMAT. *Sensors and Actuators A: Physical*, 153(2):218–221, 2009.

[119] J. P. Morrison, S. Dixon, M. D. G. Potter, and X. Jian. Lift-off compensation for improved accuracy in ultrasonic lamb wave velocity measurements using electromagnetic acoustic transducers (EMATs). *Ultrasonics*, 44 Suppl 1:e1401–4, 2006.

[120] X. Jian, S. Dixon, R. S. Edwards, and J. Reed. Coupling mechanism of electromagnetic acoustical transducers for ultrasonic generation. *The Journal of the Acoustical Society of America*, 119(5):2693, 2006.

[121] C. F. Vasile and R. B. Thompson. Excitation of horizontally polarized shear elastic waves by electromagnetic transducers with periodic permanent magnets. *Journal of Applied Physics*, 50(4):2583, 1979.

[122] P. Belanger. High order shear horizontal modes for minimum remnant thickness. *Ultrasonics*, 54(4):1078–87, 2014.

[123] A. V. Oppenheim and R. W. Schafer. *Discrete-time Signal Processing*. Prentice-Hall signal processing series. Prentice Hall, 1989.

[124] J. W. Cooley and J. W. Tukey. An algorithm for the machine calculation of complex Fourier series. *Mathematics of Computation*, 19(90):297–297, 1965.

[125] COMSOL. Comsol Multiphysics [Online]. Available: https://www.comsol.com/ [Accessed: 24-Aug-2015]., 2015.

[126] PZFlex. PZFlex Weidlinger Associates inc. [Online]. Available: https://pzflex.com/ [Accessed: 24-Aug-2015]., 2015.

[127] C. B. Scruby and L. E. Drain. *Laser ultrasonics*. Adam Hilger, Bristol, 1990.

[128] D. A. Hutchins, C. Saleh, M. Moles, and B. Farahbahkhsh. Ultrasonic NDE using a concentric laser/EMAT system. *Journal of Nondestructive Evaluation*, 9:247–261, 1990.

[129] D. A. Hutchins. Mechanisms of pulsed photoacoustic generation. *Canadian Journal of Physics*, 64(9):1247–1264, 1986.

[130] W. Gao, C. Glorieux, and J. Thoen. Study of circumferential waves and their interaction with defects on cylindrical shells using line-source laser ultrasonics. *Journal of Applied Physics*, 91(9):6114, 2002.

[131] S. Dixon, S. E. Burrows, B. Dutton, and Y. Fan. Detection of cracks in metal sheets using pulsed laser generated ultrasound and EMAT detection. *Ultrasonics*, 51(1):7–16, 2011.

[132] Z. Guo, J.D. Achenbach, and S. Krishnaswamy. EMAT generation and laser detection of single lamb wave modes. *Ultrasonics*, 35(6):423–429, 1997.

[133] R.J. Smith, W. Li, J. Coulson, M. Clark, M. G. Somekh, and S. D. Sharples. Spatially resolved acoustic spectroscopy for rapid imaging of material microstructure and grain orientation. *Measurement Science and Technology*, 25:055902, 2014.

[134] W. Gao, C. Glorieux, and J. Thoen. Laser ultrasonic study of Lamb waves: determination of the thickness and velocities of a thin plate. *International Journal of Engineering Science*, 41(2):219–228, 2003.

[135] J. L. Deán, C. Trillo, A. F. Doval, and J. L. Fernández. Determination of thickness and elastic constants of aluminum plates from full-field wavelength measurements of single-mode narrowband Lamb waves. *The Journal of the Acoustical Society of America*, 124(3):1477–89, 2008.

[136] M. G. Silk. *Ultrasonic Transducers for Nondestructive Testing*. Adam Hilger Ltd, 1984.

[137] H. Nishino, T. Asano, Y. Taniguchi, K. Yoshida, H. Ogawa, M. Takahashi, and Y. Ogura. Precise Measurement of Pipe Wall Thickness in Noncontact Manner Using a Circumferential Lamb Wave Generated and Detected by a Pair of Air-Coupled Transducers. *Japanese Journal of Applied Physics*, 50(7):07HC10, 2011.

[138] H. Nishino, K. Yoshida, and T. Asano. Efficient Transduction of Circumferential Lamb Waves by a Pair of Line Focus Type Noncontact Air-coupled Ultrasonic Transducers and its Application for Accurate Measurement of Pipe. *E-Journal of Advanced Maintenance*, 2:181–190, 2011.

[139] D. Tuzzeo and F. L. di Scalea. Noncontact air-coupled guided wave ultrasonics for detection of thinning defects in aluminum plates. *Research in Nondestructive Evaluation*, 13(2):61–77, 2001.

[140] Innerspec. Innerspec Powerbox H Manual [Online] Available: http://innerspec.com/wp-content/uploads/2016/03/TPBH-OM-C15.pdf [Accessed 26-Jun-2016]., 2016.

[141] Ritec. Ritec RPR4000 pulser receiver specs [Online] Available: http://www.ritecinc.com/index.php/our-products/systems [Accessed 26-Jun-2016], 2016.

[142] G. W. C. Kaye and T. H. Laby. Tables of Physical and Chemical Constants: 2.4.1 The speed and attenuation of sound, [Online] Available: http://www.kayelaby.npl.co.uk/general_physics/2_4/2_4_1.html [Accessed 25-Mar-2016]., 2005.

[143] Sonomatic Ltd, EMAT topside scanner [Online]. Available: http://www.vsonomatic.com/downloads/managed/430/Topside%20EMAT%20Technical%20Specifications.pdf [Accessed: 06-Sep-2016]., 2016.

[144] Lei Kang, Shujuan Wang, Tao Jiang, and Guofu Zhai. Optimal Design of Lamb Wave Electromagnetic Acoustic Transducers for Improving Their Excitation Performance. *Japanese Journal of Applied Physics*, 50(7):07HD01, jul 2011.

[145] Z. Chen. *The Finite Element Method: Its Fundamentals and Applications in Engineering*. World Scientific, 2011.

[146] W. R. Scott. Errors Due to Spatial Discretization and Numerical Precision in the Finite-Element Method. *IEEE Transactions on Antennas and Propagation*, 42(11):1565–1570, 1994.

[147] G. S. Warren and W. R. Scott. Numerical dispersion in the finite-element method using triangular edge elements. *Microwave and Optical Technology Letters*, 9(6):315–319, 1995.

[148] C. T. F. Ross. *Finite Element Methods in Structural Mechanics*. Ellis Horwood Series in Mechanical Engineering. Prentice Hall, 1985.

[149] O. C. Zienkiewicz, R. L. Taylor, and J. Z. Zhu. *The Finite Element Method: Its Basis and Fundamentals*. Elsevier Science, 2005.

[150] K. J. Bathe. *Finite Element Procedures in Engineering Analysis*. Prentice-Hall civil engineering and engineering mechanics series. Prentice-Hall, 1982.

[151] N. N. Abboud, G. L. Wojcik, D. K. Vaughan, J. Mould Jr., D. J. Powell, and L. Nikodym. Finite element modeling for ultrasonic transducers. *Proceedings of SPIE Medical Imaging*, 3341(212), 1998.

[152] I. S. Sandler. A new computational procedure for wave propagation problems and a new procedure for non-reflecting boundaries. *Computer Methods in Applied Mechanics and Engineering*, 164(1-2):223–233, 1998.

[153] J. K. Van Velsor, J. L. Rose, and J. B. Nestleroth. Detection of Protective Coating Disbonds in Pipe Using Circumferential Guided Waves. In *17th World Conference on Non- destructive testing*, pages 25–28, Shanghai, 2008.

[154] S. Wang, Z. Li, L. Kang, X. Hu, and X. Zhang. Modeling and comparison of three bulk wave EMATs. *IECON 2011 - 37th Annual Conference of the IEEE Industrial Electronics Society*, (5):2645–2650, 2011.

[155] T. Grahn. Lamb wave scattering from a circular partly through-thickness hole in a plate. *Wave Motion*, 37(1):63–80, 2003.

[156] P. Rajagopal and M. J. S. Lowe. Scattering of the fundamental shear horizontal guided wave by a part-thickness crack in an isotropic plate. *The Journal of the Acoustical Society of America*, 124(5):2895–2904, 2008.

[157] L. Cohen. Time-Frequency Distributions-A Review. *Proceedings of the IEEE*, 77(7):941–981, 1989.

[158] T. W. Parks. A Resolution Comparison of Several Time-Frequency Representations. *IEEE Transactions on Signal Processing*, 40(2):413–420, 1992.

[159] M. Niethammer, L. J. Jacobs, J. Qu, and J. Jarzynski. Time-frequency representations of Lamb waves. *The Journal of the Acoustical Society of America*, 109(5):1841, 2001.

[160] J.-C. Hong, K. H. Sun, and Y. Y. Kim. Dispersion-based short-time Fourier transform applied to dispersive wave analysis. *The Journal of the Acoustical Society of America*, 117(5):2949, 2005.

[161] S. Hill and S. Dixon. Localisation of defects with time and frequency measurements using pulsed arrays. *NDT & E International*, 67:24–30, 2014.

[162] H. Bai, A.H. Shah, N. Popplewell, and S.K. Datta. Scattering of guided waves by circumferential cracks in composite cylinders. *International Journal of Solids and Structures*, 39(17):4583–4603, 2002.

[163] O. Diligent and M. J. S. Lowe. Reflection of the s[sub 0] Lamb mode from a flat bottom circular hole. *The Journal of the Acoustical Society of America*, 118(5):2869, 2005.

[164] S. Fletcher, M. J. S. Lowe, M. Ratassepp, and C. Brett. Detection of Axial Cracks in Pipes Using Focused Guided Waves. *Journal of Nondestructive Evaluation*, 31(1):56–64, 2011.

[165] P. A. Doyle and C. M. Scala. Crack depth measurement by ultrasonics: a review. *Ultrasonics*, 16(4):164–170, 1978.

[166] D. L. Olson, A. N. Lasseigne, M. Marya, and B. Mishra. Weld features that differentiate weld and plate corrosion. *Practical Failure Analysis*, 3(5):43–57, 2003.